ISSTT2012 Program

April 2nd (Monday)

8:45 Registration
9:15 Opening Talk

9:20-9:50 Invited Talk   session chair: Brian Jackson

I-1	Pajot, François	IAS	Planck : performance of the HFI instrument during 30 months of operation in space

9:50-10:50 THz Systems I

C-1	Huebers, Heinz-Wilhelm	DLR	Progress toward a 4.7-THz front-end for the GREAT heterodyne spectrometer on SOFIA
C-2	Emrich, Anders	Omnisys Instrument	The STEAMR instrument
C-3	Reck, Theodore	JPL/Caltech	PASEO - An integrated Radiometer and Spectrometer for Improved Planetary Science

10:50-11:10 Coffee Break

11:10-12:30 Coherent Detectors I   session chair: Takashi Noguchi

C-4	Shan, Wenlei	PMO	An Integrated SIS Multibeam Receiver for Terahertz Astronomical Observation
C-5	Puetz, Patrick	KOSMA	Characterisation of Local Oscillator Noise with a 400 - 500 GHz Integrated Balanced SIS Receiver
C-6	Tong, Edward	SAO	Wideband SIS Receivers Using Series Distributed SIS Junction Array
C-7	Groppi, Chris	Arizona State University	The Kilopixel Array Pathfinder Project (KAPPa), a 16 pixel integrated SIS focal plane array

12:30-14:00 Lunch

14:00-14:30 Invited Talk   session chair: Imran Mehdi

I-2	Griffin, Matt	Cardiff University	Herschel-SPIRE Performance and Science Highlights

14:30-15:30 Coherent Detectors II

C-8	Richter, Heiko	DLR	A 2.5-THz heterodyne spectrometer front-end integrated in a pulse-tube cooler
C-9	Treuttel, Jeanne	LERMA	A Novel 330 GHz Sub-Harmonic Mixer with Independently Biased Schottky Diodes
C-10	Rea, Simon	RAL	A Compact 340 GHz Receiver Array Front-End

15:30-16:30 Coffee Break and Poster Session

16:30-17:00 Invited Talk   session chair: Sergey Shitov

I-3	Hasegawa, Tetsuo	NAOJ	ALMA: status of construction and the initial observations

17:00-18:30 ALMA

C-11	Yassin, Ghassan	University of Oxford	The Prospects of THz Technology for ALMA 'Band 11'
C-12	Hwang, Yuh-Jing	ASIAA	Development Progress and Production Plan of ALMA Band-1 Receivers in Taiwan
C-13	Tan, Boon Kok	University of Oxford	A 700 GHz Integrated Balanced SIS Mixer
C-14	Fujii, Yasunori	NAOJ	Performance of the first six ALMA Band 10 receivers

April 3rd (Tuesday)

9:00-9:30 Invited Talk　　　　　　　　　　　　　　session chair: Shuji Matsuura

I-4	Otsuji, Taiichi	Tohoku University	Emission and Detection of Terahertz Radiation Using Two-Dimensional Electrons in III-V Semiconductors and

9:30-10:30 THz Systems II

C-15	Nihei, Ryota	University of Tsukuba	Development of an ultra-sensitive far-infrared detector based on double quantum-well structure
C-16	Probst, Petra	Karlsrue Institute of Technology	YBa2Cu3O7-high-speed detectors for picosecond THz pulses
C-17	Bevilacqua, Stella	Chalmers University of Technology	Fast room temperature THz microbolometers

10:30-10:50 Coffee Break

10:50-12:30 THz components　　　　　　　　　　　session chair: Kamaljeet Saini

C-18	Crowe, Thomas	Virginia Diodes Inc.	Multiplier-based Sources for 3THz and Beyond
C-19	Siles, Jose	JPL/Caltech	Enabling Compact Multi-Pixel Heterodyne Terahertz Receivers Using On-Chip Power-Combined Multiplied
C-20	Morgan, Matt	NRAO	Graphical Prediction of Trapped Mode Resonances in Sub-mm and THz Networks
C-21	Wollack, Edward	GSFC/NASA	High Absorptance Coatings for THz Applications
C-22	Nitta, Tom	University of Tsukuba	Beam Pattern Measurements of Millimeter-wave MKIDs Camera with Direct Machined Silicon Lens Array

12:30-14:00 Lunch

14:00-14:30 Invited Talk　　　　　　　　　　　　　session chair: Charles Cunningham

I-5	Roelfsema, Peter	SRON	Herschel-HIFI THz technology in action for astrophysics

14:30-15:30 THz Systems III

C-23	Jellema, Willem	SRON	An Optical Design Concept for Future Heterodyne Instrumentation in Space
C-24	Matsuo, Hiroshi	NAOJ	Photon Counting Terahertz Interferometry
C-25	Baryshev, Andrey	SRON	Interferometry using dual photon response of submm direct detectors

15:30-16:30 Coffee Break and Poster Session

16:30-18:30 SPICA and Incoherent Detector: session chair: Ken Wood

C-26	Nakagawa, Takao	JAXA	The next-generation infrared space mission SPICA
C-27	Roelfsema, Peter	SRON	The SAFARI Imaging Spectrometer for the SPICA space observatory
C-28	Gao, Jian Rong	SRON	TES technology for SPICA-SAFARI
C-29	Morozov, Dmitry	Cardiff University	Optical performance of ultrasensitive FIR TES detectors for future space missions
C-30	den Hartog, Roland	SRON	Frequency Division Multiplexed readout of TES detectors with Baseband Feedback
C-31	Bradford, Matt	JPL/Caltech	BLISS and Ultrasensitive Bolometers for SPICA

Banquet (19:00-21:00)

April 4th (Wednesday)

9:00-9:30 Invited Talk　　　　　　　　　　　session chair: Karl Schuster

I-6	Hazumi, Masashi	KEK	LiteBIRD: A Small Satellite for the Studies of B-mode Polarization and Inflation from Cosmic Background Radiation Detection

9:30-10:30 LiteBIRD and Incoherent Detectors II

C-32	Karatsu, Ken'ichi	NAOJ	Development of 1000 arrays MKID Camera for the CMB Observation
C-33	Koga, Kensuke	Tohoku University	Development of TiN-MKIDs for CMB polarization observations
C-34	Suzuki, Aritoki	UCBerkeley	Multi-chroic dual-polarization bolometric focal plane for studies of the Cosmic Microwave

10:30-11:00 Coffee Break

11:00-12:20 Incoherent Detectors III　　　　　session chair: Chiko Otani

C-35	Endo, Akira	Delft University of Technology	DESHIMA: Redshift Machine Based on an On-chip Filterbank
C-36	Roesch, Markus	IRAM	Dual polarization Lumped Element Kinetic Inductance Detectors (LEKID) for 1.25 and 2.05mm
C-37	Ferrari, Lorenza	SRON	Taking a snapshot of KIDs
C-38	Chattopadhyay, Goutam	JPL/Caltech	Ultra-Compact Superconducting Spectrometer on a Chip at Submillimeter Wavelengths

12:20-14:00 Lunch

14:00-14:30 Invited Talk　　　　　　　　　　session chair: Wolfgang Wild

I-7	Chen, Ming-Tang	ASIAA	THE YUAN-TSEH LEE ARRAY FOR MICROWAVE BACKGROUND ANISOTROPY

14:30-15:30 THz Systems IV

C-39	Shi, Sheng-Cai	PMO	Development of THz Superconducting Receivers for DATE5
C-40	Blundell, Raymond	SAO / ASIAA	A New Telescope for Ground-based THz Astronomy
C-41	Smirnov, Andrey	Astro Space Center	THz space mission Millimetron

15:30-16:30 Coffee Break and Poster Session

16:30-17:50 Coherent Detectors III　　　　　session chair: Alain Maestrini

C-42	Goltsman, Gregory	Moscow State Pedagogical University	Study of the superconductor-normal metal interface in hot-electron bolometer mixers
C-43	Shiino, Tatsuya	University of Tokyo	The 0.9 and 1.3 THz Superconducting HEB Mixer Receiver for the ASTE 10 m Telescope
C-44	Zhang, Wen	PMO	A 1.4-THz Superconducting HEB Mixer for DATE5
C-45	Ren, Yuan	Delft University of Technology	Stabilized HEB-QCL heterodyne spectrometer at super-terahertz

Conference Summary

Adjourn

Poster Presentations

P-1	Mizobuchi, Satoko	JAXA	In-orbit Stability Evaluation of the AOS (Acousto-Optical Spectrometer) of Superconducting Submillimeter-Wave Limb-Emission Sounder (JEM/SMILES)
P-2	Schlecht, Erich	JPL/Caltech	Terahertz Radiometer for Outer Planet and Moon Atmospheres (TROPA)
P-3	Whale, Mark	University of Bern	The STEAMR Instrument: Optical Design, Development and Testing
P-4	Emrich, Anders	Omnisys Instrument	Possible Swedish contributions to the FIRE instrument
P-5	Krus, M.	Omnisys Instrument	Spectrometers for THz space applications
P-6	Risacher, Christophe	MPIfR	GREAT : Successful first year of science operation
P-7	Risacher, Christophe	MPIfR	Extension of GREAT into a first heterodyne array for far infrared spectroscopy with SOFIA
P-8	Chen, Zhe	University of Electronic Science and Technology	Development of a 220-GHz Schottky Diode Subharmonic Mixer
P-9	Thomas, Bertrand	RPG	First results of a 1.2 THz MMIC sub-harmonic mixer based GaAs Schottky diodes for planetary atmospheric remote sensing
P-10	Wang, Hui	RAL	A Performance Comparison of Discrete and Integrated Sub-Harmonic Schottky Diode Mixers at 664GHz
P-11	Lee, Jung-Won	KASI	129 GHz SIS Mixer Receiver for Korean VLBI Network
P-12	Nakajima, Tac	NAOJ	Development of a New Multi-Beam Array 2SB Receiver in 100 GHz Band for the NRO 45-m Radio Telescope
P-13	Grimes, Paul	SAO	A 350 GHz Multi-beam Receiver for the GreenLand
P-14	Ishii, Shun	University of Tsukuba	Development of a Transportable Telescope for Galactic Survey at 500 GHz in Antarctica
P-15	Khudchenko, Andrey	SRON	Sideband Separating Mixer Characterization based on SIS junction properties
P-16	Kroug, Matthias	NAOJ	Al/SiO2/Al Micro Strip Lines for THz SIS Mixers
P-17	Zhou, Yangjun	University of Oxford	The design and characterisation of ultrawide IF bandwidth SIS mixers
P-18	Chang, Hsian-Hong	ASIAA	Development of 1.4THz Hot Electron Bolometers
P-19	Hayton, Darren	SRON	Stabilized HEB receiver at 2.5 THz
P-20	Boussaha, Faouzi	JPL/Caltech	2.7 THz Waveguide Balanced HEB Mixer Development
P-21	Furuya, R.	University of Tokyo	Fabrication of HEB Mixers Using Substrate Heating in Combination with the AlN Buffer Layers
P-22	Jiang, Ling	Nanjing Forestry University	Intrinsic Mixing Behavior of Superconducting NbTiN HEB Mixer Based on in-situ Technique
P-23	Lefèvre, Roland	LERMA	Terahertz NbN hot electron bolometer fabrication process with a reduced number of steps
P-24	Miao, Wei	PMO	Non-Uniform Absorption of Terahertz Radiation in Superconducting Hot-Electron Bolometer Mixers
P-25	Bevilacqua, Stella	Chalmers University of Technology	MgB2 Hot Electron Bolometers for THz radio astronomy
P-26	Huang, Yau De	ASIAA	ALMA East Asia Front-End Integration Center
P-27	Hasegawa, Tetsuo	NAOJ/JAO	Integration and verification of ALMA receiver front ends
P-28	Henry, Manju	RAL	Upgraded Local Oscillator System for the ALMA Band 5 Receiver
P-29	Barkhof, J.	University of Groningen	Sideband Separating Mixer for ALMA Band 9 Upgrade: operational aspects
P-30	Gonzalez, Alvaro	NAOJ	Improvements in ALMA band 10 optics: Influence of IR filters and solutions
P-31	Baryshev, Andrey	SRON	Dual frequency ALMA operation extension

P-32	Hesler, Jeffrey	Virginia Diodes Inc.	Wideband THz Sources Using Waveguide Diplexers
P-33	Siles, Jose	JPL/Caltech	A High-Power Biasable 180-200 GHz Schottky Frequency Doubler Using Single-Waveguide Power-Combining
P-34	Thomas, Bertrand	RPG	W-band balanced frequency tripler using a novel coupled lines biasing scheme compatible with flip-chip mounting
P-35	Treuttel, Jeanne	LERMA	Solid State Frequency Multipliers at Sub-Millimeter Wavelength Using European Schottky Technology
P-36	Richter, Heiko	DLR	Operation of a THz quantum-cascade laser in a compact mechanical cryocooler
P-37	Eichholz, R.	DLR	Frequency selection from a multi-mode THz quantum-cascade laser by a grating monochromator
P-38	Hammar, Arvid	Omnisys	A 600 GHz Orthomode Transducer based on a Waveguide Integrated Wire Grid Polarizer
P-39	Navarrini, Alessandro	IRAM	Loss of WR10 Waveguide at 67-116 GHz
P-40	Ishidoshiro, Koji	KEK	Characterization System with Cryogenically-Cooled Loads for next-generation CMB Polarimeters
P-41	Laauwen, Wouter	SRON	Development of a Calibration Source for SAFARI on-ground Calibration
P-42	Hammar, Arvid	Omnisys	Mechanical Tolerance Analysis of the Front-end Optics for the STEAMR Instrument
P-43	Liu, Lei	University of Notre Dame	Cost-Effective Terahertz Quasi-Optical Components Based on Inkjet Printing of Carbon Nanocomposite
P-44	Takekoshi, Tatsuya	Hokkaido University	Optics design of the multi-color TES bolometer camera for the ASTE telescope
P-45	Rahman, Syed	University of Notre Dame	The Development of Terahertz Focal-Plane Array Elements Using Sb-Based Heterostructure Backward Diode
P-46	Takahashi, Kenta	RIKEN	Development of micro-stripline superconducting tunnel junction detectors for terahertz waves
P-47	Hibi, Yasunori	NAOJ	Cryogenic Multi-Channel Readout System for Submillimeter/Terahertz Photon Detectors
P-48	Matsumura, Tomotake	KEK	LiteBIRD Optics, Focal Plane Layout and Sensitivity
P-49	Watanabe, Hiroki	KEK	Development of Superconducting Cooper-pair-breaking Detectors for LiteBIRD
P-50	Kibe, Yoshiaki	Okayama University/KEK	Development of Microwave Kinetic Inductance Detector and its Read-out System for LiteBIRD
P-51	Tajima, Osamu	KEK	GroundBIRD – An experiment for CMB polarization measurements at a large angular scale from the ground
P-52	Naruse, Masato	NAOJ/Saitama University	Development of a MKID camera with high-quality Al films for millimeter-wave astronomy
P-53	Thoen, David	Delft University of Technology	Stray Light Shielding in Transmission Lines for Integrated Filterbanks
P-54	Ferrari, Lorenza	SRON	Development of antenna-coupled KIDs for large cameras
P-55	Janssen, Reinier	Delft University of Technology	Quasiparticle Diffusion and Detection Efficiency of Hybrid Kinetic Inductance Detectors
P-56	Matsuhara, Hideo	JAXA	Cold Payload Module of SPICA
P-57	Jackson, Brian	SRON	Performance Requirements for the SAFARI Detector
P-58	Jackson, Brian	SRON	The SAFARI Focal Plane Array Design Concept
P-59	Khosropanah, Pourya	SRON	Low Noise TES Array for the Short Wavelength Band of the SAFARI Instrument on SPICA
P-60	Audley, Damian	SRON	Optical Measurements of TES Bolometers for SAFARI
P-61	Ferrari, Lorenza	SRON	Focal plane scanning-system design for SAFARI on Ground Calibration
P-62	Beyer, Joern	PTB	SQUID current sensor to read out the TES-bolometers arrays for SAFARI
P-63	Karasik, Boris	JPL/Caltech	Tunable speed single-photon THz nanobolometers
P-64	Shitov, Sergey	IRE	Development of TES Bolometers with High-Frequency Readout Circuit

Planck : performance of the HFI instrument after 30 months of operation in space

F. Pajot[1*] for the Planck Collaboration[2]

1 Institut d'Astrophysique Spatiale, Université Paris Sud-11, 91405 Orsay, France
2 Planck (http://www.esa.int/Planck)
* Contact: francois.pajot@ias.u-psud.fr, phone +33 1 6985 8567

Abstract— **Launched in May 2009, the HFI instrument of the Planck satellite has been operated flawlessly for more than 30 months. The detectors, highly sensitive bolometers, were cooled and kept continuously at 100 mK, in the environment of the Earth-Sun lagrangian point L2 orbit. The performance of the detection chain will be presented, as well as the analysis of the main systematics and their impact on the data processing. These systematics include interactions of the high energy cosmic particules with the detectors and the cryochain. An outline of the main astrophysical results achieved so far will illustrate the success of the Planck mission.**

Progress toward a 4.7-THz front-end for the GREAT heterodyne spectrometer on SOFIA

H.-W. Hübers [1), 2)*], H. Richter [2)], S. G. Pavlov [2)], A. Semenov[2)], M. Wienold [3)], L. Schrottke [3)],
K. Biermann [3)], R. Hey [3)], H. T. Grahn [3)], K. Il'in[4)], and M. Siegel[4)]

*1 Institute of Planetary Research, German Aerospace Center (DLR), Rutherfordstr. 2,
12489 Berlin, Germany*
*2 Institut für Optik und Atomare Physik, Technische Universität Berlin, Hardenbergstraße 36,
10623 Berlin, Germany*
3 Paul-Drude-Institut für Festkörperelektronik, Hausvogteiplatz 5–7, 10117 Berlin, Germany
*4 Institut für Mikro-und Nanoelektronische Systeme, Karlruhe Institut für Technologie, Hertzstr. 16, 76187
Karlsruhe, Germany*
`* Contact: heinz-wilhelm.huebers@dlr.de, phone +49-30-67055 596`

Abstract──**Heterodyne spectroscopy of molecular rotational lines and atomic fine-structure lines is a powerful tool in astronomy and planetary research. It allows for studying the chemical composition, the evolution, and the dynamical behaviour of astronomical objects, such as molecular clouds and star-forming regions. For frequencies beyond 2 THz, SOFIA, the Stratospheric Observatory for Infrared Astronomy, is currently the only platform which allows for heterodyne spectroscopy at these frequencies. One example is the OI fine structure line at 4.7 THz, which is a main target to be observed with GREAT, the German Receiver for Astronomy at Terahertz Frequencies, on board of SOFIA**

We report on the development of the 4.7-THz high-frequency channel for GREAT. The local oscillator (LO) combines a quantum-cascade laser (QCL) with a compact, low-input-power Stirling cooler. The 4.7-THz QCL is based on a two-miniband design and has been developed for continuous-wave operation, high output powers, and low electrical pump powers. Efficient carrier injection is achieved by resonant longitudinal optical phonon scattering. At the same time, the operating voltage can be kept below 6 V. The amount of generated heat complies with the cooling capacity of the Stirling cooler of 7 W at 65 K with 240 W of electrical input power [1]. The whole system weighs less than 15 kg including cooler, power supplies etc. Frequency stabilization to below 300 kHz full width at half maximum can be achieved by locking the emission from the QCL to a molecular absorption line [2]. The mixer is a phonon-cooled NbN hot electron bolometer (HEB). It is a 2 μm wide, 0.2 μm long, and 5.5 nm thin NbN strip on a high resistivity (> 5 kΩ) silicon substrate located in the center of a planar logarithmic spiral antenna and glued onto the flat side of an extended hemispherical 12 mm diameter silicon lens. The design of the front-end, its implementation into GREAT, and first results of its subcomponents, in particular the LO and the mixer, will be presented.

[1] H. Richter, M. Greiner-Bär, S. G. Pavlov, A. D. Semenov, M. Wienold, L. Schrottke, M. Giehler, R. Hey, H. T. Grahn, and H.-W. Hübers, Opt. Express 18, 10177–10187 (2010).
[2] H. Richter, S. G. Pavlov, A. D. Semenov, L. Mahler, A. Tredicucci, H. E. Beere, D. A. Ritchie, and H.-W. Hübers, Appl. Phys. Lett. 96, 071112 (2010).

The STEAMR instrument

A. Emrich[1*], U. Frisk[1], P. Sobis[1], J. Embretsen[1], K. Kempe[1], S. Andersson[1], A. Murk[2], M. Whale[2], A. Hammar[1] and C. Emrich[1]

1 Omnisys Instrument AB, Västra Frölunda, S-42130, Sweden
2 Institute of Applied Physics, University of Bern, CH-3012 Bern, Switzerland
* Contact: ae@omnisys.se, phone +46-31-7343488
The work is financed by the Swedish National Space Board and XX.

Abstract——The envisaged limb viewing of STEAMR is based on a staring concept with 14 beams, polarised at ± 45 degrees, covering a nominal altitude range of 6-28 km at mid latitudes. The complete STEAMR instrument will be presented on system level, including antenna, optics, calibration system, focal plane array, 340 GHz front-ends and 12 GHz wide back-ends. Omnisys is now prime for the STEAMR instrument and is performing prototyping work for 4 complete radiometer channels of the 14 planned for the flight instrument in parallel to system studies towards ESA for the Premier satellite platform. Test results will be presented. Parts of the optics (IAP) and the calibration system is also being prototyped and the complete instrument development plan has now been addressed and presented.

The current optical design concept is based on a six-mirror system, including a Ritchey-Chretien telescope that routes the incoming beam to the focal plane unit and the optics is diffraction-limited by the 1.6 x 0.8 m aperture of the primary reflector.

The calibration system consist of a beam chopper and a reference selector and the references will be two absorptive loads at different temperatures, a nadir view (TBC) and CW source to test sideband conversion ratio and signal response of the complete receiver chain.

The receiver front-ends consists of subharmonic mixers with integrated LNA's with the LO pumped by an active x6 multiplier and x2 schottky doubler with a power consumption of < 800 mW per channel, including LO and IF LNA. These 14 front-ends are connected via an IF system to 14x2 6 GHz wide spectrometers in the back-end. 12 GHz bandwidth is being processed with 1024 channels per band with a resolution of <20 MHz after post processing. The spectrometers are based on the HIFAS ACS ASIC presented at ISSTT 2009. The complete instrument is estimated to consume 307 W and have a mass of 102.5 kg, including contingencies.

The instrument system design will also be briefly described in terms of accommodation issues on the platform, system integration and test plans as well as structural and thermal analyses results from the system study effort.

The dashed lines indicate Jupiter trajectory through STEAMR field of view
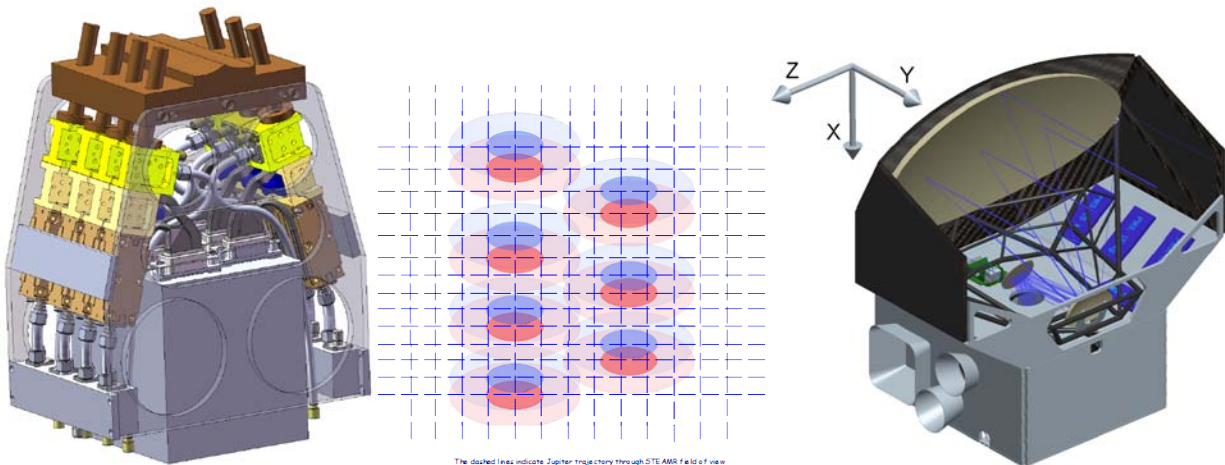
PASEO – An integrated Radiometer and Spectrometer for Improved Planetary Science

T. Reck[1*], C. Jung[1], J. Siles[1], Bertrand Thomas[2], J. Gill[1], J. Ward[1], R. Lin[1], I. Mehdi[1], G. Chattopadhyay[1]

1 The Jet Propulsion Laboratory*, Pasadena, CA, 91030, USA
2 Radiometer Physics GmbH, Meckenheim, Germany
* Contact: Theodore.reck@jpl.nasa.gov, phone 1-818-393-5902

Abstract—**A submillimeter wavelength dual-polarization sideband separating receiver is being developed to significantly improve the measurement capabilities of future planetary missions. The Planetary Atmosphere and Surface Explorer from Orbit (PASEO) is a wideband radiometer and spectrometer operating at 520-600 GHz that will provide a factor of two improvement in sensitivity over existing planetary instruments. The sideband separated output of the mixer enables an instantaneous output bandwidth of 40 GHz, providing simultaneous spectrographic observation of several important atmospheric species.**

The focus of this project is to develop the necessary components to demonstrate this instrument in preparation for future flight missions. An orthogonal-mode transducer is the first component in the receiver. This separates the polarization of the incoming signal into two channels. Then a waveguide twist is used to rotate one of these channels to the polarization of the sideband separating mixer. Each channel enters a balanced mixer that produces two IFs of 20 GHz bandwidth.

A significant portion of this project is the integration of these components into a single, high-density package. This will be accomplished by forming the passive components with Deep Reactive Ion Etching (DRIE) of silicon. By using silicon micromachining to form the waveguide components and housing of the system, the fabrication precision can be improved over that of tradition CNC machining. Techniques for coupling to the silicon devices using custom metal flanges will be discussed. VNA measurements of the silicon components will be compared with devices fabricated using standard metal machining fabrication techniques.

An Integrated SIS Multibeam Receiver for Terahertz Astronomical Observation

Wenlei Shan, Shengcai Shi, and Ji Yang
Purple Mountain Observatory, Chinese Academy of Sciences, Nanjing 210008, China

Contact: shan@pmo.ac.cn, phone +86-25-8333 2229

As expanding of the field of view of next generation single-dish Terahertz telescope, multibeam heterodyne receivers with pixel number up to 1000 are desired. This large format arrays can hardly be assembled with single elements, because the complexity of electrical wiring for biasing of SIS mixers, LNAs and electromagnetic coils will significantly decrease the operational reliability. Therefore, an integrated multibeam frontend unit with all wiring embedded in a single block should have apparent advantage in system stability and reliability. In this paper, we introduce a concept design of an integrated SIS multibeam receiver frontend. It features a single assembled block composed of machined layers, including horn antenna array, LO distribution network, SIS mixer and chip LNA mount, wiring layer, each of which performs a dedicated function. The assembled single block has common connectors for bias of all pixels in the array. In addition, since the array can be made very compact, it may allow LO distributed in a waveguide transmission line network with acceptable transmission loss. Waveguide LO distribution can largely simplify the optical design of the frontend and make the receiver compatible for space or unmanned ground-based telescope applications.

Characterisation of Local Oscillator Noise with a 400 – 500 GHz Integrated Balanced SIS Receiver

M. P. Westig[*], M. Justen, K. Jacobs, P. Pütz, M. Schultz, J. Stutzki, and C. E. Honingh

Kölner Observatorium für Submm Astronomie (KOSMA),

I. Physikalisches Institut, Universität zu Köln, 50937 Köln, Germany

* Contact: westig@.ph1.uni-koeln.de, phone +49-221-470 3489

Abstract—**Excess spectral noise originating from synthesizer driven solid-state multiplier based LO chains is sometimes observed in the IF band of THz frequency SIS and HEB heterodyne receivers for radio astronomy. In order to gain a better understanding of the origin of the noise we present our measurements on the spectral noise contribution of such a local oscillator to a 400 – 500 GHz heterodyne receiver. Using an integrated balanced SIS mixer with two separate IF output ports we are able to characterize the LO noise contribution as a function of the IF frequency for various RF frequencies. We investigate how changes in the LO operating conditions, such as the saturation level of the power amplifier in the chain, affect the measured spectral noise power of the receiver IF. Comparison measurements of the synthesizer driven LO with one using a Gunn oscillator as source are presented as well.**

Wideband SIS Receivers Using Series Distributed SIS Junction Array

Edward Tong[a], Paul Grimes[a], Ray Blundell[a], Ming-jye Wang[b], Takashi Noguchi[c]

[a] *Harvard-Smithsonian Center for Astrophysics, Cambridge, MA, USA*
[b] *ASIAA, Taipei, Taiwan*
[c] *NAOJ, Mitaka, Tokyo, Japan*

We have developed an SIS mixer based on a 3-junction series array. In this new mixer layout, shown in Fig. 1, the 3 junctions are connected together by passive network elements, such that each junction is subjected to a different Local Oscillator drive, both in amplitude and phase. In addition, since the junctions are connected in series, they have slightly different bias voltages. Only the DC bias current is the same in each of the junctions. This design helps to reduce the IF output capacitance of the mixer so as to achieve a wider IF bandwidth.

We have made receiver noise measurements on a 200 GHz receiver incorporating this type of mixer chip, the results are summarized in Fig 2. From the figure, the lowest DSB noise temperature measured was ~32 K, and the noise temperature remains below 50 K over the IF range from 3 – 12 GHz. Receivers incorporating this new mixer design are currently being installed in the Submillimeter Array. The first pair of such receivers are in routine operation across the usual SMA IF of 4 – 8 GHz, and have been used in test interferometer observations to 12 GHz IF.

We are in the process of refining the design for wider bandwidth operation.
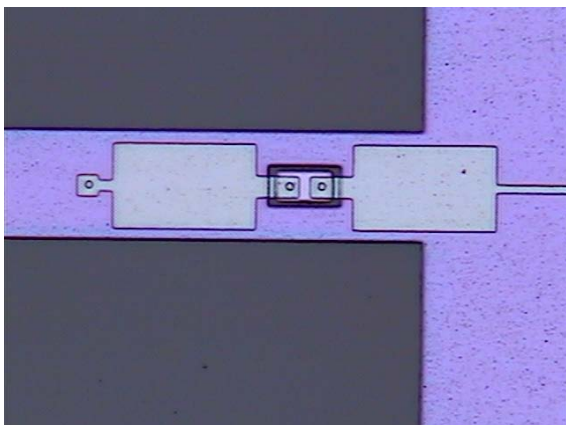
Fig. 1 Photograph of the 3-junction series array. The junctions are connected by transmission lines forming the distributed mixer. The input port is on the left and is linked to the junctions via a quarter-wave transformer.
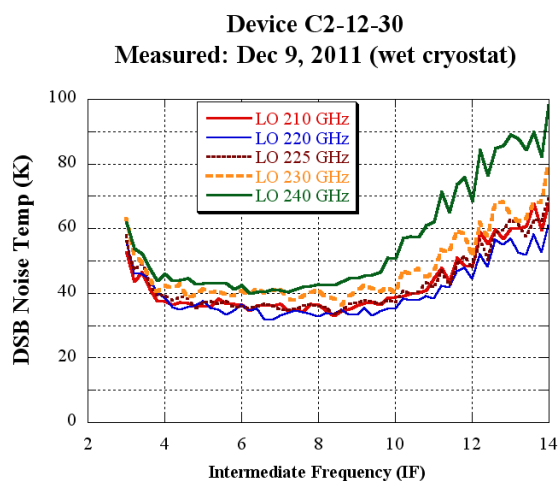
Fig. 2 Laboratory noise temperature of a receiver incorporating the 3-junction distributed mixer. Best measured Y-factor is 3, corresponding to 32 K receiver noise.

The Kilopixel Array Pathfinder Project (KAPPa), a 16 pixel integrated SIS focal plane array

C. E. Groppi[1*], C. H. Wheeler[1], H. Mani[1], S Weinreb[2], D. Russell[2], J. Kooi[2], A. Lichtenberger[3] and C. Walker[4]

1 Arizona State University*, Tempe, AZ, 85287 USA
2 California Institute of Technology, Pasadena, CA 91125
3 University of Virginia Microfabrication Laboratories, Charlottesville, VA 22904
4 University of Arizona, Tucson, AZ 85721 USA
* Contact: cgroppi@asu.edu, phone +1-480-965-6436

Abstract—**KAPPa (the Kilopixel Array Pathfinder Project) is developing key technologies to enable the construction of heterodyne focal plane arrays in the terahertz frequency regime with ~1000 pixels. The leap to ~1000 pixels requires solutions to several key technological problems before the construction of such a focal plane is possible. The KAPPa project will develop a small (16-pixel) 2D integrated SIS focal plane array for the 675 GHz atmospheric window as a technological pathfinder towards future kilopixel heterodyne focal plane arrays. KAPPa will use SIS devices fabricated on SOI membranes with beam lead alignment and connection features, designed for high yield and fast installation. A SiGe low noise amplifier with on-chip bias tee will be integrated directly into the mixer block immediately adjacent to each mixer. This amplifier has been designed to yield adequate gain and low noise temperature, while dissipating less than 2mW of power. The SIS and LNA devices will be mounted in a 2D integrated metal micromachined mixer array consisting of a backshort block containing the SIS device and LNA, and a horn block using drilled smooth-wall feedhorns. Magnetic field will be delivered to the devices via compact, permanent magnets embedded in the horn block. We will also develop cryogenically compatible IF flex circuits to replace individual semi-rigid coaxial lines for IF signal transmission. Once completed, this instrument will demonstrate the critical technologies necessary to construct coherent arrays approaching 1000 pixels for large single-dish THz telescopes like CCAT and SPT. We will report on the design and testing of a prototype pixel cell with integrated SiGe LNA and permanent magnet. This single pixel prototype will validate the KAPPA design approach before proceeding to the construction of the 16 pixel focal plane. In particular, this mixer is designed to accept both permanent magnets and an electromagnetic coil, allowing careful comparison of performance with the identical SIS chip and magnet geometry.**

Herschel-SPIRE Performance and Science Highlights

M. J. Griffin[1*] on behalf of the SPIRE Consortium

1 School of Physics and Astronomy, Cardiff University, The Parade, Cardiff CY24 3 AA, UK
* Contact: matt.griffin@astro.cf.ac.uk, phone +44-29-2087-4203

Abstract——**SPIRE, the Spectral and Photometric Imaging Receiver, is the submillimetre imager and spectrometer on board the *Herschel Space Observatory*, which was launched in May 2009 and will continue to operate until early 2013. SPIRE has a submillimetre camera operating simultaneously in three bands at 250, 350 and 500 μm, and an imaging Fourier transform spectrometer (FTS) covering 194 – 671 microns. The SPIRE detectors are arrays of spider-wed bolometers with NTD Ge thermistors, operating at a temperature of 300 mK. SPIRE is fully functional in flight, and its performance meets or exceeds pre-flight estimates in all respects, and the data processing pipelines are also producing high quality photometric and spectroscopic data. The main design features, operating modes, measured in flight performance, and scientific capabilities of the SPIRE photometer and spectrometer will be outlined, and some scientific highlights will be presented. The technical, operational, and scientific heritage the SPIRE FTS, and of *Herschel* in general, are important for future far infrared space astronomy, most immediately the SPICA mission, and these aspects will be emphasized.**

A 2.5-THz heterodyne spectrometer front-end integrated in a pulse-tube cooler

H. Richter [1)*], S. G. Pavlov [1)], A. Semenov[1)], L. Mahler[2)], A. Tredicucci [2)], H. E. Beere [3)], D. A. Ritchie[3)], K. Il'in[4)], M. Siegel[4)], and H.-W. Hübers [1), 5)]

1 Institute of Planetary Research, German Aerospace Center (DLR), Rutherfordstr. 2,
12489 Berlin, Germany
3 Cavendish Laboratory, University of Cambridge, Madingley Road, Cambridge CB3 0HE, United Kingdom NEST
CNR-INFM and Scuola Normale Superiore, Piazza dei Cavalieri 7, 56126 Pisa, Italy
4 Institut für Mikro-und Nanoelektronische Systeme, Karlsruhe Institut für Technologie, Hertzstr. 16, 76187
Karlsruhe, Germany
5 Institut für Optik und Atomare Physik, Technische Universität Berlin, Hardenbergstraße 36,
10623 Berlin, Germany

`* Contact: heiko.richter@dlr.de, phone +49-30-67055 697`

Abstract——**The terahertz (THz) portion of th e electromagnetic spectrum bears an amazing scientific potential in astronomy. High resolution spectroscop y in p articular heterodyne spectroscopy of mo lecular rotational lines and fine structure lines of atoms or ions is a powerful tool, which allows obtaining valuable information about the observed object such as temperature and dynamical processes as well as density and distribution of particular species. Examples are the OH rotational transitions at 2.5 THz, the HD rotational transition at 2.7 THz, and the OI fine structure line at 4.7 THz. These lines are, for example, major targets to b e observed with GREAT, th e German Receiver for Astronomy at Terahertz Frequencies, which will be oper ated on boar d of SOFIA. For SOFIA, a he terodyne receiver which does not require cooling by liquid cryogens will ease operation significantly, because the complexity and limitation of the operating time due to the use of cryo-liquids can be overcome.**

As part of a study for a sec ond generation heterodyne receiver on board o f SOFIA we are developing a 2.5-THz front-end which is imple mented in a pulse -tube cooler (PTC). It consists of a quant um-cascade laser (QCL) as loc al oscillator and a phonon-cooled NbN hot electron bolometric mixer. The QCL is mounted on the first stage of the PTC and operates at a temperature of approximately 50 K while the HEB is mounted on the second stage of the PTC (temperature ~5 K). Frequency stabilization to belo w 300 kHz full w idth at half maximum is achieved by locking to a mol ecular absorption line [2]. While the gas absorption cell is outside the PTC the Ge:Ga detector, which is necessary for the locking scheme, is mounted on the second cold stage. The intermediate frequency bandwidth of th e front end is 2-4 GHz. This band is down-converted to 0.3-1.5 GHz and analyzed with a digital fast Fourier transform spectrometer. We will present the design of the front-end, present the results of an end-to-end test, and discuss the prospects for an application on board of SOFIA.

A Novel 330 GHz Sub-Harmonic Mixer with Independently Biased Schottky Diodes

J.Treuttel[1*], B.Thomas[2], A.Maestrini[1&3], J.V-Siles[4], C.Lee[4] and I.Medhi[4]

*1 Observatoire de Paris, LERMA, Paris, 75014, France,*
2 Radiometer Physics GmbH, Meckenheim, Germany
*3 Université Pierre et Marie Curie, Paris, 75005, France,*
4 NASA-Jet Propulsion Laboratory, Pasadena, CA, USA,
* Contact: Jeanne.treuttel@obspm.fr, phone +33-1-40-51-20-79

Abstract – **The balanced properties and local oscillator (LO) frequency put to half the RF frequency of the sub-harmonically pumped mixers give a great advantage over single ended mixers. Moreover, biasing independently the two diodes offer the advantages of 1) reducing the LO power requirement, 2) allowing a larger range of LO power to pump the mixer and therefore improve the relative bandwidth with no other tuning than the LO frequency, and 3) compensating the asymmetries found for DC parameters characterization through I-V curve measurement. Nevertheless the implementation of DC-bias circuitry at high frequency is particularly delicate and mounting uncertainties can result in a breaking of the symmetry involved in the balance of the device and produce cross-mode coupling. Fairly large capacitors near the diode cell have been used in [1] with diodes in a balanced configuration, but this solution reduces the mode confinement near the diode and relies on the circuit mounting. Very compact on-chip capacitors have proven to be a solution but require a special effort in the fabrication of sub-micron circuits [2]. Another option consists in applying the bias through the IF port. This option offers the advantages of both biasing the diode independently with different voltage level and bypass the need of circuitry near the diodes. Multilayer transmission line designs to obtain independent DC-paths for the diodes of an anti-parallel pair mixer have been proposed in [3]. This solutions leads to a high fabrication effort and rely on the quality of the insulators and a pinhole density level. In order to bypass the drawbacks induced by these technological issues, we propose a novel sub-harmonic mixer at 330 GHz with a monolayer solution to compensate the diode imbalance of sub-terahertz devices. The circuit features a balanced pair of Schottky diodes in which the RF, LO and IF signals are transmitted on the even quasi-TEM mode of a split transmission line and the DC-bias voltage of each of the diodes comes from the IF port through a two-DC port bias tee. The implementation of the dual-DC port bias-tee with radial stub offers a simple way to use monolayer process in the 2-4 and 6-8 GHz IF frequency band. The measurements confirm that the signal propagates along the structure as predicted over the 320 - 360 GHz frequency band with an imbalance compensation under independent bias conditions for each of the diodes resulting in a improvement of the noise temperature up to 14 % at 335 GHz. This type of structure has potential applications at terahertz frequencies where high power source are scarce, and for foundries that want to avoid the use of capacitor on chip near the balanced diode cell.**
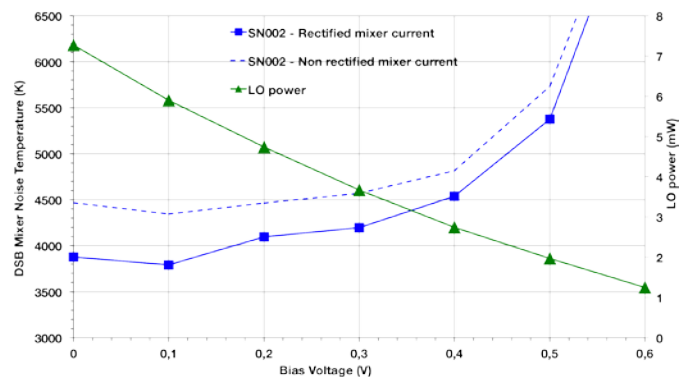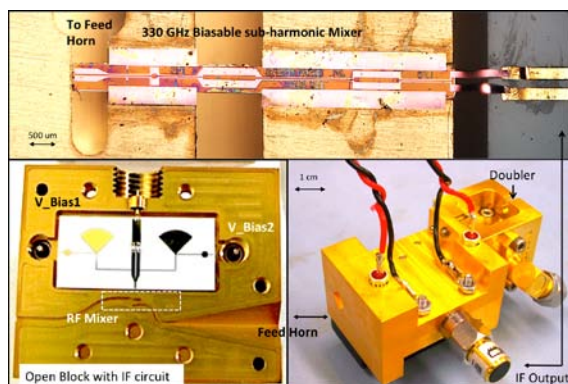
330 GHz biasable balanced sub-harmonic mixer: assembly and test at the Jet Propulsion Laboratory.

[1] E. Schlecht, J. Gill, R. Dengler, R. Lin, R. Tsang, and I. Mehdi, "A unique 520-590 GHz biased subharmonically-pumped schottky mixer," IEEE Microwave and Wireless Components Letters, vol. 17, no. 12, pp. 879–881, Dec. 2007. 1

[2] B. Thomas, A.Maestrini, B. Thomas, A. Maestrini, J. Gill, R. L. C. Lee, I. Mehdi, and P. de Maagt, "A broadband 835–900-GHz fundamental balanced mixer based on monolithic gaas membrane schottky diodes," IEEE Transactions on Microwaves Theory and Techniques, vol. No. 7, pp. 1917–1924, July 2010. 1

[3] T. Lee, C. Chi, J. Esat, G. Rebeiz, and G. Haddad, "A novel biased- anti-parallel schottky diode structure for subharmonic mixing," IEEE Microwave and Guided Wave Letters, vol. 4, no. 10, pp. 341–343, October 1994. 1, 3

A Compact 340 GHz Receiver Array Front-End

S. P. Rea[1*], M. Henry[1], H. Wang[1], B. Alderman[1], B. N. Ellison[1], Jeanne Treuttel[2], I. Maestrojuan Biurrun[3], and P. de Maagt[4]

[1]*Millimetre Technology Group, STFC Rutherford Appleton Laboratory, Didcot, United Kingdom, OX11 0QX*
[2]*Observatoire de Paris, LERMA, 75014 Paris, France*
[3]*Universidad Publica de Navarra, Campus Arrosadia s/n, Pamplona 31006, Navarra, Spain*
[4]*ESTEC, European Space Agency, P.O. Box 299, 2200AG Noordwijk ZH, The Netherlands*
* Contact: simon.rea@stfc.ac.uk, phone +44-1235-56 7157

Abstract——**This paper presents the design and measured performance of a compact 8-element Schottky diode-based heterodyne receiver array front-end. The work has been undertaken to address the growing interest in multi-pixel sub-millimetre wave instrumentation for remote sensing of the Earth. The array specification is based on the requirements of the STEAM-R instrument concept, part of the payload of the PREMIER Earth Explorer 7 candidate mission. STEAM-R, a limb-sounding radiometer operating in the spectral band 320-360 GHz, is designed to monitor the upper troposphere and lower stratosphere of the Earth's atmosphere with high vertical resolution from low Earth orbit. The instrument employs an array of receivers to provide 14 simultaneous closely-spaced views through the atmospheric limb. The receivers are accommodated in the instrument front-end in two sub-sets of 7 receivers, with each set detecting orthogonal polarisations. The spatial viewing requirements of the instrument, and a preliminary analysis of the instrument fore-optics, show that a feedhorn spacing of about 11 mm is required. An 8-element receiver array front-end, presented in Fig. 1, has been developed to demonstrate a compact receiver array suitable for STEAM-R.**

The array's 8 receivers are configured in two 4-element linear sub-arrays, each of which is made from four miniature mixer blocks. Each block incorporates a diagonal feedhorn, a sub-harmonically pumped mixer and a low noise intermediate frequency amplifier. The mixers employ anti-parallel pairs of GaAs Schottky diodes fabricated at the Rutherford Appleton Laboratory and an Avago AMMC-6222 chip is used for the amplifier. This operates over the frequency band from 7 to 21 GHz with a noise figure of 2.4 dB. All mixers are pumped from a single W-band local oscillator source: the signal, nominally 83 GHz, is first divided into two using an E-plane waveguide splitter. Each output is then frequency doubled. The 166 GHz power passes to a 4-way H-plane waveguide splitter to provide the required local oscillator input to the mixers. Each WR10 to WR5 frequency doubler employs GaAs Schottky diodes, which were also fabricated at the Rutherford Appleton Laboratory. The varactor diodes, in anti-series configuration, have been transferred to a quartz substrate to improve the power handling and conversion efficiency.

Preliminary testing of the array has demonstrated a double sideband receiver noise temperature in the range 2200-2600 K. Each mixer required an LO pump power of 2 mW. Full test results will be provided in the presentation and final paper.
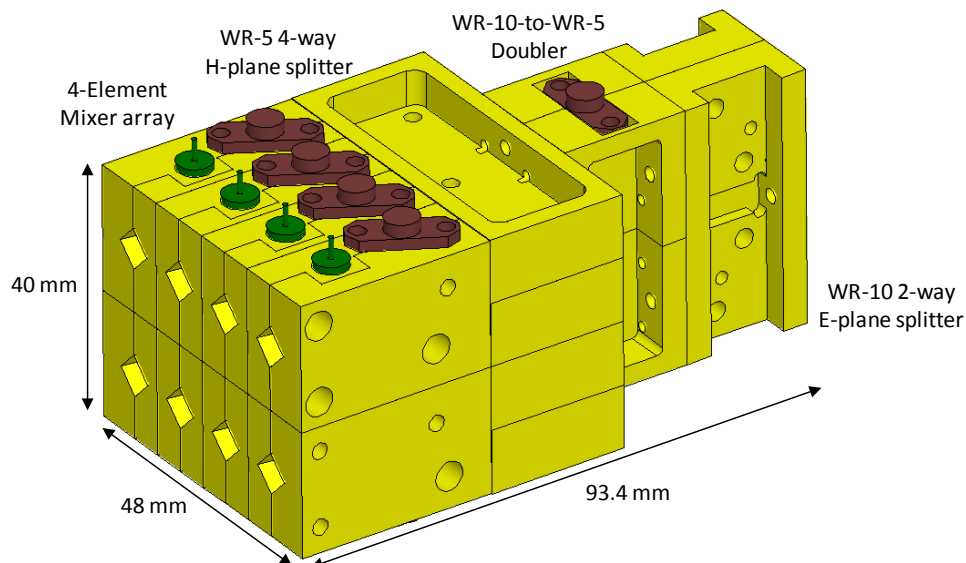
Fig. 1: 8-element receiver array front-end for frequencies around 340 GHz

ALMA: status of construction and the initial observations

T. Hasegawa[1, 2*]

1 Joint ALMA Observatory, Alonso de Córdova 3107, Vitacura 763 0335, Santiago de Chile
2 National Astronomical Observatory of Japan*, Mitaka, Tokyo, 181-8588, Japan
* Contact: tetsuo.hasegawa@nao.ac.jp, phone +81-422-34 3843

Abstract⸺**The progress of the construction of the Atacama Large Millimeter/submillimeter Array (ALMA), an international partnership of Europe, North America and East Asia in cooperation with the Republic of Chile, is presented. ALMA will be composed of 66 antenna elements, which are grouped into an array of fifty 12-m antennas (the 12-m Array) and an array of twelve 7-m antennas plus four 12-m antennas (the Atacama Compact Array = ACA). Each antenna is equipped with a 10-band receiver front end designed to cover all atmospheric windows from 30 to 950 GHz (we initially equip with seven bands on all antennas and another band for selected antennas).**

The construction of ALMA is well advanced with all the subsystems in quantity production, with many items already competed its production. These subsystems are transported to Chile and are being integrated as antenna elements and verified at the ALMA Operations Support Facility (OSF) at an altitude of 2,900 meters. The completed antenna elements are then transported to the Array Operations Site (AOS) at an altitude of 5,000 meters and deployed on the antenna stations for commissioning and science verifications. The construction of the infrastructures at AOS and OSF is in its advanced stage, with the permanent power supply system being prepared for acceptance. The technical building at AOS houses two correlators, one with 64 inputs mainly to cover the 12-m Array and another dedicated for the ACA. The ALMA software system has been developed progressively (now Ver. 8 in use and Ver. 9 under test) along with the systems to support the science users in proposal preparation and the data reduction/analysis.

So far, more than 30 antenna elements have been delivered to AOS. The Joint ALMA Observatory has started since September 2011 the Early Science Operations based on the peer reviewed proposals from the scientists over the world. Some selected results of science verification observations will be presented in the talk.

The Prospects of THz Technology for ALMA 'Band 11'

Ghassan Yassin[1], Stafford Withington[2], Brian Ellison[3] and Peter Huggard[3]

1 Department of Physics University of Oxford, Keble Road, Oxford, OX1 3RH,UK
2 Department of Physics University of Cambridge, Madingley Road, Cambridge, CB3 OHE, UK
3 Millimetre Technology Group, Rutherford Appleton Laboratory, Harwell Oxford, Didcot, OX11 0QX

e-mail: g.yassin1@physics.ox.ac.uk

The mm/submm part of the spectrum is rich in atomic, ionic and molecular lines that allow us to probe the interstellar medium (ISM) in our own and distant galaxies. As evidenced by the advent of the Herschel Space Observatory, observations at supra-THz frequencies with relatively low angular resolution provide important scientific return and demonstrate the relevance of observations deep into the submillimetre wave region. For instance, a number of important ISM diagnostic lines such as the, relatively unexplored, [NII] 205 micron fine structure emission line and a number of high-J CO transitions can be accessed. Future ground-based observations with ultra-high angular resolution will provide a unique window that will allow high-finesse study of the ISM structure formation at the redshift regime of 0.5.

The Atacama Large Millimetre/Submillimetre Array (ALMA) is the largest sub-millimetre telescope in existence and is located at one of the best observing sites on Earth at an altitude of 17000 feet in the Chilean Andes. Upon its completion in 2013, ALMA will comprise of 66 high precision antennas with each equipped with state-of-the-art receivers covering all the atmospheric windows up to 1 THz. Given that ALMA has a collecting area and angular resolution of at least 1000 times greater than all current and planned submillimetre wave telescopes, and given that interferometric observations allow deep integration to faint flux levels even in the presence of atmospheric fluctuations, it is hardly surprising that serious efforts have already started to explore the possibility of extending ALMA's capability into the highest frequency window accessible from the best ground-based site.

In this paper we will review the scientific driver, and technological prospects, for constructing a new cartridge covering the frequency range 1.0-1.5 THz known as ALMA Band 11. We will show that the development of THz technology for a receiver in this frequency range is clearly challenging, but also realistic; our confidence being based upon recent technical advances in new materials such as NbN and NdTiN for SIS tunnel junctions, power simulations tools that allow the prediction of device performance, availability of coherent sources at THz frequencies, and improvements in micromachining technology. Following a brief review of the impressive work that has been achieved by international detector groups pursuing research in this area, we will compare and contrast technologies that are most likely to meet the requirements of supra-THz observation relevant to astronomy. We will then discuss the development strategy and the development route that will lead to the provision of a high performance receiver in this frequency range suitable for use on ALMA. Our presentation will also include novel methods of THz mixer blocks fabrication, full 3-D simulations of the mixer, including the waveguide and the IF interface.

Development Progress and Production Plan of ALMA Band-1 Receivers in Taiwan

Yuh-Jing Hwang [1*], Chau-Ching Chiong [1], Yue-Fang Kuo [1], Hong-Yeh Chang [2], and Zuo-Min Tsai[3], Chi-Chang Lin[1], Shou-Shien Wong[2], Yo-Sheng Lin[2], and Huei Wang[4]

1 Academia Sinica Institute of Astronomy and Astrophysics, Taipei 10617 Taiwan, ROC
2 Department of Electrical Engineering, National Central University, Jhongli, Taoyuan 32001 Taiwan, ROC
3 Department of Electrical Engineering, National Chung-Cheng University, Minhsiung, Chiayi 62102 Taiwan, ROC
4 Department of Electrical Engineering, National Taiwan University, Taipei 10617 Taiwan, ROC
`* Contact: yjhwang@asiaa.sinica.edu.tw, phone: +886-2-2366 5340`

Abstract⸺**An international collaboration between Taiwan, Canada, and Chile are formed to develop the components and cold cartridge assembly of the ALMA Band-1 receivers. In Taiwan, a series of 31.3-45.0GHz millimeter-wave components are developed for the ALMA band-1 receivers. The components are mainly based on 0.15-um GaAs MHEMT MMICs. The key components include two three-stage 31.3-45GHz low-noise amplifiers (LNA), bandpass or high-pass filters, a cascode PHEMT mixer and a 4-12GHz IF amplifier. The MMIC designs are iterated several times, the latest results measured by probe and then tested in packaged modules.**

The 30-50GHz MMIC LNA exhibits 20-28 dB gain and 20-30K noise temperature under 16 K cryogenic temperature environments. The cascode PHEMT mixer uses a common-source transistor as gain stage and the following cascode transistor as mixing device. The measured results on the packaged module shows -5 to +2dB conversion gain under 2-dBm LO power over 4-14GHz IF frequency range. The filters designed and fabricated by GaAs foundry service shows in-band insertion loss less than 3 dB and the out-band rejection as high as 30-40dB.

The local oscillator aiming for 27.3-33GHz frequency tuning range is composed by a phase-locked GaAs HBT MMIC voltage-controlled oscillator cascaded by a buffer amplifier. For comparison on the phase noise performance, an ALMA baseline design based on the commercially available 13-17GHz YIG-tunes oscillator with active frequency doubler is also developed. The measured RMS jitter of the HBT VCO LO is around 51 fsec and the version of YIG is less than 30fs over 1K to 1MHz frequency offset.

The lens, receiver horn, orthomode transducers, and the cold cartridge assembly are developed by consortium laboratories in Canada and Chile. As the development of the key components in all three consortium laboratories approaching to the expected specification soon, a production plan is also proposed. Once the prototype cold cartridge assembly pass the qualification, production will be conducted in Taiwan to install and operate the Band-1 receivers in ALMA after the end of 2018.

Design of a 650 GHz Planar Circuit Balanced Mixer

Boon-Kok Tan, Ghassan Yassin, Paul Grimes, Karl Jacobs, and Stafford Withington

Abstract—We present the design of a broadband balanced superconductor-insulator-superconductor (SIS) mixer, which uses two back-to-back unilateral finline tapers. A key feature of our design is the use of a thin silicon-on-insulator (SOI) substrate, which enables the employment of a finline mixer at high frequencies. We integrated all of the required superconducting RF circuits onto a single chip using planar circuit technology, and retained the simplest fabrication processes without any lumped elements. This approach results in a very simple mixer-block design, which is desirable for constructing medium-format focal-plane imaging arrays. In the paper, we present in detail the electromagnetic modelling of each of the planar components making up the entire balanced mixer. The electromagnetic simulations were carried out using HFSS, and the heterodyne performance of the complete balanced chip was accessed using SuperMix.

Index Terms—Superconducting coherent detectors, system-on-a-chip, submillimeter wave integrated circuits, silicon on insulator technology.

I. INTRODUCTION

ADVANCED astronomical observations require mixers that are highly sensitive, low noise and can operate with broad RF and IF bandwidths. In recent years, submillimetre (sub-mm) receivers using superconductor-insulator-superconductor (SIS) tunnel junctions have already approached quantum-limited performance. The next paradigm is the construction of large-format focal-plane arrays. Previously, we reported a single-ended 650 GHz unilateral finline SIS mixer design [1] [2], requiring only a simple mixer-block architecture, which is highly desirable to enable the construction of compact medium-format (64 pixels) array receivers. In this paper, we upgrade the single-junction design to construct a balanced SIS mixer that can operate within ALMA Band 9 (602–720 GHz).

In contrast to the single SIS junction mixer, a balanced mixer has the ability to reject local oscillator (LO) noise, and to fully utilise the available LO power by eliminating the local-oscillator beam splitter (e.g., [3] and [4]). Our balanced SIS mixer uses two back-to-back unilateral finline tapers as waveguide to planar-circuit transitions. Unilateral finline chips have large substrate areas, which allow the elegant integration of complicated circuits [5] [6]. Both the finline tapers and the additional circuits required for balanced mixer operation are

B-K Tan and G. Yassin are with the Department of Physics (Astrophysics), University of Oxford, Denys Wilkinson Building, Keble Road, OX1 3RH, Oxford, UK. E-mail: tanbk@astro.ox.ac.uk

P. Grimes is with Harvard-Smithsonian Center For Astrophysics, 60 Garden Street, Cambridge, MA, 02138, USA.

K. Jacobs is with KOSMA, I. Physikalisches Institut, University of Cologne, Germany.

S. Withington is with the Detector Physics Group, Cavendish Laboratory, JJ Thomson Avenue, Cambridge CB3 0HE, UK.

deposited on one side of a 15 μm silicon-on-insulator (SOI) substrate [4] [7]. The very thin substrate presents only a slight dielectric loading to the waveguide, and hence prevents the excitation of high-order modes over a relatively large bandwidth. The mixer-block also becomes simpler, and requires only a single rectangular waveguide without any supporting grooves in the wall. The chip is supported via gold beam leads (a few microns thick) attached between two halves of the split block. This arrangement makes balanced THz receivers markedly easier and cheaper to fabricate.

II. BALANCED SIS MIXER DESIGN

In principle, one can form a balanced mixer by connecting two independent SIS mixers to the output ports of a 180° or 90° RF hybrid, and combine both the down-converted IF signals from the mixers using a 180° IF hybrid. Here, we chose to use a quadrature RF hybrid for its compactness, in conjunction with a 180° IF hybrid for output signal summation. As shown in Figures 1 and 2, our balanced mixer comprises six major RF components: unilateral finline tapers with matching notches, finline-to-microstrip transitions, an RF quadrature hybrid, DC/IF blocks, superconducting tuning circuits with SIS junctions, and RF chokes terminated with IF beam leads.

The easiest way to understand the operation of a balanced mixer is by considering the phases of the LO and the RF, with an additional LO noise component $LO_{(n)}$ in-phase with the LO signal itself [8] [9]. For simplicity, we have assumed that all of these incoming (GHz) signals share the same reference phase 0°. The RF signal from the sky and the LO signal generated locally, coupled onto the chip separately through two finline to microstrip transitions, enter the RF quadrature hybrid to produce two channels that each have a 90° phase difference between the RF and LO. These are written as $RF\angle 0° + (LO + LO_{(n)})\angle 90°$ in the upper arm, and $RF\angle 90° + (LO + LO_{(n)})\angle 0°$ in the lower arm, of Figure 1. Before feeding these combined signals into two separate SIS mixers, two DC/IF blocks are placed between the RF hybrids and the RF tuning circuits leading to the tunnel junctions, which prevent DC and IF coupling between the mixers. From each mixer, we now have IF outputs where the down-converted LO noise signals are $\pm 90°$ phase-shifted between the two branches. It can be seen that when the down-converted signals are combined in the 180° IF hybrid, the IF signal appears at the **sum** (Σ) port without LO noise, and the LO noise component appears at the **difference** (Δ) port without any signal. The configuration shown in Figure 1 assumes that both SIS mixers are biased with the same polarity. If they are biased with opposing polarity, one simply has to flip the polarity of the IF output of one of the mixers, since the IV characteristic of an SIS junction is anti-symmetric. In this case, the **sum** port

Fig. 1. Block diagram showing the components needed for a balanced mixer design. The phasors for the LO components are shown in black arrows, while the RF phasors are in blue. The 0° phase is referenced to the upward pointing direction and clockwise for positive phase shift.
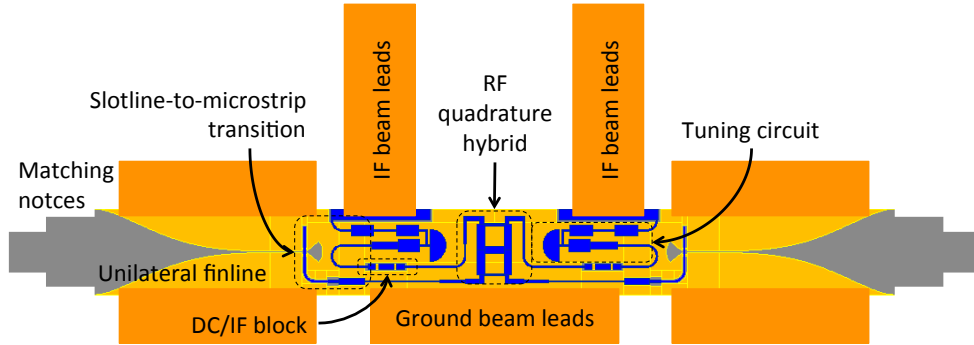

Fig. 2. Layout of the final balanced mixer chip showing various on-chip circuit components.

would be the LO noise output, while the **difference** port is the desired IF signal.

III. DESIGN OF THE RF PASSIVE CIRCUIT COMPONENTS

Conventionally, the components of a balanced SIS mixer are fabricated using mechanical machining techniques, which is challenging in the THz region. Also, the mixer blocks and other RF waveguide components (e.g., RF hybrid) are mechanically attached together (e.g., [3]), and the two single-ended SIS chips have to be carefully selected to ensure optimum performance. This approach results in a bulky, complicated assembly, which is exceptionally difficult to mass produce and pack into a focal plane imaging array. In recent years, there has been a great deal of enthusiasm to simplify these designs to enable the deployment of more advanced SIS mixers in the form of compact imaging arrays [4] [10].

We chose to use only planar circuit technology to ensure that the mixer block is kept as simple as possible. All of the RF components required are integrated on-chip, with a simple configuration consisting of a 15 μm SOI substrate ($\sim$2 mm long), a niobium ground layer (250 nm), a silicon monoxide dielectric layer (475 nm) and a niobium wiring layer (400 nm). This design removes the need for a separate hybrid block, and since both junctions are fabricated on the same chip, only a single external coil is needed to suppress the unwanted Josephson currents. The entire balanced mixer block is greatly simplified and reduced in size. The back-to-back architecture leads to a configuration that requires only a single, straight rectangular waveguide. The signal from the sky is coupled to

the chip from one side of the block via a feed horn, while the LO power is coupled to the other side via a similar feed horn. A key advantage of this arrangement is that it eliminates the need for an LO-injection beam splitter, which normally wastes 90% or more of the available LO power. The lowering of the LO power requirement opens up the possibility of using a photonic LO source (e.g., [11]) rather than the commonly used varactor multiplied sources.

The balanced SIS mixer presented here is designed to work with circular Nb/AlO$_x$/Nb SIS tunnel junctions having an area of 1 μm^2. This size corresponds to a normal resistance of approximately 20 Ω, with a current density of approximately 14 kA/cm^2, and junction capacitance of 75 fF. All of the individual on-chip RF circuit components are matched with a system-wide characteristic impedance of 20 Ω (3 μm microstrip).

A. Waveguide-to-slotline transition

The profile of the unilateral finline taper was calculated using *FinSynth*, an Oxford University software package written by North [12]. *FinSynth* uses the Optimum Taper Method to search for a finline profile that has minimum length for a predesignated return loss. The profile of the taper was synthesised by converting the computed cutoff frequency taper into a slotline taper. The final design was checked by carrying out a full 3-D electromagnetic simulation using Ansys HFSS, including the effect of superconductivity on surface impedance, and the stepped dielectric matching notches.

(a) Unilateral finline

(b) S-parameters at 700 GHz band
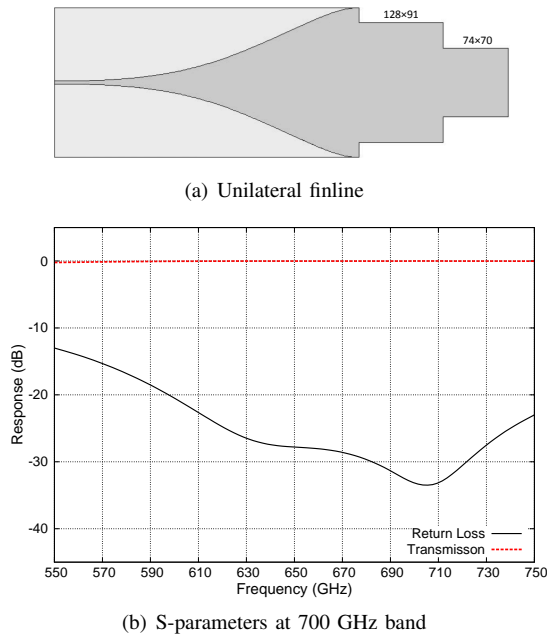
Fig. 3. (a) Layout of the unilateral finline taper with a 2-step notch. The quoted dimensions of the matching notches are in width×length, in μm. (b) HFSS simulated transmission and return loss across the designated RF bands.


(a) Slotline to microstrip transition

(b) S-parameters at 700 GHz band

Fig. 4. (a) Layout of the slotline-to-microstrip transition via CPW sections. An enlarged 3-D view of the modified-CPW cross-over is shown in the inlet for clarity view. The dimensions for most structures are in width×length. For CPW, the quoted dimensions are in $s \times (2w + s) \times$length, in μm. (b) Return loss and coupling efficiency across the designated RF band.

As seen in Figure 3 (a), the unilateral finline tapers the slot width from 160 μm (waveguide height) to 2.5 μm, which reduces the characteristic impedance of the waveguide to values suitable for CPW or microstrip matching, $\sim$20–30 Ω. It is worthwhile noting that the slotline is in fact a natural high-pass filter, which prevents the IF signal from reaching the RF port. This feature is especially important when a broad IF operating range is required [13]. A matching notch is introduced before the finline to match the impedance of the substrate loaded waveguide to the empty waveguide. In our design, we used a 2-step rectangular notch (approximately quarter-wavelength long) to achieve a wide RF bandwidth. Figure 3 (b) shows the computed scattering parameters of the unilateral finline taper with the appropriate matching notches. The performance is excellent with the return loss below –20 dB over more than a 150 GHz bandwidth.

B. Slotline-to-microstrip transition

A transition is required to transform the slotline to microstrip. However, the design of this transition is not straightforward [5] because even for a 2.5 μm slot, suitable for photolithographic fabrication, the impedance of the slotline is still much higher than a suitable microstrip. On the other hand, CPW offers a wide range of impedance values that can be exploited to bridge the slotline-to-microstrip mismatch. Neglecting the fringing effects, the characteristic impedance of CPW is determined mainly by the ratio of the central strip width (s) to the gap width (w) between the central strip and the ground plane. Figure 4 (a) shows the final design of the slotline-to-microstrip transition. The RF power is guided from the slotline to CPW using a radial slotline stub and a quarter-wavelength ($\lambda_g/4$) CPW stub. Two short air-bridges
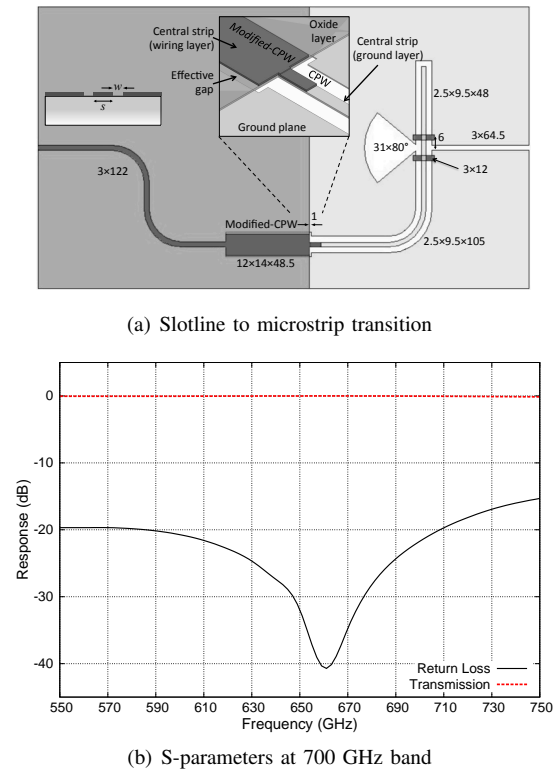
are deposited across the CPW near the slotline-CPW junction to make sure that the ground planes are equipotential.

The section labelled 'Modified-CPW' is in fact a CPW with its central strip and the ground plane separated by an oxide layer. The gap w is defined by the effective distance between the edge of the central strip on top of the oxide layer and the edge of the ground plane beneath the oxide layer. This arrangement was adopted for two reasons: Firstly, to bring the CPW central strip over the top of the oxide layer, preparing it to form a microstrip line. Secondly, it allows a very narrow CPW gap to be employed without the likelihood of shorting the central conductor to the ground plane. As seen in Figure 4 (b), this method of designing the slotline-to-microstrip transition works well, having more than 160 GHz of bandwidth with less than –20 dB return loss.

C. Tuning circuit

The tuning circuit comprises four parts: an inductive strip with a half-moon stub, an inductive strip before the junction, a multi-section transformer, and an RF choke [2] [6]. The lumped element equivalent circuit is shown in Figure 5 (a). In order to match the junction impedance across a wide bandwidth, two inductive strips, one in series and another parallel to the junction, were used to provide two resonance dips either side of the centre frequency.

The first inductor, **Tuner 1** in Figure 5 (a), is a microstrip terminated with a $\lambda_g/4$ half-moon stub, which acts as a short
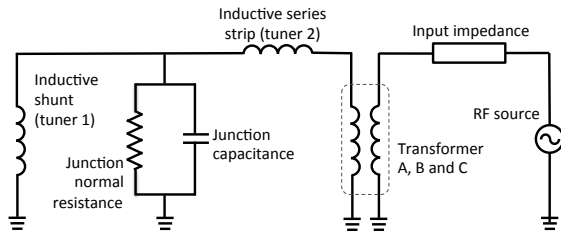
(a) Equivalent circuit
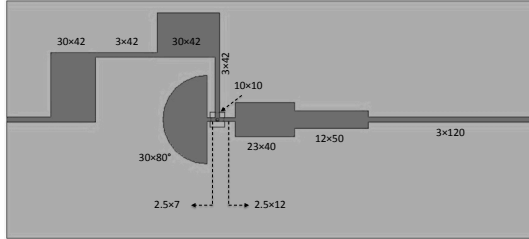
(b) Superconducting tuning circuit
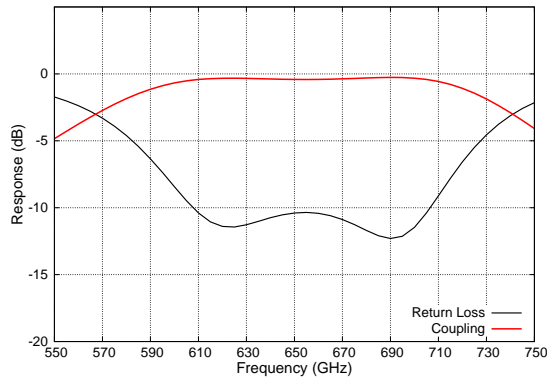

(c) S-parameters at 700 GHz band

Fig. 5. (a) Electrical diagram representing the RF tuning circuit of the finline mixer. (b) Layout of the RF tuning circuit with an RF choke to prevent RF leakage to the IF port. The dimensions for various structures are similar to the previous figures. (c) Return losses and coupling efficiency of the tuning circuit across the designed RF band.

at RF frequencies. The microstrip line transforms the short into the inductance that is required to tune out the capacitance of the junction at frequency ω_1. To first order, the length of this microstrip can be calculated using the expression $\beta l \approx Z_0 \omega_1 C$, where $\beta = \dfrac{2\pi}{\lambda}$ is the guided wavenumber, C is the capacitance of the junction, Z_0 is the characteristic impedance of the microstrip (a function of the width of the line), and l is the length of the microstrip in the unit of electrical wavelength.

The second inductive microstrip, **Tuner 2**, is placed before the junction to tune out the residual capacitance at a slightly shifted frequency ω_2. The width and the length of this microstrip section can be determined using the standard transmission line equation $Y_s = (Y_l + iY_0 \tan \beta l)/(Y_0 + iY_l \tan \beta l)$, where Y_s is the source admittance, Y_l is the load admittance, $1/Y_0$ is the characteristic impedance of the line and βl is the propagation constant. By setting the imaginary part of Y_s to zero, the length of the microstrip can be obtained in terms of

βl. The value of Y_0 is determined by the chosen width of the microstrip.

Connecting both inductive strips to the junction leads to the overall reactance being zero at two frequencies, giving the two poles in the matching diagram [14], as shown in Figure 5 (c). To match the impedance of this sub-circuit to the output impedance of the slotline-to-microstrip transition, a 3-step transformer was employed. Finally, a 5-section RF choke, consisting of alternating high and low impedance $\lambda_g/4$ sections of microstrip, was placed after the SIS junction to provide high rejection of the RF signal across the operating bandwidth: see Figure 5 (b). This filter prevents RF power leaking into the IF path.

D. RF quadrature hybrid

The RF quadrature hybrid was realised by a microstrip branch-line hybrid with a $90°$ phase difference between the two arms, as shown in Figure 6 (a). We cascaded two branch line hybrids to increase the bandwidth.

The highest impedance line, and therefore the narrowest microstrip, in the hybrid was chosen to be $2Z_0 \approx 20\Omega$, where Z_0 is the characteristic impedance of the four input/output arms. This impedance corresponds to a microstrip having a width of about 3 μm, well within standard photolithographic fabrication. A transformer was then used to transform the 10 Ω input/output microstrips back to the 20 Ω line. The distance between each T-junction is close to $\lambda_g/4$. All dimensions were then optimised for bandwidth in the final design using HFSS.

As shown in Figure 6 (b), the return loss and the coupling between the two input ports are less than –20 dB across the
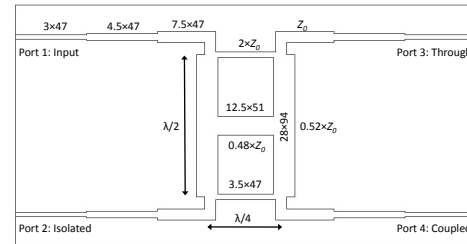
(a) Quadrature hybrid
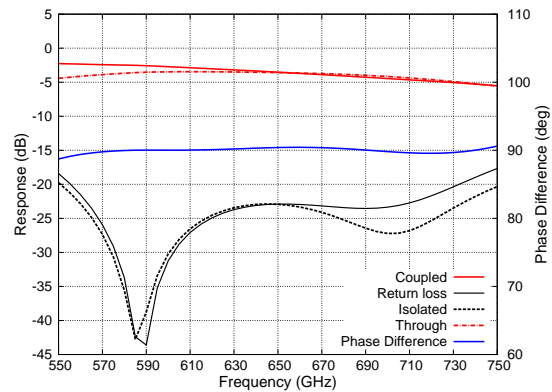
(b) S-parameters at 700 GHz

Fig. 6. (a) Layout of the $90°$ RF quadrature hybrid, with the dimension optimised by HFSS. (b) The S-parameters and the phase difference between the **coupled** and **through** arm of the hybrid across the designed RF band.

operating frequency range. The coupling to the **coupled** and the **through** arms is close to –3 dB, with only a small variation of ±0.5 dB. The phase difference between the two output arms is constant at $90° \pm 0.5°$ across the entire band.

E. DC/IF block

The DC/IF block is used to isolate the two SIS tunnel junctions, and to prevent IF power leaking between the two mixers. To avoid using lumped elements, we employed a broadside coupler. The RF power from the microstrip is coupled to the underlying CPW, both separated by an oxide layer, and back to the microstrip, as shown in Figure 7 (a). The overlapping region between the microstrip with the central strip of the CPW determines the parallel capacitance between the input and the output ports, while the gap between the microstrips, and the gap between CPW stages gives the series capacitance (see the circuit diagram in the inlet of Figure 7 (b)). To first order, the required capacitance of the structure can be estimated from the overlapping areas and gap distances. This initial value was then optimised within the HFSS model to include the effects of the inductance of the transmission lines. Since both transmission lines are not in contact with each other, they are therefore always DC-isolated, and only the RF power within the resonant frequency band is allowed to pass through with minimum return loss. In circuit terms, it acts like a bandpass filter at RF frequencies, as shown in Figure 7 (b). Again, we cascaded two broadside couplers to widen the operating RF bandwidth.

(a) DC/IF block

(b) S-parameters at 700 GHz
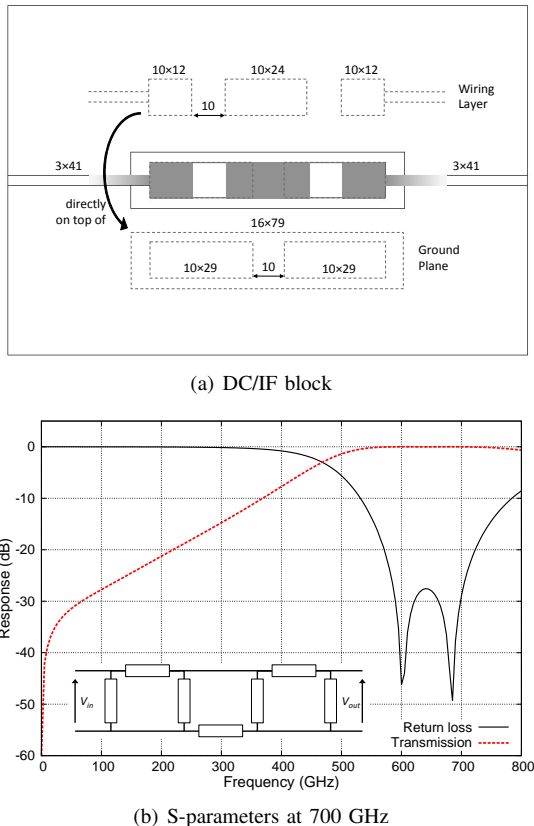
Fig. 7. (a) Layout of the broadside coupler as DC/IF block. (b) The equivalent circuit and the performance of the DC/IF block simulated using HFSS.
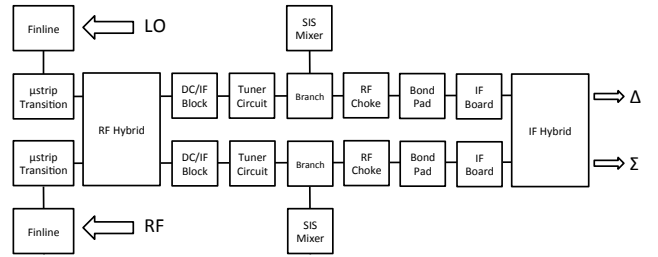
Fig. 11. Block diagram shows the various components included in the SuperMix simulation.

IV. FULL BALANCED MIXER CHIP SIMULATIONS

The entire balanced mixer chip is electrically too large for HFSS to perform full 3-D electromagnetic modelling and further optimisation. Consequently, we approached the problem with two alternative techniques: Firstly, we combined only the subsection of the RF chip that includes the RF quadrature hybrid, the DC/IF blocks and the tuning circuits, without the finline taper and the microstrip transition. In the second method, we exported the HFSS generated S-parameters of each RF circuit component into Ansoft Designer (a schematic circuit design package) to form a complete RF mixer chip model. Both methods allow us to predict the performance of the complete mixer, but do not provide a means for full optimisation.

Figures 8 and 9 show the results of the simulations using HFSS and Ansoft Designer, respectively. It can be seen that the results obtained using the different methods agree well with each other. The power coupling to the two SIS junctions is almost identical, averaging at –4±1 dB from 600–700 GHz. The phase difference between the two IF outputs from the SIS mixers is also kept to within $90 \pm 2°$ from 580–720 GHz, while the return loss and isolation between the two input ports remains below –10 dB for about 120 GHz.

In order to estimate the heterodyne mixing performance of the complete balanced mixer, we formed a full-chip Super-Mix [1] model via the HFSS generated S-parameters of individual circuit components [2], as shown in Figure 11. In Figure 10, we show an example of these calculations. Note that no IF transformer is included in these SuperMix calculations, but only two 50 Ω lines were used. As expected, the performance is good from 600–700 GHz and the IF response is flat, as shown in Figure 10 (b).

The fact that all of the simulated results from the different packages agree well is important because the circuit components presented above were simply cascaded to form the final balanced SIS mixer without further optimisation. The promising performance predicted by the packages demonstrates that our method of designing SIS mixers with complex circuit functionality is entirely feasible.

V. CONCLUSION

We have presented the design of a wideband unilateral finline balanced SIS mixer at 650 GHz using SOI planar-

[1] A Caltech superconducting SIS mixer design and analysis package [15].
[2] The 180° IF hybrid used was reported previously in [16].
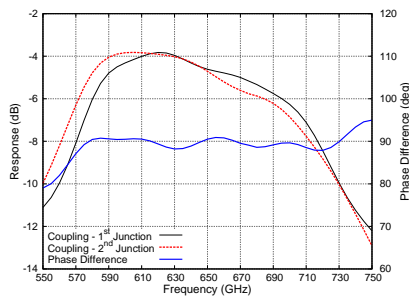
(a) Coupling and phase difference
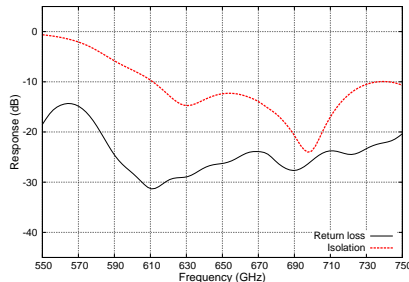
(b) Return losses and isolation

Fig. 8. HFSS simulation of a subsection of the mixer chip including the RF quadrature hybrid, the DC/IF blocks and the tuner circuits.


(a) Coupling and phase difference

(b) Return losses and isolation

Fig. 9. Ansoft Designer simulations of the full balanced chip by importing various S-parameters from HFSS. The phase different is adapted from HFSS simulation with only the quadrature hybrid, DC/IF block and the tuner circuits.
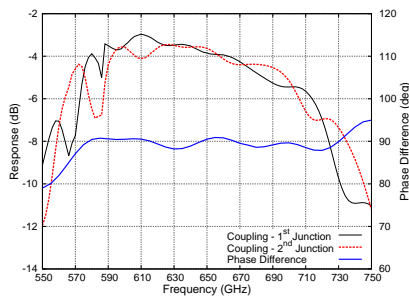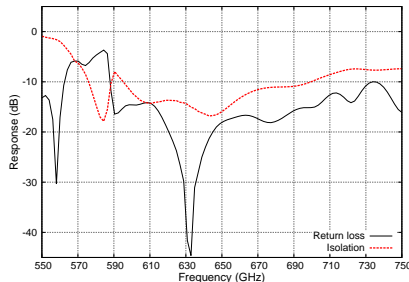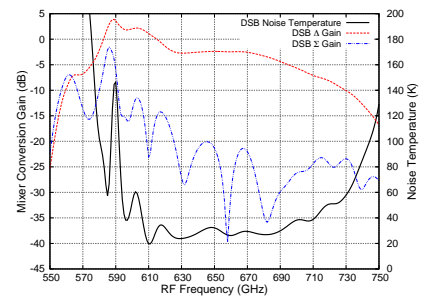
(a) RF response

(b) IF response

Fig. 10. SuperMix simulations showing the predicted behaviour of the final design of the balanced mixer chip.

circuit technologies. The design results in an easy-to-fabricate mixer chip and mixer block with elegant yet fully integrated planar circuits. The performance was simulated fully using a rigorous 3-D electromagnetic package in conjunction with SuperMix. The simulated results predict satisfactory RF and IF performance across the designated RF and IF bands.

ACKNOWLEDGMENT

REFERENCES

[1] B.-K. Tan, G. Yassin, P. Grimes, and K. Jacobs, "Designs of Broadband Unilateral Finline SIS Mixers Employing 15 μm Silicon-On-Insulator Substrate at THz Frequencies," in *Twenty-First International Symposium on Space Terahertz Technology*, Mar. 2010, pp. 204–211.

[2] B.-K. Tan, G. Yassin, P. Grimes, J. Leech, K. Jacobs, S. Withington, M. Tacon, and C. Groppi, "A 700 GHz unilateral finline SIS mixer fed by a multi-flare angle smooth-walled horn," in *Society of Photo-Optical Instrumentation Engineers (SPIE) Conference Series*, vol. 7741, Jul. 2010.

[3] Y. Serizawa, Y. Sekimoto, M. Kamikura, W. Shan, and T. Ito, "A 400-500 GHz Balanced SIS Mixer with a Waveguide Quadrature Hybrid Coupler," *International Journal of Infrared and Millimeter Waves*, vol. 29, pp. 846–861, Sep. 2008.

[4] M. P. Westig, K. Jacobs, J. Stutzki, M. Schultz, M. Justen, and C. E. Honingh, "Balanced superconductor-insulator-superconductor mixer on a 9μm silicon membrane," *ArXiv e-prints*, May 2011.

[5] G. Yassin, P. K. Grimes, O. King, and C. E. North, "Waveguide-to-planar circuit transition for millimetre-wave detectors," *Electronics Letters*, vol. 44, no. 14, pp. 866–867, 2008.

[6] B.-K. Tan, G. Yassin, P. Grimes, J. Leech, K. Jacobs, and C. Groppi, "A 650 GHz Unilateral Finline SIS Mixer Fed by a Multiple Flare-Angle Smooth-Walled Horn," *IEEE Transactions on Terahertz Science and Technology*, vol. 2, no. 1, pp. 40 –49, jan. 2012.

[7] M. P. Westig, M. Justen, K. Jacobs, J. Stutzki, M. Schultz, F. Schomacker, and C. E. Honingh, "A 490 GHz planar circuit balanced Nb-Al$_2$O$_3$-Nb quasiparticle mixer for radio astronomy: Application to quantitative local oscillator noise determination," *ArXiv e-prints*, May 2012.

[8] A. Kerr, "On the noise properties of balanced amplifiers," *Microwave and Guided Wave Letters, IEEE*, vol. 8, no. 11, pp. 390 –392, nov 1998.

[9] J. Kooi, R. Chamberlin, R. Monje, B. Force, D. Miller, and T. Phillips, "Balanced receiver technology development for the caltech submillimeter observatory," *IEEE Transactions on Terahertz Science and Technology*, vol. 2, no. 1, pp. 71 –82, jan. 2012.

[10] P. Grimes, G. Yassin, K. Jacobs, and S. Withington, "A 700 GHz single chip balanced SIS mixer," in *Sixteenth International Symposium on Space Terahertz Technology*, May 2005, pp. 46–52.

[11] P. G. Huggard, B. N. Ellison, A.-L. Fontana, B. Lazareff, and A. Navarrini, "Focal Plane Heterodyne SIS Receiver Array with Photonic LO Injection," in *Seventeenth International Symposium on Space Terahertz Technology*, May 2006, p. 153.

[12] C. North, G. Yassin, and P. Grimes, "Rigorous Analysis and Design of Finline Tapers for High Performance Millimetre and Submillimetre Detectors," in *Seventeenth International Symposium on Space Terahertz Technology*, May 2006, pp. 284–287.

[13] P. K. Grimes, G. Yassin, K. Jacobs, and J. Leech, "Design of SIS finline mixers with ultra-wide IF bands," in *Ninteenth International Symposium on Space Terahertz Technology*, W. Wild, Ed., Apr. 2008, p. 432.

[14] B.-K. Tan, "Development of coherent detector technologies for submillimetre wave astronomy observations," Ph.D. dissertation, University of Oxford, United Kingdom, 2012.

[15] J. Ward, F. Rice, G. Chattopadhyay, and J. Zmuidzinas, "SuperMix: A Flexible Software Library for High-Frequency Circuit Simulation, Including SIS Mixers And Superconducting Elements," in *Tenth International Symposium on Space Terahertz Technology*, Mar. 1999, p. 268.

[16] P. Grimes, "Design and analysis of 700 GHz Finline Mixers," Ph.D. dissertation, University of Cambridge, United Kingdom, 2006.

Performance of the first six ALMA Band 10 receivers

Y. Fujii[1], A. Gonzalez[1], M. Kroug[1], K. Kaneko[1], A. Miyachi[1], K. Kuroiwa[1], T. Yokoshima[1], K. Makise[2], Y. Uzawa[1*], and Z. Wang[2]

1 National Astronomical Observatory of Japan*, Mitaka, Tokyo, 181-8588, Japan
2 National Institute of Information and Communications Technology, Kobe, 651-2492, Japan
* Contact: uzawa@nao.ac.jp, phone +81-422-34 3807

Abstract——**We have developed and characterized the first six (preproduction) Atacama Large Millimeter/submillimeter Array (ALMA) Band 10 (787–950 GHz) receivers. The front-end optics comprises a pair of ellipsoidal mirrors, a wire grid, and two corrugated feed horns. A waveguide mixer block is attached to each feed horn in which a mixer chip employing Nb/AlOx/Nb junctions and NbTiN/SiO$_2$/Al microstrip tuning circuits is mounted to a WR-1.2 full-height waveguide. A local oscillator (LO) signal receiving horn and a waveguide 10-dB or 13-dB LO coupler are integrated in the block to provide the LO signal to the mixer chip. The LO signal is generated by a fixed-tuned x9 multiplier with an output diagonal horn located at the 110-K stage, and is then quasi-optically coupled to the mixer receiving horn. A quasi-optical attenuator is inserted in the LO optical path at the 15-K stage to adjust the output power of the individual multipliers down to a proper level for the SIS mixer. A very wide intermediate frequency (IF) system with a bandwidth of 4–12 GHz is employed. A set of detailed tests of the receiver in terms of the receiver sensitivity, beam, stability, and other many characteristics demonstrated that the first six receivers had excellent and almost the same performances as specified by ALMA. These results suggest that the subsequence full-production up to 73 receivers is achievable.**

Emission and Detection of Terahertz Radiation Using Two-Dimensional Electrons in III-V Semiconductors and Graphene

Taiichi Otsuji, *Member, IEEE*, Takayuki Watanabe, Stephane A. Boubanga Tombet, Akira Satou,
Wojciech M. Knap, Vyacheslav V. Popov, Maxim Ryzhii, *Senior Member, IEEE,*
and Victor Ryzhii, *Fellow, IEEE*

Abstract— **Recent advances in emission and detection of terahertz radiation using two-dimensional (2D) electron systems in III-V semiconductors and graphene. 2D plasmon resonance is first presented to demonstrate intense broadband terahertz emission and detection from InGaP/InGaAs/GaAs and InAlAs/InGaAs/InP material systems. The device structure is based on a high-electron mobility transistor and incorporates the author's original asymmetrically interdigitated dual-grating gates. Second topic focuses on graphene, a monolayer carbon-atomic honeycomb lattice crystal, exhibiting peculiar carrier transport and optical properties owing to massless and gapless energy spectrum. Theoretical and experimental studies toward the creation of graphene terahertz injection lasers are described.**

Index Terms—**compound semiconductors, detectors, graphene, lasers, plasmons, terahertz**

I. INTRODUCTION

IN the research of modern terahertz (THz) electronics, development of compact, tunable and coherent sources and detectors operating in the THz regime is one of the hottest issues [1]. Two-dimensional (2D) plasmons in semiconductor nano-heterostructures like electron channels in high-electron mobility transistors (HEMT's) have attracted much attention due to their nature of promoting emission and detection of THz electromagnetic radiation [2, 3]. On the other hand, graphene, a monolayer carbon-atomic honeycomb lattice crystal, has attracted attention due to its peculiar carrier transport properties owing to the massless and gapless energy spectrum [4]. Optical and/or injection pumping of graphene can exhibit negative-dynamic conductivity in the THz spectral range [5, 6], which may bring new types of THz lasers. This paper reviews recent advances in emission and detection of terahertz radiation from 2D electron systems in III-V semiconductor and graphene nano-heterostructures.

II. THz Emission and Detection Using 2D Plasmons

A. THz Emission from 2D Plasmons in HEMTs

We have proposed our original 2D-plasmon-resonant micro-chip emitter as a new terahertz light source [7-10]. The structure is based on a HEMT and featured with interdigitated dual-grating gates (Fig. 1). The dual grating gates can alternately modulate the 2D electron densities to periodically distribute the plasmonic cavities (~100-nm width in microns distance) along the channel, acting as an antenna [7]. Under pertinent drain-source dc bias conditions, dc electron drift flows may promote the instability owing to the periodic modulation of electron drift velocities [11], resulting in self-oscillation with characteristic frequencies in the terahertz regime. The device was fabricated using InGaP/InGaAs/GaAs and/or InAl/InGaAs/InP material systems [8-10]. So far a broadband THz emission ranging from 1 to ~6 THz has been obtained reflecting multimode of coherent/incoherent plasmons [2], for which oblique modes [12], hot plasmons, and chirped plasmon modes [8] are of the major causes. The DGG-HEMT THz emitter can work for terahertz spectroscopic and imaging applications as an incoherent broadband terahertz microchip source, demonstrating fine identification of water vapor
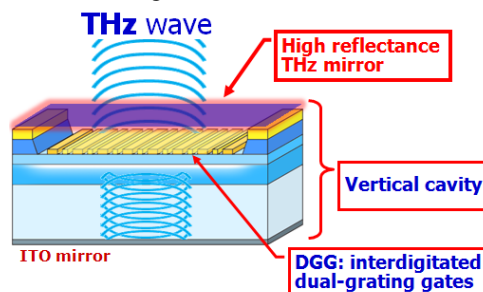
Fig. 1. Schematic and SEM images of a DGG-HEMT with a vertical cavity.

Fig. 2. Schematic view and SEM images of an A-DGG HEMT THz detector. L_{g1} = 200 nm, L_{g2} = 400 nm, d_1 = 200 nm, d_2 = 400 nm.
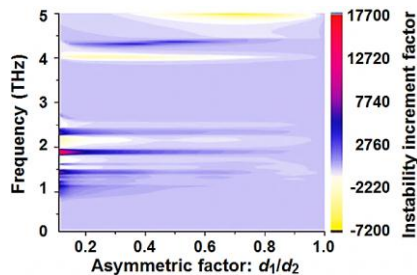

Fig. 3. Simulated relative instability-increment factors for an A-DGG HEMT as a function of the asymmetric factor d_1/d_2. L_{g1} = 200 nm, L_{g2} = 1.6 µm, $d_1 + d_2$ = 600 nm, W = 2.4 µm. Electron density under the gate G2 is 2.5×10^{11} cm^{-2} whereas that is 2.5×10^{12} cm^{-2} under the gate G1.

absorptions as well as finger prints of sugar groups [9].

In order to realize coherent monochromatic THz emission we introduced our original asymmetric DGG (A-DGG) structure (Fig. 2) [13] and an improved resonant-enhanced high-Q vertical cavity structure [7]. In the A-DGG structure the DGG is implemented with asymmetric inter-finger spaces, which originates a strong asymmetric field distribution for a unit section of the DGG periodic structure, resulting in promotion of the Dyakonov-Shur-type instability [2, 13]. We expect so called 'giant' plasmon instability as a result of cooperative effects between these two instability mechanisms, accelerating the injection locking operation (Fig. 3). Preliminary trial of the emission spectral measurement is now undergoing using fabricated InAl/InGaAs/InP A-DGG-HEMTs. Very sharp resonant-type monochromatic emission is expected.

B. THz Detection Using 2D Plasmons in HEMTs

The possibility of the THz detection in a HEMT structure is due to the nonlinearity of the 2D plasmon dynamics, which lead to the rectification of the THz radiation. As a result, a photoresponse appears as a dc voltage between source and drain in proportion to the radiation intensity (photovoltaic effect) [3]. Depending on the quality factor of the 2D plasmon cavity, which is characterized by the product of incoming THz angular frequency ω and electron momentum relaxation time τ, the

detection operation is categorized in the "resonant" mode ($\omega\tau > 1$) or "non-resonant" mode ($\omega\tau < 1$) [3, 14].

We have demonstrated so far several THz imaging experiments using standard single-gate (SG) HEMTs [14, 15] as well as DGG-HEMTs [16]. Typical result is shown in Fig. 4; the image of the tea leaves that are invisible and hidden in an aluminum-coated plastic package is clearly seen [15], confirming the potentiality of the plasmonic HEMTs as a powerful THz detector.

In order to improve the detector responsivity, pertinent antenna structure should be introduced. A smart design of a narrow band antenna has been proposed in [17] where the SG electrode is designed as a dipole antenna, demonstrating an excellent responsivity 1 KV/W at 1 THz at 300K. The obtained responsivity exceeds that for Schottky barrier diodes.

In terms of broadband antennae, log-periodic or log-spiral as well as grating-gate (GG) are frequently utilized. The DGG structure [7] is an improved type derived from the GG type but still suffers from low responsivity. Our original A-DGG structure can surpass this critical limit [13] because the unit cell of the A-DGG structure can create strong build-in asymmetric field. The THz photoresponse dramatically increases when the parts of 2D channel under the fingers of one of the two sub-gratings are depleted. The InAlAs/InGaAs/InP A-DGG HEMTs (Fig. 2) demonstrate a record-breaking responsivity of 2.2 kV/W and an excellent noise equivalent power of 15 pW/Hz$^{0.5}$ at 1 THz at 300K (Fig. 5) [18]. A fairly high responsivity (>0.5 kV/W) is also maintained over the frequencies beyond 2 THz. All these values are, to the authors' knowledge, the best ever reported at these frequencies.
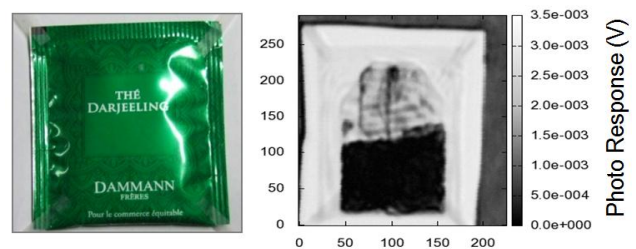

Fig. 4. Terahertz imaging for a tea bag. Left: photo image, right: THz image.
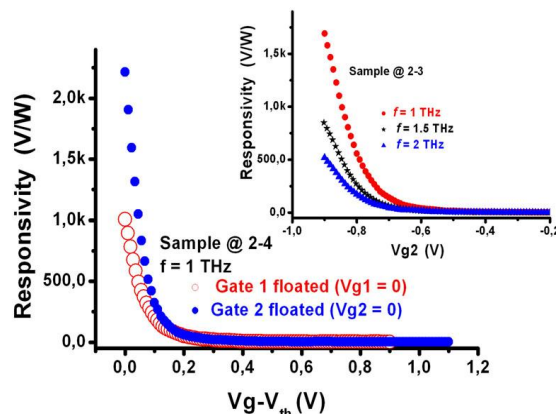
Fig. 5. Measured responsivity of fabricated A-DGG HEMTs at 300K [18].

III. THz Light Amplification by Stimulated Emission in Graphene

A. Carrier Dynamics in Optically Pumped Graphene

Carrier relaxation dynamics at relatively high temperatures in optically pumped graphene is shown in Fig. 6. When the photogenerated electrons and holes are heated, collective excitations due to the carrier-carrier scattering, e.g., intraband plasmons should have a dominant roll to perform an ultrafast carrier quasi-equilibration (Fig. 6(b)) [19]. Then carriers at high-energy tails of their distributions emit the optical phonons, cooling themselves and accumulating around the Dirac points (Fig. 6(c)). We numerically simulated the temporal evolution of the quasi-Fermi energy and carrier temperature after impulsive pumping with 0.8-eV photon energy [20]. As shown in Fig. 7, due to a fast intraband relaxation (ps or less) and relatively slow interband recombination (>>1ps) of photoelectrons/holes, the population inversion is obtainable under a sufficiently high pumping intensity > 10^7 W/cm^2 [20].

B. Observation of Amplified Stimulated THz Emission

We conducted THz time domain spectroscopy for fs-laser pumped graphene samples and showed that graphene amplifies an incoming terahertz field [21, 22]. An exfoliated monolayer-graphene/SiO$_2$/Si sample was placed on the stage and a 0.12-mm-thick CdTe(100) crystal was placed on the sample, acting as a THz probe pulse emitter as well as an electrooptic sensor [22]. A single 80-fs, 1550-nm, 4-mW, 20-MHz fiber laser was used for optical pump and probe signals as well as generating the THz probe beam. The THz probe pulse double-reflect to stimulate the THz emission in graphene, which is detected as a THz photon echo signal (marked with number "2" in Fig. 8(a)) [22]. Figure 8(b) shows the measured temporal response. The secondary pulse, the THz photon echo signal, obtained with graphene (GR) is more intense compared with that obtained without graphene. When the pumping intensity weakens below 1 x 10^7 W/cm^2 a threshold like behavior can be seen in Fig. 8(c), testifying to the light amplification by stimulated emission of THz radiation. A Lorentzian-like normal dispersion around the gain peak also provides a manifestation of the occurrence of amplification attributed to stimulated emission of photocarriers in the inverted states. If the gain medium of graphene is installed in a pertinent cavity, it will lead to a new type of THz lasers [23].

C. Toward the Creation of Graphene THz Injection Lasers

Optical pumping with rather high photon energy of the order of "~eV" significantly heats the carriers, which dramatically increases the pumping threshold, preventing from population inversion [24]. Hence, the pumping photon energy should be reduced to obtain a higher THz gain even at room temperature. In such a sense, current injection pumping is the best of solution to coupe with this issue because electrical pumping can serve any pumping energy below the order of "meV" when a p-i-n junction is formed like semiconductor laser diodes. Dual gate structure can make a p-i-n junction in the graphene channel as
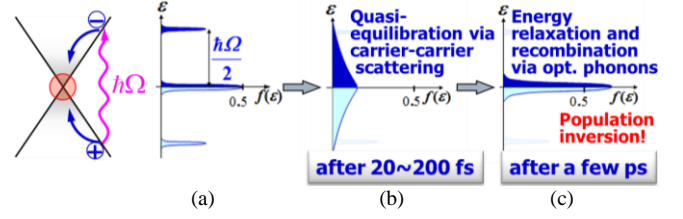

Fig. 6. Carrier dynamics in optically pumped graphene.
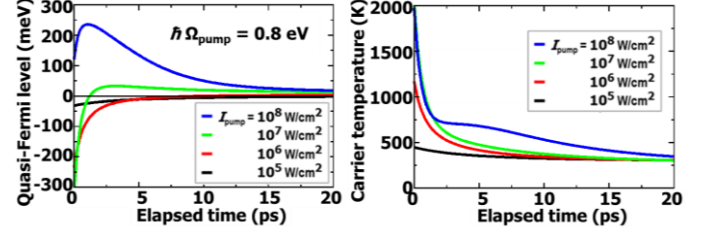
Fig. 7. Numerically simulated time evolution of the quasi-Fermi level (left) and carrier temperature (right) of monolayer graphene after impulsive pumping [20].

shown in Fig. 9 [6]. Gate biasing controls the injection level, whereas the drain bias controls the lasing gain profiles (photon energy and gain). To minimize undesired tunneling current that lowers the injection efficiency the distance between the dual gate electrodes must be sufficiently long [6, 25]. The structure- and material-dependent characteristics have been theoretically
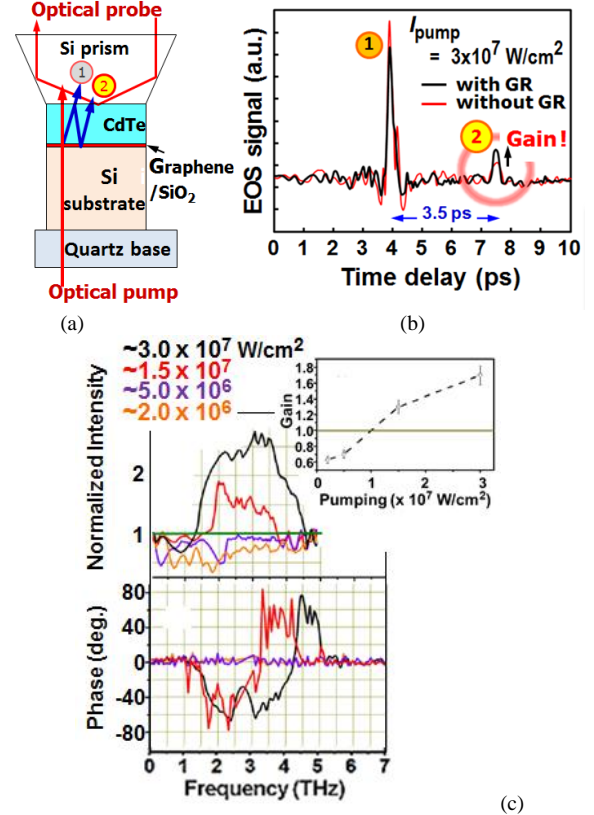

Fig. 8. THz time-domain spectroscopy for 80-fs infrared-laser pumped graphene. (a) pump and probe geometry, (b) temporal response of the THz probe pulse with the photon-echo signal, (c) Fourier spectra normalized to the one without graphene and gain vs. pumping intensity [22].
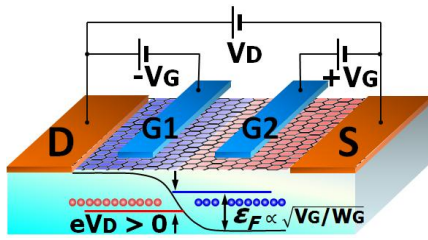
Fig. 9. Schematic for a graphene THz injection laser implemented in a dual-gate graphene-channel FET structure.

revealed in [25]. Recent development in epitaxial graphene synthesis technology enables multiple-layer stacking with keeping the monolayer graphene property, increasing the quantum efficiency in proportion to the number of the multiple graphene layers [26]. Waveguiding the THz emitted waves with less attenuation is another key issue. We theoretically discover the amplification of surface plasmon-polariton when traveling along the graphene-channel waveguide under population inversion [27]. These new findings can help create a new type of room-temperature operating graphene THz lasers.

IV. CONCLUSION

Recent advances in emission and detection of THz radiation from 2D electrons in III-V semiconductors and graphene were reviewed. 2D plasmon resonance in HEMT structures as well as ultrafast non-equilibrium dynamics of massless electrons/ holes in graphene are promising mechanisms for making new types of practical THz sources and detectors.

REFERENCES

[1] M. Tonouchi, "Cutting-edge terahertz technology," *Nature Photon.*, vol. 1, pp. 97-105, 2007.
[2] M. Dyakonov, M.Shur, "Shallow water analogy for a ballistic field effect transistor: New mechanism of plasma wave generation by dc current," *Phys. Rev. Lett.*, vol. 71, pp. 2465–2468, 1993.
[3] M. Dyakonov, and M. Shur, "Detection, mixing, and frequency multiplication of terahertz radiation by two-dimensional electronic fluid," *IEEE Trans. Electron. Dev.*, vol. 43, pp. 1640–1645, 1996.
[4] K. Geim and K. S. Novoselov, "The rise of graphene," *Nature Mater.*, vol. 6, pp. 183-191, 2007.
[5] V. Ryzhii, M. Ryzhii, and T. Otsuji, "Negative dynamic conductivity of graphene with optical pumping," *J. Appl. Phys.*, vol. 101, pp. 083114-1-4, 2007.
[6] M. Ryzhii and V. Ryzhii, "Injection and population inversion in electrically induced p–n junction in graphene with split gates," *Jpn. J. Appl. Phys.*, vol. 46, pp. L151-L153, 2007.
[7] T. Otsuji, M. Hanabe, T. Nishimura, and E. Sano, "A grating-bicoupled plasma-wave photomixer with resonant-cavity enhanced structure," *Opt. Express*, vol. 14, pp. 4815–4825, 2006.
[8] T. Otsuji, Y.M. Meziani, T. Nishimura, T. Suemitsu, W. Knap, E. Sano, T. Asano, V .V. Popov, "Emission of terahertz radiation from dual-grating-gates plasmon-resonant emitters fabricated with InGaP/InGaAs/GaAs material systems," *J. Phys.: Condens. Matters*, vol. 20, pp. 384206-1-11, 2008.
[9] Y. Tsuda, T. Komori, T. Watanabe, T. Suemitsu, T. Otsuji, "Application of plasmonic microchip emitters to broadband terahertz spectroscopic measurement," *J. Opt. Soc. Am. B*, vol. 26, pp. A52-A57, 2009.
[10] A. El Moutaouakil, T. Komori, K. Horiike, T. Suemitsu, and T. Otsuji, "Room Temperature Intense Terahertz Emission from a Dual Grating Gate Plasmon-Resonant Emitter using InAlAs/InGaAs/InP Material Systems," *IEICE Trans. Electron.*, vol. E93C, pp. 1286-1289, 2010.
[11] V. Ryzhii, A. Satou, M. Ryzhii, T. Otsuji, and M. S. Shur, "Mechanism of self-excitation of terahertz plasma oscillations in periodically double-gated electron channels," *J. Phys.: Condens. Matters*, vol. 20, pp. 384207-1-6, 2008.
[12] M.I. Dyakonov, "Boundary instability of a two-dimensional electron fluid," *Semicond.*, vol. 42, pp. 984-988, 2008.
[13] V. V. Popov, D. V. Fateev, T. Otsuji, Y. M. Meziani, D. Coquillat, W. Knap, "Plasmonic terahertz detection by a double-grating-gate field-effect transistor structure with an asymmetric unit cell," *Appl. Phys. Lett.*, vol. 99, pp. 243504-1–4, 2011.
[14] W. Knap, M. Dyakonov, D. Coquillat, F. Teppe, N. Dyakonova, J. Łusakowski, K. Karpierz, M. Sakowicz, G. Valusis, D. Seliuta, I. Kasalynas, A. El Fatimy, Y. M. Meziani, and T. Otsuji, "Field effect transistors for terahertz detection: Physics and first imaging applications," *J. Infrared Milli. Terahz. Waves*, vol. 30, pp. 1319–1337, 2009.
[15] T. Watanabe, K. Akagawa, Y. Tanimoto, D. Coquillat, W. M. Knap, and T. Otsuji, "Terahertz imaging with InP high-electron-mobility transistors," *Proc. SPIE*, vol. 8023, pp. 80230P-1-6, 2011.
[16] D. Coquillat, S. Nadar, F. Teppe, N. Dyakonova, S. Boubanga-Tombet, W. Knap, T. Nishimura, T. Otsuji, Y. M. Meziani, G. M. Tsymbalov, and V. V. Popov, "Room temperature detection of sub-terahertz radiation in double-grating-gate transistors," *Opt. Express*, vol. 18, pp. 6024–6032, 2010.
[17] T. Tanigawa, T. Onishi, S. Takigawa and T. Otsuji, "Enhanced responsivity in a novel AlGaN/GaN plasmon-resonant terahertz detector using gate-dipole antenna with parasitic elements," *68th Device Research Conf. Dig.*, pp. 167–168, Notre Dame, IN, June 2010.
[18] T. Watanabe, S. Boubanba Tombet, Y. Tanimoto, Y. Wang, H. Minamide, H. Ito, D. Fateev, V. Popov, D. Coquillat, W. Knap,Y. Meziani, and T. Otsuji, "Ultrahigh sensitive plasmonic terahertz detector based on an asymmetric dual-grating gate HEMT structure," *Solid State Electron.*, in press.
[19] M. Breusing, C. Ropers, and T. Elsaesser, "Ultrafast carrier dynamics in graphite," *Phys. Rev. Lett.*, vol. 102, pp. 086809-1-4, 2009.
[20] A. Satou, T. Otsuji, V. Ryzhii, "Theoretical study of population inversion in graphene under pulse excitation," *Jpn. J. Appl. Phys.*, vol. 50, pp. 070116-1-4, 2011.
[21] H. Karasawa, T. Komori, T. Watanabe, A. Satou, H. Fukidome, M. Suemitsu, V. Ryzhii, and T. Otsuji, "Observation of amplified stimulated terahertz emission from optically pumped heteroepitaxial graphene-on-silicon materials," *J. Infrared Milli. Terahertz Waves*, vol. 32, pp. 655-665, 2011.
[22] S. Boubanga-Tombet, S. Chan, T. Watanabe, A. Satou, V. Ryzhii, and T. Otsuji, "Ultrafast carrier dynamics and terahertz emission in optically pumped graphene at room temperature," *Phys. Rev. B*, vol. 85, pp. 035443-1-6, 2012.
[23] A. A. Dubinov, V. Y. Aleshkin, M. Ryzhii, T. Otsuji, and V. Ryzhii, "Terahertz laser with optically pumped graphene layers and fabri–perot resonator," *Appl. Phys. Express*, vol. 2, pp. 092301-1-3, 2009.
[24] V. Ryzhii, M. Ryzhii, V. Mitin, A. Satou, and T. Otsuji, "Effect of heating and cooling of photogenerated electron–hole plasma in optically pumped graphene on population inversion," *Jpn. J. Appl. Phys.*, vol. 50, pp. 094001-1-9, 2011.
[25] V. Ryzhii, M. Ryzhii, V. Mitin, and T. Otsuji, "Toward the creation of terahertz graphene injection laser," *J. Appl. Phys.*, vol. 110, iss. pp. 094503-1-9, 2011.
[26] V. Ryzhii, A. Dubinov , T. Otsuji , V. Mitin , and M. S. Shur, "Terahertz lasers based on optically pumped multiple graphene structures with slot-line and dielectric waveguides," *J. Appl. Phys.*, vol. 107, pp. 054505-1-5, 2010.
[27] A.A. Dubinov, Y.V. Aleshkin, V. Mitin, T. Otsuji, and V. Ryzhii, "Terahertz surface plasmons in optically pumped graphene structures," *J. Phys.: Condens. Matter*, vol. 23, pp. 145302-1-9, 2011.

Development of an ultra-sensitive far-infrared detector based on double quantum-well structure

R. Nihei[1,2*], K. Nishimura[1,2], M. Kawada[2], S. Matsuura[2], Y. Doi[3], T. Satoh[3], and S. Komiyama[3]

1 The University of Tokyo*, Bunkyo-ku, Tokyo, 113-0033, Japan
2 Japan Aerospace Exploration Agency, Sagamihara, 252-5210, Japan
3 The University of Tokyo, Meguro-ku, Tokyo, 153-8902, Japan
`* Contact:  nihei@ir.isas.jaxa.jp, phone +81-50-336-25435`

We are developing an ultra-sensitive far-infrared detector for astronomy as an application of CSIPs - Charge Sensitive Infrared Phototransistors. The CSIPs is fabricated in GaAs/AlGaAs double quantum-well structure (Fig.1). The detection principle of CSIPs is that the upper quantum-well (QW) as a floating gate is charged up by photo-absorption between inter-subbands of the QW, and the conductance of the lower QW is increased as the result of the charge up of the gate. We measure the change of current as a function of photon flux. The great advantage of CSIPs is the huge gain of current amplification, so that the noise performance is not limited by the readout noise. CSIPs are well established for mid-infrared photons, shorter than 30 μm in wavelength. The noise equivalent power (NEP) of CSIPs is achieved 2×10^{-19} [W Hz$^{-1/2}$] at 15 μm with the quantum efficiency of 7%.

However, in the far-infrared region (>20 μm), where is the interesting region in astronomy, much more effort to obtain the high performance CSIPs is required. We try to improve the performance of far-infrared CSIPs with a couple of approaches: designing devices structure and optical coupler. For example, the quantum efficiency in 45μm CSIPs is much smaller than values of 15μm CSIPs by two orders of magnitude because photo-couplers suited for longer wavelengths have not been examined. We investigate the antenna pattern to optimize the efficiency for far-infrared CSIPs with both theoretical and experimental approaches. It is, however, difficult to estimate the antenna pattern that depends on the detectable wavelength and the index of refraction because the reststrahlen band of GaAs hardly changes the index of refraction around 35μm. In our experiments, we improved the sensitivity of 26μm CSIPs by optimizing photo-coupler period for the first time (Fig.2).
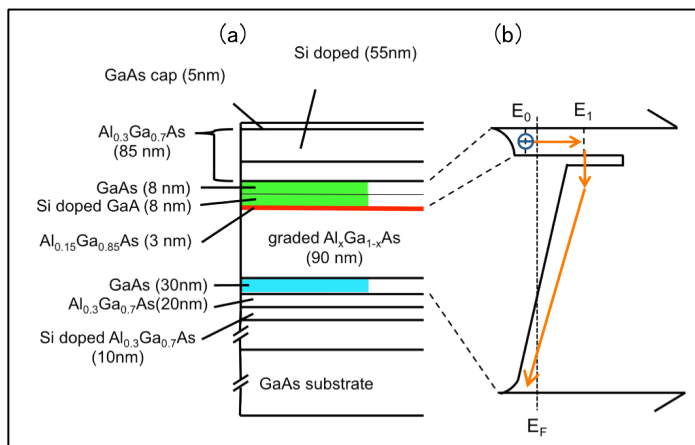

Fig.1. CSIP (a) Crystal structure. (b) Conduction band energy profile.
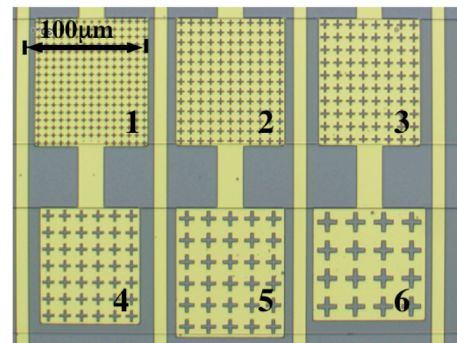
Fig.2. Square lattice metal photo-couplers. We compared the sensitivities between 6 different photo-coupler periods.

YBa$_2$Cu$_3$O$_{7-\delta}$ high-speed detectors for picosecond THz pulses

Petra Probst, Alexander Scheuring, Stefan Wünsch, *Member, IEEE,* Konstantin Il'in, Alexei Semenov, Heinz-Wilhelm Hübers, Vitali Judin, Anke-Susanne Müller, Nigel Smale, Masahiro Adachi, Seiichi Tanaka, Shin-ichi Kimura, Masahiro Katoh, Naoto Yamamoto, Masahito Hosaka, Eléonore Roussel, Christophe Szwaj, Serge Bielawski and Michael Siegel

Abstract—High-speed YBa$_2$Cu$_3$O$_{7-d}$ detectors were developed to monitor terahertz picosecond pulses in the time domain. High-T_C superconducting thin-film YBa$_2$Cu$_3$O$_{7-\delta}$ microbridges with critical temperatures of $T_C = 85$ K were embedded into a planar log-spiral antenna to couple the broadband terahertz radiation (0.1 – 2 THz). The YBa$_2$Cu$_3$O$_{7-\delta}$ detectors were installed in a liquid nitrogen cryostat equipped with 18 GHz effective bandwidth readout electronics. THz pulses generated at the electron storage ring UVSOR-II have been resolved with a temporal resolution of 30 ps (full width at half maximum) limited by the readout electronics bandwidth.

Index Terms—High-temperature superconductor YBa$_2$Cu$_3$O$_{7-\delta}$, thin-film THz detectors, picosecond THz pulses, coherent synchrotron radiation.

P. Probst, A. Scheuring, S. Wünsch, K. Il'in, M. Siegel are with the Institute of Micro- and Nanoelectronic systems, Karlsruhe Institute of Technology, 76187 Karlsruhe, Germany (corresponding author to provide phone: +49 721 608 44447; e-mail: petra.probst@kit.edu).

A. Semenov is with the Institute of Planetary Research, German Aerospace Center (DLR), 12489 Berlin, Germany (e-mail: Alexei.semenov@dlr.de).

H.-W. Hübers is with the Institute of Optics and Atomic Physics, Technical University of Berlin, 10623 Berlin, Germany, and also with the Institute of Planetary Research, German Aerospace Center (DLR), 12489 Berlin, Germany (e-mail: heinz-wilhelm.huebers@dlr.de).

V. Judin and A.-S. Müller are with Laboratory for Applications of Synchrotron Radiation, Karlsruhe Institute of Technology, 76131 Karlsruhe, Germany (e-mail: Vitali.Judin@iss.fzk.de, Anke-Susanne.Mueller@iss.fzk.de).

N. Smale is with the Institute for Synchrotron Radiation, Karlsruhe Institute of Technology, 76344 Eggenstein-Leopoldshafen, Germany (e-mail: nigel.smale@kit.edu).

M. Adachi, S. Tanaka, S. Kimura and M. Katoh are with the UVSOR Facility, Institute for Molecular Science, Okazaki 444-8585, Japan (e-mail: adachi@ims.ac.jp, stanaka@ims.ac.jp, kimura@ims.ac.jp, mkatoh@ims.ac.jp).

N. Yamamoto and M. Hosaka are with Nagoya University, Nagoya, 464-8603, Japan (e-mail: n.yamamoto@nusr.nagoya-u.ac.jp, m-hosaka@nusr.nagoya-u.ac.jp).

E. Roussel, C. Szwaj, S. Bielawski are with Laboratoire de Physique des Lasers, Atomes et Molécules, Université des Sciences et Technologies de Lille, 59655 Villeneuve d'Ascq Cedex, France (e-mail: eleonore.roussel@ed.univ-lille1.fr, christophe.szwaj@univ-lille1.fr, Serge.Bielawski@univ-lille1.fr).

I. INTRODUCTION

IN recent years the generation of ultra-short and high-power THz pulses made significant progress. In electron storage rings the emission of broadband coherent synchrotron radiation (CSR) by accelerated electrons deflected by bending magnets is used to generate picosecond THz pulses [1], [2]. However, to optimize the generation of CSR THz radiation, a detailed understanding of accelerator physics e.g. beam dynamic effects is required. For the analysis of the emitted ultra-short pulses very fast detectors with a time resolution in the single picosecond range are required.

Standard detector technologies currently in use at electron storage rings are e.g. InSb bolometers [3] or Schottky diodes [4]. However, with response times in the microsecond range InSb bolometers [3] are lacking of speed. Whereas Schottky diodes can reach response times in the picosecond range, these devices show small responsivity values and are non-linear resulting in a small dynamic range [5].

The high-temperature superconductor YBa$_2$Cu$_3$O$_{7-\delta}$ (YBCO) is a promising candidate for ultra-fast detectors. Electron energy relaxation times of only a few picoseconds were measured by electro-optical sampling in the optical frequency range which can be explained by a very strong electron-phonon coupling in YBCO thin films [6], [7].

We have developed a fabrication process for thin-film YBCO THz detectors and demonstrated a dynamic range of more than 30 dB for our YBCO microbridges [8].

In this paper we describe a high-speed YBCO direct detection system with broadband high-frequency readout with an effective bandwidth of 18 GHz (Section II). Direct measurements in the time domain revealed a system temporal resolution of 30 ps (FWHM) which was limited by the bandwidth of the oscilloscopes. Results on the detection of pulsed CSR THz radiation emitted by the electron storage ring UVSOR-II in Japan are discussed in Section III.

II. YBCO DETECTION SYSTEM

The YBCO thin film detector chip (3 mm x 3 mm) was mounted to the rear side of a silicon lens. The lens was
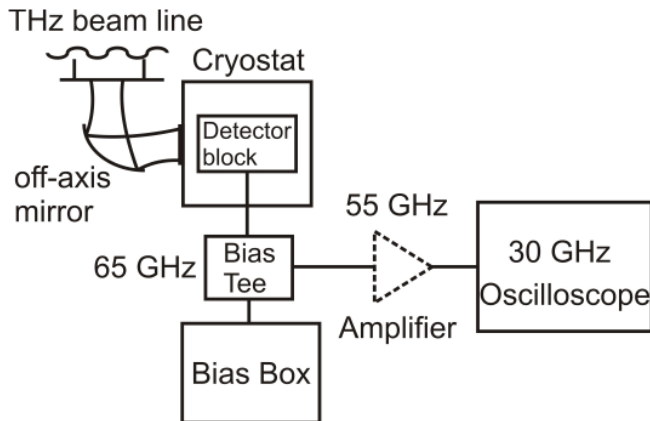
Fig. 1. Scheme of the experimental setup of the direct YBCO detection system to monitor picosecond THz pulses in the time domain. The room temperature amplifier is optional.


Fig. 2. Laser induced CSR pulse measured with the YBCO detection system at UVSOR-II. The full width at half maximum of 30 ps was limited by the bandwidth of the readout electronics.

embedded in a copper detector block to ensure good thermal coupling to the cryostat cold plate. The critical superconducting temperature of the fabricated detector ($T_C \approx 85$ K) allows us to integrate the detector into a liquid nitrogen bath cryostat. The detector block including bonds, readout lines and connectors was simulated with CST Microwave Studio® and revealed a -3 dB roll-off frequency of 30 GHz. The focused synchrotron THz radiation entered the cryostat through a polyethylene window.

The detector block was connected by a 65 GHz broadband semi-rigid cable to the room-temperature bias-tee (50 kHz – 65 GHz). If required, a room-temperature amplifier (200 kHz – 55 GHz) was used before reading out the detector signal in the time domain via a real-time oscilloscope. For our measurements discussed in Section III a 30 GHz LeCroy (LabMaster 9 Zi-A) real-time oscilloscope was used. The scheme of the complete experimental setup is displayed in Fig. 1.

The effective readout bandwidth for our detection system can be calculated according to [10] as

$$ f_{eff} = \left[\sum_i f_i^{-2} \right]^{-1/2}, \qquad (1) $$

where f_i are the electronic bandwidths of the single components. For our detection system including the room-temperature amplifier the effective bandwidth amounts to $f_{eff} \approx 18$ GHz which corresponds to a time resolution of ≈ 20 ps (full width at half maximum (FWHM)). Due to dispersion and reflections along the readout chain a slightly larger time constant is expected.

III. MEASUREMENTS

UVSOR-II, the electron storage ring of the Institute for Molecular Science in Okazaki, Japan, is operated in the beam energy range between 600 and 750 MeV. The radio frequency and the revolution frequency of the ring are 90.1 and 5.6 MHz, respectively. At UVSOR-II, CSR is emitted not only from short bunches but also from electron bunches with longitudinal microstructure of radiation wavelength scale. Laser bunch
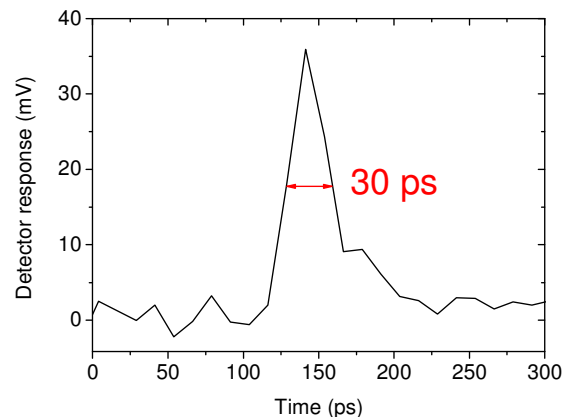
slicing is a technique for creating sub-millimeter dip structure on electron bunches using femtosecond laser pulses [11], [12].

In Fig. 2 a single shot of the detector response to CSR pulses generated by laser slicing at a laser modulation frequency of 0.15 THz is displayed. The 7 ps wide THz pulses (FWHM) resulted in pulses on the oscilloscope of 30 ps which was the limit of the readout electronics. These very fast detector responses are explained in the framework of the vortex flow model which was recently presented by the authors [9].

IV. CONCLUSION

We have developed ultrafast YBCO detectors for picosecond THz pulses which are operated at liquid nitrogen temperatures. The single THz pulses from UVSOR-II were detected with a temporal resolution of 30 ps (FWHM) allowing for the study of beam dynamic effects.

REFERENCES

[1] M. Abo-Bakr, J. Feikes, K. Holldack, G. Wüstefeld, and H.-W. Hübers, "Steady-State Far-Infrared Coherent Synchrotron Radiation detected at BESSY II," *Phys. Rev. Lett.*, vol. 88, no. 25, pp. 254801, June 2002.
[2] A. Plech, S. Casalbuoni, B. Gasharova, E. Huttel, Y.-L. Mathis, A.-S. Müller, K. Sonnad, A. Bartels, and R. Weigel, "Electro-optical sampling of terahertz radiation emitted by short bunches in the ANKA synchrotron," *Proceedings of PAC09*, vol. TU5RFP026, p. 1 – 3, 2009.
[3] QMC Instruments Ltd, http://www.terahertz.co.uk.
[4] Virginia Diodes, Inc., http://vadiodes.com/.
[5] A. Semenov, O. Cojocari, H.-W. Hübers, F. Song, A. Klushin, and A.-S. Müller, "Application of Zero-Bias Quasi-Optical Schottky-Diode Detectors for Monitoring Short-Pulse and Weak Terahertz Radiation," *IEEE Electron Device Lett.*, vol. 31, no. 7, pp. 674-676, May 2010.
[6] M. Lindgren, M. Currie, C. A. Williams, T. Y. Hsiang, P. M. Fauchet, R. Sobolewski, S. Moffat, R. Hughes, J. S. Preston and F. Hegmann, "Ultrafast Photoresponse in Microbridges and Pulse Propagation in Transmission Lines Made from High- Superconducting Y–Ba–Cu–O

Thin Films," *IEEE Journal of selected topics in quantum electronics,* vol. 2, no. 3, pp.668-678, Sep. 1996.

[7] M. Danerud, D. Winkler, M. Lindgren, M. Zorin, V. Trifonov, B. Karasik, G. N. Gol'tsman and E. Gershenzon, „Nonequilibrium and bolometric photoresponse in patterned $YBa_2Cu_3Q_{7-\delta}$ thin films," *J Appl Phys*, vol. 76, no. 3, pp. 1902-1909, Aug. 1994.

[8] P. Probst, A. Scheuring, M. Hofherr, D. Rall, S. Wünsch, K. Il'in, M. Siegel, A. Semenov, A. Pohl, H.-W. Hübers, V. Judin, A.-S. Müller, A. Hoehl, R. Müller, and G. Ulm, „$YBa_2Cu_3O_{7-\delta}$ quasioptical detectors for fast time-domain analysis of terahertz synchrotron radiation," *Appl. Phys. Lett.*, vol. 98, pp. 043504, Jan. 2011.

[9] P. Probst, A. Semenov, M. Ries, A. Hoehl, P. Rieger, A. Scheuring, V. Judin, S. Wünsch, K. Il'in, N. Smale, Y.-L. Mathis, R. Müller, G. Ulm, G. Wüstefeld, H.-W. Hübers, J. Hänisch, B. Holzapfel, M. Siegel, and A.-S. Müller, "Nonthermal response of $YBa_2Cu_3O_{7-\delta}$ thin films to picosecond THz pulses", *Phys. Rev. B*, vol. 85, 174511, May 2012.

[10] A. D. Semenov, R. S. Nebosis, Y. P. Gousev, M. A. Heusinger, and K. F. Renk, "Analysis of the nonequilibrium photoresponse of superconducting films to pulsed radiation by use of a two-temperature model," *Phys. Rev. B,* vol. 52, no. 1, pp. 581-590, July 1995.

[11] R. W. Schoenlein, S. Chattopadhyay, H. H. W. Chong,T. E. Glover, P. A. Heimann, C. V. Shank, A. A. Zholents, and M. S. Zolotorev, "Generation of Femtosecond Pulses of Synchrotron Radiation," *Science*, vol. 287, pp. 2237-2240, March 2000.

[12] S. Bielawski, C. Evain, T. Hara, M. Hosaka, M. Katoh, S. Kimura, A. Mochihashi, M. Shimada, C. Szwaj, T. Takahashi, and Y. Takashima, "Tunable narrowband terahertz emission from mastered laser–electron beam interaction," *Nature Phys.*, vol. 4, pp. 390-393, May 2008.

Fast room temperature THz microbolometers.

S.Bevilacqua, S.Cherednichenko, V.Drakinskiy, J.Stake, A.Kalabukhov
Department of Microtechnology and Nanoscience,
Chalmers University of Technology, SE-41296 Göteborg, Sweden

* Contact: serguei@chalmers.se

Abstract——We will present experimental and theoretical investigation of room temperature high speed THz detectors based on thin $YBa_2Cu_3O_7$ films. These films have TCR of 0.35%/K, and can sustain large bias current densities. With a resistivity of 100-200 $\mu\Omega\times$cm for a film thickness of 50nm, it is very straightforward to impedance match such bolometers with planar antennas. The responsivity is a function of the bolometer planar dimensions and the films thickness. The currently achieved responsivity is 30V/W and Johnson noise limited NEP is 70pW/Hz$^{0.5}$. The bolometer bandwidth is limited by the antenna bandwidth and spans from microwaves to over a few THz. Experimenatl investigation is done from 100GHz to 2.5THz. The measured response time is 2ns. We will also present results of the bolometer performance as their dimensions reduce to sub-μm.

Multiplier-based Sources for 3THz and Beyond

T.W. Crowe, S.A. Retzloff, G.S. Schoenthal and J.L. Hesler

Virginia Diodes Inc., Charlottesville, USA (Crowe@vadiodes.com)

Abstract⸺**All-solid-state local oscillators to frequencies as high as 2.7THz have now been demonstrated by two independent research teams [1,2]. These systems offer several microwatts of power with excellent line quality and frequency tunability. This power is suitable to pump the HEB mixers that have been developed by several groups for radio astronomy. The systems are also compact and suitable for use on airborne instruments, such as those being developed for SOFIA. However, the power level is not yet sufficient to pump planned HEB receiver arrays. Furthermore, astronomers desire even higher frequency systems; specifically for measurements of the important atomic oxygen line near 4.7 THz.**

  This talk will review the status of VDI's development effort for THz sources. Recent results at 2.5, 2.7 and 3.1 THz will be presented and reviewed. This will include discussion of on-going efforts to increase the source power through the use of in-phase waveguide power combining of the lower frequency varactor multipliers. The prospects for generating sufficient power for imaging arrays and the extension of the technology to 4.7 THz will be discussed.

[1]A. Maestrini, I. Mehdi, J. Ward, R. Lin, B. Thomas, C. Lee, J. Gill, G. Chattopadhyay, E. Schlecht, P. Siegel , "A 2.5-2.7 THz room temperature electronic source," Proc. 22nd Intl. Symp. Space Terahertz Technology, Tucson, 26-28 April 2011.

[2]T.W. Crowe, J.L. Hesler, S.A. Retzloff, C. Pouzou, G.S. Schoenthal, "Solid-State LO Sources for Greater than 2THz," Proc. 22nd Intl. Symp. Space Terahertz Technology, Tucson, 26-28 April 2011.

Enabling Compact Multi-Pixel Heterodyne Terahertz Receivers Using On-Chip Power-Combined Multiplied Sources

Jose V. Siles[1*], Goutam Chattopadhyay[1], Alain Maestrini[2], Robert Lin[1], Choonsup Lee[1], Cecile Jung[1], John Gill[1], Alejandro Peralta[1], Erich Schlecht[1] and Imran Mehdi[1]

1 NASA Jet Propulsion Laboratory, Pasadena, CA 91109, USA
2 Observatooire de Paris, LERMA, Paris, 75014, France

Contact: Jose.V.Siles@jpl.nasa.gov, phone +1 818-354-4006

Abstract– The submillimeter-wave range is rich in emission and absorption lines of important molecular species, whose detection and mapping are important to understand the atmospheric circulation of planets, stars and galaxy formation, and pollution and its effects on our atmosphere. Instruments using high resolution heterodyne spectrometers are best suited to study these effects. The current generation heterodyne instruments for terahertz space missions primarily use single-pixel receivers driven by all-solid-state Schottky diode frequency multiplier based local oscillators. The next generation instruments should focus on multi-pixel configurations that allow doing more science during very limited time available for effective Terahertz observations [1]. However, current available sources have low overall efficiency and output power and are not suitable for multi-pixel operation.

With more than 30 µW already available at 1.9 THz from a single-pixel multiplied source developed at JPL, one of the immediate goals would be to develop a compact 4-pixel source module easily extendable to a higher number of pixels. Such a chain would have an immediate application to airborne or space observatories for a more efficient mapping of the C+ ond OI lines. For this task, the efficiency of the overall multiplier chain needs to be increased. High-power multipliers based on traditional device topologies require a very high number of chips to accommodate multiple diodes as well as multiple power-combining/dividing waveguide structures, which makes the integration not very efficient due to undesired waveguide losses and leads to a notable increase of the design effort and the receiver size, cost and volume

In this work we present the progress towards the development of a 1.9-2.1 THz multi-pixel source using the on-chip power combining concept introduced in [2]. This topology employs the 3D capabilities of Silicon micro-machining instead of classical metal block milled housing. Input and output waveguides are placed perpendicular to the waveguide where the diodes are located and four E-probes located in-phase at the input waveguide drive four multiplying structures integrated on a single chip (see Fig. 1a). Losses due to asymmetries are minimized since power-combining is performed 'on-chip'. Alignment and symmetry are no longer determined by the tolerances involved in the metal block machining and manual assembly of multiple chips, but by the superior precision of MMIC lithography. In addition, no Y-junctions or hybrid couplers are necessary to combine the signal as was required for multichip multipliers, considerably reducing the waveguide losses and enhancing generated power. Moreover, the 'on-chip' power-combining topology provides to independent outputs with tunable output power using the dc bias lines, enabling direct multi-pixel operation without any further circuitry. Using this topology, a very compact 4-pixel 1.9-2.1 THz multiplied source can be developed featuring only 4 multiplier chips and producing at least 10 uW of output power per pixel (see Fig. 1b).
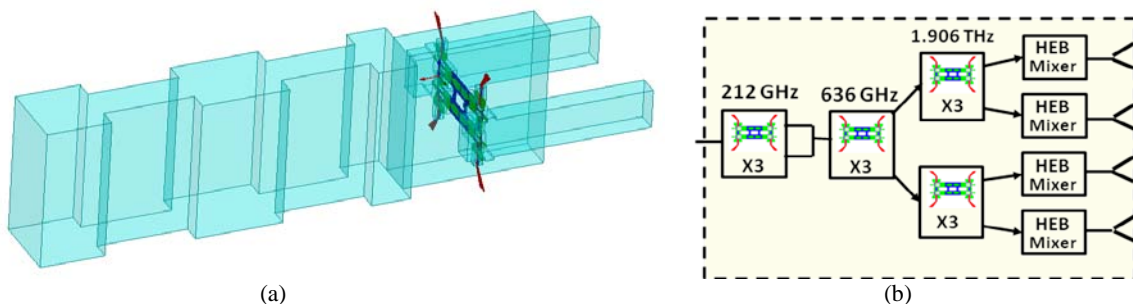
(a)   (b)

Fig. 1. MIDAS high-power dual-chip single-waveguide 190 GHz doubler design (a) and expected performance (b)

The chips for the last two stages have been already fabricated in the JPL Micro Devices Laboratory and housing blocks for testing the individual design will be fabricated soon.

[1] V. Belitsky, V. Desmaris, D. Dochev, D. Meledin A. Pavolotsky, "Towards Multi-Pixel Heterodyne Terahertz Receivers," *Proc. of the 22nd International Symposium on Space Terahertz Technology,* Apr. 2011.

[2] J. V. Siles, B. Thomas, G. Chattopadhyay, A. Maestrini, C. Lee, E. Schlecht, C. Jung and I. Mehdi, "Design of a high-power 1.6 THz Schottky tripler using 'on-chip- power combining and Silicon micromachining," *Proc. of the 22th International Symposium on Space Terahertz Technology*, Apr. 2011.
.

Graphical Prediction of Trapped Mode Resonances in Sub-mm and THz Networks

Matthew A. Morgan, *Member, IEEE* and Shing-Kuo Pan, *Member, IEEE*

Abstract—An analytical method for the visualization and prediction of trapped-mode resonances based on the dimensions of a microwave network is described. The method as explained is intuitive, easy to implement, and has proven itself to be a useful tool in the avoidance of problems associated with trapped modes prior to fabrication, as well as to correct those problems in designs for which the proposed analysis was not carried out in advance.

Index Terms—electromagnetic propagation, orthomode transducer (OMT), radio astronomy, trapped modes

I. INTRODUCTION

WHENEVER the waveguides in a network are overmoded, there exists the possibility of trapped modes. This is especially common with Orthomode Transducers (OMTs) where the required operating bandwidth makes multiple spurious modes difficult to avoid. The most common symptom of trapped modes is the appearance of a suck-out – a sharp, isolated notch in insertion loss – somewhere in the pass-band of the system. For many applications, including some in radio astronomy wherein wideband OMTs are standard components, the presence of a suck-out can be devastating.

Yet, despite a general familiarity with the causes and effects of trapped mode resonances, there appears to be no common practice for their analytical prediction prior to cutting metal. Instead, they are generally regarded as if they were random and unpredictable – perhaps because simulated models, identically lossless and possessed of mathematically-perfect symmetry, do not always reveal them. As such, mode-resonances are most often discovered for the first time during initial testing of the prototype hardware. Then, without a reliable analytical method to guide a revised design, one usually resorts to inserting pieces of absorber to dampen the trapped mode cavity, or placing tighter constraints on manufacturing symmetry to avoid excitation of the unwanted modes. At sub-millimeter wavelengths, the required symmetry
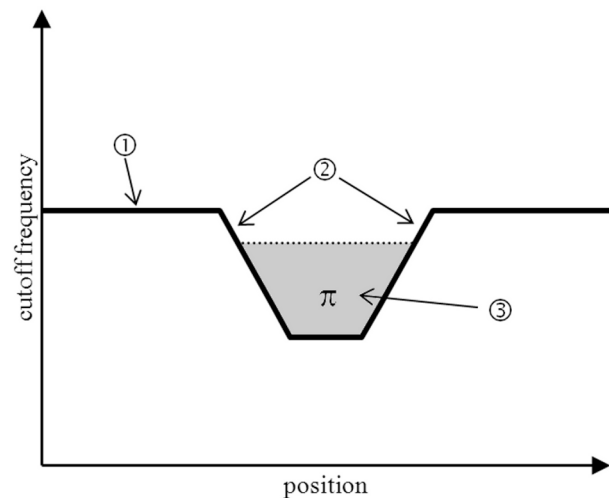
Fig. 1. Graphical representation of a trapped, resonant mode.

is practically impossible to achieve. In addition, field distortion due to losses in the walls near the cutoff of a spurious mode, which is most severe in the sub-mm-wave regime, can also induce mode conversion and provide the linkage between the dominant and trapped modes.

In light of these issues, the authors have adopted a graphical approach, which not only helps to visualize potential problems prior to fabrication, but also to suggest easy solutions for relatively mature designs that exhibit resonances. The underlying principles and implementation of this method are described in this article.

II. THE CAUSE OF TRAPPED-MODE RESONANCES

In order for a suck-out to develop, three conditions must be satisfied:
1. A spurious mode must propagate.
2. The mode must be trapped.
3. The size of the trap must be sufficient for the mode to become resonant.

Notably absent from this list is that most spurious modes also require some kind of asymmetry in the waveguide structure to be coupled with the dominant modes. While strictly true in a theoretical sense, the authors contend that truly perfect symmetry is an impossible ideal that can only be achieved in simulation. In practice, and especially at sub-millimeter-wave
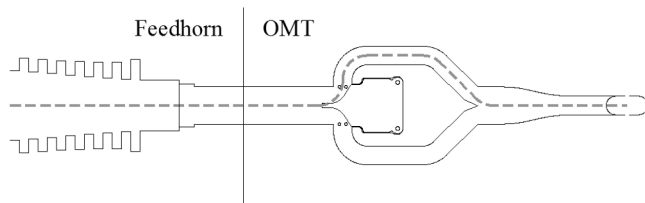
Fig. 2. Section drawing of the ALMA Band 6 (211-275 GHz) feedhorn and OMT. Mode analysis is performed along the dotted line path. Trapped modes are present in the shaded areas.

frequencies, there is always some asymmetry present, if only as a consequence of imperfect manufacturing or part-to-part alignment. Further, the development of a suck-out is intrinsically non-graceful – the onset of bad effects is practically instantaneous on either side of perfect symmetry. It is far better to assume that if a trapped mode can propagate, it will propagate. Fine-tuning the symmetry can only reduce the amount of coupling into the trapped mode, effectively increasing the loaded Q of the resonator. For these reasons, the authors believe that attempts to improve the symmetry may reduce the level of a suck-out, even to the extent that it can no longer be detected in a laboratory setup, but if the above three conditions are met, then it will always be present to some degree.

III. GRAPHICAL REPRESENTATION OF TRAPPED MODE RESONANCES

The three conditions for mode resonance introduced in the previous section can be visualized graphically as shown in Fig. 1, wherein the cutoff frequency of a spurious mode is plotted as a function of position along the signal path in a waveguide network. Since waves will propagate in this mode at any frequency above this curve, the first condition is met simply if the line at any point passes below the upper frequency limit of the operating band for the system in question. The second condition is then met if at any point the curve reaches a local minimum – a *well*, where the mode can propagate over certain frequencies that are cutoff at both ends. Finally, the third condition is met if the well is deep enough and/or long enough that the cavity is half of a guided-wavelength long at a frequency where the mode is still trapped. (To be rigorous, the exact resonant frequency will depend on the reactive impedances presented by the discontinuities at both ends, as well as intermediate reflections from internal impedance-changes, but the half-wave condition is a good approximation in most cases.) This may be estimated by integrating the propagation constant across the cavity to find the total phase

$$\theta(f) \approx \int_{x_1}^{x_2} \beta(x)dx = \int_{x_1}^{x_2} \sqrt{k^2 - k_c^2(x)}dx$$

$$= \frac{2\pi}{c} \int_{x_1}^{x_2} \sqrt{f^2 - f_c^2(x)}dx$$

(1)
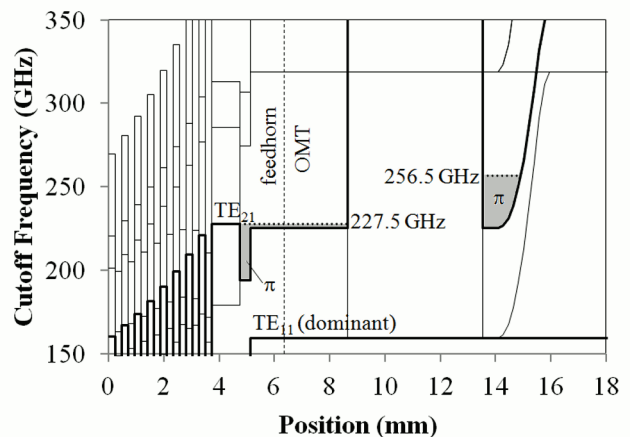
Fig. 3. Plot of the ALMA Band 6 mode analysis predicting two in-band resonances at 227.5 GHz and 256.5 GHz.

and represented graphically by shading in the bottom of the well. The resonance condition is satisfied when $\theta=\pi$. The method thus consists of plotting the cutoff frequencies of all the lowest order modes that can propagate in the structure through each branch of the waveguide network, examining these plots to identify local minima, and then evaluating the integral (1) for each of the minima to determine if the trapped mode will resonate. No assumption is made about how the trapped modes are excited. As stated above, it is simply assumed that if a mode can propagate, then it will be present at some level.

IV. ANALYSIS EXAMPLE AND MEASUREMENTS

To illustrate this method, we consider an example, shown in Fig. 2. This diagram consists of a section of a conical, corrugated feedhorn and Bøifot-style OMT made for Band 6 (211-275 GHz) of the Atacama Large Millimeter Array (ALMA) [2]. The transition from circular-to-square waveguide occurs inside the feedhorn and the flange interface between the horn and the OMT is in square waveguide. A thin, metal septum and vertical wires complete the Bøifot junction. Strictly speaking, the forward tip of the septum creates a very short section of quasi-coaxial waveguide, but this detail is omitted from the analysis for simplicity. The feed-OMT combination is modeled instead as a simple series of circular-, square-, and rectangular-waveguide sections following the side-arm branch of the OMT. The cutoff frequencies are plotted in Fig. 3.

Two trapped-mode resonances are predicted from this plot. The first, at 227.5 GHz, arises from the $TE_{21,a}$ mode trapped between the circular-to-square junction in the feedhorn and the Bøifot junction in the OMT. This resonance is particularly insidious because it requires the two components to be mated to manifest itself, and would be sensitive to (among other things) the alignment of the flanges at the interface. Measurements of either component alone may not even show a resonance, and if they did, it could be at an entirely different
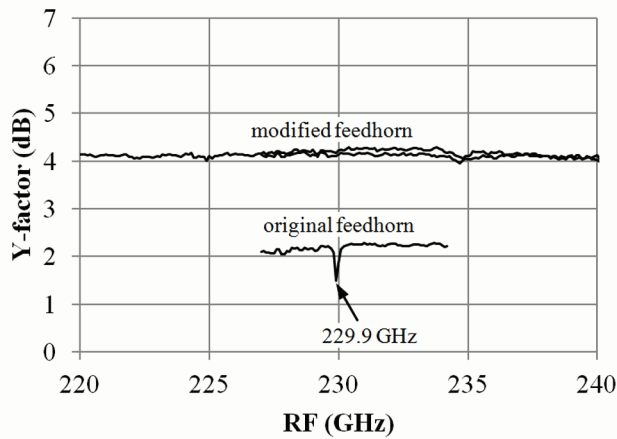
Fig. 4. Measured 230 GHz resonance in an ALMA Band 6 receiver with original and modified feedhorns. Vertical offset added for clarity.

Fig. 5. Measured 256 GHz resonance in an ALMA band 6 receiver.

frequency. This fact highlights the need to consider whole systems, not just sub-components, and to be especially careful of interfaces that occur in overmoded waveguide – or better yet, to avoid such interfaces altogether.

The second resonance, predicted at 256.5 GHz, occurs in the passive combiner between the two side-arms. The two rectangular waveguides are first joined to form a square waveguide, then the square waveguide is tapered back down to rectangular again. This causes the modes in the combiner to drop in cutoff frequency, then rise again, forming a cutoff well. As we have now seen, such a feature is a good recipe for trapped-mode resonances to occur. Both the $TE_{21,a}$ and TM_{01} modes, which are degenerate in square waveguide, exhibit this resonance.

To be fair, the potential for trapped modes were well understood by the designer of this OMT [2] who warned against carelessness at the interface to the feed and documented the tradeoffs associated with the sidearm combiner. Nevertheless, despite these warnings the issues were not fully appreciated by the broader engineering community, highlighting the lack of attention to trapped modes that is common in the design phase of a project.

Although it is unfortunate for the Band 6 project that these issues were not better understood until after most of the production feedhorns and OMTs had been fabricated, the situation does provide us a unique opportunity to verify the theory through measurement. The lower (and, it turns out, more prominent) resonance at 227.5 GHz was not observed during qualification of the prototype components because, as described earlier, it is only present at that frequency when the horn and OMT are joined together. Resonances which were measured at the component-level were dismissed as artifacts of the tapered square-to-rectangular transitions used in the test set – an assumption seemingly confirmed when those resonances disappeared after inserting resistive vanes into the tapers. Of course, since those resistive vanes absorb energy from the higher-order modes as well as the orthogonal dominant mode for which the vanes were intended, the basis for dismissing
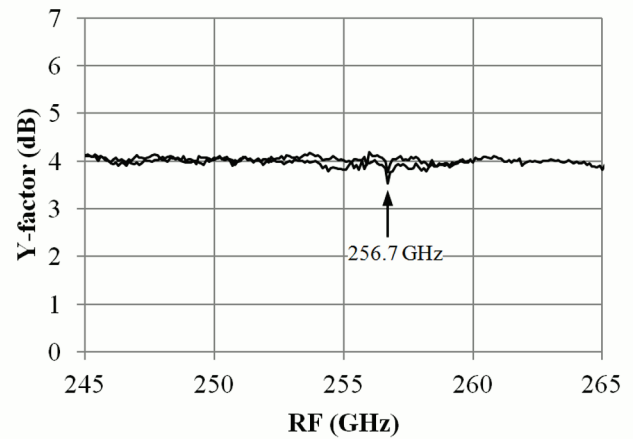
these resonances was not entirely justified.

Y-factor and noise temperature measurements proved to be the most effective way of observing these resonances in actual hardware. Fig. 4 and Fig. 5 show measurements of these resonances in an actual ALMA Band 6 receiver. Multiple curves on each plot correspond to the different LO tunings and/or upper- and lower-sidebands. The first resonance is evident in Fig. 4 at 229.9 GHz, slightly higher than predicted. A small shift upward in frequency, about 0.4%, was expected due to shrinkage of the metal (brass) which is cooled in this application to 4 Kelvin. The discrepancy here is much larger than that, however, and is probably due to the geometric approximations that were made around the septum area to simplify analysis. The cutoff plane for the $TE_{21,a}$ mode must be closer to the tip of the septum than was estimated, effectively shortening the trapped-mode cavity. Nonetheless, an error of only 1.1% relative to prediction (0.7% after accounting for thermal contraction) is an encouraging validation of the theory. The higher predicted resonance at 256.5 GHz was also detected (Fig. 5), although in fewer production units and at a weaker level. In this case, the full geometric detail of the cavity was included in the model, and the predicted location of the resonance was much more accurate.

Because the lower suck-out appears near the bottom of the Band 6 operating range, it was initially suggested that the leading square waveguide in the OMT could be lengthened, thus lowering the resonant frequency and tuning it out of band. However, the mode in question is very near cutoff in this region, and thus has an extremely long guided wavelength, approaching infinity as the resonant frequency is lowered. Large changes in length have only a small effect on resonant frequency, and no matter how long this section was made, the resonant frequency would never get lower than the cutoff of the upper step in the well at 225.5 GHz, which is still in band. Close examination of Fig. 8 suggests a better solution. With the TE_{21} mode cutting off very near to 230 GHz in the circular throat of the feedhorn, the well is just barely deep enough as it is to support the first resonance. This analysis confirmed that a mere 0.8% increase in the diameter of this one section would

be sufficient to eliminate the resonance with a comfortable margin. Interestingly, the suck-out in this way is not tuned out of band, but entirely out of existence, vanishing from the spectrum in place, and with little observable effect on the behavior of the rest of the system. This modification was made in a small number of later feedhorns and the resulting clean spectrum for a typical unit is shown in Fig. 4. The curve exhibiting the resonance was offset vertically for clarity.

V. CONCLUSIONS

The causes and effects of trapped-mode resonances or suck-outs in overmoded waveguide systems have been reviewed in detail. A graphical technique for visualizing the conditions that lead to trapped-mode resonances has been described, and used to analyze a number of real-world examples in the sub-millimeter-wave regime. The technique was then verified by comparing measured evidence of trapped modes in fabricated hardware against the predictions. Despite a number of simplifying assumptions, the suck-outs were observed within 1% of their predicted frequencies, and disappeared from the data when the corrective modifications suggested by the technique were implemented. These examples highlight the power of this kind of analysis to visualize the problems as well as the simplest solutions to trapped-modes in complex waveguide networks.

REFERENCES

[1] A. Wexler, "Solution of Waveguide Discontinuities by Modal Analysis," *IEEE Trans. Microwave Theory Tech.*, vol. 15, no. 9, pp. 508-517, September 1967.
[2] E. Wollack, W. Grammer, and J. Kingsley, "The Bøifot Orthomode Junction," *ALMA Memo Series*, no. 425, May 2002.

High Absorptance Coatings for THz Applications

E.J. Wollack

NASA Goddard Space Flight Center, Observational Cosmology Laboratory, Greenbelt, MD 20771
Contact: edward.j.wollack@nasa.gov

Abstract⎯⎯ **High absorptance materials find application throughout the electromagnetic spectrum as radiation terminations, calibration standards, and glint reduction coatings. Successful use of materials at millimeter through sub-millimeter wavelengths requires an accurate knowledge and control over their thermal, mechanical, and electromagnetic properties in order to achieve the desired response while minimizing mass and volume. In practice, the achieved *blackness* is intimately linked to the material properties and geometry. Here, we summarize the characteristics of a variety of tunable artificial dielectric mixtures appropriate for THz applications at room and cryogenic temperatures. Theoretical guidelines for their application will be provided in the context of the effective-medium mean-field-approximation. The performance of these coatings as elements of reflectance standards, radiometric flux calibrators, passive thermal radiators, and stray light suppression baffles for imaging systems will be reviewed.**

Development of Direct Machined Silicon Lens Array for Millimeter-wave Kinetic Inductance Detector Camera

Tom Nitta[1,2*], Masato Naruse[3], Yutaro Sekimoto[2], Kenji Mitsui[2], Norio Okada[2], Kenichi Karatsu[2], Masakazu Sekine[2,4], Hiroshi Matsuo[2], Takashi Noguchi[2], Yoshinori Uzawa[2], Masumichi Seta[1], and Naomasa Nakai[1]

[1] *Institute of Physics, University of Tsukuba, Tsukuba, Ibaraki, 305-8577, Japan*
[2] *National Astronomical Observatory of Japan, Mitaka, Tokyo, 181-8588, Japan*
[3] *Graduate School of Science and Engineering, Saitama University, Saitama, Saitama, 338-8570, Japan*
[4] *Department of Astronomy, The University of Tokyo, Bunkyo-ku, Tokyo, 113-0033, Japan*
* Contact: tom.nitta@nao.ac.jp, phone +81-422-34-3942

Abstract— **We have developed 220 GHz camera using microwave kinetic inductance detectors (MKIDs) for astronomical observations. The optical system of the MKID camera is based on double slot antennas and an extended hemispherical silicon lens array. The diameter of the lens was determined as three times larger than the wavelength at 220 GHz. The 220 GHz camera has 9 pixels. The silicon lens array has been directly machined by high-speed spindle on an ultra-precision machine. The shape fabrication error and the surface roughness of the top of the lens were less than 20 μm (Peak-to-Valley) and about 0.7 μm (rms), respectively. The beam patterns of the MKID camera were measured and are in good agreement with the calculations.**

I. INTRODUCTION

Wide field-of-view observations of millimeter-wave and submillimeter-wave emissions are required in order to study star forming regions and distant galaxies which are obscured by dust (for example, [1]). For this purpose, the construction of ground based telescopes such as CCAT [2], and Antarctica Terahertz Telescope [3], as well as the development of large format cameras are planned in the world. Wide-field observations with large format camera play a complementary role with high angular and high frequency resolution observations with the Atacama Large Millimeter/submillimeter Array (ALMA) [4] whose early science observations have just started.

Microwave Kinetic Inductance Detectors (MKIDs) [5] with superconducting microresonators are a promising technology for large format (>1000 pixels) cameras [6]. MKIDs have been widely developed in the millimeter and sub-millimeter wave ranges [7]-[10]. MKID consists of superconducting resonators whose resonance frequencies are distributed in the microwave range, typically 1-12 GHz. Incident photons, which have higher energy than the superconducting gap energy (2Δ), break cooper pairs and create quasi-particles in the resonator. The increase of number of quasi-particles induces a change of the surface impedance of the superconducting film, which decreases the resonance frequency and the quality factor of the resonator. Millimeter

and sub-millimeter wave signals are observed by monitoring the shift of the resonance frequency.

The coplanar waveguide (CPW) quarter-wave resonator is well-matched with a planar antenna which is used to couple the signal from the telescope optics to the MKIDs. Most planar antennas require additional focusing elements for efficient coupling to the telescope optics, such as substrate lenses or feed horns. In this study, we adopted the lens array and planar antennas as the optical system for the millimeter wave camera.

II. LENS DESIGN AND FABRICATION

A. Design of Extended Hemispherical Lenses

The optical system of the MKID camera for the 220 GHz band is based on double slot antennas and an extended hemispherical lens array. The double slot antenna is patterned at the end of the quarter-wave resonator, which is in the opposite side of the feed line. The high-purity polycrystalline silicon (11N purity) was chosen as a suitable lens material because it has small dielectric loss in the millimeter and sub-millimeter bands [11].

The geometrical parameters of the double slot antenna were optimized for a target frequency to minimize return loss (S_{11}) and to achieve symmetrical beam patterns and low side lobe levels. The optimized parameters for the 220 GHz band were 382 μm in length, 25 μm in width and 212 μm in slot separation. The lens diameter is determined as three times of the target wavelength. Here the extension thickness L is defined as L = d - R. Where, d is the distance between the antenna and the top of the lens, and R is the lens radius. In order to determine the extension thickness, the beam patterns of an extended hemispherical silicon lens fed by a double slot antenna were calculated with HFSS, a 3-D full-wave electromagnetic field simulator. Numerical calculations are based on [12]. The extension thickness (L) is optimized considering the beam pattern quality, such as side lobe level and symmetry of main beam. It was determined to be L=0.73

mm for 220 GHz.

B. Fabrication and Evaluation of the Silicon Lens

A small diameter lens array has been fabricated with techniques such as photolithography or laser machining [13]-[15]. Ultra-precision cutting by using ball end mills was tried as another efficient technique to process the high-purity polycrystalline silicon in shape of the lens. The 220 GHz lens diameter and the lens spacing were 4.09 mm and 0.3 mm, respectively. To achieve 0.3 mm in lens spacing and get a surface accuracy in the order of μm, a small diameter end mill was needed. In addition, it required a rotating speed of more than several tens of thousands rpm to keep cutting velocity of end mill. Therefore, a combination of the ultra-precise processing machine, Toshiba ULG-300, and the high-speed spindle, Toshiba ABC-20M, is used for this process. The machining tools are made of TiAlN coated ceramic end mill with radius of 0.5 mm and 0.15 mm. Figure 1 shows the photograph of the 9 pixel 220 GHz silicon lens array under processing, and table 1 shows the processing conditions of the silicon lens array.

A three-dimensional coordinate measuring machine was used to measure the shape of the lenses. The shape error from the designed value was less than 20 μm (Peak-to-Valley). The surface roughness of the top of the lens was also measured by using the non-contact three-dimensional measuring machine. The surface roughness of the top of the lens was around 0.7 μm in rms. This value is small enough for use in the millimeter wave range.

III. BEAM PATTERN MEASUREMENTS

A. Measurement System

The MKID camera was fabricated by using silicon lens array and Al-based MKIDs. Epitaxial Al(111) film has been grown on a Si(111) wafer by using molecular beam epitaxy [16]. The thickness of the aluminum film was 150 nm. The CPW geometry had a 3 μm-wide central line and 2 μm-wide gaps.

A ^{3}He sorption cooler mounted on a liquid helium cryostat was used for beam pattern measurements of the MKID camera. Temperature of the cold stage was kept at around 300 mK and the holding time is about 8 hours. Figure 2 shows the photograph of the beam pattern measurement system. The millimeter wave signals were radiated from a rectangular probe horn, and scanned around the vacuum window of the cryostat. The response of MKIDs was measured from the S_{21} spectrum taken by a vector network analyzer.

B. Results

Figure 3 shows the measurement results of 2D far-field beam pattern of the extended hemispherical silicon lens fed by the double slot antenna at 220 GHz. The dynamic range of this measurement system was about 20 dB, which is limited by the Al MKID's sensitivity at the measurement temperature of 300 mK. The half-power beam width is about 20 degree, and the comparison of the 220 GHz beam pattern between the measurements and the calculations showed good agreement.

|	
Rotating speed	40000 [rpm]
Rotation unbalance	Below 10 [nm]
Cutting feed rate	100-120 [mm/min]
Cutting depth	20-100 [μm]
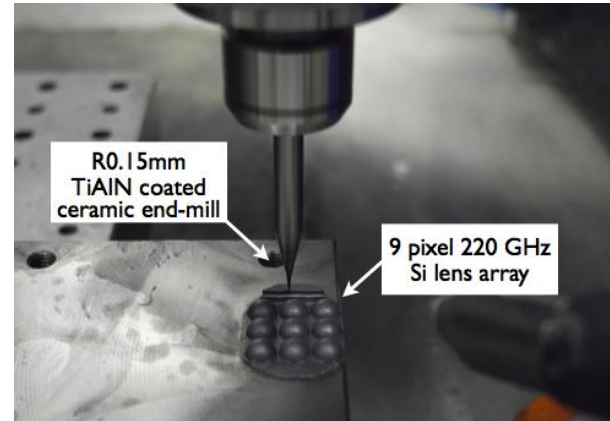
Fig. 1. The photograph of the 9 pixel 220 GHz silicon lens array under processing.
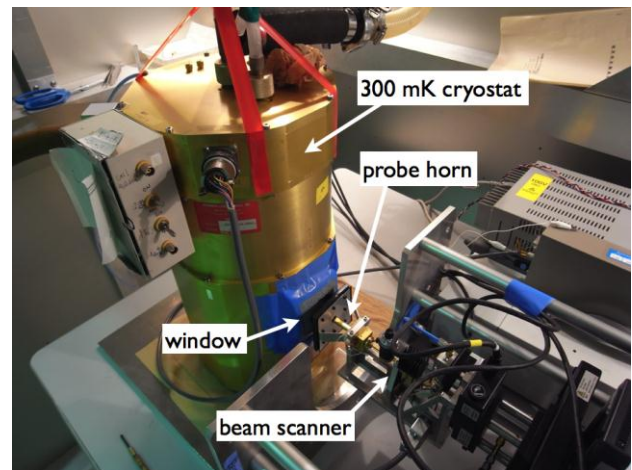

Fig. 2. The photograph of the beam pattern measurement system.
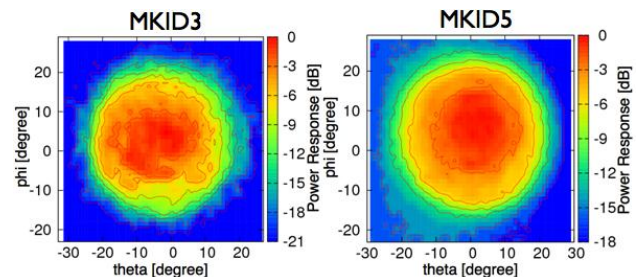
Fig. 3. The measurement results of 2D far-field beam patterns of the extended hemispherical silicon lens array fed by the double slot antennas at 220 GHz. The contours were every 3 dB steps.

IV. CONCLUSION

In this paper, we reported the development of millimeter wave MKID camera with direct machined silicon lens array, and the measurements of their beam patterns. The silicon lens array has been shaped with ultra-precision cutting techniques, and high-speed spindle. The shape error from the design value and the surface roughness of the top of the lens were less than 20 μm (Peak-to-Valley) and about 0.7 μm (rms), respectively, which shows a good enough processing accuracy for the millimeter wave range. The comparison of the measured beam patterns to the calculations showed good agreement. This proved that the silicon lens array, processed with the ultra-precision cutting, is capable to perform as the optical system of the millimeter wave camera.

REFERENCES

[1] A. Blain, I. Smail, R. Ivison, J. Kneib, and D. Frayer, "Submillimeter galaxies," *Physics Reports*, vol. 369, no. 2, pp. 111–176, 2002.

[2] T. Sebring, "The cornell caltech atacama telescope: progress and plans 2010," in *Proceedings of SPIE*, vol. 7733, 2010, pp. 77331X–1.

[3] T. Ichikawa, "Future plans for astronomy at dome fuji," *Proceedings of the International Astronomical Union*, vol. 5, no. H15, pp. 632–633, 2009.

[4] A. Wootten and A. Thompson, "The atacama large millimeter/submillimeter array," *Proceedings of the IEEE*, vol. 97, no. 8, pp. 1463–1471, 2009.

[5] P. Day, H. LeDuc, B. Mazin, A. Vayonakis, and J. Zmuidzinas, "A broadband superconducting detector suitable for use in large arrays," *Nature*, vol. 425, no. 6960, p. 817, 2003.

[6] J. Zmuidzinas, "Superconducting microresonators: Physics and applications," *Annual Review of Condensed Matter Physics*, vol. 3, no. 1, 2012.

[7] A. Monfardini *et al.*, "A dual-band millimeter-wave kinetic inductance camera for the iram 30 m telescope," *The Astrophysical Journal Supplement Series*, vol. 194, p. 24, 2011.

[8] S. Yates, J. Baselmans, A. Endo, R. Janssen, L. Ferrari, P. Diener, and A. Baryshev, "Photon noise limited radiation detection with lens-antenna coupled microwave kinetic inductance detectors," *Applied Physics Letters*, vol. 99, p. 073505, 2011.

[9] A. Neto, A. Iacono, G. Gerini, J. Baselmans, S. Yates, A. Baryshev, and H. Hoovers, "Leaky lens based uwb focal plane arrays for sub-mm wave imaging based on kinetic inductance detectors," in *Proc. of European Conference on Antennas and Propagation (EuCAP)*, 2009, pp. 1824–1827.

[10] P. Maloney *et al.*, "Music for sub/millimeter astrophysics," in *Proceedings of SPIE*, vol. 7741, 2010, p. 77410F.

[11] J. Lamb, "Miscellaneous data on materials for millimetre and submillimetre optics," *International Journal of Infrared and Millimeter Waves*, vol. 17, no. 12, pp. 1997–2034, 1996.

[12] D. Filipovic, S. Gearhart, and G. Rebeiz, "Double-slot antennas on extended hemispherical and elliptical silicon dielectric lenses," *IEEE Trans. Microwave Theory Tech.*, vol. 41, pp. 1738–1749, 1993.

[13] N. Llombart, G. Chattopadhyay, and C. Lee, "Micro-lens antenna for integrated thz arrays," in *Proc. Int. Workshop on Antenna Technology (iWAT)*, 2010, pp. 1–4.

[14] N. Llombart, B. Thomas, M. Alonso, C. Lee, G. Chattopadhyay, L. Jofre, and I. Mehdi, "Silicon based antennas for thz integrated arrays," in *Proceedings of the 5th European Conference on Antennas and Propagation (EuCAP)*, 2011, pp. 3176–3179.

[15] S. Yates, J. Baselmans, A. Baryshev, A. Neto, G. Gerini, R. Barends, Y. Lankwarden, B. Young, B. Cabrera, and A. Miller, "Antenna coupled kinetic inductance arrays for space and ground based imaging arrays," in *AIP Conference Proceedings*, vol. 31, no. 1, 2009, p. 144.

[16] M. Naruse, Y. Sekimoto, T. Noguchi, A. Miyachi, T. Nitta, and Y. Uzawa, "Development of crystal al mkids by molecular beam epitaxy," *Journal of Low Temperature Physics*, pp. 1–6, 2011.

Herschel-HIFI THz technology in action for astrophysics

P.R. Roelfsema[1,2], and F.P. Helmich[1,2*] on behalf of the HIFI consortium

1 SRON Netherlands Institute for Space Research, Landleven 12, 9747 AD Groningen, The Netherlands
2 Kapteyn Astronomical Institute, University of Groningen, Groningen, The Netherlands
* Contact: f.p.helmich@sron.nl, phone +31-50-363 4799

Abstract—The Heterodyne Instrument for the Far-Infrared (HIFI) on board of the Herschel Space Observatory is providing the astronomical community with very spectral resolution data covering many water lines, inaccessible from ground or airborne platforms and unbiased spectral surveys up to the important frequency of the [CII] line at 1.9 THz.

In this paper we present an overview of the most significant results found to date, especially on the water observations in a wide range of astrophysical objects. The performance of HIFI is very much related to a thorough characterization of the flight instrument. We will discuss the main parameters involved and indicate the main steps taken since the in-orbit performance paper.

An Optical Design Concept for Future Heterodyne Instrumentation in Space

W. Jellema[1,2]*, A. Baryshev[1,2], H. van Driel[3,1] , R. Huisman[1], M. Eggens[1], G. Chattopadhyay[4], P.F. Goldsmith[4], M. Whale[5], N. Trappe[6], J. A. Murphy[6], M. Arkhipov[7], S. Likhachev[7], and N. Kardashev[7]

[1]*SRON Netherlands Institute for Space Research*, Landleven 12, 9747 AD, Groningen, The Netherlands*
[2]*Kapteyn Astronomical Institute, University of Groningen, P.O. Box 800, 9700 AV, Groningen, The Netherlands*
[3]*Faculty of Mathematics and Natural Sciences, University of Groningen, Nijenborgh 4, 9747 AG, Groningen, The Netherlands*
[4]*NASA-Jet Propulsion Laboratory, California Institute of Technology, 4800 Oak Grove Drive, Pasadena, CA 91109, United States*
[5]*Institute of Applied Physics, University of Bern, Sidlerstrasse 5, CH-3012, Bern, Switzerland*
[6]*National University of Ireland, Maynooth, Co. Kildare, Ireland*
[7]*Astro Space Center, Lebedev Physical Institute of Russian Academy of Sciences, 84/32 Profsoyuznaya Street, Moscow, 117997, Russia*

* Contact: W.Jellema@sron.nl, phone +31-50-363 4058

Abstract— **Existing ground- and space-based astronomical observatories like Herschel-HIFI, SOFIA and ALMA currently provide a wealth of high spectral resolution data in the far-infrared domain that are of key importance in modern astrophysics. Whereas the science goals of future space missions like JWST and SPICA can be targeted with highly sensitive direct detectors and medium spectral resolution spectrometers, a next generation space instrumentation will eventually require high resolution spectroscopy with $R \approx 10^7$ to 10^8 at far-infrared wavelengths probing the physical conditions and chemistry involved in for example star formation processes. Future heterodyne instrumentation requires in addition to enhanced spatial resolution and frequency extension into the 2-6 THz frequency range the application of heterodyne receiver arrays improving the overall mapping and observing efficiency.**

In this paper we present results of an optical design study into future heterodyne instrumentation for space. As a specific case we propose an instrument concept which can for example be applied to the Russian Millimetron mission. In addition to the required development of super-THz mixer, LO and low-dissipation IF amplifier technology overcoming thermal constraints related to the application of arrays, the optical design of a compact instrument accommodating multiple bands of heterodyne receiver arrays is considered as one of the main design challenges. We propose a highly flexible and modular system inspired by Herschel-HIFI enabling the operation of compact THz heterodyne arrays and offering dual-polarization and/or dual frequency observing capabilities. As future missions most likely feature a cooled telescope, with complementary direct detection instrumentation requiring low thermal backgrounds, special attention has been paid to the thermal architecture in relation to the Local Oscillator injection scheme.

Photon Counting Terahertz Interferometry

H. Matsuo

National Astronomical Observatory of Japan, Tokyo 181-8588, Japan
Contact: h.matsuo@nao.ac.jp, phone +81-422-34-3915

Abstract—I have proposed in the 22nd ISSTT symposium in 2011 that a combination of intensity interferometer with photon counting terahertz detector can be a powerful tool for future high angular resolution observation in terahertz frequencies. I name it as Photon Counting Terahertz Interferometry (PCTI). Advantage of PCTI is that high efficiency observation is expected in terahertz frequencies when brightness temperature of sources are higher than about 100 K, and that bunched photon can be used to measure delay time of photon arrival, hence phase information can be obtained. Possible applications are for high angular resolution observations of far-infrared atomic fine structure lines, and for searching and imaging studies of exo-planets.

There are many challenges to realize PCTI, such that fast photon counting detectors in terahertz frequencies are required, that accurate photon arrival timing be measured, and that efficient recording and usage of photon statistics be realized. I will be discussing current status of these challenges and a roadmap to realize PCTI. Some experimental evaluation of bunched photon measurements will be presented.

Interferometry using dual photon response
of submm direct detectors

A. M. Baryshev[1,2], R. Hesper[2], A. Khudchenko[1], T.M. Klapwijk[3]

1 SRON Space Research of Netherlands* Groningen, 9747 AD, The Netherlands
2 Kapteyn Astronomical Institute, Groningen, 9747 AD, The Netherlands
3 Delft University of Technology, Delft, 2628 CJ, The Netherlands
* Contact: a.m.baryshev@sron.nl, phone +31-50-3638287

Abstract— **When two or more photons arrive to a detector at the same time they produce an interference signal with frequency which is the difference of photons individual frequencies. If the detector's internal integration time is small enough this differential photon signal is present at the detector's output. This signal preserves photon's differential phase and thus can be used for non beam combining interferometry. In this contribution we demonstrate experimentally the single station differential photon operation mode as well as differential dual photon non beam combining interferometer using two of such detectors. We use superconductor-insulator-superconductor (SIS) junction as a fast direct detector. Applications of this dual photo interferometry for current and future instruments will be discussed. Directions and approach to detector parameter optimization and development towards realization of described the interferometry principle will be discussed.**

The next-generation infrared space mission SPICA

T. Nakagawa, H. Matsuhara, Y. Kawakatsu (JAXA), and SPICA Preproject Team

Abstract⸺**SPICA (Space Infrared Telescope for Cosmology and Astrophysics) is an astronomical mission optimized for mid- and far-infrared astronomy with a cryogenically cooled 3.2 m telescope. Its high spatial resolution and unprecedented sensitivity in the mid- and far-infrared will enable us to address a number of key problems in present-day astronomy, ranging from the star-formation history of the universe to the formation of planets. To reduce the mass of the whole mission, SPICA will be launched at ambient temperature and cooled down on orbit by mechanical coolers on board with an efficient radiative cooling system, a combination of which allows us to have a 3-m class cooled (6 K) telescope in space with moderate total weight (3.7t). SPICA is proposed as a Japanese-led mission together with extensive international collaboration. The most important international partner is ESA. The assessment study on the European contribution to the SPICA project has started under the framework of the ESA Cosmic Vision 2015-2025. Korea has also established a formal SPICA tema at KASI. Taiwan and US participations are also being discussed extensively. The target of launch is around 2020.**

The SAFARI Imaging Spectrometer for the SPICA space observatory

P,R, Roelfsema[*,1,2], P Najarro, M. Giard, C,K, Wafelbakker[1], B. Jackson[1], W.Jellema[1],
on behalf of the SAFARI consortium

1 SRON Netherlands Insitute for Space Research, Groningen, The Netherlands;
2 Kapteyn Astronomical Institute, Groningen, The Netherlands
3 CAB-INTA, Madrid, Spain, 4 IRAP, Toulouse, France
* Contact: p.r.roelfsema@sron.nl, phone +31-50-363 4074

Abstract—— **The Japanese SPace Infrared telescope for Cosmology and Astrophysics, SPICA, will provide astronomers with a long awaited new window on the universe. Having a large cold telescope cooled to only 6K above absolute zero, SPICA will provide a unique environment where instruments are limited only by the cosmic background itself. A consortium of European and Canadian institutes has been established to design and implement the SpicA FAR infrared Instrument SAFARI, an imaging spectrometer designed to fully exploit this extremely low far infrared background environment provided by the SPICA observatory.**

SAFARI, is an imaging Fourier Transform Spectrometer (FTS) designed to provide continuous coverage in photometry and spectroscopy from 34 to 210 µm, with a field of view of 2'×2' and various spectral resolution modes up to R = 2000 (at 100 µm). Like the SPIRE instrument on Herschel, SAFARI utilizes a Mach-Zehnder interferometer as a means to obtain spectral information. In such an interferometer the incoming beam is split over two optical branches which each contain moveable mirrors. The two beams are recombined and the combined beam is subsequently forwarded to the detectors. By moving the mirrors in the beams the path length along the two branches differs and the resulting combined signal yields an interferogram as function of the Optical Path length Delay (OPD). This interferogram corresponds to the Fourier transform of the incoming spectrum. By employing a detector array instead of a single pixel in the image plane, interferograms can be obtained simultaneously for a large on-sky area. By subsequently applying a Fourier transform to all interferograms, spectra are obtained simultaneously for all ~4000 pixels covering the instrument field of view. Observations obtained by scanning the mirror of the FTS (along the magnetic bearings) over the full stroke yield spectra with a resolution of R~2000 in the middle of the wavelength band. For lower resolution (SED mode) spectra a shorter scan is taken. Additionally the instrument can operate in a photometric mode in which the FTS is fixed at one end of its stroke.

To cover the full 34 to 210 µm wavelength range the SAFARI detector system utilizes three large-format detector arrays. As the telescope spatial resolution decreases towards longer wavelengths, fewer detectors are required to have full spatial sampling of the 2'×2' field of view in the longer wavelength bands. The detector system elements are divided over the following main units: 3 "Focal Plane Arrays", each containing one detector array, its multiplexed SQUID amplifier readout electronics, and shielding and filtering needed to operate these components within the SPICA environment, a 136 K Low-Noise Amplifier that amplifies the weak outputs from the cryogenic electronics, and the Detector Control Unit (DCU) containing control and readout electronics both at room temperature.

SAFARI's large instantaneous field of view combined with the extremely sensitive Transition Edge Sensing detectors will allow astronomers to very efficiently map large areas of the sky in the far infrared – in a square degree survey within a 1000 hours many thousands of faint sources will be detected. A large fraction of these sources will be fully spectroscopically characterised by the instrument. Efficiently obtaining such a large number of complete spectra will be essential to address several fundamental questions in current astrophysics: how do galaxies form and evolve over cosmic time?, what is the true nature of our own Milky Way?, and why and where do planets like those in our own solar system come into being?

TES technology for SPICA-SAFARI

J.R. Gao[1,6], D. Glowacka[2], D. Goldie[2], D. Griffin[4], R. Hijmering[1], B. Jackson[1], P. Khosropanah[1], P. Mauskopf[3], D. Morozov[3], A. Murphy[5], C. O'Sullivan[5], M. Ridder[1], N. Trappe[5], S.Withington[2]

1 SRON Netherlands Institute for Space Research, Utrecht/Groningen, the Netherlands
2 Cambridge University, Cavendish Laboratory, Cambridge CB3 0HE, UK
3 Cardiff University, School of Physics and Astronomy, Cardiff, CF24 3AA, UK
4 Rutherford Appleton Laboratory, Harwell Science and Innovation Campus, Didcot OX11 0QX, UK
5 National University of Ireland, Maynooth, Ireland
6 Kavli Institute of NanoScience, Delft University of Technology, Delft, the Netherlands

Contact:j.r.gao@tudelft.nl, phone:+31152577811

Abstract—**To prepare the detector technology for the SAFARI imaging spectrometer on the Japanese Space Infra-Red Telescope for Cosmology and Astrophysics telescope (SPICA) and explore detector technologies for other future FIR space telescopes, several European research groups, supported in part by the European Space Agency, are collectively developing transition edge sensor (TES) and array technologies suitable for the short wavelength band (34-60 μm) and long wavelength band (110-210 μm) of SAFARI. To take maximum advantage of the cooled-aperture telescope (~5 K), the detector sensitivity (NEP) for SAFARI should be a few times 10^{-19} WHz$^{-1/2}$. The challenge of achieving this ultra-high detector sensitivity is further complicated by the requirements for moderate saturation powers (a few fW), fast response times (detector roll-off > 40 Hz for the short-wavelength band), and high optical efficiencies. Furthermore, the imaging array pixels should be packed such that they can simultaneously fulfill the instrument's requirements for optical sampling, low noise operation, and compatibility with a multiplexed readout.**

Enormous progress has already been made as a result of the joint effort made by the European groups. For example, the detector sensitivity is approaching the SAFARI requirements. In this paper we will give an overview of the achieved results with regard to the detector physics, TES single pixels, arrays, single- and multi-pixel feedhorns, optical performance modeling, and measurement techniques for both the short-wavelength and long-wavelength bands of SAFARI.

Optical performance of ultrasensitive FIR TES detectors for future space missions

D. Morozov[1][*], P. D. Mauskopf[1], P. A. R. Ade[1], D. Griffin[2], J.R. Gao[3,4], H. F. C. Hoevers[3], P. Khosrapanah[3], M. Ridder[3], M. Bruijn[3], D. Goldie[5], D. Glowacka[5], S. Withington[5] and N. Trappe[6]

1 Cardiff University, School of Physics and Astronomy, Cardiff, CF24 3AA, UK
2 Rutherford Appleton Laboratory, Harwell Science and Innovation Campus, Didcot OX11 0QX, UK
3 Space Research Organization of the Netherlands, Utrecht 3584, the Netherlands
4 Kavli Institute of NanoScience, Delft University of Technology, Delft, the Netherlands
5 Cambridge University, Detector and Optical Physics Group, Cavendish Laboratory, Cambridge CB3 0HE, UK
6 National University of Ireland, Maynooth, Ireland

```
         * Contact:  Dmitry.Morozov@astro.cf.ac.uk, phone +44-2920-870159
This work is supported by ESA TRP contract: ITT-1-5922/08/NL/EM TES spectrometer.
```

Abstract—Future Far-Infrared Fourier transform spectrometer instruments such as SAFARI-SPICA require sensitive detector arrays with high optical coupling efficiency over extremely wide bandwidths ($\Delta\lambda/\lambda \sim 1$). In principle, this can be achieved with multi-moded coupling optics and detectors with thin superconducting film absorbers operating above the gap. We describe the design, modeling and optical performance of single and multi-moded horns coupled to different cavity and absorber geometries in the wavelength ranges from 34-60 μm (SAFARI S-band) and 100-210 μm (SAFARI L-band). We define the coupling efficiency of an optical configuration to be the ratio of the power absorbed by the detector from a far field source divided by the power absorbed by an ideal black absorber with an area equal to the unit cell in the focal plane (e.g. the square of the pixel spacing for a square array). The system optical coupling efficiency is determined by the forward beam efficiency of the horn, reduced by additional power reflected out of the horn by the cavity/absorber combination as well as power radiated out of gaps in the cavity. We compare single-mode simulations and measurements of S-band and L-band detectors in hemispherical cavities. The simulated and measured coupling efficiencies depend on the horn and cavity geometries, the effective impedance and area of the absorbing metal films. We measure a coupling efficiency of 70% for an S-band detector in a 500 μm diameter hemispherical cavity with an absorber area of 200 x 200 μm^2, a square impedance of 400 Ohms coupled to a conical horn with exit aperture 46 μm. We also measure a coupling efficiency of 40% for an L-band detector in a 500 μm diameter hemispherical cavity with an absorber area of 320 x 320 μm^2, a square impedance of 90 Ohms coupled to a conical horn with an exit aperture of 120 μm. Both measurements agree with simulations of the absorption efficiencies for these geometries. Finally, we describe the design and measurements of optimized L-band and S-band detector arrays coupled to square horn arrays.

Dark performance of the S-band detectors is presented by SRON group (abstract by P. Khosropanah *et al* at this conference).

Frequency Division Multiplexed readout of TES detectors with Baseband Feedback

R.H. den Hartog[1*], M.D. Audley[2], J. Beyer[3], D. Boersma[1], M.P. Bruijn[1], L. Gottardi[1], B. Jackson[2], A. Nieuwenhuizen[1], J. van der Kuur[1], B-J van Leeuwen[1], D. van Loon[1]

1 SRON Netherlands Institute for Space Research*, Sorbonnelaan 2, 3584 CA, Utrecht, the Netherlands
2 SRON Netherlands Institute for Space Research, P.O. Box 800, 9700 AV, Groningen, the Netherlands
3 PTB, Abbestrasse 2-12, Berlin, D-10587, Germany
`* Contact: r.h.den.hartog@sron.nl, phone +31-88-777 5678`

Abstract——**SRON is developing an electronic system for the multiplexed read-out an array of transistion edge sensors (TES) by combining the techniques of frequency domain multiplexing (FDM) with base-band feedback (BBFB). FDM is based on the amplitude modulation of an orthogonal set of AC bias carriers with the signals detected by the TES detectors. It allows the read-out of multiple TES pixels in one channel using a single SQUID-based pre-amplifier, thus significantly reducing the heat-load on the array via the external wiring. BBFB cancels the error signal in the SQUID sumpoint and further improves the bandwidth and the loop gain.**

The astronomical applications are the read-out of soft X-ray microcalorimeters in an instrument on the European X-ray mission-under-study Athena and far-infrared bolometers for the SAFARI instrument on the Japanese mission SPICA. In recent work we showed that the basic requirements on the electronic read-out noise were met, and demonstrated multiplexed closed-loop low-noise read-out of 51 pixels.

In this paper we present the baselined system design of the FDM read-out for the Safari instrument, and demonstrate multiplexed low-NEP operation for TES bolometers, as a step towards the Safari Demonstration Model. The cross-talk between pixels is measured and the relative contribution of various mechanisms discussed.

BLISS and Ultrasensitive Bolometers for SPICA

C. M. Bradford[1,2*], A. D. Beyer[1,2], T. Prouve[1,2], M. Kenyon[1], P. Echternach[1], W. Holmes[1], B. Bumble[1],
M.C. Runyan[2], and J. J. Bock[1,2]

1 Jet Propulsion Laboratory, California Institute of Technology, Pasadena, CA 91109
2 California Institute of Technology, Department of Physics, Pasadena, CA 91125
`* Contact: bradford@caltech.edu, phone +1-818-726-8622`

Abstract—**We are developing the Background-Limited Infrared-Submillimeter Spectrograph (BLISS) for SPICA to provide a breakthrough capability for far-IR survey spectroscopy. The 3.2-meter, T<6K telescope allows mid-IR to submm observations which are limited only by the natural backgrounds, and BLISS will operate near this fundamental limit as a dispersive spectrograph. BLISS-SPICA will provide a line sensitivity of 10^{-20} W m^{-2}, thereby enabling spectroscopy of dust-obscured galaxies at all epochs back to the first billion years after the Big Bang (redshift 6), and study of all stages of planet formation in circumstellar disks.**

BLISS covers the 35-430 μm waveband at moderate resolving power (400<R<700) in six grating spectrometer bands, each coupling at least 2 sky positions simultaneously. The instrument is cooled to 50 mK with an on-board adiabatic demagnetization refrigerator (ADR) for optimal sensitivity. All technical elements of BLISS have heritage in mature scientific instruments, and many have flown. The instrument is carefully designed to fit within the stringent SPICA resource allocations for mass and heat lift, and to mitigate the impact of cosmic rays. We report on this design and our progress in prototyping the BLISS spectrometers and prototype cooler.

We also report progress in detector development for BLISS. BLISS uses ~4000 transition-edge sensors (TESs) read out with a cryogenic time-domain SQUID multiplexer. Each BLISS bolometer is a metalized micro-mesh silicon nitride (SiN) absorber with a superconducting thin film thermistor suspended by four long, thin SiN support beams. The detectors must have a noise equivalent power (NEP) of 5-10 x10^{-20} W Hz$^{-1/2}$, more than an order of magnitude lower than any previously-fielded far-IR / submm detector. As of this writing, we have measured 2x10^{-19} W Hz$^{-1/2}$ for several devices in a prototype array which uses elemental iridium thermistors (T_c=130 mK) each suspended with (4) 0.25 μm x 0.4 μm cross section SiN legs, read out using the cryogenic multiplexer, and cooled using an ADR. We are improving the fidelity of our 50 mK testbed and are currently measuring devices with MoCu bi-layer thermistors with T_c below 70 mK, with which we expect to exceed the BLISS sensitivity requirement with adequate speed of response.

LiteBIRD: A Small Satellite for the Studies of B-mode Polarization and Inflation from Cosmic Background Radiation Detection

Masashi Hazumi[1*] on behalf of the LiteBIRD working group
1 High Energy Accelerator Research Organization (KEK), Tsukuba, Ibaraki, 305-0801, Japan
* Contact: masashi.hazumi@kek.jp, phone +81-29-864-5339

Abstract—LiteBIRD [Lite (Light) satellite for the studies of B-mode polarization and Inflation from cosmic background Radiation Detection] is a small satellite to map the polarization of the cosmic microwave background (CMB) radiation over the full sky at large angular scales with unprecedented precision. Cosmic inflation, which is the leading hypothesis to resolve the problems in the Big Bang theory, predicts that primordial gravitational waves were created during the inflationary era. Measurements of polarization of the CMB radiation are known as the best probe to detect the primordial gravitational waves. The LiteBIRD working group was authorized by JAXA and has more than 50 members from Japan, USA and Canada. The scientific objective of LiteBIRD is to test all the representative inflation models that satisfy single-field slow-roll conditions and lie in the large-field regime. To this end, the requirement on the precision of the tensor-to-scalar ratio, r, at LiteBIRD is equal to or less than 0.001. The LiteBIRD plans to scan the full sky from L2 or LEO with an optics based on a 0.6m crossed Mizuguchi-Dragone telescope and a rotating half-wave plate at the sky side. Our baseline design of the focal plane adopts multi-chroic antenna-coupled superconducting detector arrays that are read out with high multiplexing factors in the frequency domain for a compact focal plane. We need about 2000 TES bolometers at 100mK to achieve the target sensitivity of 2μKarcmin. The cryogenic system is based on the JT/Stirling technology developed for SPICA, and the ADR system shares the design with future X-ray satellites. With the multi-chroic focal plane, the compact refractive telescope and the cryogen-free cooling system, LiteBIRD is light enough to fit multiple launch options.

Development of 1000 arrays MKID Camera for the CMB Observation

K. Karatsu[1*], M. Naruse[1,2], T. Nitta[1,3], Y. Sekimoto[1,2], M. Sekine[1,2], T. Noguchi[1], Y.Uzawa[1], H. Matsuo[1], and H. Kiuchi[1]

1 National Astronomical Observatory of Japan*, Mitaka, Tokyo, 181-8588, Japan
2 Department of Astronomy, The University of Tokyo, Bunkyo-ku, Tokyo, 113-0033, Japan
3 Institute of Physics, University of Tsukuba, Tsukuba, Ibaraki, 305-8577, Japan
* Contact: kenichi.karatsu@nao.ac.jp, phone +81-422-34-3863

Abstract— **The antenna-coupled Microwave Kinetic Inductance Detector (MKID) is being developed at NAOJ in cooperation with KEK and RIKEN, aiming for a precise measurement of the Cosmic Microwave Background (CMB) with LiteBIRD: a future satellite mission lead by KEK. In particular, the B-mode polarization of the CMB is one of a few probes for inflation era, which is far beyond the epoch of recombination. Many observations have been attempted to find it, but all haven't succeeded so far because of the lack of sensitivity. We need a millimeter camera with higher sensitivity and larger number of arrays to find it. MKID camera, which consists of array of superconducting resonators, is one of the possibilities to satisfy such requirements. The advantages of MKID camera are: hundreds of pixels can be read out with only single line by frequency dominant multiplexing; the fabrication process is simple and that leads to high yield rate (more than 90 %) of the array; high sensitivity with NEP (Noise Equivalent Power) of about 10^{-19} can be ideally achieved.**

We have successfully developed 102 pixels of MKID camera for the frequency of 440GHz with epitaxially-grown aluminum (Al) on silicon (Si) wafer, and measurement of beam pattern with Si lens array is underway. In parallel, we are developing 1000 pixels camera with mosaic design. Each module consists of 256 KIDs which is larger than the existing camera, so that we are also constructing a new test-bench with optimizing the system. The optimization includes antenna design, Si lens size for each pixel and optics system inside the cryostat.

We would like to present the status of the development of the 1000 pixels camera with its performance assessment such as yield rate, comparison of the measured parameters (resonant frequency, Q value etc.) to the design values and its optical characteristics.

Development of TiN-MKIDs for CMB polarization observations

Kensuke Koga[1,2*], Seiichiro Ariyoshi[2], Mitsuhiro Yoshida[3], Noboru Furukawa[2],
, Masashi Hazumi[3], Chiko Otani[1,2]

[1] *Graduate School of Science, Tohoku University*, Sendai 980-8578, Japan.*
[2] *Terahertz Sensing and Imaging Team, RIKEN, Sendai 980-0845, Japan.*
[3] *High Energy Accelerator Research Organization (KEK), Tsukuba 305-0801, Japan.*
* Contact: koga@riken.jp, phone +81 48-467-9720

Abstract—To understand the cosmic inflation observationally, one of the most important observations is that of B-mode polarization of cosmic microwave background (CMB) in the frequency range of 60~250GHz. For the observations, the detector array with noise equivalent power of less than 10^{-18}W/$\sqrt{Hz}$ and more than 1,000 elements is required. We are developing the superconducting detectors called microwave kinetic inductance detectors (MKIDs[1]) for the observations. MKIDs utilize the change in the resonance features due to the inductance change of the superconducting circuit operated in the microwave frequency. When MMW radiation is absorbed by the superconductor and Cooper pairs are broken in it, then its kinetic inductance changes. We can easily achieve the multiple (more than 1,000) channels in parallel by differentiating the resonance frequency of each element.

For the improvement of the sensitivity, the selection of material is crucial. We choose titanium nitride (TiN) as a good candidate because (1) its critical temperature (Tc) can be changed by the composition (0 <Tc< 5K), (2) the normal-state resistivity is large (facilitating photon absorption and providing a large kinetic inductance), and (3) the resonator of reactively sputtered TiN films show low loss (Q $>10^7$)[2]. We fabricated TiN films in various RF sputtering conditions and confirmed that T_C of TiN films varied with its composition by changing the flow rate of N_2 gas (Tc = 0.50K ~ 4.06K) . Then, we fabricated the TiN-MKIDs device, checked its response to the MW readout signals (Q ~ 3×10^5 @ 0.3K), and confirmed temperature dependence of the resonance peak. In this presentation, we will report the current status and the future prospect.

References: [1] P.K. Day et al., Nature 425, 817 (2003). [2] H.G. Leduc et al., arXiv:1003.5584v1 (2010).

Multi-chroic dual-polarization bolometric detectors for studies of the Cosmic Microwave Background

Aritoki Suzuki*, Kam Arnold*, Jennifer Edwards†, Greg Engargiola‡, Adnan Ghribi*, William Holzapfel*,
Adrian T. Lee*, Xiao Fan Meng¶, Michael J. Myers*, Roger O'Brient‖, Erin Quealy*, Gabriel Rebeiz†,
Paul Richards*, Darin Rosen* and Praween Siritanasak**

*University of California, Berkeley, Physics, Berkeley, California 94720 USA
†University of California, San Diego, Electrical and Computer Engineering, La Jolla, CA 92092 USA
‡Lawrence Berkeley National Laboratory, Berkeley, CA 94720 USA
§University of California Berkeley, Electrical Engineering, Berkeley, CA 94720 USA
¶University of California Berkeley, Electrical Engineering, Berkeley, CA 94720 USA
‖California Institute of Technology, Physics, Pasadena, CA 91125 USA
**University of California, San Diego, Physics, La Jolla, CA 92092 USA

Abstract—We are developing multi-chroic antenna-coupled TES detectors for CMB polarimetry. Multi-chroic detectors increase the mapping speed per focal plane area and provide greater discrimination of polarized galactic foregrounds with no increase in weight or cryogenic cost. In each pixel, a silicon lens-coupled dual polarized sinuous antenna collects light over a two-octave frequency band. The antenna couples the broadband millimeter wave signal into microstrip transmission lines, and on-chip filter banks split the broadband signal into several frequency bands. Separate TES bolometers detect the power in each frequency band and linear polarization. We will describe the design and performance of these devices and present optical data taken with prototype pixels. Our measurements show beams with percent level ellipticity, percent level cross-polarization leakage, and partitioned bands using banks of 2, 3, and 7 filters. We will also describe the development of broadband anti-reflection coatings for the high dielectric constant lens. The broadband anti-reflection coating has approximately 100% bandwidth and no detectable loss at cryogenic temperature. Finally, we will describe an upgrade for the POLARBEAR CMB experiment and installation for the LiteBIRD CMB satellite experiment both of which have focal planes with kilo-pixel of these detectors to achieve unprecedented mapping speed.

I. INTRODUCTION

Characterization of the Cosmic Microwave Background (CMB) B-mode polarization signal will test models of inflationary cosmology, as well as constrain the sum of the neutrino masses and other cosmological parameters. The low intensity of the B-mode signal combined with the need to remove polarized galactic foregrounds requires an extremely sensitive millimeter receiver and effective methods of foreground removal. Current bolometric detector technology is reaching the limit set by the CMB photon noise. Thus, we need to increase the optical throughput to increase an experiment's sensitivity. To increase the throughput without increasing the focal plane size, we can increase the frequency coverage of each pixel. Increased frequency coverage per pixel has additional advantage that we can split the signal into frequency bands to obtain spectral information. The detection of multiple

frequency bands allows for removal of the polarized foreground emission from synchrotron radiation and thermal dust emission, by utilizing its spectral dependence. Traditionally, spectral information has been captured with a multi-chroic *focal plane* consisting of a heterogeneous mix of single-color pixels. To maximize the efficiency of the focal plane area, we developed a multi-chroic *pixel*. This increases the number of pixels per frequency, at no extra cost per focal plane area, weight and cryogenic cost. For earlier development of this work, please refer to O'Brient *et al.* [1].

In section II, we discuss the design and fabrication of the multi-chroic pixel. In section III, we describe the test setup. In section IV, results are presented. We show our development in broadband anti-reflection (AR) coating in section V. Finally, we conclude in section VI with fabrication of arrays of multi-chroic detectors and plans for implementing these multi-chroic detector arrays in next-generation CMB experiments.

II. PIXEL DESIGN

Figure 1 shows our prototype pixel. We used an AR coated silicon hemisphere with a silicon extension to form a synthesized elliptical lens to increase the gain of the antenna [2], [3] (Figure 1, left). The AR coating was a thermoformed Ultem1000 plastic shell epoxied on the silicon lens. The choice of the extension length of the synthesized lens is a compromise between the pixel's directivity and gausianity of the beam. We chose the extension length for the elliptical point $(0.38 \times \text{radius})$ to maximize directivity. The silicon half-space also increases front-to-back ratio to approximately 10:1 due to its high dielectric constant, and it makes the antenna more efficient.

For the antenna, we used a sinuous antenna. The sinuous antenna is a broadband antenna that has log-periodic and self-complementary structure and provides a stable input impedance over a wide frequency range[4]. Its self-complementarity is broken by the presence of the silicon half-space, but its impedance stays stable enough that antenna's
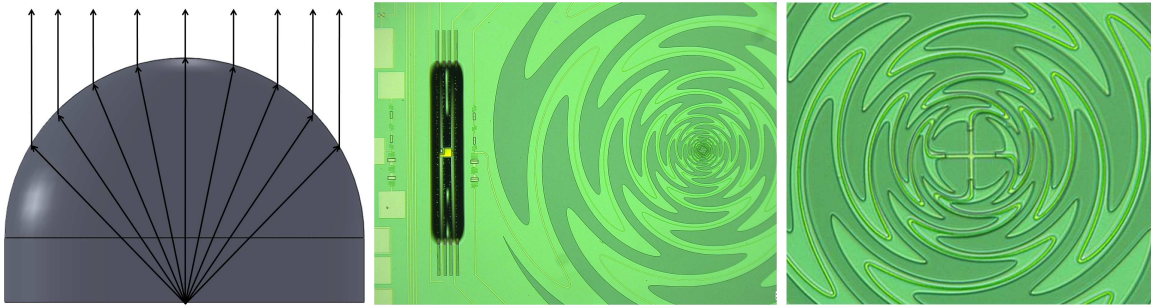
Fig. 1. (Left) side view of the silicon hemisphere lens with spacer. Spacer height is $0.38\times$ hemisphere's radius to place the antenna at the elliptical point. Rays drawn are schematic drawing. (Center) photograph of the lumped diplexer pixel. The antenna is 1500 μm radius sinuous antenna. The black rectangular structure is the released TES bolometer. A lumped diplexer is between the antenna and the TES bolometer. (Right) Close-up of the center of the sinuous antenna. Crossed line is the microstripline. Two lines from orthogonal polarization crosses on the same layer.
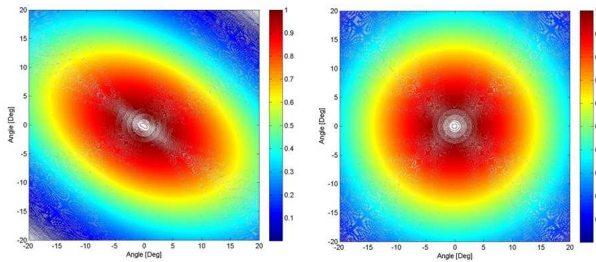
Fig. 2. Simulated beam at 80 GHz with a 540 μm radius sinuous antenna (left) and a 1500 μm radius sinuous antenna (right). The simulation was performed with the 3D EM software HFSS. Due to a long required computational time, the lens size was reduced to 6.35 mm diameter.

Fig. 3. (Left top) photograph of a distributed diplexer. Stubs are shorted to the ground plane at the ends. A distributed triplexer has similar appearance except there is one more filter branch attached to the junction. (Left bottom) photograph of the lumped diplexer. The meander structure is the inductor created from a narrow (2 μm) microstrip line. The rectangular structures are capacitors. (Right) photograph of the channelizer filter attached to a 540 μm radius sinuous antenna. The spiral structure is the sinuous antenna, and each leg of the V-shaped structure is the channelizer filter for one of the linear polarizations.

reflection coefficient to an optimized constant real impedance transmission line stays below -10dB over its range[2]. The sinuous antenna is favored over other log-periodic antennas for its sensitivity to linear polarizations. It also has a small polarization axis rotation as a function of frequency[2]. We want to keep the logarithmic expansion coefficient, frequency of repetitive structure, (τ) as close to unity as possible to keep the impedance fluctuation and polarization axis rotation as small as possible. A smaller expansion coefficient requires a smaller antenna and microstrip features. We chose $\tau = 1.3$ given micro-fabrication limitations. We chose the inner and outer radii of the antenna to be 15 μm and 1500 μm respectively. With an expansion factor of 1.3, the 1500 μm radius fits 16 repetitions (*cells*) of the antenna. A four-arm, self-complementarity sinuous antenna on silicon radiates at 360 μm radius for 70 GHz, the lowest frequency we use. From the results of 3D EM simulation with HFSS, we found out that a larger outer radius was required to obtain stable input impedance and round beam shape at our operating frequencies (Figure 2). This result was also observed experimentally by testing samples with antennas of different sizes. We will show results from a distributed diplexer, a distributed triplexer and a channelizer, which had a sinuous antenna with a radius of 540 μm. These result demonstrate the multiplexing technique. We will then show the beam performance of an antenna with a 1500 μm radius using a lumped diplexer.

Power from the antenna is coupled to microstrip lines to allow RF frequency-selection with on-chip filters prior to detection at the bolometers. The metalized *arms* of the sinuous antenna are used as the ground plane of the microstrip line so that we can bring microstrip line to the center of the antenna without interfering with the antenna. This scheme allows a planar design, and this allows large array fabrication with lithography technique. To simplify the fabrication process, microstrip lines for orthogonal polarizations cross at the center on the same layer (Figure 1, right). They do not couple to each other since odd-mode excitation of the antenna creates a virtual short at the intersection.

For the multiplexing method, we explored four schemes of paritioning: distributed diplexers, distributed triplexers, lumped element diplexers and channelizers with seven frequency bands (Figure 3). Both the diplexer and triplexer were developed with terrestrial observations in mind. We strategically placed bands between atmospheric emission lines to avoid detecting photons from the hot atmosphere. Both the distributed element filter and lumped element filter designs were based on a 0.5 dB ripple three-pole Chebyshev band pass filter, as a compromise between loss due to the filter elements and roll-off speed[5]. The quarter-wavelength stub

filter consists of three stubs of shorted $\lambda/4$ lines separated by $\lambda/4$ lengths of microstrip lines. For a lumped filter design, we designed an inductor with short lengths of narrowed (2 μm) microstrip line. For a capacitor, we designed a parallel plate capacitor with two layers of niobium separated by silicon dioxide. For calculating the required values of inductor and capacitor, we followed O'Brient *et al.* and Kumar *at al/* [6], [7]. Filters for each frequency were independently optimized usint the Sonnet EM 2.5 dimension simulation package. The effect of superconducting kinetic inductance was account for using a surface impedance of 0.11pH/sq[8]. The distances between the microstrip junction and each filter were adjusted until -20 dB isolation between frequency bands was obtained.

The channelizer was designed with a satellite mission in mind, where atmospheric lines are not a problem. Therefore, optimal performance is obtained by partitioning bands that are adjacent to each other. In the channelizer, lumped band pass filters are spaced in a log-periodic frequency schedule, and attached to the transmission line from high to low frequency. Within the filter's resonant band pass, the signal is transmitted through the filter to its associated bolometer, while other frequencies continue on the main transmission line. Galbraith and Rebeiz realized a three-pole channelizer at lower frequencies using surface mount lumped components[9]. We adapted this design to thin film fabrication[6]. We made a seven channel channelizer to cover the 70 to 220 GHz range.

The signals are detected by superconducting Transition Edge Sensor (TES) bolometers. Microstrip lines from the antenna are terminated by a 20 Ω resistor made of aluminum-titanium bilayer. We made a dual-transition TES with 1 Ω aluminum-titanium bilayer and 10 Ω aluminum in series. We used the same metal layer for the termination resistor and the TES thermistor to simplify fabrication. The superconducting transition temperature of the aluminum-titanium bilayer was tuned to be around 0.5 Kelvin by changing the thickness of the titanium. Aluminum's superconducting transition is assumed to be 1.2 Kelvin. This difference in Tc allows us to operate the TES bolometer over two orders of magnitude difference in receiving power, such that we can use aluminum-titanium transition for CMB observations while the aluminum transition is used in lab tests. Between the termination resistor and TES, we left layers of aluminum-titanium as well as a 1.5 thick micron gold. This provides additional heat capacity, allowing detector time constants to be tuned to match the readout bandwidth. The bolometer structure is supported on four 0.8 micron thick and about five hundred micron long nitride legs to provide thermal isolation from the rest of the chip. A summary of the layers of the device and the fabrication processes is shown in Table I.

III. TEST SETUP

We tested the prototype pixel in an 8 inch IR Labs dewar. We modified the dewar by adding a 4 inch diameter optical window made from Zotefoam. For infrared filters, two layers of 0.125 inch thick expanded teflon and a metal mesh low pass filter with 18cm^{-1} cut off are anchored to a liquid

Material	[μm]	Deposition	Etch
Silicon	500	test-grade 6in.	XeF_2
Silicon Dioxide	0.05	thermal growth	CF_4 RIE
Low Stress Nitride	0.7	LPCVD	CF_4 RIE
Niobium	0.3	DC Mag. Sputter	CF_4/O_2 RIE
Silicon Dioxide	0.5	350°C PECVD	CHF_3/O_2 RIE
Niobium	0.3	DC Mag. Sputter	CF_4/O_2 RIE
Silicon Dioxide	0.2	350°C PECVD	CHF_3/O_2 RIE
Niobium	0.3	DC Mag. Sputter	CF_4/O_2 RIE
Al/Ti Bilayer	0.04	DC Mag. Sputter	Pre-mixed Wet Etch
	0.08		SF_6 RIE
Gold	1.5	Evaporation.	Photo.Res. Lift-off

TABLE I
SUMMARY FABRICATED DEVICE LAYERS AND FABRICATION PROCESSES. THE LAYERS ARE IN THE ORDER OF PREPARATION. DIMENSION IS THE THICKNESS OF THE LAYERS.
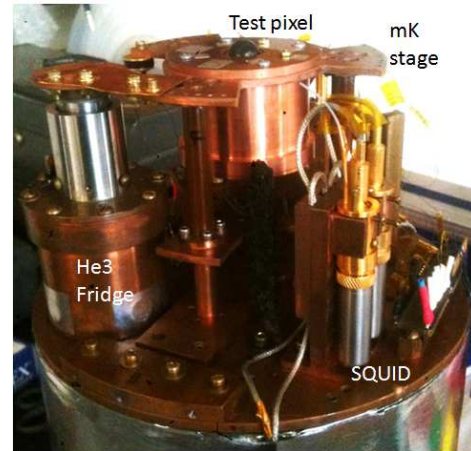

Fig. 4. Photograph of the milli-kelvin stage of the IR Labs dewar. Homemade 3He fridge sit on the left side of the dewar. Milli-Kelvin stage is isolated from 4 Kelvin plate by thin vespel leg approximately 2 inch long and 0.010 inch thick. Silicon lens of the test pixel is visible at the center of milli-kelvin stage. Quantum Design DC SQUID readout was used to read out TES bolometer, that is visible on the right.

nitrogen temperature. Two metal mesh low pass filters with cut off at 14cm^{-1} and 12cm^{-1} are mounted at liquid helium buffer to further reduce the optical loading. The pixel stage is isolated from the liquid helium buffer with thin walled vespel tubes. The stage is cooled to 0.25 Kelvin with homemade 3He adsorption fridge. We mounted the test pixel behind the 14mm diameter hemispherical silicon lens with 2mm thick flat silicon spacer. The test pixel was fabricated on top of 0.675 mm thick silicon, thus combination of spacer and the test pixel locate the antenna right at the elliptical focus. The TES bolometer is DC voltage biased with 0.02Ω of shunt resistor in parallel with the bolometer. Current through the bolometer is read out by commercially available laboratory DC SQUID from Quantum Design with its input inductor coil in series with the bolometer.

We produced beam maps of the pixel by scanning 0.25 inch diameter temperature modulated source (liquid nitrogen soaked eccosorb and room temperature eccosorb) 10 inches away from the antenna. We scanned 3 inch × 3 inch patch with step size of 0.125 inch on motorized XY stage.

We measured the response of the pixel to a linear polarized source by rotating wire grid polarizer between the pixel and the temperature modulated source. We measured spectra of the device using Michaelson Fourier transform spectrometer (FTS). The FTS uses temperature modulated source with 1200 Kelvin ceramic heater and 300 K eccosorb. Mirrors are 6 inch by 6 inch large in cross-section. Beam splitter was 0.010 inch thick mylar that has a beam splitter minima at 360 GHz. We focused the output of the FTS onto the pixel using ultra high molecular weight polyethylene lens. The efficiency of the device was measured with beam filling temperature modulated source. For a single moded antenna detector, the power difference between two temperature source is $k_B \Delta T \Delta \nu$ in the Rayleigh-Jean limit. Here k_B is the boltzmann constant, ΔT is the difference in temperature of modulated source. We used liquid nitrogen soaked eccosorb and room temperature eccosorb for $\Delta T = 223$ Kelvin. $\Delta \nu$ is the integrated bandwidth of the peak normalized spectrum measured with FTS. We divide power received on detector with $k_B \Delta T \Delta \nu$ to measure an end-to-end efficiency which includes dewar loss.

IV. RESULTS

The results from lab measurements are summarized in Table II. To analyze the spectra, the interferogram from the FTS was apodized with triangular window function prior to the Fourier transformation. Then the spectrum was divided by analytical beam splitter function to remove its effect. The resulting spectra from distributed diplexer and distributed triplexer are shown in Figure 5, and the spectra from lumped filter diplexer and channelizer are shown in Figure 6. Peaks of the spectra were normalized to a measured optical efficiency of each band. The results show that we successfully partitioned a broadband signal into 2, 3 and 7 bands with matching band shape for orthogonal polarizations. We did not know the material properties ahead of the test pixel fabrication to get the band location correct. The POLARBEAR CMB experiment successfully tuned their band location of the filters by making correction to the filter design with feedback from lab measurements [5]. Our filter can be tuned in the same way in future fabrications.

The beam maps from a lumped diplexer pixel with a 1500 μm radius sinuous antenna are shown in Figure 7. We characterize the beam property by fitting ellipse at -3 dB contour and define ellipticity as $\epsilon = (a - b)/(a + b)$, where a and b are the major and the minor axes of the ellipse, respectively. Ellipticity from large antenna is 1.1% and 1.3% for 90 GHz and 150 GHz band respectively. At this level, we were limited by measurement systematics. Comparing 1500 μm radius antenna measurements with the 540 μm radius antenna, we clearly see the improvement in beam ellipticity for the large antenna at low frequencies, as predicted from 3D EM simulation.

Polarization measurement results are shown in Figure 8 and tabulated at Table II. We expect the wiregrid to have approximately 1% leakage, thus we are limited by systematics for low cross-pol measurement. We also see the that polarization

performance for the lower frequency improves with the larger antenna.

V. ANTI-REFLECTION COATING

One of the optical challenges of building a multi-chroic system is the production of broadband anti-reflection (AR) coatings. Since our pixel uses silicon lens that has a high dielectric constant ($\epsilon = 11.7$) there would be a 30% reflection without an AR coating. Also in the future CMB experiments such as POLARBEAR-2, reimaging lenses will be fabricated from alumina which also has a high dielectric constant $\epsilon = 9.6$. Solving the broadband AR coating issue is one of the keys to make the multi-chroic technology viable.

The bandwidth of the coating increases with the number of correctly tuned layers, but absorptive loss will also increase. Thus we want to keep the number of layers as low as possible and still provide enough bandwidth. The coating must stay on the lens at cryogenic temperatures. For millimeter wave application, the thickness of the AR coating will be order 100 μm. Thus it is too thin to easily machine and too thick for vapor deposition. We would also like to be able to tune the dielectric constant of the coating to obtain optimal coating performance.

We calculated that a 2-layer coating with dielectric constants of 2 and 5 with thicknesses of one-quarter wavelength at the of center frequency will give sufficient bandwidth to cover 90 GHz and 150 GHz bands. To cover 90,150 and 220 GHz bands simultaneously, we need a 3-layer coating with dielectric constants of 2,4, and 7 with thickness of a quarter of wavelength at the center frequency. We chose to use mixtures of various types of epoxies (Stycast 1090, Stycast 1266, Stycast 2850FT) and filler ($SrTiO_3$) which can be molded into appropriate AR coating layers.

First we measured the dielectric constant of the materials using the FTS. The Stycast 1090, Stycast 1266 and Stycast 2850FT have dielectric constants of 2.05, 2.60 and 4.95 respectively. We also successfully obtained epoxy with an intermediate dielectric constant by mixing two types of epoxy as shown in Figure 9. To get dielectric constant higher than 4.95, we mixed Stycast 2850FT with $SrTiO_3$ filler which was shown to have a high dielectric constant [10]. We were able to fabricate materials with a dielectric constant as high as 7.5.

To test the multi-layer AR coating, we applied two layers of coating made from Stycast 1090 and Stycast 2850FT on flat 2 inch alumina sample which has a dielectric constant of 9.6. We then cooled the sample to 140 Kelvin using liquid nitrogen and measured transmission using the FTS. As shown in Figure 9, uncoated alumina shows high Fabry-Perot fringes due to high reflection whereas coated sample has high transmittance over a wide band. We are currently preparing 3-layer coatings in similar way to demonstrate even wider bandwidth.

To make a sufficiently precise coating on a lens, we designed a mold that leaves a thin gap between lens and mold. The cavity was made using a precision machined ball-ended mill which has 0.0005 inch tolerance. Combined with machining tolerance, we were able to create coatings with a
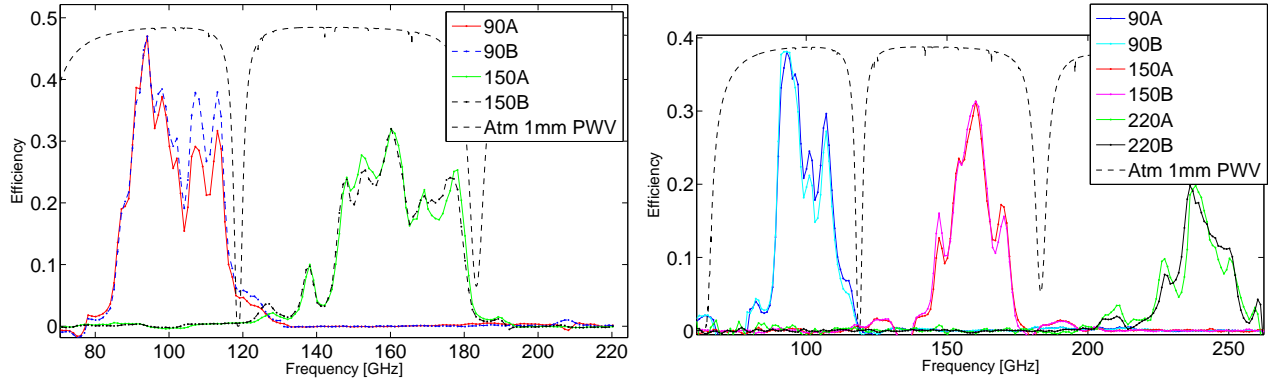
Fig. 5. Spectrum of a distributed diplexer (left) and a distributed triplexer (right). *A* and *B* refers to two orthogonal linear polarization channels. Peaks are normalized to the measured optical efficiency. See Table II for details. Dotted black lines are expected transmission through 1mm PWV of atmosphere.
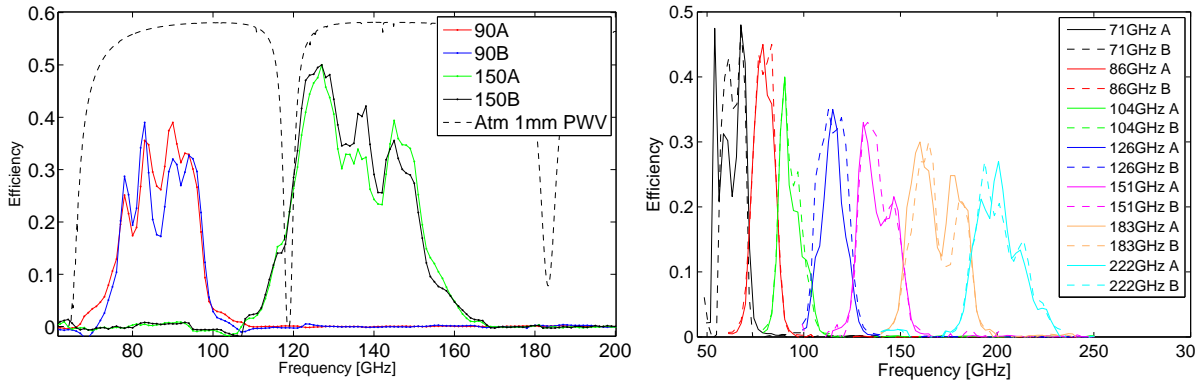

Fig. 6. Spectrum of a lumped diplexer (left) and a channelizer (right). *A* and *B* refers to two orthogonal linear polarization channels. Peaks are normalized to measured optical efficiency. See Table II for details. Dotted black lines are expected transmission through 1mm PWV of atmosphere.
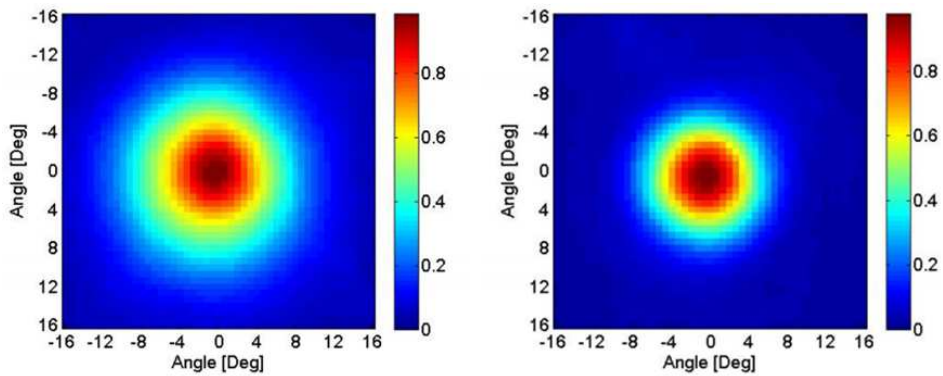
Fig. 7. Beam map measurement from a lumped diplexer. Plots were peak normalized. Lumped diplexer was the only test structure that was attached to large (1500 μm radius) sinuous antenna. Ellipticity was calculated by fitting an ellipse on the -3 dB contour and used the definition $\epsilon = (a - b)/(a + b)$, where a and b are the major and the minor axes. Ellipticities were 1.1% and 1.3% for 90GHz and 150GHz band respectively.
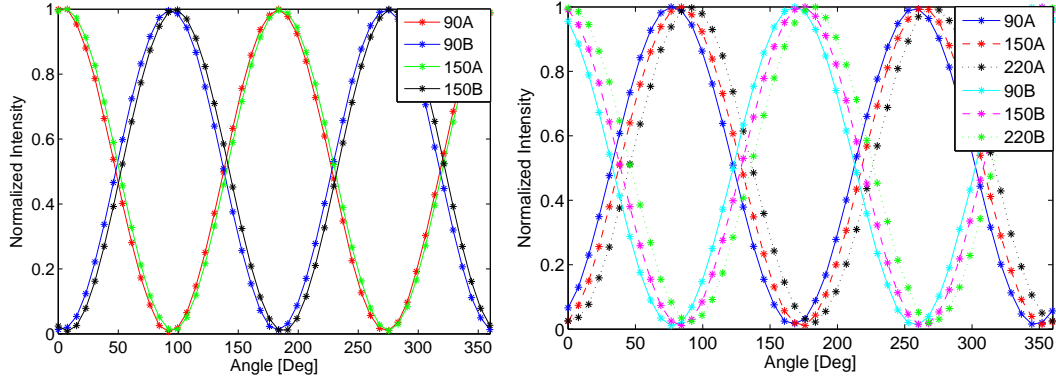
Fig. 8. Responses of the lumped diplexer (left) and distributed triplexer (right) to a linearly polarized source as a function of relative angle between antenna and the polarizer. Plots were peak normalized prior to fitting by sum of a sine function and a constant. Cross-pol for each channels are summarized in Table II.

Filter Type	Ant rad [μm]	ν_0 [GHz]	$\Delta\nu$ [GHz]	Opt Eff	Ellipticity	Cross-pol
Lumped Diplexer Low	1500	87	17.0	39%	1.1%	< 0.3%
Lumped Diplexer Mid	1500	135	26.4	50%	1.3%	< 1.6%
Stub Diplexer Low	540	101	20.2	47%	4.9%	< 2.3%
Stub Diplexer Mid	540	162	26.2	32%	1.0%	< 1.6%
Stub Triplexer Low	540	100	16.6	38%	3.0%	< 2.5%
Stub Trilexer Mid	540	158	17.7	31%	1.5%	< 2.1%
Stub Trilexer High	540	239	19.6	20%	4.0%	< 4.3%

TABLE II
SUMMARY FROM ONE OF THE POLARIZATIONS OF EACH DIPLEXER AND TRIPLEXER. ν_0 IS THE CENTER FREQUENCY OF THE BAND AND $\Delta\nu$ IS INTEGRATED BANDWIDTH. CROSS-POL VALUES ARE UPPER LIMIT VALUE AS WE EXPECT LEAKAGE FROM WIRE-GRID
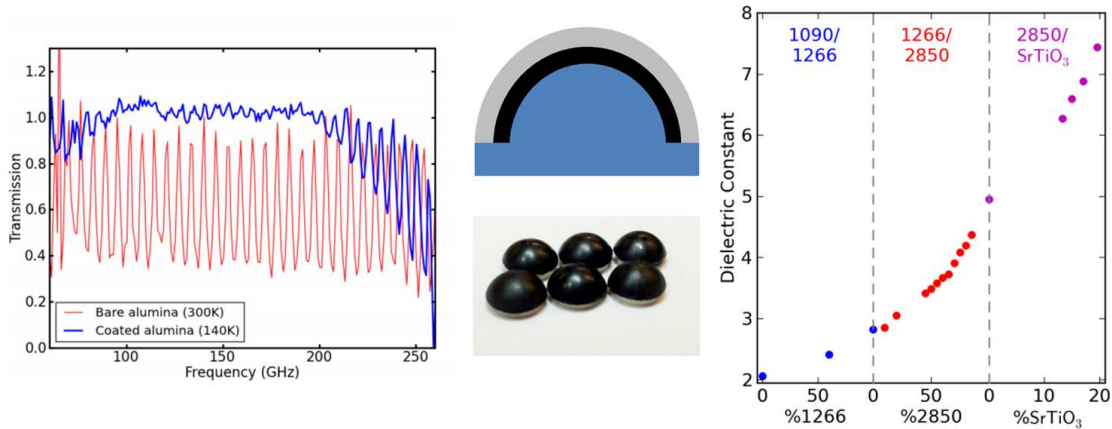
Fig. 9. (Left) Transmission of 2-layer AR coated alumina (blue) and uncoated alumina sample (red) measured with an FTS. Fabry-Perot fringes disappears over 70% of bandwidth for the AR coated sample. (Center top) Cut-away drawing showing how two layer coatings are applied. For a silicon lens, the inner layer (black) would be Stycast 2850FT ($\epsilon = 4.95$) and outer layer would be Stycast 1090 ($\epsilon = 2.05$). (Center bottom) alumina lens coated with 2-layers of AR coating. Inner layer is Stycast 2850FT and the outer layer is Stycast 1090. (Right) Plot of measured dielectric constant of the material and various epoxy and filler mix. Left region is a mix of S 1090 and Stycast 1266, center region is a mix of Stycast 1266 and Stycast 2850FT and right section is the mix of Stycast 2850FT and SrTiO$_3$ powder. Percentage on the x-axis is the percentage of mass of second material in the mix.

tolerance of 0.001 inch, which is approximately 10% of the thickness of the layer. We filled the cavity with the appropriate amount of epoxy measured by its weight. Then we inserted the lens in a mold that keeps its concentricity and accurate depth. Epoxy cures in a few hours in a $100°$C oven. We repeated the process with molds with different spacings.

To test its cryogenic adhesion property, we made twelve 2-layer coated lenses as shown in Figure 9. We kept one sample as a control, nine samples were slowly cooled to liquid nitrogen temperature in a 6 inch IR Labs dewar. Two additional samples were rapidly thermal cycled between room tempeature and liquid nitrogen temperature until failure. Failure for those samples occurred after 18 and 50 dunks. Nine samples went through ten slow thermal cycles in the dewar and all survived. These nine samples were then dunked 18 times in liquid nitrogen, bringing them back up to room temperature each time, and all survived. There was no change to the control sample that was kept at room temperature. We conclude that the adhesion of the coating is good enough for our applications given the results of this testing.

VI. CONCLUSION
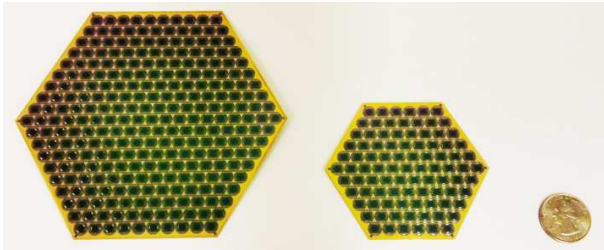
Fig. 10. Photograph of the fabricated detector arrays and US 25 cent coin for size comparison. Larger hexagonal array is 13 cm across and it has 271 pixels. Smaller hexagonal array is 8cm across and it has 91 pixels. Both wafers has lumped diplexer (90 GHz and 150 GHz) with 1500 μm radius sinuous antenna.

Fig. 11. CAD drawing of the proposed POLARBEAR-2 forcal plane (left) and LiteBIRD focal plane (right). POLARBEAR-2 focal plane mounts seven heagonal wafers with lumped diplexer with total of 7588 bolometers. LiteBIRD focal plane uses two types of detectors. There will be eight low frequency wafers with larger lenses and five high frequency wafers near the center of the focal plane. LiteBIRD focal plane will have 2022 bolometers total.

To bring the proto-type multi-chroic pixels closer to readiness for future CMB experiments, we fabricated the arrays of multi-chroic detectors shown in Figure 10. We fabricated these on 6-inch wafers. The larger array has a side-to-side length of 13cm, containing 271 pixels. The smaller array has

a side-to-side length of 8cm, with 91 pixels. Each pixel uses a dual-polarized diplexer (90 GHz and 150 GHz bands) with a 1500 μm radius sinuous antenna. The next generation CMB B-mode experiments such as POLARBEAR-2 and LiteBIRD are planning to use these multi-chroic detectors to increase their mapping speed. CAD drawings of the proposed focal planes for POLARBEAR-2 and LiteBIRD are shown in Figure 11. POLARBEAR-2 will use 7 of these 13 cm hexagonal arrays in its focal plane. The total number of bolometers will be 7588. POLARBEAR-2 will achieve an array noise equivalent temperature (NET) of 6 μK$\sqrt{s}$. LiteBIRD , a compact satellite CMB B-mode experiment, is planning to use two types of triplexer pixel: low frequency pixels (60,78 and 100 GHZ) and high frequency pixels (140, 190 and 280 GHz). The current design uses eight low frequency arrays and five high frequency arrays. There will be 2022 bolometers with an array NET of 1 μK$\sqrt{s}$.

We have successfully demonstrated multi-chroic detection with single pixels. With correct design of the antenna, we produced a detector with a round beam and low cross-pol performance. We have also presented a solution for broadband AR coatings, and we have fabricated arrays of multi-chroic detectors which will be used in future CMB experiments.

REFERENCES

[1] O'Brient, R., Ade, P., Arnold, K., Edwards, J., Engargiola, G., Holzapfel, W., Lee, A. T., Meng, X., Myers, M., Quealy, E., Rebeiz, G., Richards, P., and Suzuki, A., "A dual-polarized multichroic antenna-coupled tes bolometer for terrestrial cmb polarimetry," *SPIE proceedings* (2010).

[2] Edwards, J., O'Brient, R., Lee, A., and Rebeiz, G., "Dual polarized sinuous antennas on extended hemispherical silicon lenses," Antennas and Propagation, IEEE Transactions, submitted (2011).

[3] Filipovic, D., "Double-slot antennas on extended hemispherical and elliptical silicon dielectric lenses," *Microwave Theory and Techniques, IEEE Transactions* 41(10), 1738–1749 (1993).

[4] Duhamel, R., "Dual polarized sinuous antennas," (1987). United States Patent 4658262.

[5] Arnold, K., *Design and Deployment of the* POLARBEAR *Cosmic Microwave Background Polarization Experiment*, PhD thesis, University of California, Berkeley (2010).

[6] O'Brient, R., *A Log Periodic Focal-Plane Architecture for Cosmic Microwave Background Polarimetry*, PhD thesis, University of California, Berkeley (2010).

[7] Kumar, A., Vayonakis, A., LeDuc, H., Day, P., Golwala, S., and Zmuidzinas, J., "Millimeter-wave lumped element superconducting bandpassfilters for multi-color imaging," *Applied Superconductivity, IEEE Transaction* 19(3), 924–929 (2009).

[8] Kerr, A., "Surface impedance of superconductors and normal conductors in em simulators," tech. rep., ALMA (1999). http://www.alma.nrao.edu/memos/.

[9] Galbraith, C. and Rebeiz, G., "Higher order cochlea-like channelizing filters," *Microwave Theory and Techniques, IEEE Transactions* 56(7), 1675–1683 (2008).

[10] Lee, S., Hyun, J., Kim, H., and Paik, K., "A study on dielectric constants of Epoxy/SrTiO$_3$ composite for embedded capacitor films (ecfs)," *Advanced Packaging, IEEE Transaction* 30(3), 428–433 (2007).

DESHIMA: Redshift Machine Based on an On-chip Filterbank

A. Endo[1*], J.J.A. Baselmans[2], P.P. van der Werf[3], D.J. Thoen[1], R.M.J. Janssen[1], P.J. de Visser[1,2],
T.M. Klapwijk[1], L.Ferrari[4], S.J.C. Yates[4], A.M. Baryshev[4,5], and Y.J.Y. Lankwarden[2],

1 Kavli Institute of NanoScience, Faculty of Applied Sciences, Delft University of Technology, Lorentzweg 1, 2628 CJ Delft, The Netherlands
2 SRON, Sorbonnelaan 2, 3584 CA Utrecht, The Netherlands
3 Leiden Observatory, Leiden University, PO Box 9513, NL-2300 RA Leiden, The Netherlands
4 SRON, Landleven 12, 9747 AD Groningen, The Netherlands
5 Kapteyn Astronomical Institute, University of Groningen, P.O. Box 800, 9700 AV Groningen, The Netherlands
* Contact: A.Endo@tudelft.nl, phone +31-15-27-86113

Abstract—**DESHIMA (<u>De</u>lft <u>S</u>RON <u>High-z</u> <u>M</u>apper) is a project to build an imaging spectrograph to instantaneously cover the entire bands of multiple submillimeter telluric windows in the range of 320-950 GHz, with a resolving power sufficient for resolving redshifted atomic and molecular lines from submillimeter galaxies (f/df ~ 1000). We are currently following a design which utilizes the rapidly advancing technology of superconducting microresonators twofold. The signal received by the antenna is separated into different frequency channels by using submillimeter wave resonators, made of superconducting NbTiN, as band pass filters. At the exit of each channel is a microwave resonator with a strip of Al, making the resonator act as a Microwave Kinetic Inductance Detector (MKID). The first prototype of such an integrated filterbank (IFB) device, which uses a circuit consisting of coplanar waveguides on a Si substrate, showed strong coupling to stray light radiation. In the conference we will report the current status of the development of DESHIMA, with special focus on the first optical experiment of an IFB, as well as possible solutions for reducing stray light coupling.**

Dual polarization Lumped Element Kinetic Inductance Detectors (LEKID) for 1.25 and 2.05mm

M. Roesch[1*], A. Monfardini[2], A. Bideaud[2], N. Boudou[2], M. Calvo[2], S. Doyle[3], S. Leclercq and K.-F. Schuster[1] for the NIKA collaboration

1 IRAM, St. Martin d'Heres, France*
2 Institut NEEL, Grenoble, France
3 Cardiff School of Physics and Astronomy, Cardiff University, Cardiff, UK
`* Contact:  roesch@iram.fr, phone +33-47682 4921`

Abstract⎯**The development of Lumped Element kinetic Inductance (LEKID) detectors for the IRAM 30m telescope in the framework of the NIKA collaboration (Neel-IRAM KID array) has recently shown considerable promising direct absorption properties as mm-wavelength detectors for astronomical applications yielding an average optical NEP of ~2 x 10-16 W/Hz^1/2.**
The pixel geometry of these detectors allows absorbing power in only one polarization and limits therefore the optical efficiency of the LEKIDs. To increase the mm-wave absorption and thus the responsivity of the detector, a new dual polarization pixel geometry has been designed and tested for the two frequency bands at 1.25 and 2.05 mm wavelength. We present here the measurement results of the optical absorption done at room temperature using a reflection measurement setup in order to determine the optical efficiency of this pixel design for the two polarizations. We also show cryogenic measurements of 132 pixel arrays including FTS measurements to confirm the increased optical efficiency. First results indicate sensitivities, expressed in noise equivalent temperature, of NET=2mK/Hz^1/2 per beam for the 2.05 mm band, which corresponds to a factor of 2 of improvement compared to the classical single polarization design.

Taking a snapshot of KIDs

L. Ferrari[1*], A. M. Baryshev[1,2], J. J. A. Baselmans[3], A. Endo[4], Y.J.Y. Lankwarden[3], and S.J.C. Yates[1]

1 SRON Space Research of Netherlands* Groningen, 9747 AD, The Netherlands
2 Kapteyn Astronomical Institute, Groningen, 9747 AD, The Netherlands
3 SRON Space Research of Netherlands, Utrecht, 3584 CA, The Netherlands
4 Delft University of Technology, Delft, 2628 CJ, The Netherlands
`* Contact: lorenza@sron.nl, phone +31-50-3638321`

Abstract— **The inherent multiplexing capability of Microwave Kinetic Inductance Detectors (MKIDs) is one of the great advantage of this type of technology. However the cross-talk between and variations of the resonator frequencies complicate the design and operation of large MKID arrays.. We have developed an optical facility to take snapshot of individual KID pixels. It reimages the KID chip in optical wavelength on-to an image plane outside the cryostat. While scanning a small optical source in this plane we detect the resonator response using conventional microwave technique. In this way we can correlate the resonance frequency of each resonator with its position on the chip. This allows to determine the resonator frequencies pattern across the array chip and enables a comparison with the array design. The measurement of electronic cross talk is also readily available from these measurements. In addition, by using higher magnification optics we can resolve individual KID resonator with greater detail and image its readout current distribution.**

Ultra-Compact Superconducting Spectrometer on a Chip at Submillimeter Wavelengths

G. Chattopadhyay[1*], P. Barry, C. M. Bradford, P. Day, S. Doyle, S. Hailey-Dunshath, A. Kovacs, H. G. Leduc, N. Llombart, C. McKenny, , D. P. Marrone, P. Mauskopf, R. O'Brient, S. Padin, E. Shirokoff, J. Siles, L. Swenson, and J. Zmuidzinas

[1]*NASA-Jet Propulsion Laboratory, California Institute of Technology, Pasadena, CA 91109, USA.*
* Contact: goutam@jpl.nasa.gov, phone +1-818-216-1091

Abstract—— **In this paper we will describe a novel, moderate-resolving-power (R~700), ultra-compact spectrograph-on-a-chip for millimeter and submillimeter wavelength which is currently under development. It's very small size, wide spectral bandwidth, and highly multiplexed detector readout will enable construction of powerful multi-beam spectrometers for high-redshift observations. The octave-bandwidth background-limited performance of this spectrometer is comparable to that of a diffraction grating, but in a photo-lithographically developed thin-film package with size ~10 λ x 10 λ. In general, even the most compact grating spectrometers are 2-D structures with size ~ $\lambda R/\sqrt{\varepsilon}$. The grating sizes for these spectrometers are prohibitive, approximately 1 meter for R=1000 at λ=1 mm in free space, and ~30 cm in silicon. This fundamental size issue is a key limitation for space based spectrometers for astrophysics applications. On the other hand, our photo-lithographic on-chip spectrometer camera is compact delivering 200 – 500 km/s spectral resolution over and octave bandwidth for every pixel in a telescope's field-of-view.**

The spectrometer employs a filter bank consisting of planar, lithographed superconducting transmission line resonators. Each mm-wave resonator is weakly coupled to both the feedline and to the inductive portion of a lumped element Microwave Kinetic Inductance Detector (MKID). Incoming mm-wave radiation breaks Cooper pairs in the MKID, modifying its kinetic inductance and resonant frequency, allowing for frequency-multiplexed readout. The design is realized using thin film lithographic structures on a Si wafer, with titanium nitride MKID resonators. In this paper, we will discuss the design and optimization of the MKID detectors for the spectrometer and the measured performance of a laboratory test device. We will also describe the ongoing development of a demonstration instrument which will consist of two 500-channel, R=700 spectrometers, one operating in the 1-mm atmospheric window and the other covering the 650 and 850 micron bands.

THE YUAN-TSEH LEE ARRAY FOR MICROWAVE BACKGROUND ANISOTROPY

Ming-Tang Chen[1], Chao-Te Li, Yuh-Jing Hwang[1], Homin Jiang[1], Chih-Chiang Han[1], Yau-De Huang[1], Michael Kesteven[3], Derek Kubo[1], Pierre Martin-Cocher[1], Philippe Raffin[1], Warwick Wilson[3], Paul T. P. Ho[1,4], Chih-Wei Huang[2], Patrick Koch[1], Yu-Wei Liao[1], Kai-Yang Lin1,[1], Guo-Chin Liu[5], Hiroaki Nishioka[1], Keiichi Umetsu[1], Fu-Cheng Wang[2], and Jiun-Huei Proty Wu[2]

[1] *Academia Sinica, Institute of Astronomy and Astrophysics, P.O. Box 23-141, Taipei 106, Taiwan*
[2] *National Taiwan University, Taipei 106, Taiwan*
[3] *Australia Telescope National Facility, P.O. Box 76, Epping, NSW 1710, Australia*
[4] *Harvard-Smithsonian Center for Astrophysics, 60 Garden Street, Cam- bridge, MA 02138, USA*
[5] *Tamkang University, Tamsui, Taipei County, Taiwan 251*
Contact: mchen@asiaa.sinica.edu.tw, phone +886-2-2366 5348

Abstract—— **The Yuan Tseh Lee Array for Microwave Background Anisotropy (AMiBA) is a forefront interferometric array for research in cosmology. The Array is consisted of thirteen antennas, each equipped with a cryogenic receiver operating in the atmospheric window at 86-104 GHz, and with full polarization capabilities. The dish size of 1.2 meter is to sample large-scale structures (20′), while interferometry provided mode st resolutions (2′). A novel wide-band analog correlator was designed that is easily expandable for more interferometer elements. Monolithic millimeter-wave integrated circuit technology was used throughout as much as possible in order to miniaturize the components and to enhance mass production. It targets specifically the distribution of high-redshift clusters of galaxies via the Sunyaev-Zeldovich Effect (SZE), as a means to probe the primordial and early structure of the universe. AMiBA is sited on Mauna Loa at an elevation of 3,400m in Hawaii. The construction of AMiBA includes a novel hexapod mount, a carbon fiber platform, carbon fiber reflectors, MMIC receivers, a broadband correlator, numerous electronics, a retractable cover, site infrastructures, and software development. The AMiBA has deployed the initial 7-element interferometer to Hawaii in 2005, and subsequently expanded to the present 13-element configuration in Oct 2009. Full science operations have begun in early 2010. This paper will review the development of the telescope and its observation progress.**

Development of THz Superconducting Receivers for DATE5

S.C. Shi[1,2*] and DATE5 Team

1 Purple Mountain Observatory, CAS, NanJing, Jiangsu, 210008, China
2 Key Lab of Radio Astronomy, CAS, NanJing, Jiangsu, 210008, China
* Contacts: scshi@mail.pmo.ac.cn, phone +86-25-8333-2204

Abstract—**Dome A, Antarctic, with an altitude of 4093 m and temperature below -80 Celsius degree in winter, is regarded as the best site on earth for astronomical observations in the THz regime. Purple Mountain Observatory as well as its collaborators is proposing to build a 5-m THz telescope (DATE5) there. Here we introduce the site survey at Dome A and the proposed DATE5 telescope. In particular, the development of THz superconducting receivers for DATE5 will be addressed.**

A New Telescope for Ground-based THz Astronomy

K. Asada[2], R. Blundell[1*], R. Burgos[1], M. T. Chen[2], P. Grimes[1], P. T. P. Ho[1,2], Y. D. Huang[2], M. Inoue[2], E. Keto[1], P. Martin-Cocher[2], G. Nystrom[2], S. N. Paine[1], P. Raffin[2], and E. Tong[1]

[1] *Smithsonian Astrophysical Observatory*, 160 Concord Ave., Cambridge, MA 02138, USA*
[2] *Academia Sinica Institute of Astronomy and Astrophysics, P.O. Box 23-141, Taipei 10617, Taiwan*
* Contact: rblundell@cfa.harvard.edu, phone +1 617 495 7367

Abstract— **In the spring of 2010, the Academia Sinica Institute of Astronomy and Astrophysics, and the Smithsonian Astrophysical Observatory, acquired the ALMA North America prototype antenna – a state-of-the-art 12-m diameter dish designed for submillimeter astronomy. Together with the National Radio Astronomy Observatory and the MIT-Haystack Observatory, the plan is to retrofit this antenna for cold-weather operation and equip it with a suite of instruments designed for a variety of scientific experiments and observations.**

The primary scientific goal is to image the shadow of the super-massive black hole in M87 in order to test Einstein's theory of relativity under extreme gravity. To do this, the highest angular resolution imaging is required, which can only be achieved by linking this antenna with others already in place to form a telescope almost the size of the Earth. For this reason, we are developing plans to install this antenna close to the peak of the Greenland ice sheet. This location will produce an equivalent north-south separation of almost 9,000 km when linked to the ALMA telescope in Northern Chile, and an east-west separation of about 6,000 km when linked to SAO and ASIAA's Submillimeter Array on Mauna Kea, Hawaii, and will provide angular resolution almost 1000 times better than that of the most powerful optical telescopes.

Of the many other opportunities that will become available to scientists using this telescope, astronomical observations in the partially transparent atmospheric windows between 200 and 300 microns wavelength will be possible for a significant fraction of the time. The Herschel Space Observatory has been making exciting astronomical discoveries in this wavelength range for the past two years. However, the liquid cryogens aboard Herschel will eventually run out, beyond which time no further observations will be possible. Access to the sky in this spectral range is limited to the driest, highest and coldest places on Earth, such as current observatory sites in Antarctica and Northern Chile. Atmospheric measurements made at Summit Station, close to the peak of the Greenland ice sheet, indicate that observations in the atmospheric windows down to 200 micron will be possible during the dry winter season. This new telescope will have ten times the collecting area of the Herschel dish, and will be able to capitalize on the pioneering work of the Herschel Space Observatory.

In this presentation, we will discuss our plans to retrofit the telescope for cold weather operation, the potential instrumentation for THz observations, and the projected schedule.

THz space mission Millimetron

A. V. Smirnov[1*], N. S. Kardashev[1], A.M. Baryshev[2] on behalf of Millimetron consortium

1 Astro Space Center, Lebedev Physical Institute, Moscow, Russia
2 SRON Netherlands Institute for Space Research, Groningen, the Netherlands
* Contact: asmirn@asc.rssi.ru, phone +7-495-333 2312

Abstract— **We present an overview and current status of the astronomical mission Millimetron. Millimetron is a space-borne observatory with a cooled 10-m diameter telescope optimized for operation in the submillimeter and far-infrared ranges. Due to an unprecedented sensitivity in one of the basic observation mode, as a single-dish observatory and an unprecedented high resolution in another mode, as an element of a space-earth VLBI system, Millimetron will be able to solve various of key problems in current astrophysics such as study of the formation and evolution of stars and planets, galaxies, quasars and many others. There will be no cryogenic liquids on board, which will reduce the mass of the observatory. Instead the mission will be cooled passively with heat shields and actively with mechanical coolers. This combination of passive and active cooling will provide a 10-m space telescope cooled down to 4.5K. The planned launch year of the Millimetron observatory is 2017.**

Study of the superconductor-normal metal interface in hot-electron bolometer mixers

I. Tretiakov, M. Finkel, P. Larionov, A. Maslennikova, S. Ryabchun, N. Kaurova,
B. Voronov,and G. Goltsman*

Moscow State Pedagogical University, 1 Malaya Pirogovskays St, Moscow, 119992, Russia*

* Contact: goltsman@rplab.ru, phone +7-499-246 6321

Abstract——**During the last few years significant progress has been made in the field of hot-electron bolometer (HEB) mixers. It has been possible to combine a low noise temperature and high stability of phonon-cooled HEBs with an ultrawide gain bandwidth of the diffusion-cooled HEBs in a single device and thus create HEB mixers which offer a noise temperature of 5hν/kB across a 7-GHz band. The essential ingredient of this success is the *in situ* fabrication technology, where the deposition of the gold contacts follows the deposition of the superconducting film without vacuum breaking.**

Despite the evident technological breakthrough, the details of certain physical processes occurring both at the superconductor-normal metal (SN) interface and in the superconducting bridge are not completely understood in terms of their influence on the mixer performance. In particular, it is still unclear to what extent the properties of the SN interface are affected by the deposition temperatures of the superconductor and the normal metal, and also by the time interval elapsed between the deposition processes. We will gain some insight into the matter by studying the behaviour of the superconducting transition as a function of the deposition temperatures and time delay. A better understanding of this issue will allow us to move forward the HEB mixer technology towards new applications.

The 0.9 and 1.3 THz Superconducting HEB Mixer Receiver for the ASTE 10 m Telescope

T. Shiino[1*], R. Furuya[1], T. Soma[1], T. Sakai[1], Y. Watanabe[1], N.Sakai[1], L. Jiang[2],
O. Ohguchi[1], H. Maezawa[3], T. Yamakura[4], Y. Irimajiri[5], and S. Yamamoto[1]

1 The University of Tokyo*, Hongo, Tokyo, Japan
2 Nanjing Forestry University, Nanjing, Jiangsu, China
3 Osaka Prefecture University, Sakai, Osaka, Japan
4 Tsukuba University, Tsukuba, Ibaraki, Japan
5 National Institute of Information and Communications Technology, Koganei, Tokyo, Japan
* Contact: `shiino@taurus.phys.s.u-tokyo.ac.jp`, phone +81-3-5841-4217

Abstract⸺In the THz region, there exist many spectral lines of various fundamental atoms, ions and molecules, which give us novel information on chemical and physical state of interstellar clouds including star and planet forming regions. Although observations of these lines have successfully been done with Herschel HIFI, further observations with higher angular resolution from the ground-based telescope are still important for some THz atmospheric windows. With this in mind, we have been developing superconducting HEB (Hot Electron Bolometer) mixers for the THz frequency region at The University of Tokyo. By use of these mixers, we have prepared a cartridge-type THz heterodyne receiver for the 0.9 THz and 1.3-1.5 THz bands, and have successfully conducted a commissioning run on the ASTE 10 m telescope (Atacama Chile).

The receiver is the ALMA cartridge type with a single beam. It can observe the dual bands (0.9 THz and 1.3-1.5 THz) simultaneously in the DSB mode by using the wire grid. The IF band is 1.0-1.2 GHz. As for local oscillators (LOs), we use 3 different multiplier chains driven by a microwave synthesizer for the 3 observation frequencies; 0.9, 1.3, 1.5 THz. In the commissioning run, the LOs for 0.9 and 1.3 THz have been installed. We employ the in-house waveguide HEB mixers for the both bands. Although SIS mixers now show a better performance than HEB mixers at 0.9 THz, we use the HEB mixer to demonstrate observation capability of our HEB mixer. We use NbTiN superconducting films fabricated on a quartz substrate for the HEB mixers. The thickness of superconducting microbridges is 10.8 nm. The receiver performance is measured in the test cryostat, and the minimum receiver noise temperatures achieved are as low as 390 K for the 0.8 THz, 490 K for the 1.5 THz mixers.

The lowest system noise temperature including atmospheric attenuation is around 1000 K at 880 GHz, when the precipitable water vapor is 0.18 mm. From the continuum observation of Jupiter, the beam efficiency is derived to be about 30% at 880 GHz for the illumination of the inner 7 m area of the 10 m telescope. Furthermore, we have succeeded in detecting the spectral line of ^{13}CO (*J*=8-7; 881.3 GHz) toward the Orion A molecular cloud. Now we are improving the mixer to expand the IF bandwidth for the next run, which is expected in 2012.

A 1.4-THz Superconducting HEB Mixer for DATE5

W. Zhang[1,2*], W. Miao[1,2], Q.J. Yao[1,2], Z.H. Lin[1,2], K. Zhang[1,2], W.Y. Duan[1,2], and S.C. Shi[1,2*]

1 Purple Mountain Observatory, CAS, NanJing, Jiangsu, 210008, China
2 Key Lab of Radio Astronomy, CAS, NanJing, Jiangsu, 210008, China
* Contacts: wzhang@pmo.ac.cn, scshi@mail.pmo.ac.cn, phone +86-25-8333-2204

Abstract——**Purple Mountain Observatory as well as its collaborators is proposing to build a 5-m THz telescope (DATE5) at Dome A, Antarctic. Two THz heterodyne receivers, with one at 1.4 THz, are being considered as its first generation instrument. Here we report on the development of a 1.4-THz superconducting hot-electron bolometer (HEB) mixer for DATE5, which adopts a twin-slot antenna design. The direct-detection spectral (FTS) response of the 1.4-THz superconducting HEB mixer, with the HEB device fabricated at MSPU, has been measured, giving a frequency coverage of 0.8~1.5THz. And the measured FTS response appears in good agreement with the simulated one. Preliminary noise-temperature measurement at a lower frequency of 0.85 THz shows a receiver noise temperature of 1500 K. The estimated performance at 1.4 THz should be less than 1000 K in terms of the measured FTS response. Detailed simulation and experimental results will be presented.**

Stabilized HEB-QCL heterodyne spectrometer at super-terahertz

Y. Ren[1,2,3,*], J.N. Hovenier[1], D.J. Hayton[4], M. Cui[4], J.R. Gao[1,4*], T.M. Klapwijk[1], S.C. Shi[2], T-Y. Kao[5], Q. Hu[5], and J. L. Reno[6]

1Kavli Institute of NanoScience, Delft University of Technology, Lorentzweg 1, 2628 CJ Delft, The Netherlands
2Purple Mountain Observatory (PMO), Chinese Academy of Sciences, 2 West Beijing Road, Nanjing, JiangSu 210008, China.
3Graduate School, Chinese Academy of Sciences, 19A Yu Quan Road, Beijing 100049, China
4SRON Netherlands Institute for Space Research, Sorbonnelaan 2, 3584 CA Utrecht, The Netherlands
5Department of Electrical Engineering and Computer Science, Massachusetts Institute of Technology, Cambridge, Massachusetts 02139, USA.
6Sandia National Laboratories, Albuquerque, NM 87185-0601, U.S.A.
* Contact: y.ren@tudelft.nl

Abstract—In the terahertz (THz) frequency range a high resolution heterodyne spectrometer is of crucial importance for astronomical observations and atmospheric remote sensing applications, based on its combination of high spectral resolution and sensitivity. As the mixer, a superconducting NbN hot-electron bolometer (HEB) mixer has demonstrated excellent sensitivities up to 5.3 THz. As the local oscillator (LO), terahertz quantum cascade lasers (QCLs) have shown advantages at frequencies above 2 THz, based on their single mode emission, wide frequency operating range, high output power and long term stability. Several progresses have been made for a THz QCL to be used as the local oscillator (LO) in a heterodyne receiver, such as a heterodyne spectroscopy measurement in the lab.[1]

Here we report a new experiment on high-resolution heterodyne spectrometer using a 3.5 THz QCL as LO and a HEB as mixer by stabilizing both frequency and amplitude of the QCL. We have already achieved the following results. The frequency locking of the QCL was demonstrated by using a molecular absorption line, a proportional-integral-derivative (PID) controller, and a direct power detector [2]. The intensity of the QCL emission is also stabilized by means of swing-arm actuator placed in the beam path using a second PID controller [3].

[1] Y. Ren, J.N. Hovenier, R. Higgins, J.R. Gao, T.M. Klapwijk, S.C. Shi, B. Klein, T-Y. Kao, Q. Hu, and J. L. Reno, High-resolution heterodyne spectroscopy using a tunable quantum cascade laser around 3.5 THz. Appl. Phys. Lett., **98**, 231109(2011).
[2] Y. Ren, J.N. Hovenier, M. Cui, D.J. Hayton, J.R. Gao, T.M. Klapwijk, S.C. Shi, T-Y. Kao, Q. Hu, and J. L. Reno, Frequency locking of 3.5 THz quantum cascade lasers using a gas cell, Appl. Phys. Lett. (submitted)
[3] D.J. Hayton, J.R. Gao, J.W. Kooi, Y. Ren, W. Zhang and G. de Lange, Stabilized hot electron bolometer heterodyne receiver at 2.5 THz, Appl. Phys. Lett. (submitted)

In-orbit Stability Evaluation of the AOS (Acousto-Optical Spectrometer) of Superconducting Submillimeter-Wave Limb-Emission Sounder (JEM/SMILES)

S. Mizobuchi[1*], K. Kikuchi[2], S. Ochiai[2], T. Nishibori[1], and H. Ozeki[3]

1 Japan Aerospace Exploration Agency*, Tsukuba, Ibaraki, 305-8505, Japan
2 National Institute of Information and Communications Technology, Koganei, Tokyo, 184-8795, Japan
3 Toho University, Funabashi, Chiba, 274-8510, Japan
* Contact: mizobuchi.satoko@jaxa.jp

Abstract——The Superconducting Submillimeter-Wave Limb-Emission Sounder (SMILES) had observed submillimeter-wave radiation from atmospheric minor constituents for having a better understanding of mechanism controlling the stratospheric ozone amounts and those relating to climate change. The SMILES has been attached to the Japanese Experiment Module (JEM) on the International Space Station (ISS). The observation was started in October 2009, and had been performed for more than a half year.

We adopted two sets of Acousto-Optical Spectrometer (AOS) for detecting submillimeter-wave radiation signal as spectral image. For giving the best performance on the data retrieval, the instrumental function should be determined as precisely as possible. One of the most sensitive instrumental functions is the response function which characterized the response against the input signal of the AOS. However, we found a systematic discrepancy among SMILES data products, some of which may be attributed to insufficient modeling of the response function.

Usually, several kinds of measurements and analysis are conducted within prelaunch activities in order to understand the detailed characteristic of each instrument. That is because these checks sometimes require dedicated equipments or tools that cannot be brought due to the limits of available resources, and it is not easy to know the each instrument behavior after combining all instruments as one detector. On the other hands, instrument performance can be changed because of launch impacts, the in-orbit actual performance can be different from the one at ground, and the performance can change with time. Therefore, it would be advantageous to have an alternative way to characterize the instrument function in orbit.

SMILES have the way to calibrate the function by using comb signals that are originally used for the frequency calibration of the spectrometer. Using in-orbit calibration data, we tried to check stability of parameters which characterize the instrument function of AOS. In this presentation, these results are discussed and reported.

Terahertz Radiometer for Outer Planet and Moon Atmospheres (TROPA)

E. T. Schlecht*, V. Jamnejad[1], R. F. Jarnot[1], R. Raffanti[2], and R. Lin[1]

[1] Jet Propulsion Laboratory, California Institute of Technology*, Pasadena, CA 91109*

[2] Techne Instruments 4920 Telegraph Avenue Oakland CA 94609

Abstract ⸺**We are developing a prototype instrument platform to demonstrate the feasibility of a wideband spectrometer for planetary applications under a three-year NASA research program. This development focuses on three specific areas needing advancement. First, the terahertz portion consists of an optical bench with dual heterodyne Schottky-mixer based receivers, one for each band. The beams entering the horns of the two receivers are de-multiplexed from the input beam by a polarizing beam splitter. The blocks containing the 560 and 1200 GHz mixer are more highly integrated than previous space instruments to reduce mass and volume. The receivers take a fundamental pump frequency near 30 GHz and multiply up to the submillimeter range.**

Second, a rapid-tuning, low-phase noise, and low-power 33 GHz range LO synthesizer is being prototyped. The low phase noise requirement is needed because of the factor of 36 multiplication to reach 1200 GHz, giving a requirement that the integrated phase noise from 100 kHz up be less than 0.6 degrees. The synthesizer will require about 6 watts.

Finally, we are developing an advanced polyphase filter back-end spectrum analyzer with a bandwidth of 750 MHz, and power consumption of about 3 Watts and 4096 channels. This system is based on a simple three-chip architecture, having a commercial 1.5 GS/s analog-to-digital converter, an ASIC to do the filtering and an advanced FPGA for data processing and control.

I. Introduction.

For several years now, ESA and NASA have turned their attention to an Outer Planet Flagship Mission (OPFM) to the Jupiter system (focusing on Ganymede, Europa and other Galilean moons, as well as Jupiter itself [1]) and to the Saturn system (focusing on Titan [2]). Both studies call for inclusion of a submillimeter/Terahertz instrument to perform a new category of measurement. More recently, the mission has been accepted for funding as an ESA L-class mission[3]. The Jupiter measurements will greatly expand on those from the Juno mission currently being built. The prime target will be Jupiter's stratosphere, which links the deeper troposphere whose dynamics are dominated by Jupiter's internal energy sources with the upper atmosphere that interacts strongly with the space environment. In the lower atmosphere small-scale convection control the dynamics, but these generate the larger scale waves that travel up from the cloud levels to the stratosphere, where they interact with larger scale flows. These processes are presently very poorly understood; improving the understanding of these dynamics is a key goal of the sub millimeter instrument.

We are reporting on a NASA-funded brassboard of the instrument known as the Terahertz Radiometer for Outer Planet and Moon Atmospheres (TROPA). The Terahertz spectrometer will
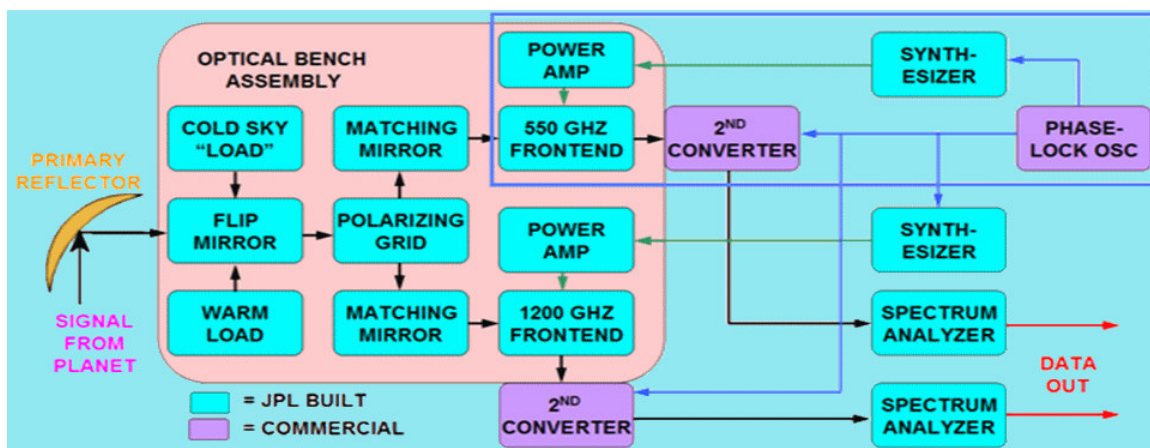
Fig. 1. Block diagram of TROPA, showing the optical bench, receiver front ends, synthesizers and back end spectrum analyzers.

complement microwave and IR instruments; it is the only technology capable of resolving winds, temperature, pressure and composition in this critical layer of the atmosphere, and will fill the gap left by the other measurement technologies. It operates in the submillimeter frequency range, with two receivers: one for 520 to 590 GHz, one for 1100 to 1300 GHz. See the block diagram in Figure 1. It has two features that differentiate it from previous space-borne radiometers in this frequency range: the wide tunability and rapid frequency switching (<20 ms). The receivers are based on Schottky diode mixers, developed at JPL, and have a sensitivity of about 2500 K at 550 GHz, 6000 K at 1200 GHz. The mixers are pumped by local oscillator (LO) sources also developed at JPL, and also based on cascaded chains of Schottky diode frequency multipliers to provide about 3 mW at 600 GHz. The mixers translate the input signals to an intermediate frequency (IF) that is analyzed in a new, low-power digital polyphase backend spectrum analyzer with 750 MHz bandwidth, 4096 channels, and consuming approximately 3 W. The sources for the LO multiplier chains is a pair of rapid-tuning, state of the art low power LO synthesizers, with output frequencies around 100 GHz, and consuming approximately five watts each. The total instrument should have a total power consumption of about 20 watts, and a mass of 10 kg.

II. Optical Bench Design.

The input signal from the planet will be received and concentrated by the primary telescope into the optical bench that splits the two frequencies and conveys the separated beams into the receiver front ends. The design started with a lower-frequency optical bench designed by one of the authors [4] for MIRO, a comet observation submillimeter-wave instrument at 190 and 564 GHz. The fundamental principle is that the frequency separation is not made by frequency dependent components, but rather by a polarizing beam splitter. The receivers for the two frequencies are cross-polarized. Since each receiver only accepts a single polarization in any case, no signal is lost that would not be lost even without the polarizer, and the loss is greatly reduced and the optics greatly simplified.
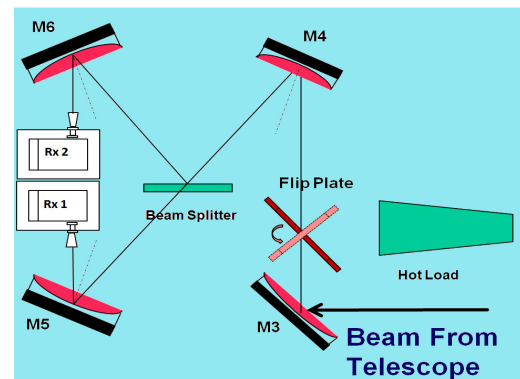
Fig. 2. TROPA optical bench schematic.

The scheme devised for TROPA is illustrated in Figure 2. The incident beam from the telescope is deflected from its input direction into the plane of the optical bench by mirror M3. It passes a flip mirror toward mirror M4. The flip mirror allows the beam incident on M4 to be selected between the calibration hot load and the beam from M3. M4 re-directs the beam toward the beam splitter. The splitter is aligned to pass the horizontally polarized signal toward M5 and the 1200 GHz receiver, Rx 1, and reflects the vertically polarized signal toward M6 and the 560 GHz receiver, Rx 2.

Designing the optical bench is an exercise in constrained optimization. The initial design uses a Gaussian beam methodology [5], where the beams between each optical element is described by the waist diameter, w_0, and location. The scientific requirements on the instrument dictate that the spot resolution at the planet be the diffraction limited for the given reflector diameter at each frequency. This implies that the main telescope be illuminated with the same taper for each frequency. Thus the Gaussian beam diameters in the far field of M3 should be the same. Since the far-field spreading half-angle, θ_S of a Gaussian beam is given by [5]

$$\theta_S \cong \frac{\lambda}{\pi w_0},$$

(1)

for wavelength λ. Hence, the output beams of M3 must have their waist to wavelength ratio matched. Furthermore, for both frequencies the radii of curvature and beam radii must be
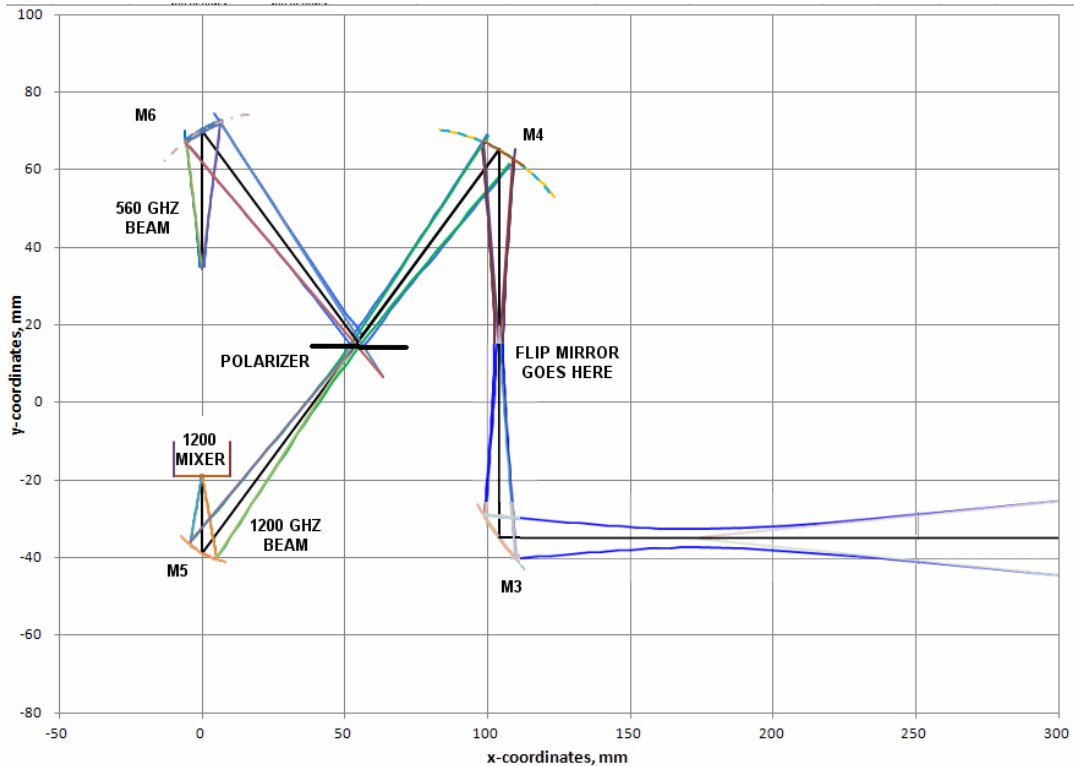
Fig. 3. TROPA optical bench spreadsheet design.

matched to the focus-to-ellipsoid distance of the reflectors. There are also the geometrical requirements for the position and sizes of the blocks, and the horn antennas of each frequency. The beams must not impinge on the blocks. Since the block sizes are similar to those in reference [4], this becomes more difficult at the higher frequencies, especially the 1200 GHz channel.

Finally, the beams are matched to the receiver horns by M5 and M6. The horn used for the 560 GHz band is a commercially procured corrugated scalar horn. The 1200 GHz horn is a diagonal design, machined directly into the block. In order to facilitate optimization of the design, a spreadsheet has been generated that directly plots the beam radii and foci. Figure 3 shows the plots of the current design. A Solidworks file has been produced that generates a solid model for the mirrors based on the parameters (semi-major and semi-minor axes) determined by the spreadsheet. Machining will begin shortly.

III. Front End Receivers.

560 GHz receiver. The 530 to 590 GHz mixer block incorporates two features that differentiate if from most [6]: **(A)** to be compatible with the TROPA optical bench design described above, the RF beam must enter at right angles to the LO waveguide. Most previous JPL mixer blocks have the RF and LO ports co-linear. **(B)** The second unusual feature is incorporation of a waveguide twist at the RF input. Almost all submillimeter waveguide blocks we use have the electric field parallel to the split between the two halves of the block, making the split in the E-plane rather than the H-plane. This is because a) it is easier to machine and b) lower

loss than the alternative H-plane split, because the waveguide surface currents would then be required to flow across the split. However, in our optical bench scheme, one receiver must receive signals with E-field parallel to the bench plane, and one with the E-field normal to the bench plane. We decided to make the 560 receiver perpendicular, thus requiring a rotation of its input waveguide. (If the input and output guides were co-linear, the twist could be in the LO waveguide, but in the right-angle alignment we are using that would put the input in the top of the block.)

Fig. 4. New 560 GHz block with polarization twist.

The 560 GHz block is shown in Figure 4. It has been received but not assembled and tested yet; that will occur shortly.

1200 GHz mixer. We have measured the 1200 GHz mixer. This is the highest frequency we have ever measured for a subharmonically pumped mixer using JPLs planar process (In fact, all higher frequency mixers the authors are aware of, including other JPL fabricated mixers are fundamentally pumped). The receiver chain is shown in Figure 5 and an initial measurement is reported in the poster presented at this conference by B. Thomas [7]. The noise temperature is in the range of 4000 to 6000 K double sideband (DSB).

Compact 1200 GHz Blocks. We are in the process of designing a new pair of blocks for the 1200 GHz channel. One will include a new 570 to 650 GHz tripler that is intended to expand the frequency range of the receiver to higher frequencies, as mentioned above. This block also includes the right angle bend necessary for compatibility with the optical bench design. Using this design, several goals are accomplished: first, it allows us to implement a new concept with a dual-combined tripler/mixer block (see Figure 6). The two blocks fit together

Fig. 5. 1200 GHz receiver: the mixer is at far left, with 600 GHz tripler and 200 GHz doubler next. Four right-most blocks are the amplifiers.

Fig 6. Combined/compact 1200 tripler/mixer block.

as if they were one, and take up the same 20×20×20 mm^3 space as a single block. This makes it possible to keep a collinear RF/LO design for the 1200 GHz mixer. The co-linear design has the advantage of shorter high-frequency waveguides, giving lower loss and better performance. The bend occurs in the 200 GHz waveguide input to the 600 GHz tripler, rather than at 600 or 1200 GHz.

An additional advantage is that the design is compatible with the current 1200 GHz block design described in task 2. The original block (Figure 5) has a horn with two wide a beam to work with the optical bench. We are also going to try a second design for the 1200 that will also work with either the new tripler, or the previous version.

IV. Digital Back End Spectrometers.

The ASIC-based digital back end spectrometers have been received, and are currently being tested. These are of a new type of digital polyphase spectrometer recently developed for space-borne astronomical applications [8]. The principal of operation is similar to a windowed FFT. To improve the spectral resolution, the input data is first windowed using a 4-tap poly-phase FIR filter bank (PFB) that provides better spectral bin isolation and improved side-lobe isolation than a Hamming filter.

The spectrometer implementation has been re-designed for the TROPA program, specifically to allow for rapid switching between widely spaced spectral lines, while maintaining the original version's low power low mass properties.

Another change is to incorporate the interface to the control computer on a sub-board. In this case, the interface is to an Ethernet LAN port to simplify the rapid transmission of data to the host computer. The analyzer appears in Figure 7. Visible are the digitizer (ADC), spectrometer ASIC, and FPGA data processor. The new components (SYNC connector) and LAN interface are also shown.

Results from the first tests (at the manufacturer) are shown in Figure 8. A single signal at 60 MHz is shown, as well as the results from an on-chip vector test generator (VTG). The signal
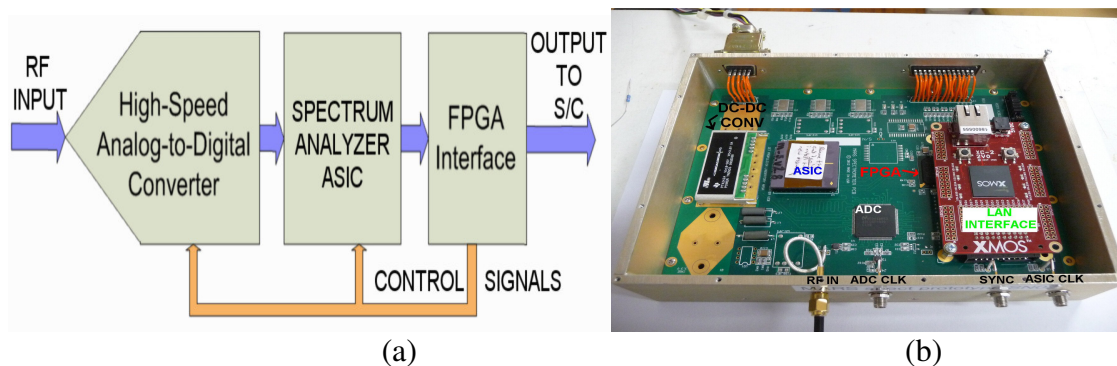
Fig. 7. New digital back end. (a) General block diagram. (b) Photo of spectrum analyzer. The ADC and polyphase ASIC are near center, and the new interface is at the right.

generator result shows that the digitizer (ADC) works and that the analyzer can correctly generate a single frequency spectrum. The VTG result shows that all 4096 spectral channels are working properly.

Figure 9 shows a similar test performed at JPL using our control software. A (somewhat noisy) signal generator produces a tone around 200 MHz tone as input. The right panel shows a zoomed in region about the tone.

The two next steps are to first, modify the code in the XMOS Ethernet interface to the raw ADC data to be output to the controller computer, then tune the ADC for best interleaving performance. For reliable operation we are using both halves of the ADC, each clocking on alternate halves of a 750 MHz signal to get the aggregate 1.5 GSps digitization rate. For this to work at these high data rates, the two ADCs must be "tuned" to match their characteristics to properties to yield a correctly digitized signal. To accomplish this, the raw data must be available to the computer in a pass-through mode for processing by the calibration software.

The second step is to modify the XMOS code again to provide the synchronization function that the instrument requires. Since the original version of the back end was designed for astronomical use, the spectra were simply accumulated for maximum sensitivity, for as long as
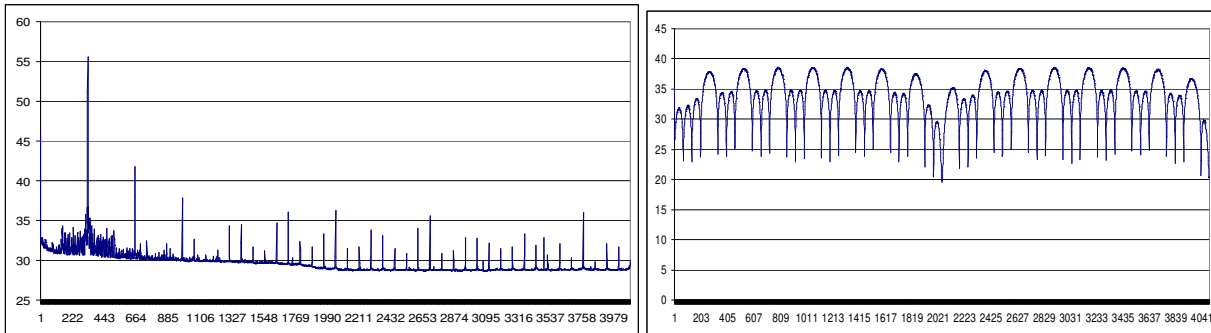
Fig. 8. New digital back end "first light". At left, a 60 MHz -3 dBm signal is shown, with 183 kHz resolution (750 MHz bandwidth/4096 channels). At right a vector test generator result shows normal output from all channels.
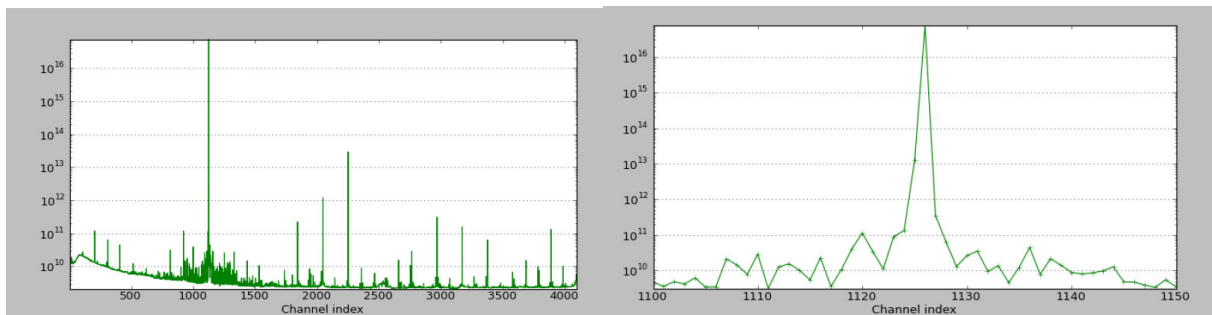
Fig. 9. Response of digitizer to 206 MHz tone input. Channel number = 4096*200MHz/750MHz=1125.

the telescope could be pointed at the target. The planetary version requires switching from line to line for about 100 ms per observation and the spectra must be accumulated separately for the different lines. This will be accomplished by use of an extra synchronization line to allow communication of the switching from the controller to the spectrometer.

The XMOS processor will be replaced by a rad-hard FPGA for the flight implementation. We are developing a next-generation ASIC polyphase spectrometer with 1.5 GHz bandwidth, 8192 channels, and embedded ADCs. The embedded ADCs provide the state-of-the-art in terms of power consumption, and will double the bandwidth of the spectrometer while reducing its power consumption to below 1 W.

V. Low-power, Fast Switching Wideband Synthesizer.

The synthesizers that pump the receiver LO multiplier chains must meet several critical requirements for this application:
1. Frequency range 28 – 36 GHz, to be multiplied by three into the 100 GHz band. The output is amplified and then multiplied by six to pump the two mixers.
2. Low power, well under 10 watts each.
3. They must be able to switch frequencies rapidly. Since the observation time is about 100 ms, a switching time of about 10 ms is necessary to not lose excessive observing time.

4. The phase noise must be low, since the phase error grows as 20log(N) dB for a multiplication ratio of N. Unlike most communications synthesizer, the main frequency range of concern is in the range starting from half the spectrometer channel bandwidth and higher. [9], [10].
5. Frequency steps (at the VCO band of 8 GHz) about 10 MHz. This is determined by the 750 MHz spectrometer bandwidth times the multiplication ratio to the highest frequency band, 36. Steps of 10 MHz at the synthesizer frequency yield 360 MHz steps at the 1200 GHz signal frequency.

The original intention was to procure commercial synthesizers. But due to the unusual requirements, we decided to prototype the synthesizer at JPL.

The block diagram is given in Figure 10(a). It utilizes a space qualified CMOS SOI fractional-N PLL, with a maximum input frequency of 3 GHz. In order to both meet the wide tuning range, and low phase noise above 100 kHz frequency offset, it was decided to base the synthesizer on a 7-9 GHz YIG tuned oscillator. Since this is well above the input frequency of the PLL, a ÷4 prescaler is used. Likewise, since the output frequency is 28 to 36 GHz, a ×4 multiplier will be used. This A single package will be used to house the prescaler and multiplier chain, whose block diagram is detailed in Figure 10b. It is based on commercial

(a)

(b)

Fig. 10. 28-36 GHz synthesizer block diagram. (a) General block diagram. The output goes to a passive X3 tripler. (b) Synthesizer coupler-prescaler-multiplier.

multiplier chips from Triquint and Hittite. This unit is currently being designed.

The estimated power consumption of the synthesizer is 2.8 Watts, including the PLL (.13 W)
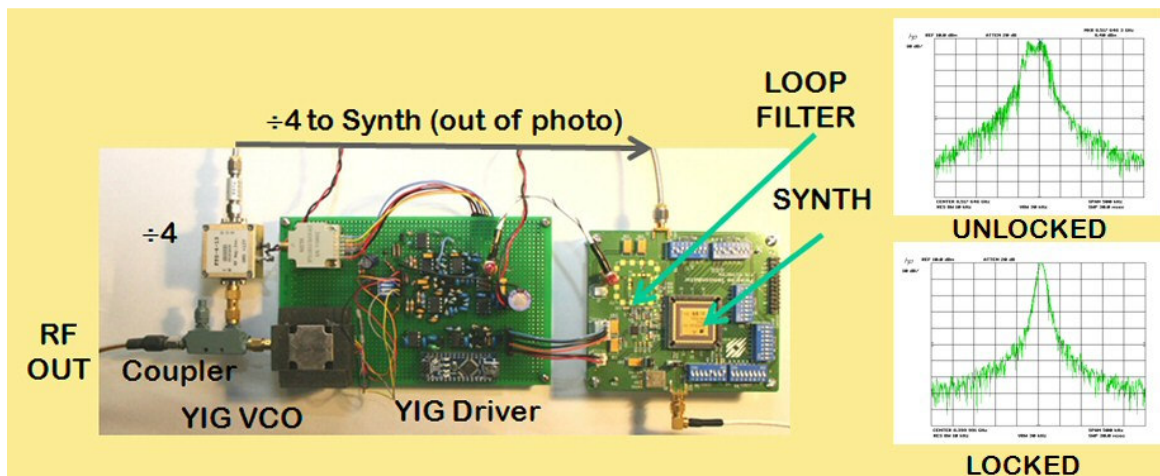
Fig. 11 Synthesizer prototype with spectrum analyzer plots showing effect of phase lock.

but *not* including the YIG-tuned oscillator (YTO). The oscillator power draw depends on the current through the YIG tuning coil. This can be minimized by using a permanent magnet YIG tuned oscillator (PMYTO). These have a permanent magnet designed to set the zero current frequency at the center of the desired band. This minimizes the total current needed to tune the YTO. The bias current for the YTO is specified as approximately 100 mA at 8.5 volts, hence 0.85 W.

The prototype synthesizer is based around an evaluation board for the PLL, and a prototype YIG driver board designed by the authors based on classic designs from HP spectrum analyzers and signal generators. The synthesizer also includes a small controller board based on an Atmel ATmega168 microcontroller. The prototype is shown in Figure 11, and until the multiplier is assembled, it uses a temporary coax based prescaler and sampling coupler. The current draw is about 0.4 A at 8.5 V, i.e. about 3.4 W, including the prescaler, which is a more power hungry version of the HM362 that has been purchased for the TROPA synthesizer. The synthesizer has been phase locked, and we are currently preparing to measure the phase noise. The initial spectrum analyzer scans (also in Figure 11) indicate the difference

Fig. 12 Synthesizer phase noise estimate with individual contributions.

between the locked and unlocked YTO. The oscillator is sensitive to low-frequency noise, with a $1/f$ type integrating response [7]. Closing the loop clearly stabilizes the output signal as expected. The next steps are to program the microcontroller and narrow the loop bandwidth to fit the YTO. The expected phase noise profile is shown in Figure 12.

VI. Conclusion.

Intermediate results of a program to develop an instrument for Terahertz observation of planetary observations have been presented. Progress is proceeding along several technological fronts: Terahertz receiver front ends, back end spectrum analyzer, optical bench and wideband frequency synthesizer. Future publications will detail the completion of these tasks.

REFERENCES
[1] Jupiter System Observer Mission Study: Final Report, Task Order #NMO710851, 01 November 2007. Jupiter Ganymede Orbiter: ESA Contribution to the Europa Jupiter System Mission, 12 Feb 2009.
[2] Titan Explorer Flagship Mission Study, Public Release Version, January 2008. Titan Saturn System Mission: Final Report on the NASA Contribution to a Joint Mission with ESA, 30 Jan 2009.
[3] European Space Agency, "JUICE Assessment Study Report: Exploring the emergence of habitable worlds around gas giants," ESA/SRE(2011)18, December 2011, http://sci.esa.int/science-e/www/object/index.cfm?fobjectid=49837

[4] V. Jamnejad, "A dual band telescope for microwave instrument on Rosetta Orbiter (MIRO)," Proceedings 1999 IEEE Aerospace Conference, vol. 3, pp 265-269, 1999.

[5] P.E. Goldsmith, *Quasioptical Systems*, IEEE Press, New York, 1998.

[6] E. T. Schlecht, J. J. Gill, R. H. Lin, R. J. Dengler, and I. Mehdi, "A 520-590 GHz Crossbar Balanced Fundamental Schottky Mixer," *IEEE Microwave And Wireless Components Lett.*, Vol. 20, No. 7, pp. 387-389, July 2010.

[7] B. Thomas, "First results of a 1.2 THz MMIC sub-harmonic mixer based on GaAs Schottky diodes for planetary atmospheric remote sensing," 23rd International Symposium Space Terahertz Technology, Tokyo Japan, 2-4 April, 2012.

[8] B. Richards, N. Nicolici, H. Chen, K. Chao, D. Werthimer, and B. Nikolić, "A 1.5GS/s 4096-Point Digital Spectrum Analyzer for Space-Borne Applications," IEEE Custom Integrated Circuits Conference, 2009. CICC '09., San Jose, CA,13-16 Sept. 2009.

[9] E. Schlecht, "Wide-band heterodyne submillimetre wave spectrometer for planetary atmospheres," *21st International Symposium On Space Terahertz Technology*, Oxford, 23-25 March, 2010.

[10] J. L. Besada, "Influence of Local Oscillator Phase Noise on the Resolution of Millimeter-Wave Spectral-Line Radiometers," *IEEE Transactions On Instrumentation And Measurement*, VOL. IM-28, NO. 2, JUNE 1979

The STEAMR Instrument: Optical Design, Development & Testing

Mark Whale, *Member, IEEE,* Matthias Renker, Axel Murk, Urban Frisk, Olle Janson, Luc Blecha, Gabriel Paciotti, Graham Bell, Richard Wylde, and Anthony Murphy *Member, IEEE*

Abstract—The STEAMR instrument is a Swedish national contribution to the ESA PREMIER mission, which is a candidate for the upcoming Earth Core Explorer mission. The STEAMR instrument is envisaged as a multi-beam limb sounding satellite, which will utilise 14 simultaneously observing beams in two 12 GHz wide bands from 323 to 357 GHz. To maximize spatial sampling in the elevation direction the observing beams have an elliptical geometry, which defines the incoming beams as being astigmatic. In this paper we present an antenna optics scheme which corrects for this inherent astigmatism, thereby ensuring optimum imaging of the incoming to the circularly symmetric receiver feed horns. Furthermore, the design, synthesis and electromagnetic verification of a prototype focal plane array for the STEAMR instrument is also reported.

I. Introduction

THe STEAMR instrument is a Swedish national contribution to the upcoming ESA PREMIER mission, which is a candidate for the Earth Core Explorer mission [1]. The aim of the PREMIER mission (Process Exploration through Measurement of Infrared and millimetre-wave Emitted Radiation) will be to advance current understanding of the processes that link trace gases, radiation and chemistry in the upper troposphere and lower stratosphere. The composition and dynamics of the atmosphere at this boundary have an important impact on chemical exchanges and the Earth's radiative balance.

The STEAMR instrument is envisaged as a passive multi-beam limb sounder which will observe over a nominal altitude range of 6-28 km and azimuthal range of 10 km in a push-broom beam pattern configuration - c.f. Fig. 1. In order to max-imise spatial sampling the 14 observing beams are separated into two groups of seven, polarised at $\pm 45°$. The minimum beam sampling rate of the observing beams is approximately 18 dB in terms of amplitude radius. The elliptical geometry of the observing beams defines the incident beam patterns as astigmatic. Here we define astigmatic in terms of a skew Gaussian beam treatment, wherein the beams are treated with independently propagating Gaussian beam parameters in the

M. Whale, A. Murk and M. Renker are with the Institute for Applied Physics, University of Bern, Sidlerstrasse 5, Bern, Swtzerland e-mail: whale@iap.unibe.ch

U. Frisk is with Omnisys Instrument AB, Vüstra Frölunda, S-42130, Sweden

O. Janson is with the Swedish Space Corporation, P.O.Box 4207, SE-171 04, Solna, Sweden

L. Janson and G. Paciotti are with Almatech, Parc scientifique de l'EPFL, PSE-D, CH-1015 Lausanne, Switzerland

G. Bell and R. Wylde are with Thomas Keating Ltd., Station Mills, Billingshurst, West Sussex, RH14 9SH, United Kingdom

A. Murphy is with the Experimental Physics Department, National University of Ireland, Maynooth, Co. Kildare, Ireland
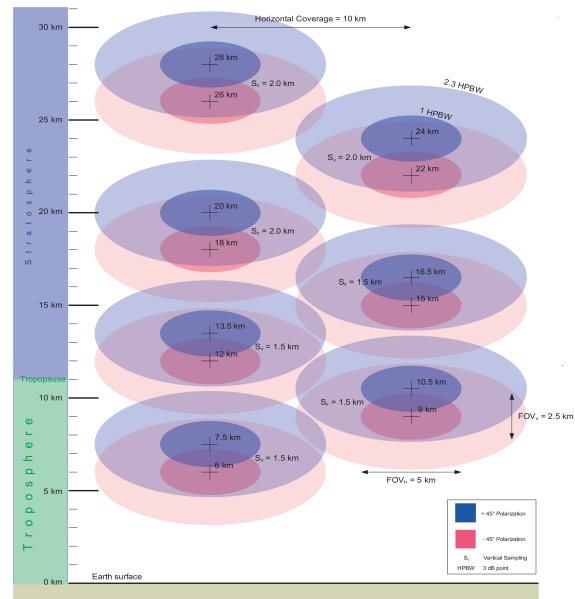
Fig. 1: Limb view geometry of the STEAMR antenna [1].

orthogonal azimuth and elevation directions. Correction of this astigmatism is necessary in order to achieve optimum imaging between the primary reflector and the feed horns. Concurrent with this requirement for anastigmatic imaging is the requirement for maximal power throughput of the individual beams. This requirement necessitates the use of a focal plane array (FPA) unit, whose function is to intercept the individual beams at the output focal plane of the complete antenna optics.

II. Antenna Optics Scheme

The antenna optical scheme is treated in three distinct sections. The primary and secondary reflectors, M1 and M2, form an off-axis Ritchey-Chrétien telescope. This particular telescope design is chosen for its larger field of view over classical Cassegrain or Gregorian designs, thereby providing the best possible imaging requirements for the widely spread multiple observations beams [2]. The aperture of the M1 reflector is elliptical, thus defining the output beam pattern geometry. The observing requirements for STEAMR, as is typical in millimetre wave radiometer antennas, places a higher priority on beam efficiency over antenna pattern resolution [3], [4], and as such the edge taper of the primary aperture is 25 dB in terms of 1-D fundamental Gaussian beam illumination. The subsequent four relay reflectors, referred to as M3, M4,

M5 and M6, comprise the beam forming network which is designed to correct the inherent beam astigmatism. This anastigmatic correction is achieved through treating the incoming beams as skew Gaussian, with independently evolving beam parameters in the azimuth and elevation directions such that
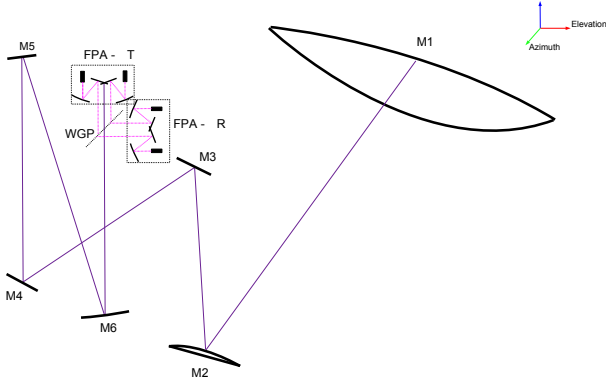
Fig. 2: Simplified ray-trace model of the STEAMR antenna optics, listing the component reflectors including FPAs, where the subscripts T and R refer to transmission and reflection through the wire grid polariser (WGP)

The anastigmatic imaging solution is then achieved through manipulation of the *ABCD* matrix description of the system. To provide the required degrees of freedom for this anastigmatic solution, the reflectors must be biconic, with independent lengths in the orthogonal azimuth and elevation plane order for the beams at the output focal plane of the an optics to maintain the maximum achievable mutual separ the output focal plane must be located at a phase sh $n + \pi/2$ radians with respect to the primary aperture matrix solution must also ensure a waist at both the c focal plane and the telescope aperture, with the ortho beam widths matched to the primary aperture rim in to provide the required edge taper for the two ortho directions.

As can be seen in Fig. 3 the combination of biconic r tors M3 and M4 produce the required matching of amp and phase shift at the plane of the M5 reflector, beyond the beams evolve equivalently for the two orthogonal tions, thereby forming a circularly symmetric, anastig beam. A complete description of this anastigmatic im solution is given in [5].

The physical interpretation of this imaging system re the use of so-called astigmatic off-axis reflectors [6]. reflectors are a special case of biconic reflectors whose orthogonal geometries are defined as off-axis conics, with conic parameters defined in the standard manner for off-axis quasioptical reflectors. With this definition a complete model of the STEAMR antenna optics scheme has been implemented in the GRASP physical optics software package for numerical electromagnetic analysis.

III. FOCAL PLANE ARRAY

The STEAMR FPA, as shown in Fig. 2, is composed of two imaging arrays FPA-T and FPA-R, were T and R refer respectively to transmission and reflection at the wire grid polariser

(a) Beam width
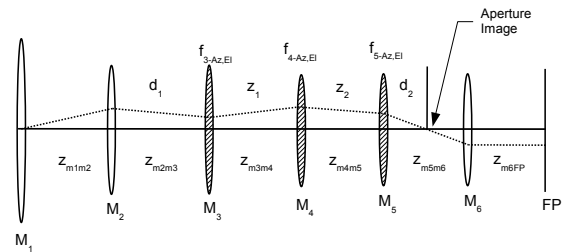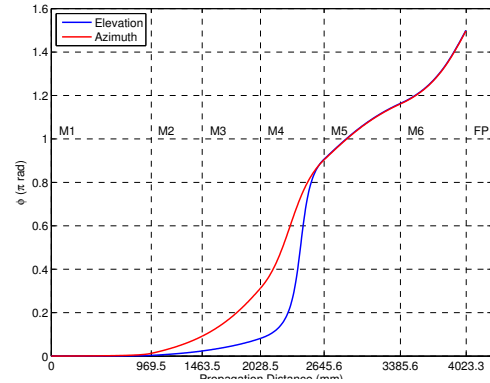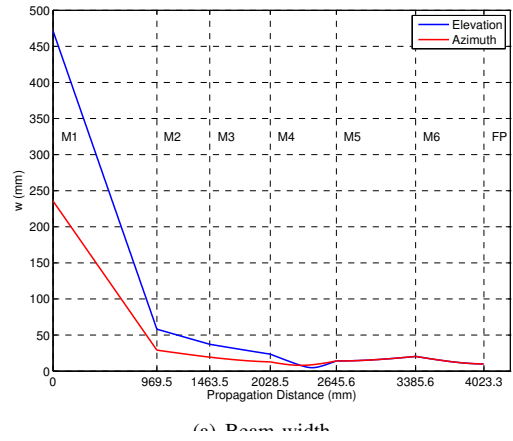
Fig. 4: Thin lens representation of the STEAMR antenna optics from the primary aperture (M1) through to the output focal plane (FP). The anastigmatic network, i.e. M3, M4 and M5 are shown as hatched filled lenses.

(WGP). The WGP separates the incident 14 beams into the two groups of seven. The optical path for each pixel in both arrays is equivalent, with the complete phase shift between the apertures of the primary reflector and the feed horns being 2π radians, thereby ensuring frequency independent coupling. This FPA has been developed on the heritage of two similar array units [7] and [8], which utilise monolithically machined facet reflector arrays to couple multiple beams at an antenna focal plane to their corresponding receiver elements. This type of reflector array has been selected for two chief reasons. Firstly, the output focal plane, being a Fourier transform of the antenna farfield, ensures that the beams experience their maximum mutual separation. However, to place feed horns
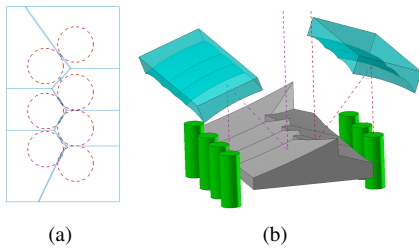
Fig. 5: FPA M7 facet reflector geometry (a), showing individual beam footprints for the 18 dB radius at the central frequency (340 GHz). A 3D CAD model of the complete FPA optics is shown in (b).

directly at this plane is undesirable. The maximum separation between the beams is insufficient to allow for feed horns of the desired directivity to occupy the focal plane and would overlap. If lower gain feeds were located here, this would alter the edge taper on the primary aperture and subsequently the beam field of view. Furthermore, locating the feeds at this plane would imply frequency dependent coupling between the feed and primary reflector apertures.

The maximum mutual separation between the focal plane beams in terms of Gaussian beam amplitude is 18 dB determines the maximum reflector truncation - c.f. Fig. 5(a). This is significantly lower than is desired for such an optical system where optimal power throughput is required. Typical truncation for such a system would be of the order of 35 dB [9]. This truncation leads to both reduction in power throughput per beam and introduces losses through diffraction and scattering. These issues were alleviated in two ways. The geometry of the reflector facets has been optimised for maximum area per beam, resulting in the complex 'saw-tooth' structure shown in Fig. 5(b). The feed horns have also been optimised for highly centralised aperture field distribution and low side lobes [10]. A full treatment of the design, analysis and electromagnetic measurement of a breadboard model of the STEAMR FPA is given by [11] and [12].

A breadboard model of the FPA was synthesized in conjunction with industrial partners, which can be seen in Fig. 10. High density CMM measurements, shown in Fig. 6, revealed that conformance of the breadboard facet reflector to stringent tolerance requirements was very high, with a maximum measured surface roughness RMS of $0.294 \mu m$.
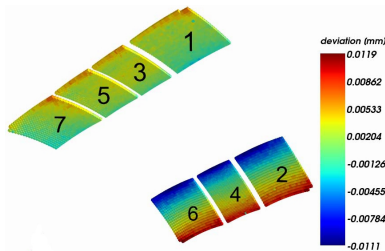
Fig. 6: Deviation distribution of the CMM measured FPA reflector surfaces from nominal surface for the facets of the FPA base plate.

IV. ELECTROMAGNETIC SIMULATIONS

The complete STEAMR antenna optics model was numerically analysed using the antenna design software GRASP,

with Physical Optics (PO) and Physical Theory of Diffraction (PTD) approximations being used for the major reflectors, and the Method of Moments (MoM) approximation to account for the complex geometries of the FPA reflectors [12]. From these data we can confidently draw conclusions of the performance of the antenna optics model.
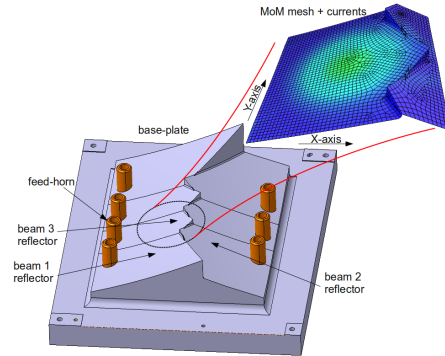
Fig. 7: CAD model of FPA baseplate, with example of MoM mesh and calculated current surface field.

Farfield beam pattern simulations reveal that overall the beams exhibit the desired elliptical patterns (Fig. 8(a)), with the outermost beams in the upper and lower ranges displaying a minor degree of rotation in the positive and negative elevation directions respectively, with the centrally located beams displaying the highest conformity with desired patterns in Fig. 1. Furthermore, at the -30 dB amplitude level there exist some asymmetrical sidelobes, once again for the beams at the extremities. Specific antenna performance requirements
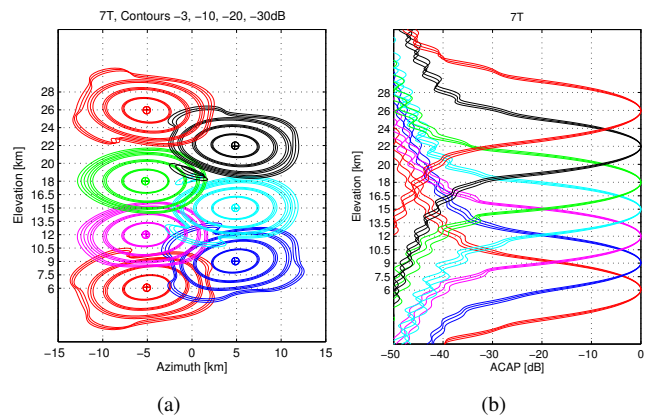
Fig. 8: Farfield contour plots for one set of seven beams from FPA-T, with contour levels spaced at -3, -10, -20 and -30 dB for frequencies 323, 340 and 357 GHz (a), and ACAPs for the same beams three contours per beam for frequencies 323, 340 and 357 GHz (b).

necessitate that the azimuthally collapsed antenna patterns (ACAPs) first sidelobe amplitudes be $\leq$-30 dB. The ACAPs are generated through numerically integrating the individual beams across the azimuth direction. ACAPs for the T beam set in Fig. 8(b) show that this requirement is fulfilled, with the R beam set performing equivalently. The full width half maximum (FWHM) requirement in elevation is $\leq$3 km, which is met by all beams. Beam pointing in the elevation direction is also critical for accurate observations, and the residual pointing offsets from the nominal values reveal good performance with

maximum offsets of the order of < 100 m. Complete power throughput for all beams across the frequency band is $> 98\%$.

V. BEAM PATTERN MEASUREMENTS

The farfield beam patterns of the FPA feed horns have been measured using a submillimetre optical test bench and compared with theoretical predictions - c.f. Fig. **??**. These measurements reveal strong agreement with predictions. Minor disparities in the cross-polar measurements are here attributed to measurement misalignment, with peak measured cross-polar amplitude being under -30 dB across the frequency band.
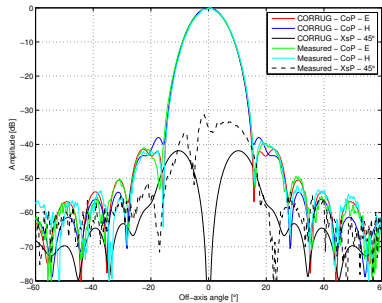
Fig. 9: Measured and simulated copolar and crosspolar amplitude patterns for the STEAMR FPA feed horn at 340 GHz.

A breadboard model of the STEAMR FPA has been synthesised and its optical performance quantified through near field beam pattern measurements. Comparisons between MoM sim-
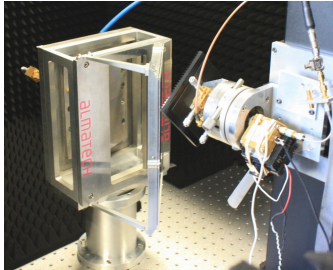
Fig. 10: Optical test bench for STEAMR FPA breadboard, showing arrangement for near field beam pattern measurement.

ulations and beam pattern measurements for the three pixels with highest beam truncation reveal excellent performance of the FPA, with power coupling coefficients integrated between simulations and measurements being $> 98\%$ for all beams tested over the complete bandwidths [11].

VI. CONCLUSIONS

A complete antenna optics scheme for the STEAMR instrument has been presented, whose optical performance meets the imaging requirements of the proposed instrument. The inherent astigmatism of the farfield beams has been corrected optically, thus ensuring optimum imaging. The design for a breadboard FPA, which couples the individual beams from the focal plane to the corresponding feed horns has also been presented as part of the complete optics scheme. This FPA has been synthesised and the results of electromagnetic testing have already shown excellent conformity with theoretical predictions. The complete antenna optics scheme has been modeled in the GRASP

(a)

(b)
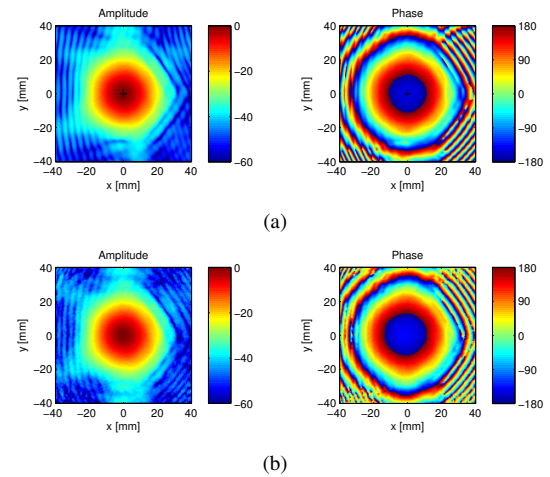
Fig. 11: Sample copolar amplitude and phase patterns for single FPA pixel from MoM simulations (a) and near field beam pattern measurements (b).

software package, and resultant simulations the observing beams conform well within predefined requirements for the antenna.

REFERENCES

[1] (2008, Nov.) PREMIER: Process Exploration through Measurements of Infrared and Millimetre-wave Emitted Radiation. ESA. [Online]. Available: http://esamultimedia.esa.int/docs/SP1313-5-PREMIER.pdf
[2] R. N. Wilson, *Reflecting Telescope Optics I*. Reading, MA: Springer, 1972.
[3] Y. Lo and S. Lee, *Antenna Handbook III: Antenna Applications*, 1st ed. Springer, 1993, vol. 2.
[4] N. Skou and D. L. Vine, *Microwave Radiometer Systems: Design and Analysis*, 2nd ed. Artech House, 2006, vol. 2.
[5] M. Whale, J. Murphy, A. Murk, M. Renker, U. Frisk, and O. Janson, "A compensating anastigmatic submillimetre array imaging system for STEAMR," submitted for publication.
[6] A. Wagner-Gentner, U. Graf, M. Philipp, and D. Rabanus, "A simple method to design astigmatic off-axis mirrors," *Infrared Physics and Technology*, vol. 50, no. 1, pp. 42 – 46, Nov. 2007.
[7] T. Luethi, D. Rabanus, U. U. Graf, C. Granet, and A. Murk, "CHARM - a Compact Heterodyne Array Receiver Module for KOSMA with scalable fully rectective focal plane array optics," in *Proc. 79th Annual Scientific Meeting of the Astronomische Gesellschaft*, vol. 326, no. 7, Cologne, Germany, 2005.
[8] U. U. Graf *et al.*, "SMART: The KOSMA Sub-Millimeter Array Receiver for Two frequencies," in *Proceedings of the SPIE, Millimeter and Submillimeter Detectors for Astronomy*, vol. 4855, 2003, pp. 322 – 329.
[9] P. F. Goldsmith, *Quasioptical Systems*. New York: IEEE Press, 1998.
[10] P. A. S. Cruickshank, D. R. Bolton, D. A. Robertson, R. J. Wylde, and G. M. Smith, "Reducing standing waves in quasi-optical systems by optimal feedhorn design," in *Infrared and Millimeter Waves, 2007 and the 2007 15th International Conference on Terahertz Electronics. IRMMW-THz. Joint 32nd International Conference on*, Sept 2007, pp. 941–942.
[11] M. Renker, M. Whale, A. Murk, J. A. Murphy, and R. Wylde, "Analysis and simulation of edge effects of focal plane array facet reflectors with high filling factor," in *33rd ESA Antenna Workshop on Challenges for Space Antenna Systems*, vol. 4855, ESTEC, Noordwijk, The Netherlands, oct 2011.
[12] M. Renker, M. Whale, and A. Murk, "Antenna simulations and measurements of focal plane array facet reflectors," submitted for publication.

Possible Swedish contribution to the FIRE instrument

A. Emrich[1*], U. Frisk[1], P. Sobis[1], D. Murtagh[2], J, Urban[2], M. Krus[1] and A. Hammar[1]

1 Omnisys Instrument AB, Västra Frölunda, S-42130, Sweden
2 Chalmers University of Technology, Göteborg, Sweden
`* Contact:  ae@omnisys.se, phone +46-31-7343401`
`The work is financed by the Swedish National Space Board.`

Abstract⎯⎯**Currently, a new Mars exploration program for the 2020's, named Mars Exploration with Lander-Orbiter Synergy (MELOS), is being discussed in Japan. One of the orbiters of MELOS is proposed to explore the Martian meteorology and climate system; more specifically, the dust meteorology, water cycle, atmospheric circulation, atmospheric chemistry, and mechanisms of dust storm development.**

A submillimetre wave atmospherice mission sounding instrument with a passive heterodyne spectrometer called Far-InfraRed Experiment (FIRE) for MELOS has been proposed. It consists of a dual polarization 610 GHz channel (H2O, H2O2 and HDO), a 560 GHz channel (12CO and 13CO) as well as a 340 GHz channel (TBC). The front-ends are based on subharmonic mixers coupled to cascaded schottky doublers and active x6 multipliers with power amplification at 70 and 75 GHz for the 560&610 GHz channels. For the 350 GHz channel, only one schottky doubler is needed. A 400 mm antenna is currently presumed with an estimated mass of 0.7 kg.

The back-end consist of high resolution FFT spectrometers with 200 MHz bandwidth and 4096 channels and autocorrelation spectrometers with 2 GHz bandwidth and 1024 channels. The complete radiometer package will have an estimated power consumption of < 40 W with possibility to perform science with less than 20 W in a time multiplexed fashion. Much of the receiver system development will be based on current activities at Omnisys, including the STEAMR instrument development, TERACOMP (557 GHz receiver under FP7 contract) and 500+ GHz activities in collaboration with Chalmers/MC2.

The design of the instrument and test results of different subsystems will be presented at the conference.

Spectrometers for THz space applications

M. Krus[1], S. Andersson[1] and A. Emrich[1*]

1 Omnisys Instrument AB, Västra Frölunda, S-42130, Sweden

* Contact: mk@omnisys.se, phone +46-31-7343401

Abstract——**Omnisys have designed a new generation of FFT spectrometers focused on either deep space missions or broadband applications. For deep space, the FFT is optimised between 100-500 MHz and >2048 channels and with as low power consumptions as 3 W per FFT, using a shared FPGA. The broadband FFT's cover 5 GHz bandwidth with a frequency resolution of more than 64 k channels. The power consumption of broadband FFT is 20 W. Test results will be presented.**

Omnisys also provide autocorrelation based spectrometers with broader bandwidth and less resolution and considerably lower power consumption and mass budgets for a certain bandwidth. Examples of applications using this technology is the STEAMR instrument and it is also considered for the MWS, MWI and ICI instruments on METOP.

GREAT : Successful first year of science operation

Heyminck,S.[1], Graf, U.[2], Güsten, R.[1], Stutzki, J.[2], Hübers, H-W.[3][4], Harthogh, P.[5], Bell, A.[1], Bielau, F.[2], Busch, A.[1], Castenholz, C.[1], Castenholz, R.[1], Henseler, A.[1], Honingh, C.E.[2], Jacobs, K.[2], Jarchow, C.[5], Kasemann, C.[1], Klein, B.[1], Klein, T.[1], Korsitzky, H.[3], Krämer, I.[1], Leinz, C.[1], Lengowski, M.[3], Meyer, K.[1], Moratschke, D.[2], Philipp, M.[2], Pütz, P.[2], Rabanus, D.[2], Ricken, O.[1], Risacher, C.[1], Schieder, R.[2], Schmidt, B.[2], Schneider, G.[1], Schultz, M.[2], Semenov, A.[3], Steinmetz, E.[4], van der Wal, P.[1], Wagner, A.[2], Wiesemeyer, H.[1], Wunsch, A.[1], Xing, G.[2]

1 -- Max-Planck-Institut für Radioastronomie, Auf dem Hügel 69, 53121 Bonn, Germany
2 -- I. Physikalisches Institut der Universität zu Köln, Zülpicher Straße 77, 50937 Köln, Germany
3 -- Deutsches Zentrum für Luft- und Raumfahrt, Institut für Planetenforschung, Rutherfordstr. 2, Berlin, Germany
4 -- Institut für Optik und Atomare Physik, Technische Universität Berlin, Hardenbergstraße 36, Germany
5 -- Max-Planck-Institut für Sonnensystemforschung, Max-Planck-Straße 2, 37191 Katlenburg-Lindau, Germany

* Contact: crisache@mpifr.de, phone +49-228-525 338

Abstract—GREAT, the German REceiver for Astronomy at Terahertz frequencies, is a modular dual-color heterodyne instrument for the Stratospheric Observatory for Infrared Astronomy (SOFIA). First light was recorded during the SOFIA observatory characterization flight #4 on April 1, 2011. Since then, receiver system showed state-of-the art performance on more than a dozen science flights.

A collection of three frequency channels (L1: 1.25-1.53 THz, L2: 1.82-1.91THz and M: 2.51 THz) has been commissioned and operated so far. Two of them form a flight configuration and can take data simultaneously. The commissioning of our M-Band channel in July 2011 impressively demonstrated the flexibility offered by a PI instrument like GREAT to fly latest technologies only weeks after they become available. We present the instrument as operated in 2011, its performance in flight, and give an outlook on the upcoming developments for the 2012/13 observing cycle #1.

Extension of GREAT into a first heterodyne array for far infrared spectroscopy with SOFIA

C. Risacher[1*], S. Heyminck[1], T. Klein[1], I. Camara[1], R. Guesten[1], U. Graf[2], K. Jakobs[2], N. Honingh[2], J. Stutzki[2], H-W. Hübers[3], H. Richter[3], and A. Semenov[1]

1 Max Planck Institut für Radioastronomie *, Bonn, Germany, 53212, Germany
2 Physikalisches Institut des Universitaet zu Koeln, Köln Germany
3 German Aerospace Center (DLR), Berlin, Germany
* Contact: crisache@mpifr.de, phone +49-228-525 338

Abstract——**The NASA-DLR airborne observatory SOFIA started routine operations in 2011. The current German PI instrument (GREAT) consists of heterodyne receivers observing in selected ranges in the frequency window 1250-2700 GHz. The instrument is built in a modular fashion and allows the parallel operation using two separate cryostats easily interchangeable. The current instruments are single-pixel receivers and are cooled using liquid Helium cryostats. This paper presents two additional new cryostats, which will be cooled using a closed–cycle Pulse Tube coolers, and will consist of small arrays of HEB mixers. The first receiver will observe in the 1.9-2.5 THz range using dual polarization 7-pixel HEB arrays. The local oscillator will be based on photonic mixers. The second receiver will observe the O[I] line at 4.7 THz. The local oscillator will use quantum cascade lasers.**

We will present the design, and status of the fabrication of those receivers, which are planned to be installed onboard SOFIA in the coming 2 years.

Development of a 220-GHz Schottky Diode Subharmonic Mixer

Zhe Chen, Bo Zhang, Xiaofan Yang, and Yong Fan

School of Electronic Engineering
University of Electronic Science and Technology of China
Chengdu, Sichuan, 611731, China

E-mail: zhechen_uestc@126.com

Abstract- **In this paper, the design of a waveguide fix-tuned 220GHz subharmonically pumped mixer using Schottky planar diodes is demonstrated. It is supposed to be applied in an experimental short-range and high-speed communication system. The anti-parallel pair of planar Schottky diodes from the Rutherford Appleton Laboratory (RAL) was flip-chip mounted and soldered onto a suspended 75µm-thick quartz microstrip circuit. Initial measurements yielded a double sideband (DSB) equivalent noise temperature below 2500K and conversion loss less than 10dB over the range from 200GHz to 235GHz with the IF frequency fixed at around 3GHz and LO power lower than 6mW. The optimum DSB noise temperature of 1368K and conversion loss of 6.5dB were obtained at 204GHz.**

Index Terms–**Planar Schottky diodes, subharmonic mixer, 220GHz.**

I. INTRODUCTION

Terahertz (THz) waves fall between 100GHz to l0THz in the frequency region of the electromagnetic spectrum. Their corresponding wavelengths range from 30cm to 30µm. Sandwiched between the millimeter wave and light wave range, this field possesses some valuable properties and has recently elicited increasing interest [1-3].

In the lower range of THz frequency band, there are several useful frequencies. 220 GHz is an atmospheric window frequency, thus it offers a large potential to implement short-range and high-speed communication. In most THz applications including communication application, the receiving of THz waves is bound to be involved. Since state-of-the-art electronic amplifiers are rarely reported in frequencies above 300GHz, THz receivers are mostly of the heterodyne type, which employs mixers as the first stage. So their performance plays a critical role in the overall receivers. Mixers based on Schottky diodes have the advantage of operating well at either cryogenic or room temperatures, although not with the sensitivity of SIS or HEB mixers applied in low temperature environment for radio astronomy application. Due to this, heterodyne receivers incorporating Schottky diode mixers are simpler to integrate into compact systems. They are also easy for taking long term or repeated measurements since they operate at room temperature. In a word, for our application, Schottky diode mixers are able to be regarded as a flexible and reliable device with moderate performance at THz band. Mixers with subharmonic pump utilizing an anti-parallel pair of Schottky diodes are widely applied in THz band, since the LO frequency is about only half of that in the corresponding fundamentally pumped ones, which could greatly ease the requirement for LO source.

This paper presents the development of a waveguide fix-tuned 220GHz subharmonically pumped mixer using Schottky planar diodes as a key component of an experimental short-range and high-speed communication system in the future.

II. MIXER DESIGN AND ITS PERFORMANCE

The Schottky diodes play a vital role in the performance of mixers. For the past ten years, planar Schottky diode technology has made great progress. The diodes applied in this paper are from RAL, featuring a low parasitic capacitance and series resistance [4] and in an anti-parallel configuration. The architecture of the subharmonic mixer based on a traditional E-plane split-block waveguide architecture [5] is showed in Fig.1. The architecture is also partly in light of B. Thomas's design [6]. A grounded RF probe, the antiparallel diode pair in series with the transmission line, the LO filter to block the RF signal, a probe crossing the LO waveguide and the IF filter are included. The pair of planar diodes is flipped-chip mounted onto the suspended 75µm-thick quartz microstrip. The gold track at the RF end is grounded by contacting the RF waveguide wall, which provides the return ground for DC current from any imbalance between the diode pair without biasing the diode pair asymmetrically [7]. At the other end, the microstrip circuit is connected to a K-connector as the IF output port. The reduced height waveguide configuration at both RF and LO ports is for broadband operation.

The non-linear behavior of the diodes was analyzed using the standard diode model provided in the Advanced Design System (ADS) suite [8]. The performance of the mixer was simulated using a combination of Agilent's ADS and Ansoft's HFSS [9]. The electromagnetic (EM) fields of passive elements of the mixer were solved in HFSS. The EM simulated

results were then imported to ADS to perform the circuit optimization.
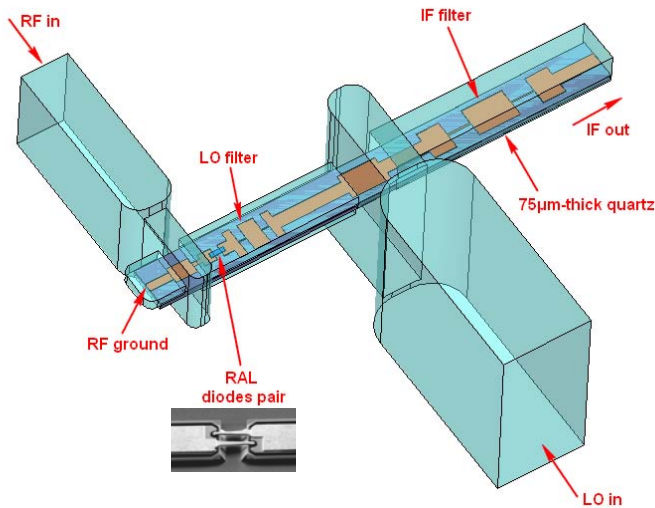
Fig. 1. The architecture of the mixer

Fig. 2 is the inside view of the assembled bottom block and the appearance of the mixer is shown in Fig. 3. The fabrication and measurement of the mixer were also carried out at RAL. The simulated DSB conversion loss is shown in Fig. 4 alongside the measured DSB conversion loss. The LO fundamental source was provided by a 0.05-20GHz synthesizer, which was used to drive a commercial sextupler followed by a power amplifier, both from Radiometer Physics GmbH (RPG). The output power of the LO source chain was calibrated with an Erickson power meter. The mixer was measured using the classic Y-factor method. The equivalent noise temperature of the receiver was measured by presenting alternatively a room temperature and a liquid nitrogen-cooled blackbody in front of the feed-horn. The optimum DSB mixer noise temperature was measured as 1368 K at 204GHz with LO power of 5mW.
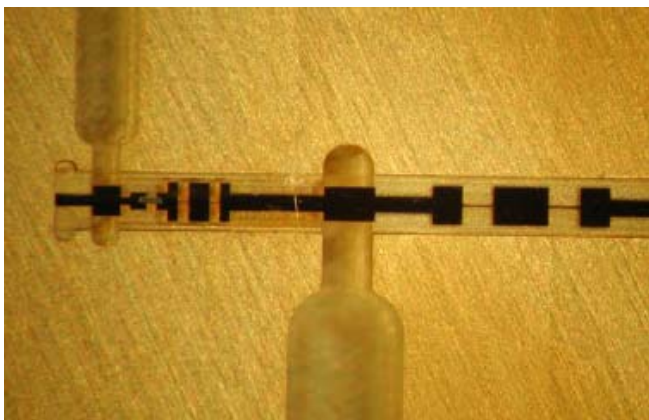
Fig. 2. The inside view of the assembled bottom block
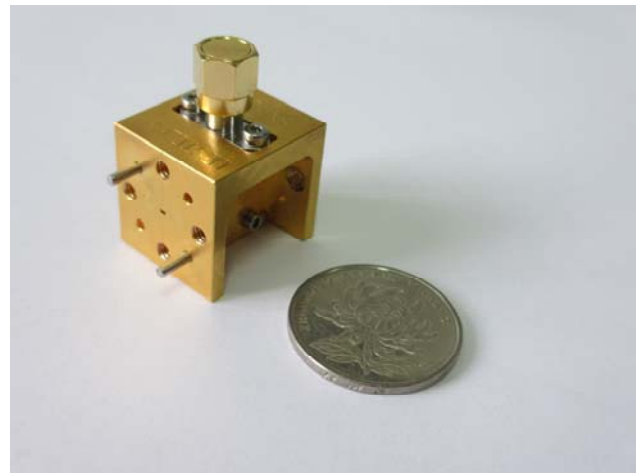
Fig. 3. The photograph of the fabricated mixer
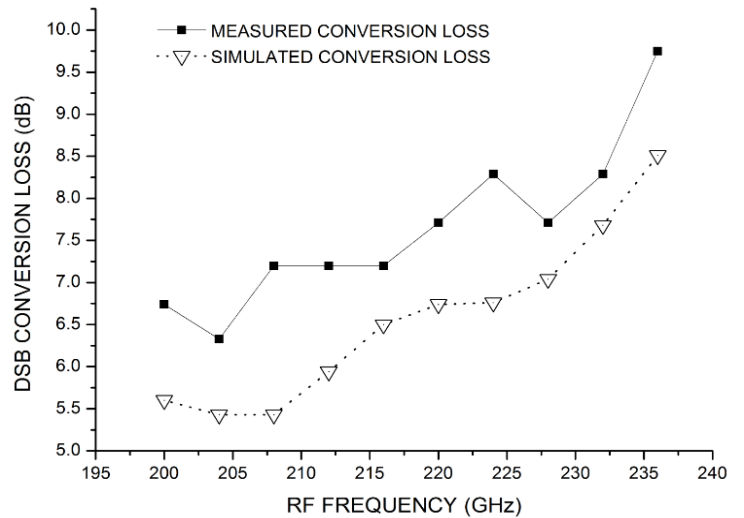
Fig. 4. The mixer's simulated and measured performance

III. CONCLUSION

This paper presents the development of a 220-GHz subharmonic mixer for a future communication system based on RAL's planar Schottky diodes. Good measured noise and conversion loss performance has been obtained. The measurement results are in accord with the simulation prediction. Work is still in progress to optimize the bandwidth and noise and conversion loss performance. In the future, the methodology for designing this mixer will contribute to the development of terahertz receivers at higher frequencies.

REFERENCES

[1] P.H. Siegel, "Terahertz Technology," *IEEE Trans. Microw. Theory Tech.*, vol. 50, no. 3, pp. 910-928, Mar. 2002.

[2] I. Hosako, N. Sekine, "At the dawn of a new era in terahertz technology," *Proceedings of IEEE,* vol. 95, no. 8, pp. 1611-1623, Aug. 2007.

[3] P. de Maagt, P. H. Bolivar, "Terahertz science, engineering and systems – from space to Earth application," in K. Chang, (ed.), "Encyclopedia of RF and microwave engineering" (Wiley, 2005), vol. 6, pp. 5175-5194.

[4] B. Alderman, H. Sanghera, C. Price, B. Thomas, and D.N. Matheson "Fabrication of Reproducible Air-Bridged Schottky Diodes for use at 200 GHz," *Proceedings of the joint 32nd IR and MMwave Conference & 15th THz Electronics 2007*, Cardiff, Sept. 2007, pp. 848-849.

[5] A.V. Räisänen, D. Choudhury, R. J. Dengler, J. E. Oswald, and P. Siegel, "A novel split-waveguide mount design for millimeter- and submillimeter-wave frequency multipliers and harmonic mixers," *IEEE Microw. Guided Wave Lett.*, vol. 3, no. 10, pp. 369-371, Oct. 1993.

[6] B. Thomas, A. Maestrini, and G. Beaudin, "A low-noise fixed-tuned 300-360-GHz sub-harmonic mixer using planar Schottky diodes," *IEEE Microw. Wirel. Compon. Lett.*, vol. 15, no. 12, pp. 865-867, Dec. 2005.

[7] S. Marsh, B. Alderman, D. Matheson, and P. de Maagt, "Design of low-cost 183 GHz subharmonic mixers for commercial applications," *IET Circuit Devices Syst.*, vol. 1, no.1, pp. 1-6, Feb. 2007.

[8] *Advanced Design System, Version 2009*, 2009.

[9] *High Frequency Simulation Software*, V12. Pittsburgh, PA: Ansoft Corporation, 2009

First results of a 1.2 THz MMIC sub-harmonic mixer based GaAs Schottky diodes for planetary atmospheric remote sensing

B. Thomas[1&2], J. Siles[1*], E. Schlecht[1], A. Maestrini[3], G. Chattopadhyay[1], C. Lee[1], C. Jung[1], I. Mehdi[1], and S. Gulkis[1]

1 NASA - Jet Propulsion Laboratory, California Institute of Technology, Pasadena, CA, USA
2 Radiometer Physics GmbH, Meckenheim, Germany
3 Université Pierre et Marie Curie-Paris 6, LERMA, Paris, France
`* Contact:  jose.v.siles@jpl.nasa.gov, phone +1-818-354-4006`

Abstract- **We present here the first measurement results of a 1200 GHz heterodyne receiver front-end prototype based on this Schottky GaAs membrane technology. The 1200 GHz sub-harmonic mixer design, previously reported, uses a suspended MMIC GaAs membrane that feature a balanced pair of planar Schottky diodes and an on-chip MIM capacitor for DC forward biasing capabilities. The possibility to bias the sub-harmonic mixer is very important in order to release constraints on the amount of LO power required at 600 GHz. Measurement results show a DSB mixer noise temperature better than 6000 K and DSB mixer conversion losses better than 15 dB are achieved in the RF range 1130 GHz to 1220 GHz. The estimated LO input power available is between 1 mW and 1.5 mW. For this relatively low LO power levels, the optimum bias voltage is approx. 0.85 V with a rectifying current of 170 uA. These performance values are in agreement with predictions, but it is believed that the performance can be improved by selecting devices with better electrical characteristics and increasing the amount of LO power available.**

I. INTRODUCTION

A Submillimetre Wave Instrument (SWI) has been proposed as a potential payload instrument for the JUICE mission (JUpiter ICy moon Explorer, the formerly joint ESA/NASA mission called EJSM) [1]. The primary scientific objectives are to investigate the exchange mechanisms in the middle atmosphere of Jupiter by the remote sensing of key molecular species such as the water line at 557 GHz and the methane line at 1256 GHz. As a secondary objective, it would also investigate the exosphere/ionosphere dynamics and thermo-physical surface properties of Jupiter's moons. The proposed radiometric and spectroscopic instrument features two heterodyne channels, one centered around 560 GHz close to the water line, and another one centered around 1200 GHz close to the methane line.

Significant effort has already been done in order to demonstrate high sensitivity and broad bandwidths at frequencies around 560 GHz, using MMIC GaAs membrane Schottky diode based sub-harmonic mixer. Moreover, previous developments of local oscillators for the HIFI instruments onboard HERSCHEL satellite using similar JPL Schottky technology enabled few mW of output power to be available from 540 to 640 GHz [2]. Building on these achievement, the successful demonstration of an all-solid-state, semiconductor

based heterodyne receiver channel front-end operating at room temperature or compatible with passive cooling temperatures in space (approx. 100 K) with high enough sensitivity and covering the 1100 to 1300 GHz range is now possible.

The 1200 GHz channel is under development at JPL. The receiver architecture is directly inherited from the HIFI project for the LO generation at 600 GHz. Using identical MMIC GaAs membrane process, a novel 1200 GHz MMIC sub-harmonic mixer has been designed, and is presented here.
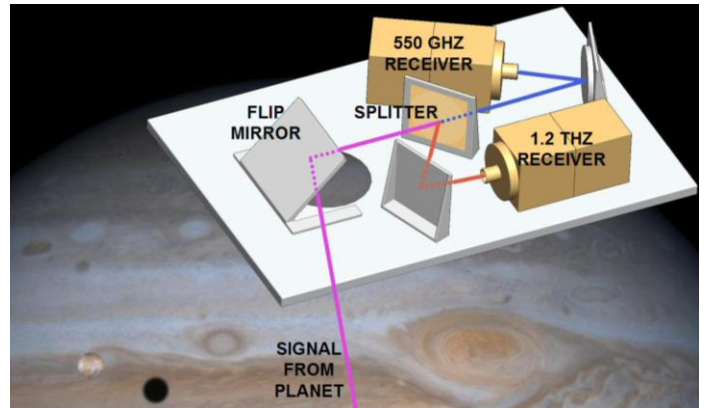
Fig.1: artistic representation of the SWI Front-End dual-channels receiver baseplate with a 557 GHz receiver channel, and a 1.2 THz receiver channel.

II. 1.2 THz MIXER DESIGN

The 1200 GHz sub-harmonic mixer design has been previously described for a scaled version at 874 GHz [3]. The design methodology and prediction tools are described in [4]. It's a balanced design with the diodes placed along the cross-section of the channel. It creates an open loop at the second harmonic of the Local Oscillator signal, whose propagation is cut-off by the channel cross-section dimensions, as for a balanced tripler. This topology allows for a good phase balance between both diodes at RF and LO frequencies, without the need to use very short fingers as for an anti-parallel configuration, therefore relaxing some constraints on the diode fabrication process at these high frequencies.
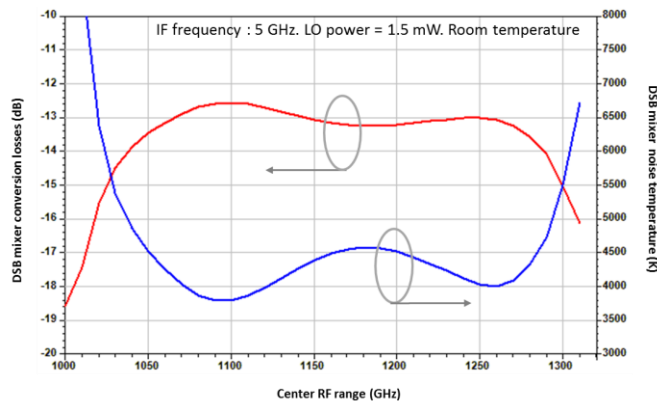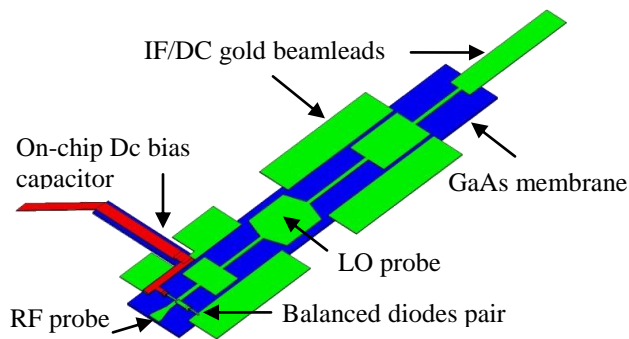
Fig.1. Top: 3D view of the MMIC 1200 GHz sub-harmonic mixer based on MMIC GaAs membrane Schottky diodes, including the on-chip DC bias capacitor (in red). Bottom: Predicted performance of the MMIC 1200 GHz sub-harmonic mixer at room temperature. IF is fixed to 5 GHz, LO bias is set to 1.5 mW and mixer is DC forward bias to 0.5V per anode.

Moreover, the RF and LO grounding of the diodes is done with the beamleads which are located on each side of the circuit, allowing for a very short distance between the ground and the diodes, therefore increasing the RF, LO and IF bandwidth significantly. In this topology, the diodes are also very close to the RF waveguide which contributes to reduce the suspended stripline transmission losses between the diodes and the RF waveguide.

The optimization and simulation of the mixer is done using a combination of 3D-EM simulations using HFSS (Ansys) [5] and ADS (Agilent) [6]. As shown in Fig. 1, the predicted DSB mixer noise temperature of the mixer is between 4000 and 4500 K at room temperature in the frequency range 1050 to 1280 GHz, corresponding to DSB conversion losses between 12.5 dB and 14 dB approximately. With an available input LO power increasing to 4-6 mW, simulation results show that it is possible to improve the mixer conversion losses by 1 or 2 dB, and the DSB mixer noise temperature by up to 1000 K.

III. 1.2 THz MIXER FABRICATION

The 1.2 THz sub-harmonic mixer relies on the MMIC GaAs and gold beamleads "Momed" circuit fabrication process developed by JPL in the framework of previous space

instruments such as EOS-MLS and Herschel-HIFI [7]. An MIM on-chip capacitor allows to bias the diodes in-series. The MMIC, shown in Fig. 2, is suspended along the cross-waveguides channel by clamping the ground beamleads when closing both halves of the split waveguide block.

The block shown in Fig. 3 has been machined at JPL, and includes an SMA connector for DC biasing, a K-connector for IF output, and an integral diagonal feed horn for RF testing. The LO connection is done by a precision UG387 waveguide flange.
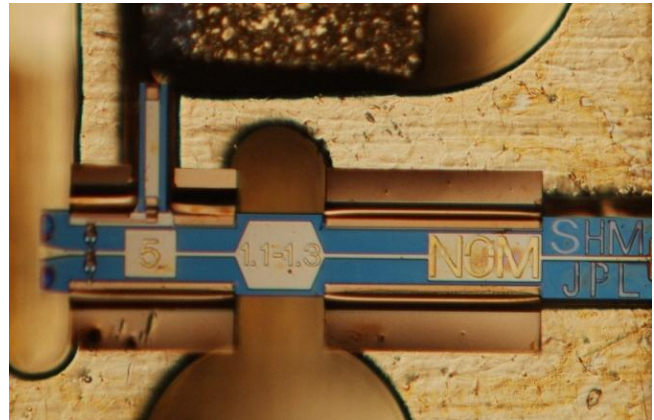
Fig.2. View of the 1.2 THz MMIC membrane sub-harmonic mixer mounted inside the lower half of the split-waveguide block.

IV. 1.2 THz RECEIVER CHANNEL TEST RESULTS

The complete 1200 GHz receiver channel includes a 600 GHz LO source based on MMIC membrane 200 GHz doubler and 600 GHz tripler inherited from the HIFI Local Oscillator developments [2][8], and a 1100-1300 GHz MMIC membrane biasable sub-harmonic mixer. The Local Oscillator can output between 1.5 mW and 2 mW of power at room temperature, in the frequency range 550-605 GHz.

Fig.3. View of the complete 1.2 THz receiver chain, including a W-band power amplifier stage, a 200 GHz doubler, a 300 GHz tripler and a 1200 GHz sub-harmonic mixer with integrated feedhorn antenna.

The measurements are performed at room temperature in laboratory environment conditions.
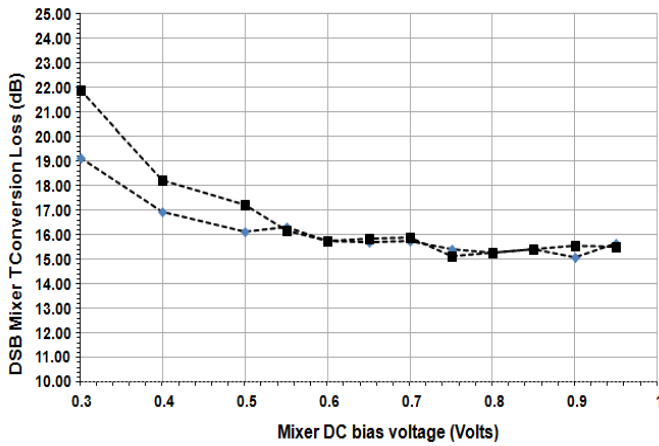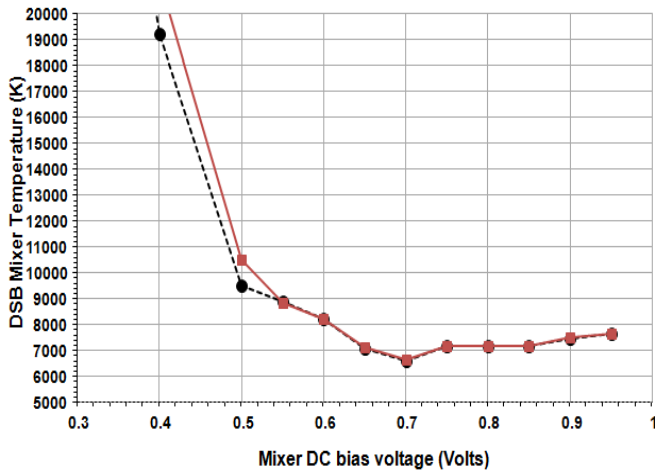
Fig.3. Preliminary measurement results of the 1200 GHz sub-harmonic mixer VS DC bias voltage of both diodes in series. Top: DSB mixer noise temperature. Bottom: DSB mixer conversion losses for two blocks under test. Available LO input power: 1-1.5 mW. Center frequency: 1193 GHz.

Preliminary results obtained at room temperature are shown in Fig. 4. For an input power available limited to 1.5 mW max., the optimum mixer DC biasing voltage is estimated at 0.7-0.85 V, corresponding to a DC bias voltage per diode of 0.35-0.45 V, in agreement with the simulations. DSB mixer noise temperature better than 5000 K and DSB conversion losses better than 15 dB have already been obtained at different frequencies within the 1100-1220 GHz band.

Further tests are on-going to characterize the mixer performances over the entire 1100-1300 GHz frequency range, in vacuum environment at the temperatures compatible with passive cooling in space.

CONCLUSION

Future sub-millimeter wave instruments for the remote sensing of planets' atmospheres such as the Earth, Mars, Jupiter and Saturn will greatly benefit from the recent advances in receiver sensitivity and integration up to 1200 GHz, as described in this paper. The development of MMIC Schottky technology and powerful Local Oscillator sources widely tunable and operating at room temperature are pivotal for THz receiver development.

ACKNOWLEDGMENT

REFERENCES

[1] P. Hartogh, et al., "*Sub-millimeter Wave Instrument for EJSM*", EJSM Instrument Workshop, July 2009, Maryland, USA.

[2] A. Maestrini, et al., "A 540-640 GHz High Efficiency Four Anode Frequency Tripler", *IEEE Transactions on Microwave Theory and Techniques*, Vol. 53, pp. 2835-2843, September 2005.

[3] B. Thomas, et al. "Design of an 874 GHz Biasable Sub-Harmonic Mixer Based on MMIC Membrane Planar Schottky Diodes", *proceedings of the 33rd International Conference on Infrared, Millimeter, and Terahertz Waves*, California Institute of Technology, Pasadena, California, September 15-19, 2008.

[4] B. Thomas, et al., "THz cooled MMIC Schottky mixer design for the remote sensing of outer planets' atmospheres", *proceedings of the joint 5th ESA Workshop on Millimetre Wave Technology and Applications & 31st ESA Antenna Workshop*, pp. 101-108, ESTEC, Noordwijk, The Netherlands, May 18-20, 2009.

[5] *High Frequency Simulation Software,* v11.0, Ansys Corporation, Pittsburgh, PA, USA.

[6] *Advanced Design System, Agilent Technology*, Palo Alto, CA, USA.

[7] S. Martin, et al., "Fabrication of 200 to 2700 GHz multiplier devices using GaAs and metal membranes", *in IEEE MTT-S Int. Microwave Symp. Dig.*, 2001, vol. 3, pp. 1641-1644.

[8] E. Schelcht, et al., "A High-Power wideband Cryogenic 200 GHz Schottky 'Substrateless' Multiplier: Modeling, Design and Results", proceedings of the 9th Int. Conf. on Terahertz Electronics, Charlottesville, VA, USA, Oct. 2001.

A Performance Comparison of Discrete and Integrated Sub-Harmonic Schottky Diode Mixers at 664GHz

H. Wang[1*], H. Sanghera[1], B. Alderman[1], S. P. Rea[1], B. N. Ellison[1], and P. de Maagt[2]

1 STFC Rutherford Appleton Laboratory, Harwell Oxford, Didcot, OX11 0QX, UK
[2]ESTEC, European Space Agency, P.O. Box 299, 2200AG Noordwijk ZH, The Netherlands
* Contact: hui.wang@stfc.ac.uk, phone +44-1235-446343

Abstract— **This paper compares the performance of three sub-harmonic mixer designs operating over the spectral band 640-690 GHz. The mixers employ either discrete GaAs Schottky diodes soldered on quartz substrate or integrated GaAs membrane Schottky diode technology. Schottky diode-based sub-millimeter wave receivers are a key enabling technology for remote sensing of the Earth. For example, the Ice Cloud Imager (ICI), part of the European Post-EPS mission currently undergoing Phase A/B1 study, is dedicated to the observation and characterization of ice clouds in spectral bands up to 664GHz. Furthermore, both passive and active imaging systems operating at 664 GHz are being widely developed for security applications.**

In this context, three mixers were designed for the 640-690 GHz range. The first mixer uses a discrete anti-parallel pair of Schottky diodes on an 8 μm GaAs substrate with associated matching circuitry on a 25 μm quartz substrate. The design is shown in the top left figure below. Simulations predict a minimum double sideband mixer conversion loss of 8.8 dB at 664 GHz, with a local oscillator power requirement of 5mW. is below 10 dB over the frequency range 640–690 GHz. The second and third mixers are both based on integrated 8 μm thick GaAs membrane technology. The mixer circuit is composed of a pair of Schottky diodes in a balanced series configuration integrated on an 8 um thick GaAs membrane matching circuit. The same mixer design can either be used as a biasless version, top right figure, or a biasable mixer with integrated on-chip capacitor, as shown bottom centre. A DC voltage can be applied on both diodes via the on-chip capacitor in order to reduce the local oscillator power requirement. Simulations predict a reduction in LO power of 40% with negligible degradation in mixer performance.

All three mixers are being manufactured at the Rutherford Appleton Laboratory. This is also our first demonstration of an integrated circuit with on-chip capacitor on GaAs membrane. Full test results will be presented in the paper and presentation.
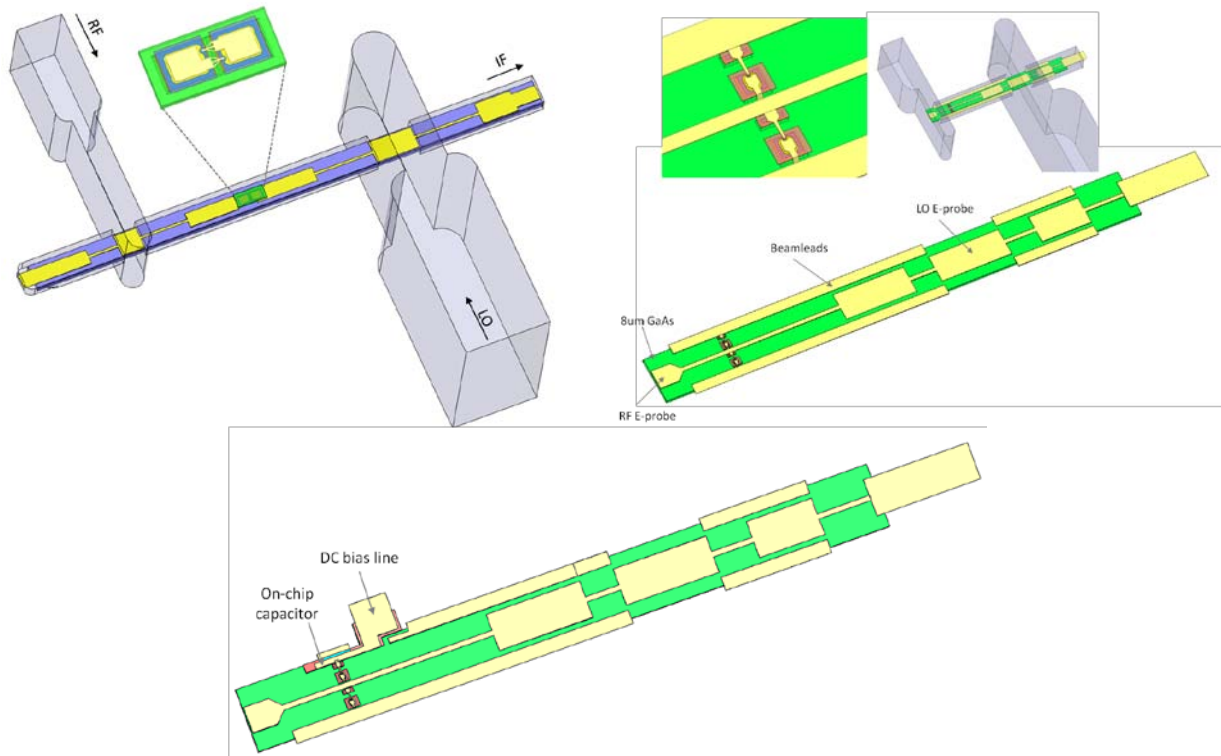
Figure 1: GaAs Schottky diode based subharmonic mixers at 664GHz. Top right, discrete anti-parallel diodes on quartz; top left, integrated series diodes on a GaAs membrane and, bottom, biased diodes on a GaAs membrane with an integrated on-chip capacitor.

129 GHz SIS Mixer Receiver for Korean VLBI Network

Jung-Won Lee[1], Ming-Jye Wang[2] , Sooyeon Kim[1], Chao-Te Li[2], Tse-Jun Chen[2], Yong-Woo Kang[1],
Wei-Chun Lu[2] , Sheng-Cai Shi[3] & Seog-Tae Han[1]

[1] Korea Astronomy and Space Science Institute, Daejeon, Korea
[2] Academia Sinica Institute of Astronomy and Astrophysics, Taipei, R.O. China
[3] Purple Mountain Observatory, Chinese Academy of Science, Nanjing, P. R. China

We have developed superconducting mixer receivers for 129 GHz VLBI observation in Korean VLBI Network(KVN). The developed mixer has a radial waveguide probe with simple transmission line LC transformer as a tuning circuit to its 5 series-connected junctions, which can have 125-165 GHz as operation RF frequency. For IF signal path a high impedance quarter-wavelength line connects the probe to one end of symmetric RF chokes. DSB receiver noise of the mixer was about 40 K over 4-6 GHz IF band whereas we achieved about uncorrected SSB noise temperature of 70 K and better than 10dB IRR in 2SB configuration with 8-10 GHz IF band. Insert-type receiver cartridges using the mixers have been assembled for all three KVN stations.

Development of a New Multi-Beam Array 2SB Receiver in 100 GHz Band for the NRO 45-m Radio Telescope

T. Nakajima, K. Kimura, T. Katase, M. Koyano, H. Inoue, T. Sakai, H. Iwashita, C. Miyazawa,

S. Asayama, N. Kuno, H. Ogawa, T. Onishi, R. Kawabe, and T. Noguchi

Abstract— **We have developed a new multi-beam array receiver in 100-GHz band for the 45-m millimeter wave telescope located at Nobeyama Radio Observatory, Japan. This receiver has four (=2×2) beams and uses a ortho-mode transducer and two sideband-separating (2SB) mixers, both of which are based on the waveguide type for each beam. This new receiver is named "FOREST" (FOur-beam REceiver System for the 45-m Telescope). The RF range is 80-116 GHz and the IF ranges are 4.0-8.0 GHz for LSB and 4.0-12.0 GHz for USB. We have also developed new optics for the receiver and new IF chains for the 16 IF signals obtained by the receiver system. The SSB receiver noise temperature with 4.0-8.0 GHz IF are measured to be lower than approximately 50 K over the RF range of 80-116 GHz. The new receiver system has been installed in the telescope, and we successfully detected the ^{12}CO (J=1-0) lines toward IRC+10216 in May 2011. These are the first astronomical observations with the waveguide-type dual-polarization sideband-separating multi-beam array receiver system in 100-GHz band.**

Index Terms—**Radio Astronomy, Receivers, Superconducting microwave devices**

Fig. 1. Photograph of the 45-m telescope in NRO.

I. INTRODUCTION

THE 45-m telescope (Fig.1) is located at Nobeyama Radio Observatory (NRO) in Nagano, Japan and is one of the largest millimeter-wave telescope in the world. The 45-m telescope is equipped with low-noise high electron mobility transistor (HEMT) amplifier and superconductor-insulator-superconductor (SIS) receivers covering the observing frequency range of 20 to 116 GHz, along with powerful spectral-line and continuum back-ends. Scientific outcomes

T. Nakajima is with Nagoya University, Furo-cho, Chikusa-ku, Nagoya, Aichi 464-8601, Japan, on leave from National Astronomical Observatory of Japan (e-mail: nakajima@stelab.nagoya-u.ac.jp).

H. Iwashita, C. Miyazawa, S. Asayama, N. Kuno, R. Kawabe, and T. Noguchi are with National Astronomical Observatory of Japan, 2-21-1 Osawa, Mitaka, Tokyo 181-8588, Japan.

K. Kimura, T. Katase, M. Koyano, H. Ogawa, and T. Onishi are with Osaka Prefecture University, 1-1 Gakuen-cho, Naka-ku, Sakai, Osaka 599-8531, Japan.

H.Inoue, and T.Sakai are with the University of Tokyo, 2-21-1 Osawa, Mitaka, Tokyo 181-0015, Japan.

from this instrument include discoveries of a super-massive black hole [1][2] as well as finding of a number of interstellar molecules [3][4], and cover a wide range of research fields, such as formation of stars and planetary systems, the structure and activity of galaxies, and interstellar chemistry. Thus, the 45-m telescope is one of the most important millimeter wave single dish telescope in the ALMA era. The 45-m telescope has undergone a major upgrade, with an installation of three new 100-GHz band receivers [5][6], an intermediate frequency (IF) transmission system, an Analogue-to-Digital Converter (ADC) with a sampling rate of 4 GHz, and a new 32 GHz wide spectrometer [7]. These instruments are called "new observation system".

The 100-GHz band SIS receivers are the most important ones for this telescope, because they cover the highest frequency range of this telescope and also there are fundamental transitions of carbon-monoxide (CO) line in this band. Two type SIS receivers in 100-GHz band are operated in the old observation system. One is S80/S100, which is single-beam, one-polarization, and single-sideband (SSB) operation mode. Another one is BEARS (SIS 25-BEam Array Receiver System). This receiver is 25 multi-beam, one-polarization, and double-sideband (DSB) operation mode [8][9]. However, both of the receivers were developed more than 10 years ago, thus the

receiver noise temperatures are higher than the other receivers in 100 GHz band in the world. Therefore, we are developing three type new sideband separating (2SB) SIS receivers in new observation system. The single-beam receiver named T100 [5], the 2-beam receiver named TZ [6], and new multi-beam array receiver named FOREST. In the present paper, we describe the new multi-beam array receiver and demonstrate its performance.

II. OPTICS
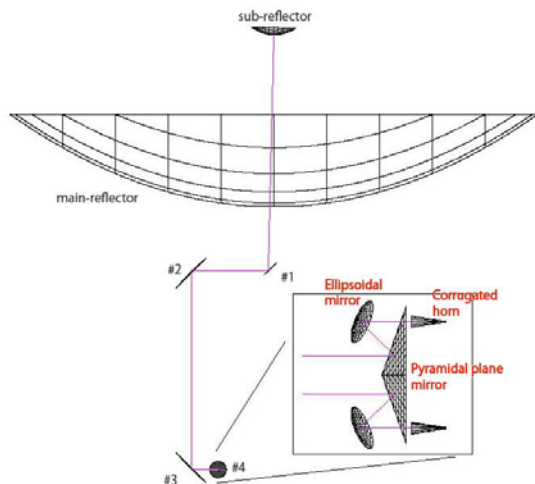
Fig. 2. Optical design of the 45-m telescope.

A. Optical Design

We have designed the receiver optics adapted the antenna optics. We used the method of both Gaussian optics and physical optics to design the receiver optics such as an ellipsoidal mirror and a corrugated feed horn. Fig.2 shows the design of the receiver optics. This receiver has four (=2x2) beams, which has 44″ of beam separation. The radio frequency
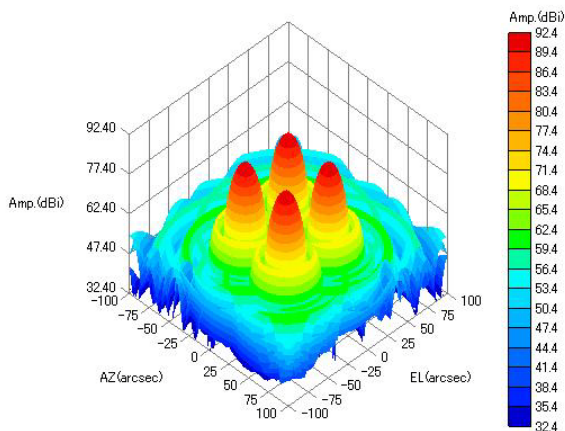
(RF) signal is split to four-way by the plane mirror shaped pyramidal structure at the center and is focused by the ellipsoidal mirror to each horn.

Fig.3 shows the antenna beam radiation. Aperture efficiency is calculated about 0.76 at 100 GHz without surface error, ohmic loss, blocking in this calculation.

B. Corrugated Horn

Corrugated horns are commonly used with reflector antenna systems. Because corrugated horns can reduce the edge diffraction, improved pattern symmetry and reduced cross-polarization can be obtained [10]. Such improved performance was needed for a horn that is to be used over a wide range of the RF frequency. We repeatedly calculated the appropriate corrugation pattern from the basic design. As a result, we obtained a return loss lower than -25 dB, a maximum cross-polarization level lower than -25 dB, and good similarity between the calculated beam profiles of the E-plane and H-plane. We fabricated the horn using the direct-dig method, rather than the electro-forming method [11].

III. RECEIVER

A. Receiver Configuration

The 3D CAD image of the receiver system is shown in Fig.4. This receiver is composed of an ortho-mode transducer (OMT) and two 2SB mixers, which are both based on a waveguide technique [12], and an IF quadrature hybrid in each beam. The RF signal is down converted to 6 GHz band using 2SB mixers. We can obtain 16 IF signals independently and simultaneously. The IF band width of USB and LSB are 8 GHz (4-12 GHz) and 4 GHz (4-8 GHz), respectively. The SIS junctions adopted herein were developed at the Advanced Technology Center (ATC) of NAOJ. A four-series array was composed of Nb/AlOx/Nb junctions. The reason for using the series junction is that a wider bandwidth of RF frequency can be achieved. Moreover, the series junction barely saturates and the intensity can be calibrated with high accuracy [13]. We designed new

Fig. 3. Four beam antenna radiation.
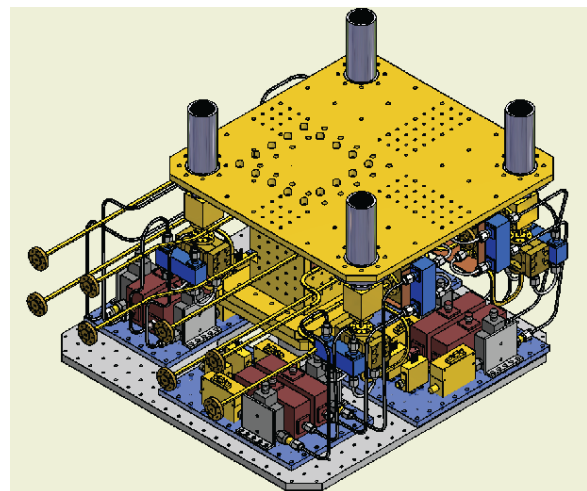
Fig. 4. CAD image of the receiver components.
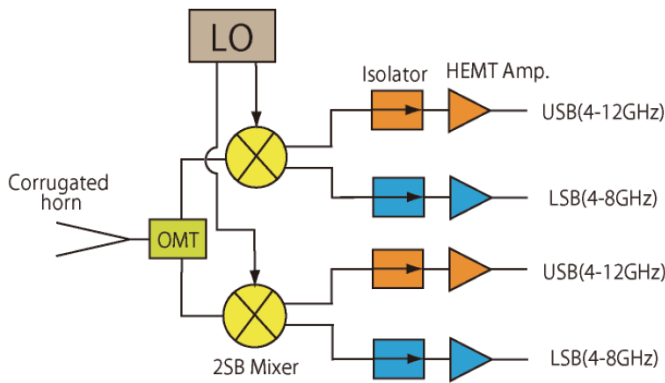
Fig. 5. Block diagram of 1-beam components.

wave-guide type OMT with wide frequency band. The OMT consists of a square to smooth taper double-ridge transition guide followed by a Bφifot type junction of two side arms with central guide [14].

The block diagram of 1-beam components is shown in Fig.5. We can obtain 4 IF signals independently and simul- taneously. The IF frequency ranges are 4-8 GHz for LSB and 4-12 GHz for USB. Thus, we can observe ^{12}CO (J=1-0), ^{13}CO (J=1-0) and C^{18}O (J=1-0) lines simultaneously.

B. Receiver Performance

The noise temperature of the 2SB receiver was measured by a standard Y-factor method. The DSB receiver noise temperatures were including the noise contribution from the vacuum window, the feed horn, and the IF amplifier chain approximately 20~30 K over the LO frequency range of 80-115 GHz, which corresponds to 4-5 hf / k. The SSB receiver noise temperatures of each sideband were measured to be lower than approximately 50 K over the RF frequency range of 85-115 GHz (Fig.6).
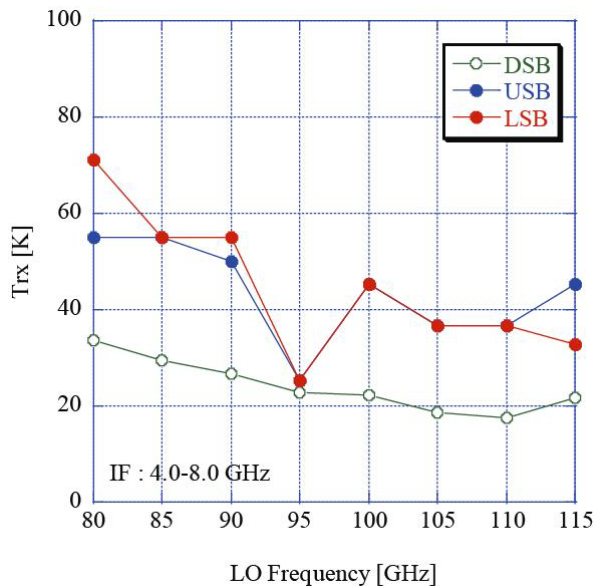
Fig. 6. Receiver noise temperatures of DSB and 2SB (SSB) mode.

IV. INSTALL & TEST OBSERVATIONS
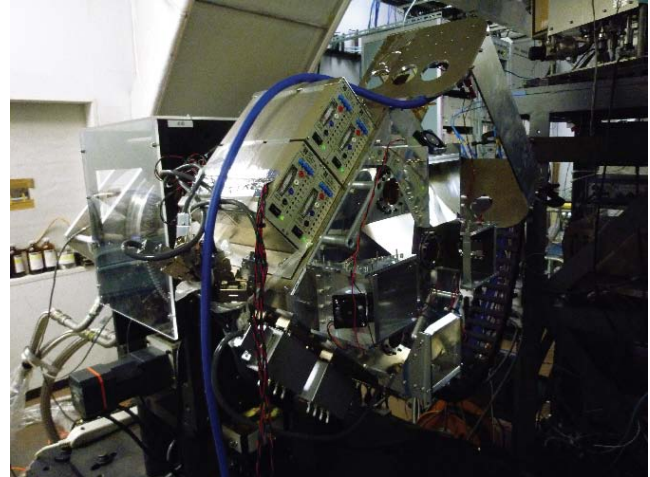
Fig. 7. Photograph of the receiver system in the receiver cabin of the telescope.

We have installed the receiver in the 45-m telescope on May 6, 2011 (Fig.7). The SSB receiver noise temperatures, including the receiver optics, were measured to be about 50-100 K for all 2SB mixers. The beam pattern of the antenna is obtained from the resultant map of the Saturn (Fig.8). The elongated feature in three directions is the effect of sub- reflector stays.

The first astronomical signal was obtained ^{12}CO (J=1-0) spectra at 115.271 GHz from the IRC+10216 on May 19, 2011.
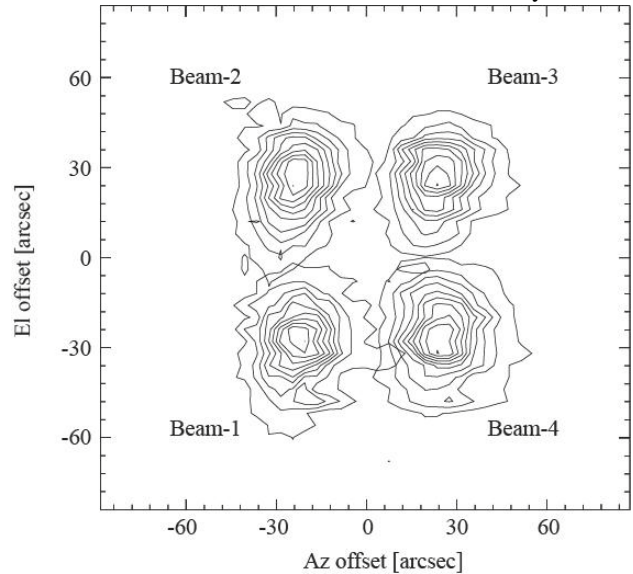
Fig. 8. Beam pattern.

These are the first astronomical observations with the waveguide-type dual-polarization sideband-separating multi-beam array receiver system in 100-GHz band (Fig.9). The system noise temperature, including the atmosphere, is about 300-400 K in 115 GHz. In our plan, we will start a scientific use with this new multi-beam array receiver from Dec. 2012.
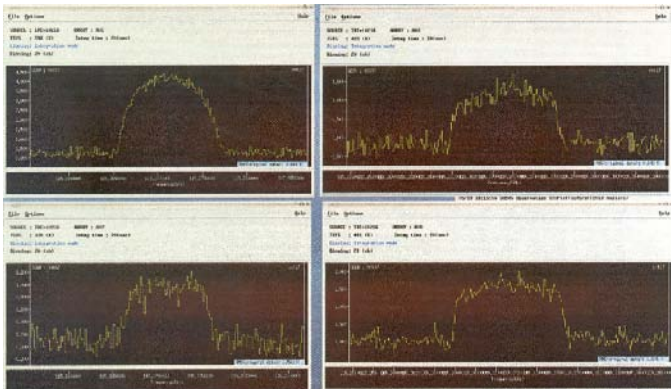
Fig. 9. First light spectrum in quick look images.

V. CONCLUSION

We have developed a new multi-beam waveguide-type dual-polarization sideband-separating SIS receiver system in 100 GHz band on the 45-m radio telescope at the Nobeyama Radio Observatory, Japan.

This receiver has four (=2×2) beams, with about 16″ of the HPBWs at 100 GHz. It has 44″ of beam separation and allows on-the-fly (OTF) mapping observation. The receiver of each beam is composed of an OMT and two 2SB mixers, both of which are based on a waveguide technique, and has four intermediate frequency bands of 4.0-8.0 GHz for LSB and 4.0-12.0 GHz for USB.

The SSB receiver noise temperatures of each sideband were measured to be lower than approximately 50 K over an RF frequency range of 85-115 GHz.

The new receiver system was installed in the telescope, and we successfully observed a ^{12}CO (J=1-0) emission line toward a IRC+10216 on May 19, 2011.

ACKNOWLEDGMENT

REFERENCES

[1] Nakai, N., Inoue, M., & Miyoshi, M. 1993, Nature, 361, 45
[2] Miyoshi, M., Moran, J., Herrnstein, J., Greenhill, L., Nakai, N., Diamond, P., & Inoue, M. 1995, Nature, 373, 127
[3] Kawaguchi, K., Kasai, Y., Ishikawa, S., & Kaifu, N. 1995, PASJ, 47, 853
[4] Kaifu, N., et al. 2004, PASJ, 56, 69
[5] Nakajima, T., et al. 2008, PASJ, 60, 435
[6] Nakajima, T., et al. 2012, submitted to PASJ
[7] Kamazaki, T., et al. 2012, PASJ, 64, 29
[8] Sunada, K., Yamaguchi, C., Nakai, N., Sorai, K., Okumura, S., & Ukita, N. 2000, SPIE, 4015, 237
[9] Yamaguchi, C., Sunada, K., Iizuka, Y., Iwashita, H., & Noguchi, T. 2000, SPIE, 4015, 614
[10] Clarricoats, P. J. B., & Olver, A. D. 1984, Corrugated horns for microwave antennas (London: Peter Peregrinus Ltd)
[11] Kimura, K., Iwashita, H., Asayama, S., Sugimoto, M., Kikuchi, G., & Ogawa, H. 2008, Int. J. Infrared Millimeter Waves, 29, 713
[12] Asayama, S., Ogawa, H., Noguchi, T., Suzuki, K., Andoh, H., & Mizuno, A. 2004, Int. J. Infrared Millimeter Waves, 25, 107
[13] Kerr, A. R. 2002, ALMA Memo, 401
[14] Asayama, S., & Nakajima, T. submitted to J. Infrared Millim. Terahertz Waves

A 350 GHz Multi-beam Receiver for the GreenLand Telescope

P.K. Grimes[1*], R. Blundell[1], S.N. Paine[1] and E. Tong[1]

[1] *Smithsonian Astrophysical Observatory*, 160 Concord Ave., Cambridge, MA 02138, USA*
Contact: pgrimes@cfa.harvard.edu, phone +1(617)496-7640

Abstract—SAO and ASIAA are undertaking a project to place the ALMA North America prototype antenna at Summit Station, a NSF research station located close to the highest point (3210m above MSL) on the Greenland ice sheet. The primary science goal of this telescope – now renamed the GreenLand Telescope (GLT) – is to carry out mm-wave VLBI observations of the central black-hole in M87. VLBI observations will occupy only a small amount of the available observing time at this excellent sub-mm and THz site, and so additional instruments are required to maximize the scientific return from this project.

We are developing a multi-beam SIS receiver for the 325-375 GHz and 385-425 GHz atmospheric windows. Possible science projects for the receiver include a follow-up survey of CO(3-2) in galaxies found by the ALFALFA HI survey and mapping of H_2D^+ in cold molecular clouds regions, as well as surveys for high redshift C(II) and other molecular species. This project will also lead to the development of higher frequency multibeam receivers for this telescope, operating in the 450 and 350 micron windows.

The receiver will use a close-packed hexagonal array of 48 smooth-walled feed-horns, to be designed and manufactured by Oxford Astrophysics. The single-piece horn array will form the mechanical support for a set of mixer modules. Each module will contain an 8-way LO corporate power divider network and 8 SIS mixers in blocks incorporating waveguide LO couplers, and arranged in a 4x2 configuration. Initially a single module will be built to prototype the array, before final production of additional modules to fully populate the array.

The receiver will use either SiGe LNAs developed at SAO, or InP or SiGe MMIC amplifiers. Power dissipation at cryogenic temperatures will be the determining criteria for amplifier selection, and hence the IF bandwidth of the receiver. The receiver backend spectrometer system will be based on CASPER based systems under development at SAO.

Development of a Transportable Telescope for Galactic Survey at 500 GHz in Antarctica

Shun Ishii, Masumichi Seta, Naomasa Nakai, Yusuke Miyamoto, Makoto Nagai, Hitoshi Arai, Hiroyuki Maezawa, Taketo Nagasaki, Naoki Miyagawa, Hideaki Motoyama, Yutaro Sekimoto, and Leonardo Bronfman

Abstract—We have developed a transportable 30-cm submillimeter-wave telescope to operate at the Dome Fuji station in Antarctic plateau. Transportability is an important requirement in the design; the telescope can be divided into several components by hands. The maximum weight of the components is restricted to be below 60 kg, so that the telescope can be assembled without a lifting machine. A small 4K mechanical cooler is used for cooling down a SIS mixer. Total power consumption was designed to be less than 2.5 kW. The 30-cm offset Cassegrain antenna produces a $9'$ beam that is same angular resolution of those of the Columbia-CfA and U. Chile CO (J=1-0) survey. The optical system is designed to satisfy the frequency independent matching condition at the subreflector and the feed horn of the SIS mixer, so we could accommodate a higher frequency receiver without changing mirrors. A quasi-optical filter was employed for single the sideband operation in observation of the CO (J=4–3) line at 461 GHz and the [CI] ($^3P_1$-$^3P_0$) line at 492 GHz. It is equipped with a 1 GHz width spectrometer that covers a velocity width of 600 km·s^{-1} with a velocity resolution of 0.04 km·s^{-1} at 461 GHz. We carried out test observations at a 4400-m altitude site in northern Chile during winters of 2010 and 2011. The typical system noise temperature including atmospheric loss was 3000 K (SSB) at 461 GHz that is mainly limited by atmospheric opacity. The beam size was measured to be $9'.4 \pm 0'.4$ by cross scanning of the sun. We estimated the main beam efficiency to be $87 \pm 5\%$ by observing the new moon. We succeeded in mapping Orion Molecular Cloud A and M17 SW in CO (J=4-3) followed by test observations toward Orion KL in both CO (J=4-3) and [CI] ($^3P_1$-$^3P_0$).

Index Terms—Antarctic plateau, transportable telescope, sub-millimeter astronomy.

I. INTRODUCTION

GALactic survey is a fundamental approach to understand characteristics of interstellar medium in the Milky Way. In millimeter-wave region, several surveys have revealed its mass, distribution, kinematic information and physical property. Colombia-CfA and U. Chile 1.2 m telescopes identified giant molecular clouds (GMCs) throughout the Milky Way in the CO (J=1-0) line at 115 GHz [1], [2], [3]. The Massachusetts-Stony Brook Galactic CO surveys essentially detected all clouds of size larger than 20 pc in $8° < l < 90°$

Shun Ishii, Masumichi Seta, Naomasa Nakai, Yusuke Miyamoto, Makoto Nagai, Hitoshi Arai, Taketo Nagasaki, and Naoki Miyagawa are with Institute of Physics, University of Tsukuba, Tsukuba, Ibaraki, 305-8571 Japan (e-mail: ishii.shun.fw@u.tsukuba.ac.jp).

Hiroyuki Maezawa is with Osaka Prefecture University, Japan.

Hideaki Motoyama is with National Institute of Polar Research, Japan.

Yutaro Sekimoto is with National Astronomical Observatory of Japan, Japan.

Leonardo Bronfman is with Universidad de Chile, Chile.

[4]. A 60 cm telescope named AMANOGAWA telescope that surveyed with the CO (J=2-1) line at 230 GHz [5], [6]. Physical parameters of GMCs such as temperature and density are derived by intensity ratio of molecular line in different transitions. They found that global decrease of gas density with the distance from the Galactic center in increasing.

Submillimeter CO lines are preferable to restrict physical condition of GMCs. Atomic carbon and nitrogen may be good probe for atomic phase of interstellar medium. Although some telescopes observed the Milky Way, the observed area is limited only around the Galactic center [7], on the Galactic equator [8] and on some major GMCs because of atmosphere is very opaque for submillimeter-wave.

A dryer and higher altitude site is needed for submillimeter-wave observations. The atmospheric transparency is mainly determined by the amount of water vapor and oxygen. Several sites with better atmospheric transparency have been developed such as Mauna Kea in Hawaii and the Atacama Desert in Chile. The atmospheric transparency at these sites is not high and stable enough for submillimeter-wave observation above 450 GHz. Antarctic plateau is good site for a galactic plane survey in submillimeter-wave. We have developed a transportable telescope for this new survey in the CO (J=4–3) line at 461.04 GHz and [CI] ($^3P_1$-$^3P_0$) at 492.16 GHz in 500 GHz band. In this paper we describe design of the telescope for operation in Antarctica and show results of the performance in the test observations.

Japanese Antarctic station, the Dome Fuji station is expected as one of the best sites for submillimeter-wave astronomy because of its high altitude of 3800 m and low average temperature of $-54°$C [9]. Dome Fuji is located in latitude $77° \ 19'$ S and longitude $39° \ 42'$ E [10]. Dome Fuji is about 1000 km away from a Japanese station at the coast, Syowa. Basic transportation means are snow vehicles and sledges, although Dome Fuji is accessible by a small plane. Currently, a telescope must be assembled without a lifting machine at Dome Fuji. The capacity of electric power is limited. Fig. 1 shows the location of Dome Fuji and other stations on a map of Antarctica where astronomical observations could be conducted.

It has been known that the average fraction of the sky obscured by clouds has been 30% in 1995-1997 [9]. The mean wind speed is 5.8 m·s^{-1} [9] and the speed hardly exceeds 10 m·s^{-1}. The zenith opacity at 220 GHz in summer was very low and stable ($\tau_{220} = 0.045 \pm 0.007$), that is much better than that of Atacama Desert in Chile in their same seasons and is comparable in their best seasons [11]. We showed in
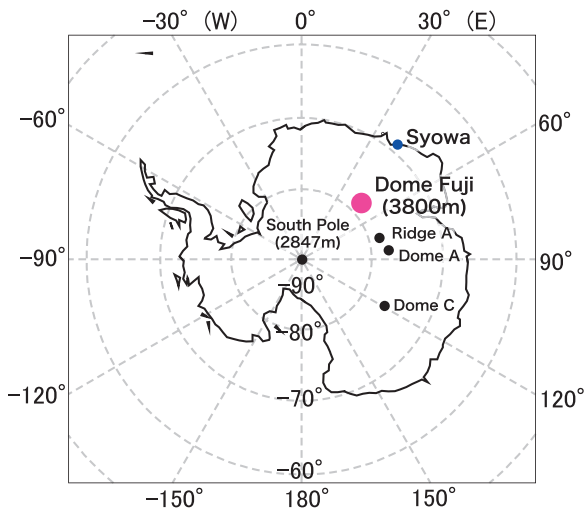
Fig. 1.   Location of Dome Fuji and other sites on Antarctica

Fig. 2.   Block diagram of the system of the 30-cm telescope. The individual components are shown with different colors.

simulation that several submillimeter atmospheric windows open through the year between 340 and 1000 GHz. Several THz windows open in winter at 1.0-2.0 THz. Furthermore, low fluctuation of the opacity is an advantage of Dome Fuji. This enables us to continue a submillimeter-wave observation for a long time under good atmospheric condition. For these advantages of topographic and climatic condition, we are developing Dome Fuji as a site for astronomical observation from submillimeter to near-infrared region [12], [13].

II. THE 30-CM TELESCOPE

The size for a main reflector of 30 cm is chosen to produce $9'$ beam at 461 GHz so that we can compare the data with the data of CO (1–0) and CO (2–1) directly. Transportability is important requirement to the 30-cm telescope for the operation at Dome Fuji. We designed the 30-cm telescope to be divided into several components by hands. The maximum weight of each component is restricted to be below 60 kg for fulfilling this requirement. We also set the upper limit on the total power consumption of 2.5 kW to satisfy the condition of the electric capacity at Dome Fuji. Fig. 2 shows a system diagram of the 30-cm telescope. We adopted a standard-type heterodyne radio telescope that consists of an antenna system, a local oscillator (LO), a mixer on a cryo-receiver, an intermediate frequency (IF) system, a back end system, and a control system.

The main reflector and a subreflector construct an offset Cassegrain antenna system. There is no blockage by the subreflector and its stay. The focal length of the main reflector is 258.40 mm. The subreflector is an offset hyperboloid with the diameter of the subreflector is 60.40 mm. We stipulated for an edge taper level on the subreflector to be -17.0 dB to suppress the side lobe level. We designed the antenna to implement the Mizuguchi condition for minimizing the cross-polarization loss and the Rusch condition for minimizing the spillover loss [14]. This provides us with high main beam efficiency, which is important for observing broad and weak emission lines seen in the galactic plane. The surface accuracy of the main reflector and subreflector is less than 5 μm. This
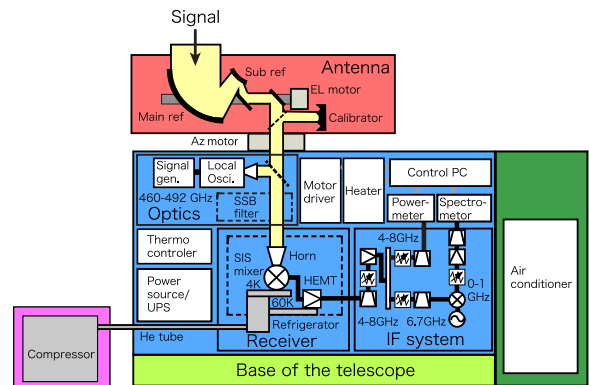
accuracy enables us to observe the radio wave with wavelength of ~ 100 μm in the future.

The beam from the antenna is led to a feed horn at Coudé focus via a transmission optical system, which consists of 4 plane mirrors, 2 ellipsoidal mirrors, wire grids, and a quasioptical single sideband (SSB) filter. We designed the transmission optical system based on Gaussian beam propagation. We also adopted a condition of frequency-independent matching between the subreflector and the feed horn [15]. This enables us to replace the receiver for an observation of higher frequency wave without a replacement of the optical system. We set the edge taper of mirrors after subreflector to -40.0 dB. The edge clearance of the beam for space is set to -50.0 dB. We adopted a diagonal horn as the feed horn because of it produces good beam despite of easy manufacturing. We designed the horn to fit the beam parameter of the optical system based on [16]. A aperture radius and a slant length of the horn are 3.475 mm and 20.00 mm, respectively.

The observation is done with the SSB mode to measure the intensity of lines with high accuracy. We adopt a pair of Frequency Selective Polarizers (FSP) as a quasioptical-type SSB filter. A FSP consists of a wire-grid backed by a flat mirror with a small gap. This filter is a modified Martin-Puplett interferometer and used for Superconducting Submillimeter-Wave Limb-Emission Sounder (SMILES) [17], [18]. We designed a frequency characteristic of the filter to achieve the SSB observation for CO (4–3) in a lower sideband and [CI] (1–0) in an upper sideband for IF of 7.2 GHz. We found the optimum value of the gap width to be 2.644 mm to transmit two emission lines with high image rejection ratio.

We adopted a Superconducor-Insulator-Superconducor (SIS) mixer associated with Parallel-Connected Twin Junctions (PCTJ) which was made at Nobeyama Radio Observatory. The junction consists of niobium and aluminum oxide as the superconductor and the insulator, respectively. It need no mechanical tuner for impedance matching of the SIS device and low noise (less than 200 K in DSB mode) is expected. The device is mounted on a mixer block, which is made of copper and plated by gold. The RF signal and the LO signal are led to the SIS mixer via the feed horn combined with the mixer block. We selected a small 4K Gifford-McMahon cryocooler for cooling down the SIS mixer with weight and

Fig. 4.   Results of scanning of the sun (a red line) and fitting (a green line) by model of beam pattern. The left figure is IF output in azimuth direction and the right figure is ones in elevation direction.

Fig. 5.   Spectra of CO (4–3) and [CI] (1–0) toward Orion KL
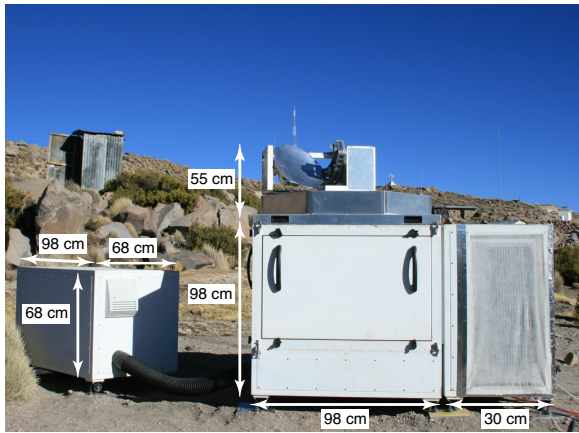
Fig. 3.   Photograph of the 30-cm telescope in Chile with its size. The length of the telescope is 98 cm in depth.

power saving. The cryostat has a cylindrical form and its size is 32 cm of diameter and 50 cm of height. The weight of the cryocooler including the cryostat is about 15 kg and its consumption power is 1.3 kW. These are suitable for the operation at Dome Fuji. The cooling capacities of the 60K stage and the 4K stage are 2.5 W and 0.1 W, respectively. A small pot filled with liquid helium is attached to the top of the cryocooler to reduce the fluctuation of temperature of the 4K stage using its large thermal capacity. A HEMT amplifier was employed as a first amplifier on the 60K stage. The gain and the noise temperature of the HEMT amplifier are about 30 dB and 6.5 K within the fist IF band, respectively. The SIS mixer is biased by a port of the isolator using a source meter with the four-wire method. The output signal of the cryostat is transmitted to a spectrometer after amplified again and down-converted to 0–1 GHz in the IF system.

We employ an FX-type 1 GHz spectrometer and the power meter for the back system. It covers ± 300 km·s^{-1} in velocity at 500 GHz band, that is wide enough to cover observed CO (4-3) line width at the Galactic center [7]. The velocity resolution is 0.04 km·s^{-1}, which is much narrower than the typical line width of CO line width of a few s^{-1} for molecular clouds. The linearity of the spectrometer is kept within 5% over 10 dB.

III. PERFORMANCES

We measured the beam pattern of the feed horn by a planer scanning of a submillimeter. The pattern has symmetry shape and its size (HPBW) is 26.3 ± 1.3 mm. The designed value of the HPBW at the position is 26.0 mm with taking into account the effect of the beam width of a probe horn. Therefore there is no discrepancy between this results and the design.

The receiver noise temperature is 900 K in SSB mode at the output port of the IF system. The little bit high noise temperature results from high physical temperature of 4.9 K of the SIS mixer, 60 K of the HEMT, and loss in the IF cable between the SIS mixer and the HEMT.

The 30-cm telescope was evaluated by the test observation in Chile during winters 2010 and 2011 after the laboratory
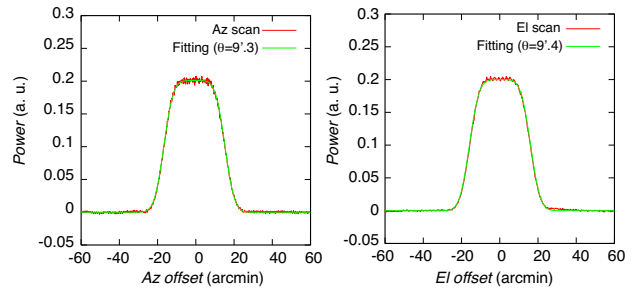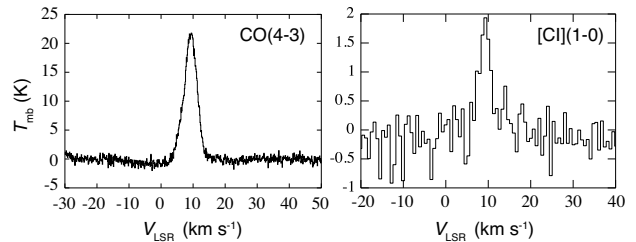
testing. It aims to operate and measure performance of the telescope before observations at Dome Fuji. We selected Parinacota in northern Chile as a site for the test observation as shown in Fig. 3. It is located about 2000 km north from Santiago and its latitude is 4400 m. Its latitude and longitude are $18°12'$ S and $69°16'$ W, respectively. We succeed in assembling the telescope only by four peoples within three days. The weight of equipment in the telescope is about 300 kg. The total weight of the whole system of the telescope that includes 2 generators and 5 wooden boxes for the transportation is 700 kg. The heaviest one in these components is the antenna system whose weight is about 55 kg.

The beam pattern of the antenna was evaluated by the scanning of the sun. The IF output is a convolution of the beam pattern and the brightness distribution of the sun. The Gaussian beam pattern is evaluated assuming that sun is modeled as a flat uniform circle. We fitted the scanning data using this model to estimate the angular resolution (HPBW) of the telescope. Fig.4 illustrates the scanning data and the beam pattern in the azimuth (left) and elevation (right) direction. The red and green lines represent the IF output by scanning and the fitting curve described further below, respectively. The HPBW of the beam in the azimuth and elevation directions is estimated to be $9'.4 \pm 0'.4$ and $9'.3 \pm 0'.4$ at 461 GHz, respectively.

We derived the moon efficiency η_{moon} using the scanning data of the new moon. We used a following equation, $\eta_{\text{moon}} = T_A^*/T_s$, where T_A^* is the measured antenna temperature of the new moon, T_s is the brightness temperature of the new moon, which is assumed to be 110 K (brightness temperature at $\lambda = 1$ mm, [19]). The moon efficiency was estimated to be $87 \pm 5\%$ at 461 GHz by this equation. The aperture efficiency η_A is also calculated to be $70 \pm 4\%$ at 461 GHz assuming that the

moon efficiency is regarded as the main beam efficiency. We also regard the moon efficiency as the main beam efficiency when we derive the main beam temperature from the intensity of the line.

The atmospheric opacity at 461 GHz is measured with the tipping-scan method using the telescope at Parinacota. The zenith opacity of the atmosphere ranged 0.6–1.5. The system noise temperature including atmospheric loss was 2000–5000 K during the observation. These values indicate the receiver noise temperature is about 900 K in SSB mode. Therefore there is no discrepancy between the results at laboratory and the observing site. An average of the system noise temperature was 3000 K during observation. We abandoned the observed data with the system noise temperature higher than 5000 K.

We show our first CO (4–3) and [CI] (1–0) spectra toward Orion KL in Fig. 5. In CO (4–3) spectrum, the peak temperature is 21.7 ± 0.5 K and integrated intensity from 6 and 12 km·s^{-1} is 92 ± 2 K km·s^{-1}. The peak velocity is 9.4 ± 0.1 km·s^{-1} and the velocity width (FWHM) of the spectrum is 4.4 ± 0.1 km·s^{-1}. In order to assess the adequacy of the data, we compared our CO (4–3) spectrum with an existing data taken by the 2.2-m ESO telescope at La Silla in Chile [20]. The velocity and integrated intensity was compared after applying convolution to correct for the difference of the angular resolution of the telescope. The corrected values were coincident each other within the error. We also detected the [CI] (1–0) as is shown in right of Fig.5.

We performed large-scale mapping of CO(4–3) in Orion A GMC during September and October, 2011. Fig.6 shows an integrated intensity map of CO(4–3) toward Orion A. The velocity range for integration is between 0 and 20 km·s^{-1} in v_{LSR}. We also mapped M17 GMC with CO(4–3).

We are upgrading the receiver to install a sideband-separating SIS mixer based on the ALMA band 8 receiver [21]. We expect to achieve lower noise temperature of the receiver with this upgrading. The telescope will be tested its performance in cold environment in a laboratory. After the test, we plan to start the operation at Dome Fuji in 2014.

Fig. 6. Integrated intensity map of the CO(4–3) toward Orion A GMC

REFERENCES

[1] T. M. Dame, H. Ungerechts, R. Cohen, E. de Geus, I. Grenier, J. May, D. Murphy, L. Nyman, and P. Thaddeus, "A composite co survey of the entire milky way," *The Astrophysical Journal*, vol. 322, p. 706, 1987.

[2] L. Bronfman, H. Alvarez, R. Cohen, and P. Thaddeus, "A deep CO survey of molecular clouds in the southern Milky Way," *The Astrophysical Journal Supplement Series*, vol. 71, pp. 481–548, 1989.

[3] T. M. Dame, D. Hartmann, and P. Thaddeus, "The milky way in molecular clouds: A new complete co survey," *The Astrophysical Journal*, vol. 547, no. 2, pp. 792–813, 2001.

[4] P. Solomon, A. Rivolo, J. Barrett, and A. Yahil, "Mass, luminosity, and line width relations of Galactic molecular clouds," *The Astrophysical Journal*, vol. 319, pp. 730–741, 1987.

[5] S. Sakamoto, T. Hasegawa, M. Hayashi, T. Handa, and T. Oka, "An out-of-plane CO(J= 2–1) survey of the Milky Way. I. The Data," *The Astrophysical Journal Supplement Series*, vol. 100, p. 125, 1995.

[6] T. Yoda, T. Handa, K. Kohno, T. Nakajima, M. Kaiden, Y. Yonekura, H. Ogawa, J. Morino, and K. Dobashi, "The AMANOGAWA-2SB Galactic Plane Survey I. Data on the Galactic Equator." *Publications of the Astronomical Society of Japan*, vol. 62, pp. 1277–1289, 2010.

[7] S. Kim, C. Martin, A. Stark, and A. Lane, "Antarctic Submillimeter Telescope and Remote Observatory Observations of CO J= 7-6 and J= 4-3 Emission toward the Galactic Center Region," *The Astrophysical Journal*, vol. 580, p. 896, 2002.

[8] T. Oka, K. Kamegai, M. Hayashida, M. Nagai, M. Ikeda, N. Kuboi, K. Tanaka, L. Bronfman, and S. Yamamoto, "Atomic carbon in the southern Milky Way," *The Astrophysical Journal*, vol. 623, no. 2, pp. 889–896, 2005.

[9] T. Yamanouchi, N. Hirasawa, M. Hayashi, S. Takahashi, and S. Kaneto, "Meteorological characteristics of Antarctic inland station, Dome Fuji," *Mem Natl Inst Polar Res Spec Issue*, pp. 94–104, 2003.

[10] O. Watanabe, K. Kamiyama, H. Motoyama, F. Fujii, H. Shoji, and K. Satow, "The Paleoclimate record in the ice core at Dome Fuji station," *East Antarctica, Annals of Glaciology*, vol. 29, pp. 176–178, 1999.

[11] S. Ishii, M. Seta, N. Nakai, S. Nagai, N. Miyagawa, A. Yamauchi, H. Motoyama, and M. Taguchi, "Site testing at Dome Fuji for submillimeter and terahertz astronomy: 220 GHz atmospheric-transparency," *Polar Science*, vol. 3, no. 4, pp. 213–221, 2010.

[12] H. Okita, T. Ichikawa, T. Yoshikawa, R. Lundock, and K. Kurita, "Antarctic infra-red telescope with a 40cm primary mirror (airt40): development and improvement," in *Proceedings of SPIE*, vol. 7733, 2010, p. 77331U.

[13] M. Seta, "Infrared and THz facilities for Dome F," *Proceedings of the International Astronomical Union 288*, 2012.

[14] K. W. Brown and A. Prata Jr, "A Design Procedure for Classical Offset Dual Reflector Antennaswith Circular Apertures," *IEEE Transactions on Antennas and Propagation*, vol. 42, no. 8, pp. 1145–1153, 1994.

[15] T. S. Chu, "An imaging beam waveguide feed," *IEEE Transactions on Antennas and Propagation*, vol. 31, no. 4, pp. 614–619, 1983.

[16] J. F. Johansson and N. D. Whyborn, "The diagonal horn as a submillimeter wave antenna," *IEEE Transactions on Microwave Theory and Techniques*, vol. 40, no. 5, pp. 795–800, 1992.

[17] J. Inatani, S. Ochiai, T. Manabe, M. Seta, and R. Wylde, "A new configuration of the Martin-Puplett interferometer with low-reflection," *IEEE Seventh International Conference on Terahertz Electronics Proceedings*, pp. 260–263, 1999.

[18] T. Manabe, J. Inatani, A. Murk, R. Wylde, M. Seta, and D. Martin, "A new configuration of polarization-rotating dual-beam interferometer for space use," *Microwave Theory and Techniques, IEEE Transactions on*, vol. 51, no. 6, pp. 1696–1704, 2003.

[19] J. Linsky, "A recalibration of the quiet Sun millimeter spectrum based on the Moon as an absolute radiometric standard," *Solar Physics*, vol. 28, no. 2, pp. 409–418, 1973.

[20] A. Schulz, E. Kruegel, and U. Beckmann, "CO(J = 4-3) map of OMC 1," *The Astrophysical Journal*, vol. 264, pp. 629–636, Oct. 1992.

[21] M. Kamikura, Y. Tomimura, Y. Sekimoto, S. Asayama, W. Shan, N. Satou, Y. Iizuka, T. Ito, T. Kamba, Y. Serizawa *et al.*, "A 385–500 GHz sideband-separating (2SB) SIS mixer based on a waveguide split-block coupler," *International journal of infrared and millimeter waves*, vol. 27, no. 1, pp. 37–53, 2006.

Sideband Separating Mixer Characterization based on SIS junction properties.

A.V. Khudchenko[1*], R. Hesper[2], A.M. Baryshev[1,2], F.P. Mena[3], J. Barkhof[2], T.M. Klapwijk[4] and M.C. Spaans[2]

1 Netherlands Institute for Space Research, Groningen, The Netherlands
2 NOVA/Kapteyn Astronomical Institute,University of Groningen, The Netherlands
3 Electrical Engineering Department, Universidad de Chile, Santiago, Chile
4 Kavli Institute of Nanoscience, Delft University of Technology, The Netherlands
`* Contact:  A.Khudchenko@sron.nl, phone +31-50-363 4018`

Abstract——**For high-frequency observational bands like ALMA Band 9 (600—720 GHz), dominated by atmospheric noise, implementation of sideband-separating mixers can reduce, up to a factor of two, the integration time needed to reach a certain signal-to-noise ratio for spectral line observations. Because of very high oversubscription factor for observation in ALMA Band 9, mixer upgrade to a Sideband Separating (2SB) configuration is an attractive option for ALMA future development.**

We have built a 2SB mixer, which has demonstrated a sideband rejection ratio as high as 15 dB over the full RF band, well within the ALMA specifications of 10 dB. The SSB noise temperature is, also within the ALMA requirements of 336 K over 80% of the band, and 500 K over the entire band.

Using the SIS junction properties the full characterization of the 2SB receiver was made. The sideband rejection ratio is determined mainly by the RF and IF hybrid amplitude misbalances, which we have measured separately. To determine RF hybrid misbalance the test signal was applied in the RF port and ratio of the SIS pumping currents was measured. For IF hybrid characterization SIS junctions were used as a known noise level sources, while biased at 5 mV and 8 mV. We have also approved experimentally and theoretically that the bias inversion of one of the SIS junctions is switching upper and lower sidebands in the IF chain and can be used as a fast method to measure the sideband rejection ratio.

We will present the 2SB mixer in details and will discuss the possible schemes of the ALMA Band 9 upgrade.

Al/SiO₂/Al Micro Strip Lines for THz SIS Mixers

M. Kroug[1*], K. Kuroiwa[2], Y. Uzawa[1]

1 National Astronomical Observatory of Japan*, Mitaka, Tokyo, 181-8588, Japan
2 Osaka Prefecture University
* Contact: `matthias.kroug@nao.ac,jp`, phone +81-422-3433879

Abstract——**Future wave-guide coupled SIS mixers for the supra THz range will most likely rely on normal metal embedding circuits since high quality superconductors that can be grown on quartz substrates and whose f_{gap} substantially exceeds 1 THz are currently not available. We have fabricated Al / SiO₂ / Al micro strip lines, integrated with standard Nb/AlO$_x$/Nb SIS junctions (already explored by several groups back in the 1990s [1]), and make a direct comparison with strip lines based on NbTiN/SiO₂/Al. The latter `hybrid type` has been extensively studied in our lab in the course of developing mixers for the ALMA Band10 receiver and low loss performance has been demonstrated in the 790-950 GHz range. Both types of strip lines are made on the same wafer and evaluation of resonant phenomena allow us to estimate the phase velocity and rf losses at frequencies up to ~1.2 THz. We propose a new mixer design using these Al/SiO₂/Al strip lines, compared with the NbTiN/SiO₂/Al based circuit we expect additional coupling losses of 30–50 % depending on the resistivity of the Al films.**

[1] **M. Bin et.al., Appl. Phys. Lett. 68, 1714 (1996)**

Performance of a 230 GHz Finline SIS Mixer With a Wide IF Bandwidth

Yangjun Zhou[*1], Ghassan Yassin[1], Paul Grimes[2], Jamie Leech[1], Karl Jacobs[3],Christopher Groppi[4]

1.Astrophysics, Dept. of Physics, University of Oxford, Denys Wilkinson Building, Keble Road, Oxford, OX1 3RH
2. Harvard-Smithsonian Centre For Astrophysics, Cambridge, MA 02138 USA
3. KOSMA, I.Physikalisches Institut, University of Cologne, 50937 Cologne, Germany
4.ASU School of Earth and Space Exploration, Tempe, AZ 85287-1404 USA
[*]Contact: yangjun.zhou@physics.ox.ac.uk, phone +44 1865 283011

Abstract—Here we present the design and performance of a novel unilateral finline Nb-AlO$_x$-Nb SIS (Superconductor-Insulator-Superconductor) mixer, operating around 230 GHz, with a target IF bandwidth of 2-13 GHz. The mixer is intended to be used in GUBBINS [1], a prototype high brightness sensitivity, low spatial resolution heterodyne interferometer. A key feature of the mixer design is the use of a unilateral finline taper to provide a smooth transition from high-impedance waveguide to low-impedance microstrip suitable for feeding a 1μm^2 SIS junction. The use of a finline transmission line allows other complicated planar circuits to be compactly integrated on the substrate and allows the use of an easy-to-fabricate mixer block. Also the employment of the silicon substrate allows trenches to be fabricated around individual SIS mixer devices on the wafer, allowing the devices to be separated easily without dicing. To realise the wide IF bandwidth, a separate IF matching board, consisting of a few sections of microstrip, was designed to match the dynamic output impedance of SIS mixer to the LNA.

In this paper, the SIS mixer design will be described in detail, including the electromagnetic simulations of the passive circuit with HFSS. We have fabricated and tested several of these SIS mixers over RF bandwidth 190-260 GHz. We have obtained a best noise temperature of 75 K at 208.8 GHz over IF bandwidth 4-6 GHz. However, the noise temperature measured across IF bandwidth 2-18 GHz shows that an IF resonance exists around 8 GHz, caused by an excess capacitance due to the large surface area of the microstrip transition and RF matching circuitry. An improved design is described, suitably modified to shift the IF resonance out of the target IF band.

I. Introduction

SIS heterodyne receivers have been successfully used for radio astronomy in the millimeter and sub-millimeter band for many years. They can offer quantum-limited noise temperatures (a few times $h\nu/k$) and mixer conversion gain [2], but many designs are limited to an IF bandwidth of a few GHz. For most astronomical applications, it is desirable to have as wide an IF bandwidth as possible. This is true for both extragalactic molecular line observations and CMB continuum observations. For spectroscopic observations wide IF bandwidths allows multiple spectral lines to be included in a single observation, while for continuum sources, wider IF bandwidths enable higher brightness sensitivities. We intend to use our wide IF band SIS mixers as detectors for the GUBBINS interferometer which is designed to carry out observation of the Sunyaev-Zeldovich (S-Z) effect near the

null frequency of around 227 GHz. GUBBINS is now under construction at the University of Oxford [1].

The SIS mixer described here is based on a previously reported antipodal finline SIS mixer design [3], [4]. This mixer, however, features a new unilateral finline and is fabricated on a silicon substrate. The finline taper used here provides a smooth transition from the high-impedance waveguide to low impedance, 2.5μm wide slotline over a wide RF bandwidth with low return loss (<-15dB). A planar circuit then couples the RF power from the slotline to a microstrip line which couples RF power to the SIS junction.

There are a number of key problems which need to be solved when designing an SIS mixer with a wide IF band. For the double-sideband (DSB) SIS mixer, the mixer needs to have an RF bandwidth at least twice as wide as the IF bandwidth so that both the signal and image sidebands, either side of the LO frequency can be downconverted efficiently to IF frequencies. If the frequency of the top end of the IF band is high enough i.e. a substantial fraction of the RF frequency, extra circuitry is required to prevent the IF signal from leaking into the RF circuit. In particular, the planar circuit of the SIS mixer must be carefully designed to present a low capacitance over a large IF band, to allow an IF transformer circuit to adequately match the dynamic impedance of the mixer to the input impedance of the first-stage cold LNA.

II. SIS Mixer Design

The SIS mixer chip, showing the RF and IF components, is displayed in Fig.1. A 1μm^2 Nb/AlO$_x$/Nb high current density (14KA/cm^2) SIS tunnel junction is employed, with $\omega R_n C \approx 2$ at 230 GHz. A target normal resistance of 20 Ω was chosen, with a characteristic capacitance of 75 fF. The planar circuit for the mixer is deposited on one side of a 60 μm thick silicon substrate. A schematic diagram of the planar circuit is shown in Fig. 2. The unilateral finline can be seen at the centre of the substrate, partially terminated by a radial stub. The extension of the finline layer acts as the ground plane for the following microstrip circuits, with 490 nm of silicon monoxide acting as an insulating layer.

The RF radiation is coupled into the device via a spline horn [5] attached to the waveguide port of the mixer block. The Nb
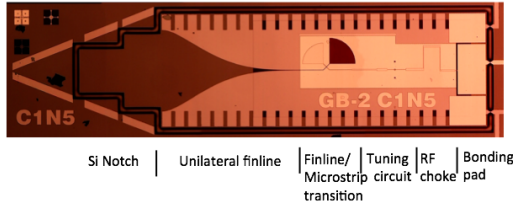
Fig. 1. Overview of a 230 GHz unilateral finline mixer, showing the planar circuits including the finline transition, slotline-to-microstrip transition, tuning circuit and RF choke, deposited on a 60 μm silicon substrate.

Fig. 3. The SIS mixer chip mounted in the WR4 waveguide, supported by grooves on either side of the waveguide. The SIS mixer is connected to the IF transformer by 25μm diameter aluminium wires. The mixer block provides a ground connection to the device via bonding wires at either sides of the device.

Fig. 2. Magnified view of the broadband power coupling and tuning network around the SIS junction, consisting of a Slotline-to-Microstrip Transition, a Chebyshev Transformer, Tuner1, Tuner2 and an RF Choke.The arrow indicates the power propagation direction.

(Fig.1), to minimise the impedance mismatch between the empty waveguide and the waveguide loaded with the silicon ($\epsilon_r = 11.8$)) substrate.

The mixer device is mounted in the E-plane of a WR-4 rectangular waveguide, supported by grooves on either side of the waveguide. As shown in Fig.1, serrations of length $\lambda_g/4$ are added to both sides of the finline to provide a virtual RF short for the finline to the waveguide walls [3]. The RF signal is then coupled from the 2.5μm slotline, to a 2.5μm microstrip by employing a double radial-stub fabricated across the dielectric layer. On top of the 2.5μm slotline which terminates the finline transition, a 490 nm SiO insulating layer and a 2.5μm microstrip line is deposited. This allows the RF power to be directly coupled from the slotline to the microstrip line, via the SiO layer (see the 'Finline/Microstrip Transition' section in Fig.1). To optimise the coupling, the microstrip stub is terminated by an open-ended quarter-wave radial stub, while the slotline stub is terminated by a short-ended quarter-wave radial stub. So at the crossing point, the slotline stub ends up as an open circuit, whilst the microstrip ends up as a short circuit. This design forces the RF signal to propagate from the slotline to the microstrip with minimal mismatch loss. At the crossing point, the minimum width of both the microstrip and the slotline, fabricated using photolithography, is only 2.5μm. If the width can be further reduced, better coupling can be obtained since the characteristic impedance between the slotline and the microstrip becomes more closely matched.

The RF signal is coupled from the 2.5 μm width microstrip to the SIS junction (shown as a square in Fig.2) via a series of RF transformers. Two inductive stubs, labelled "Tuner 1" and "Tuner 2" in Fig.2, lie before and after the SIS junction. These stubs are designed to tune out the junction capacitance

unilateral finline, transmits the RF signal from the waveguide mode, to the slotline line mode with low return loss over an RF bandwidth of 100 GHz, centred at 230 GHz.

The unilateral finline intrinsically has a cutoff frequency above the IF frequency along the whole finline transition. This prevents the IF signal leaking into the finline transition and thus no RF bandpass filter is required between the finline and the tuning circuit. Compared with antipodal finline [4], the total length of the unilateral finline is much smaller, with no sacrifice of the IF or RF performance. The reduced length of the unilateral finline reduces the capacitance between the finline metalization and the waveguide groove, which is desirable when designing a mixer with a wide IF bandwidth.

The profile of the unilateral finline was designed using the transverse resonance technique in conjunction with the optimum taper method, as described in [6]. The slotline width is reduced smoothly from the waveguide width to 2.5μm to match to the characteristic impedance of the following microstrip line (20-30Ω), where the SIS junction is embedded. The optimum taper method [6], allows the length of the finline taper to be kept as short as possible, without limiting the RF bandwidth. The profile of the finline was further verified in Ansoft's 3D electromagnetic simulation software, HFSS, including the effect of the superconductivity of the Nb film. A two-stage notch in the substrate is employed

Fig. 4. Assembly of the mixer block, fed by a spline horn. It is equipped with magnetic coil, bias tee, temperature sensor and is bolted to a supporting bracket.
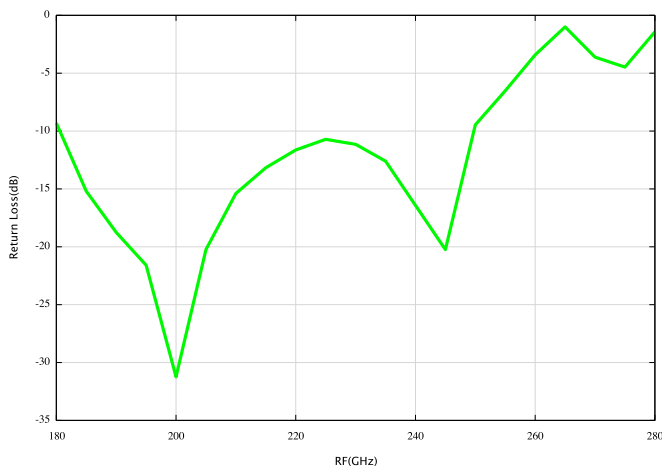

Fig. 5. HFSS calculated S-parameter as a function of RF frequency.

at two slightly different frequencies either side of the centre frequency, thus broadening the RF bandwidth. Also, compared to a radial-stub tuning circuit [7], the straight-stub tuning used here has a smaller surface area and hence smaller capacitance, which makes it easier to achieve a broader IF bandwidth. The port impedance Z_1 has a substantial mismatch with the port impedance Z_2, denoted in Fig.2. Thus we employ a 3-stage Chebyshev transformer to minimise the mismatch between them. Fig.5 shows the calculated S-parameter for the full SIS mixer chip in RF band, given by HFSS.

A six-step RF choke follows the tuning circuit, blocking the RF power over a wide RF bandwidth, while providing maximum transmission in the IF band. 'Tuner 2' also acts as part of the RF choke. The IF power from the RF choke is transmitted to the IF bonding pad, at the rear of the device. On either side of the IF bonding pad, there are two ground bonding pads to provide ground contact to the mixer block. These bonding pads are gold sputtered to prevent the Nb layer from oxidising. The IF pad is connected to an IF transformer circuit, fabricated on 0.635mm thick Roger's Duroid 6010LM, through one or two 20μm diameter aluminium bond wires.

A multi-stage impedance matching transformer is incorporated onto the IF board to match the IF output impedance of the mixer to the 50Ω input impedence of the IF amplifier. The design process for the IF transformer is as follows:

1) Obtain the S-parameter data in the IF band for the mixer chip's planar circuit before and after the junction, also including the IF bonding pad.
2) Represent the mixer chip as an RLC equivalent circuit at IF frequencies in Ansoft Designer, using the S-parameters obtained in step (1). Obtain the output impedance from the IF output port.
3) Design an IF impedance matching circuit from the complex output impedance obtained in (2), to a purely real 50Ω impedance. Constrained by the available size of the pocket for the IF board in the mixer block, a six-stage microstrip line IF transformer was employed. The first two stages tune out the capacitance at slightly two different frequencies and the left four stages act as a Chebyshev transformer to match the resistance. The overall IF transformer is then further optimised in Ansoft Designer to obtain the best performance.

The mixer block for housing the SIS mixer chip was fabricated in Arizona State University and is shown in Fig.4. Inside the block, the SIS mixer sits in the E-plane of the waveguide, supported by the grooves by either sides of the waveguide, which are recessed in the lower half of the block. The SIS mixer is fed by a spline horn [5], attached to the input port of the waveguide. The magnetic field, used to suppress Josephson pair tunnelling of the SIS junction, is provided by a magnetic coil mounted on the top half of the mixer block. The DC bias voltage is supplied to the SIS mixer, by a bias tee, connected to the IF transformer board via a standard SMA connector.

III. EXPERIMENTAL DESCRIPTION AND RESULTS ANALYSIS

The apparatus used for the RF testing of the SIS mixers is shown in Fig.6. Outside the dewar, the RF and LO signal were combined together using a partially reflecting Mylar beamsplitter. The Y-factors for the mixer were measured using using hot (300 K) and cold (77K) Eccosorb loads. The IF signal was amplified by a 3-13 GHz 4K lnP LNAs (Low Noise Amplifier) supplied by S. Weinreb (batch number: 111-CIT-4254-077). and further amplified by a warm (300K) amplifier chain. The amplified IF power is then detected by a diode detector.
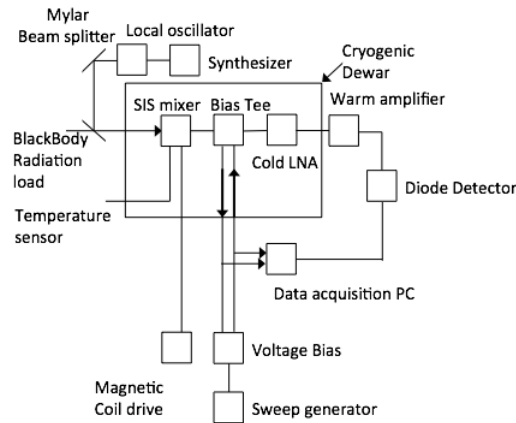
Fig. 6.   Experimental setup used for measuring the mixer performance.
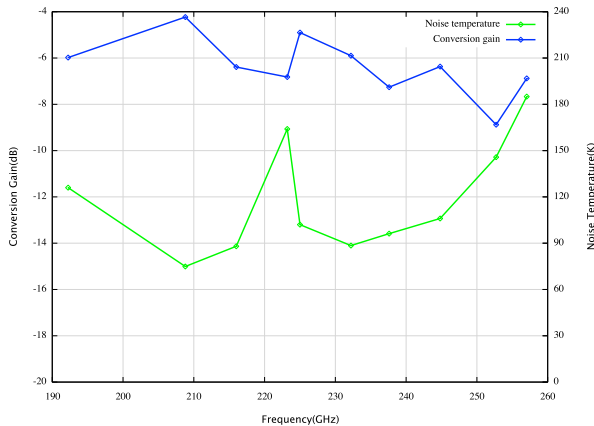
Fig. 7.   The measured noise temperature and gain as a function of RF frequency. Note the double-dip shape of the noise temperature profile, consistent with the tuning circuit design.

The measured DSB noise temperature and gain across RF range in IF band 4-6 GHz is shown in Fig.7, as a function of RF frequency between 192-263 GHz. The SIS mixer was easily pumped by the LO to saturation, with the LO and RF signal combined by a 8μm Mylar beamsplitter. The noise temperature/gain results presented here were measured with
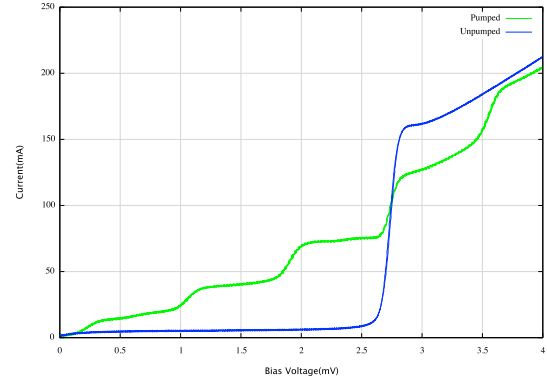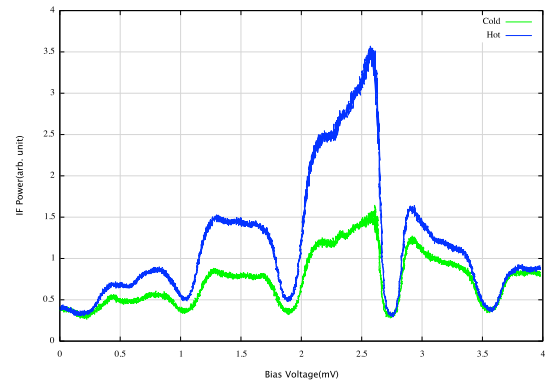
Fig. 8.   The IV and IF characteristic of the SIS mixer tested with LO injection at 208.8 GHz.
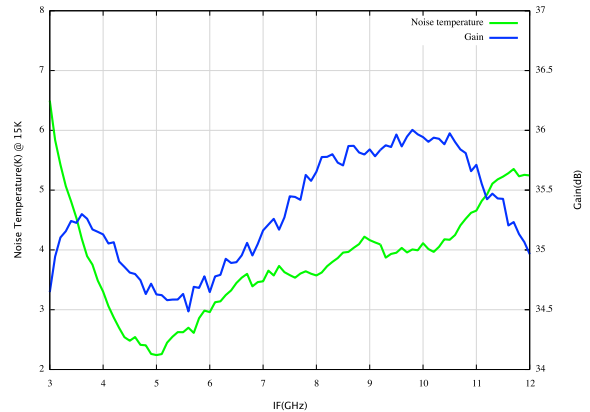
Fig. 9.   The expected noise temperature and gain of the LNA @ 15K, as a function of IF frequency [8].

a 12 μm beamsplitter. We obtained a best noise temperature of 75 K at 208.8 GHz and an average noise temperature of 100 K across the RF band 190-260 GHz, presented in Fig.7. In the upper frame of Fig.8, we have plotted the IF output under the hot and cold radiation with LO injection at 208.8 GHz, as a function of DC bias voltage, used to calculate the Y-factor and the noise temperature. In the lower frame, we have show the corresponding pumped and unpumped IV curves. The measured IF noise temperature contribution is approximately 9K, slightly higher than expected from the
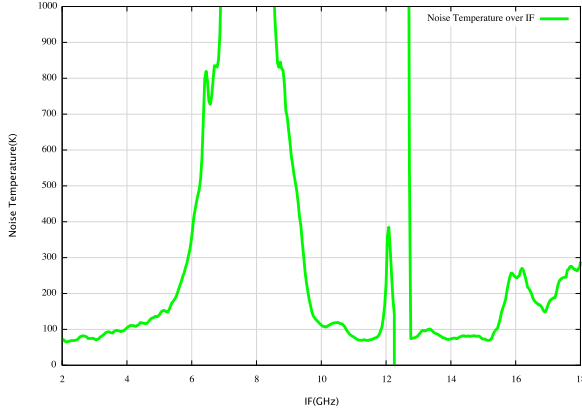
Fig. 10. The measured noise temperature of the SIS mixer, with LO injection at 208.8 GHz, as a function of IF frequency, measured using a spectrum analyzer.
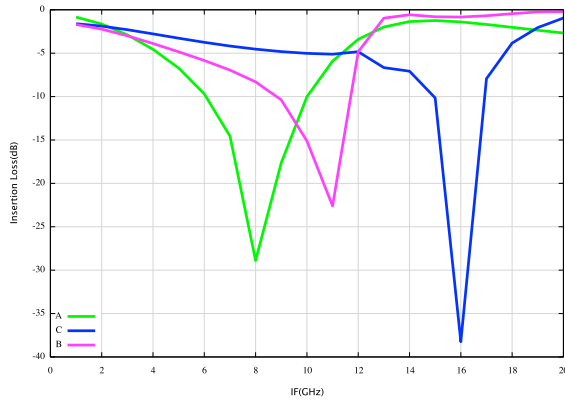
Fig. 11. The insertion loss of the full SIS mixer, simulated by HFSS, across the IF band. The letters denote various stub designs: (A) 90° microstrip stub with a 90° slotline stub with unchanged radius, (B) 60° microstrip stub and 60° slotline stub with unchanged radius, (C) 60° microstrip microstrip stub and 60° slotline stub with the radius cut by 40%.

manufacturer's supplied data for the LNA, shown in Fig.9. The noise temperatures measured are above the state-of-art performance for SIS mixer operating around 230 GHz. We suspect that the noise performance above 240 GHz is being degraded by noise added by unwanted sidebands being generated in our ×18 LO source. Another reason for the elevated noise temperatures is the presence of an IF resonance at 8 GHz, which leads to the noise temperature being elevated in part of the band (5.5–6 GHz) defined by our IF bandpass filter (see below and Fig.10).

All the noise temperature and gain measurements presented above were obtained using a bandpass filter to constrain the IF detection bandwidth to 4-6 GHz. The noise temperature was also measured as a function of IF frequency, without a bandpass filter, using a spectrum analyser (Fig. 10). The noise temperature deteriorates severely in a 4 GHz wide region, centred around 8 GHz. The HFSS simulation reveals that the IF return loss at 8 GHz becomes 0dB for the SIS mixer. This is caused by an IF resonance being formed by a combination of
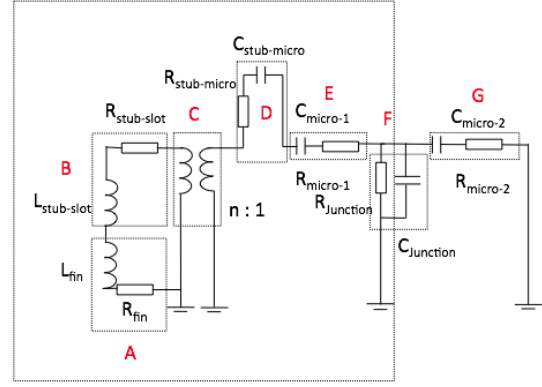
Fig. 12. RLC equivalent circuit representing the SIS mixer in the IF band. The circuit components outlined correspond to the following elements of the mixer chip's planar circuit (A) the unilateral finline, (B) the radial slotline stub, (C) the slotline-to-microstrip transition, (D) the radial microstrip stub, (E) 'Chebyshev transformer' and 'Tuner 1', referred to Fig.2, (F) the SIS tunnel junction, (G) 'RF choke' and 'Tuner 2', again referred to Fig.2

the unilateral finline, the slotline-to-microstrip transition, part of the RF tuning circuit and the SIS junction. In the IF band, the wavelength is much longer than the physical dimensions of the planar circuit, which allows us to treat these planar circuits as simple lumped elements. The LRC equivalent circuit, illustrating the resonant circuit is shown in Fig.12. The planar circuits enclosed in the large dotted frame constitute the resonant circuit. The SIS junction shares the same ground with the unilateral finline, so a closed loop is formed between the finline and the SIS junction, whose resonant frequency accidentally falling between 3-13 GHz. The planar circuit after the SIS junction and the capacitance of the SIS junction do not form part of the resonant circuit. The capacitance is contributed by all the microstrip transmission lines, mainly the large-area of the 90° radial stub. The inductance arises from the slotline structures, e.g. the unilateral finline and the slotline radial stub. The resonant frequency is given by,

$$f = \frac{1}{2\pi\sqrt{LC}} \tag{1}$$

where, referring to Fig.12,

$$L = L_{stub-slot} + L_{fin} \tag{2}$$
$$C = C_{stub-micro} + C_{micro-1}. \tag{3}$$

We can thus conclude that the large area of the 90° microstrip stub and the 90° slotline stub is mainly responsible for the 8 GHz resonance. It shorts out the IF signal generated by the SIS junction at 8 GHz, resulting the IF output resistance at 8 GHz approaching zero, which cannot be matched by the IF transformer.

IV. DESIGN MODIFICATION

Given the problems of the IF resonance described in the last section, the design was modified aiming to shift the 8 GHz

IF resonance to a higher frequency. According to Eq.1, this can be easily achieved by decreasing L and C. However, the RF coupling in the slotline-to-microstrip transition is a strong function of the radius of the stubs, which provide the best coupling with a radius of $\lambda_g/4$. So, while carefully balancing both the IF and RF performance, the radii of the stubs were reduced by 40% and the angles were reduced to 60°. The total area and hence capacitance of the microstrip and slotline stubs were thus reduced by 76%. From Eq.1, the resonant frequency will thus be doubled to around 16 GHz.

Our expected shift in the IF resonant frequency was confirmed by a full HFSS simulation, shown by the blue curve in Fig.11. The IF resonant frequency is seen to be shifted to 16 GHz, as expected. Minor changes were made to the tuning circuit and the Chebyshev transformers, to improve the matching to the modified slotline-to-microstrip transition. The SIS mixer was re-simulated in HFSS in both the IF and RF band, and the results are shown in Fig.13. The IF performance in Fig.13 was calculated, combining the SIS mixer with the 6-stage IF transformer board, used to matching the dynamic output impedance from the mixer chip to the LNA.
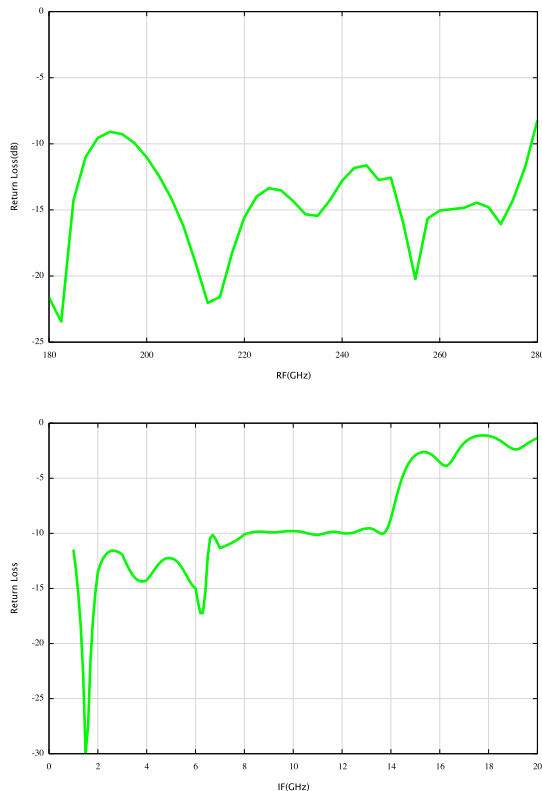
Fig. 13. Top: HFSS calculated S-parameters for the modified SIS mixer in RF band 180-280 GHz. Bottom: HFSS calculated S-parameter for the modified SIS mixer in IF band 0-16 GHz. An 6-stage IF transformer is included here to provide good IF matching between 0-14 GHz.

V. CONCLUSION

The design and measurement of a unilateral finline SIS mixer, operating around 230 GHz, has been described. The design features a unilateral finline which gives broad RF bandwidth. The passive superconducting components have been rigorously simulated using the 3-D electromagnetic simulator HFSS and planar circuit simulator Designer. The measured noise temperature in the RF band were found to be compatible with these simulations. The noise temperature was found to be degraded by an IF resonance around 8 GHz, caused chiefly by the excessive capacitance of the microstrip/slotine radial stubs. The measured IF performance was found to be consistent with a lumped element simulation of the IF circuitry. The initial design was then improved by reducing the surface area of microstrip/slotline stubs, shifting the IF resonance frequency to 16 GHz away from the centre of the target IF band. We hope to fabricate and test a new batch of mixers using the improved design in the near future.

REFERENCES

[1] P.K.Grimes, M.J.R. Brock, C.M.Holler, J.John, M.E.Jones, O.G.King, J.Leech,A.C.Taylor, G.Yassin,K.Jacobs and C.Groppi, "GUBBINS: A novel millimeter-wave heterodyne interferometer", 20_th *International Symposium on Space Terahertz Technology*, Charlottesville, 20-22 April 2009

[2] M.J.Feldman, "An Analytic Investigation of the Superconductor Quasi-particle Mixer in the Low Power Limit", *Accepted IEEE trans, Magn, Univ. of Rochester, Rochester NY 14627*, Charlottesville, 20-22 April 2009

[3] G.Yassin, R.Padman. S.Withington and K.Jacobs ,"A broad band antipodal finline mixer for astronomical imaging arrays", *Electron Lett.*, vol.33,pp 498-500,1997.

[4] Paul K.Grimes, Ghassan Yassin, Karl Jacobs, and Jamie Leech ,"Design of SIS finline mixers with ultra-wide IF bands", *Electronics letter*, 3rd July 2008, Vol.44, No.14

[5] Granet C., James G.L., Bolton R. and Moorey G., (2004) "A smooth-walled spline-profile horn as an alternative to the corrugated horn for wide band millimeter-wave applications" IEEE Trans. Antenna Propagat., 52(3), pp. 848-854

[6] G.Yassin, P.K.Grimes, O.G.King and C.E.North "Waveguide-to-planar circuit transition for millimetre-wave detector", 17_th *International Symposium on Space Terahertz Technology*, Paris, 10-12 May 2006

[7] C.North, G.Yassin, and P.Grimes, "Rigorous Analysis and Design of Finline Taper for High Performance Millimeter and Submillimeter Detectors", 17_th *International Symposium on Space Terahertz Technology*, Paris, 10-12 May 2006

[8] S. Weinreb, Private Communication.

Development of 1.4THz Hot Electron Bolometers

Ming-Jye Wang[1], Hsian-Hong Chang[1], Wen Zhang[2], Wei Miao[2], Sheng-Cai Shi[2]

1. *Institute of Astronomy and Astrophysics, Academia Sinica, Taiwan*
2. *Purple Mountain Observatory, Nanjing, China*

Nowadays, hot electron bolometer (HEB) is the most convincing devices on detecting THz signal. Noise temperatures of HEBs with near 10 times of quantum limit noise level have been demonstrated at frequency up to several THz. Therefore, HEBs are potentially to be used in Dome A 5-meter Telescopes and Greenland Telescopes which are two of the best sites for THz astronomical telescopes.

The HEB devices are designed for the 1.4 THz window of atmosphere by using superconducting NbTiN mirco-bridge on silicon substrate with twin-slot antenna. The length and width of slots and the separation of slot antenna are $L=0.285\lambda_0$, $W=0.0234\lambda_0$, and $S=0.164\lambda_0$ respectively, where λ_0 is 214 μm at 1.4 THz. The signal is transferred between slot antenna and NbTiN superconducting micro-bridge by a co-planar waveguide (CPW) with characteristic impedance of 37 Ω. The size of NbTiN superconducting bridge is 2 μm(W) by 0.3 μm(L) and its normal state resistance is targeting to 60 Ω to match the impedance of feed-point from CPW.

The thin superconducting NbTiN films are deposited using Ar and N_2 mixture by a DC sputtering system. The superconducting transition temperature and sheet resistance of 8 nm thick film is around 11 K and 330 Ω/square. The micro-bridges are patterned by E-bean lithography technique and reactive ion etching process. The temperature dependence of resistance of HEB device typically shows two superconducting transitions at 11 K and 8.5 K, which is from micro-bridge and contact pad respectively. The critical currents of devices have a value around 200 μA. More device's parameters and performance will be presented in this paper.

Stabilized HEB receiver at 2.5 THz

D.J. Hayton[1]*, J.R. Gao[1,2]*, J.W. Kooi[3], Y. Ren[2,4], W. Zhang[4] and G. de Lange[1]

[1]*SRON Netherlands Institute for Space Research, Landleven 12, 9747 AD Groningen, The Netherlands*
[2]*Kavli Institute of NanoScience, Delft University of Technology, Lorentzweg 1, 2628 CJ Delft, The Netherlands*
[3]*California Institute of Technology, MS 301-17, Pasadena, California, 91125, USA*
[4]*Purple Mountain Observatory (PMO), Chinese Academy of Sciences, 2 West Beijing Road, Nanjing, JiangSu 210008, China.*
* Contact: D.J.Hayton@sron.nl

Abstract— We report on a method to stabilize a hot electron bolometer (HEB) mixer. HEB mixers are currently the most sensitive heterodyne receivers above 1.5 THz, with applications that include astronomical observations, atmospheric remote sensing and imaging. However, when compared with other mixers such as Schottky diode and superconductor-insulator-superconductor (SIS) receivers, HEBs suffer from inferior stability. This ultimately places undesirable constraints on observation strategies. Astronomical sources, in particular, are often weak with the signal deeply embedded in the noise, requiring long integration periods.

In this paper we report a new stabilization technique that utilizes the sensitive direct detection properties of an HEB to implement feedback control of the local oscillator (LO) laser power by means of novel swing-arm actuator placed in the optical beam path. Rapid control of the LO power is used to maintain a constant operating bias point of the HEB and thus stabilize the mixer conversion gain and output noise, leading to longer Allan times. We demonstrate that this technique yields a factor of 50 improvement in the spectroscopic Allan variance time which is shown to be over 30 sec in a 12 MHz noise fluctuation bandwidth. Furthermore, this method can in principle compensate for the signal direct detection effect often observed in small area HEB's. We also show that this technique can be applied when measuring receiver noise temperature with consistent results for three different methods. The swing-arm actuator is thus shown to be an effective substitute for a rotating polarizer.

This method can easily be applied to practically any LO source and at any frequency since the modulation of LO power is achieved using a dedicated optic element. LO stabilization is demonstrated here for a CO_2 pumped gas laser at 2.5 THz. The enhanced stability afforded by the proposed technique will make astronomical observing routines such as 'on the fly mapping (OTF)' significantly more efficient as fewer off source reference scans will be needed.

2.7 THz Waveguide Balanced HEB Mixer Development

F. Boussaha[*], J. Kawamura, J. Stern, A. Skalare, and V. White, C. Jung

Jet Propulsion Laboratory, California Institute of Technology, Pasadena CA 91109 USA

* Contact: faouzi.M.boussaha@jpl.nasa.gov, +1 818 354 4488

Abstract— **We develop balanced waveguide-based mixers operating at molecular transition frequencies of OH and HD lines expected respectively at 2.5 and 2.7 THz. The receivers use NbN HEB mixers and 90° quadrature hybrids. Beyond 1.5 THz, the realization, among others, of the waveguides by conventional machining fabrication techniques becomes complicated and novel techniques such as gold-plating and silicon micromachining technologies are used. Hence, waveguides as well as channels that hold mixers are not machined directly on a metal part as usual but defined on an intermediate piece made of a thick silicon substrate by means of UV-photolithography and gold microplating techniques. The concept would facilitate the downscaling for operation at higher frequencies, particularly around 5 THz for the detection of atomic oxygen OI line. We present in detail the main steps of the development and first experimental results.**

Fabrication of HEB Mixers Using Substrate Heating in Combination with the AlN Buffer Layers

R.Furuya[1*], T.Shiino,[1] T.Soma[1], O.Ohguchi[1], H.Maezawa[2], N. Sakai[1], and S.Yamamoto[1]

1 University of Tokyo, School of Science*, Bunkyo, Tokyo, 113-0033, Japan
2 Osaka prefectural University, School of Science, Sakai, Osaka, 599-8531, Japan
`* Contact: furuya@taurus.phys.s.u-tokyo.ac.jp, phone +81-3-5841-4217`

Abstract——An HEB mixer is the most sensitive heterodyne mixer above 1.3 THz, and extensive efforts have been done for its development during the last decade. One of the important issues for the HEB mixer is to extend its IF bandwidth. In contrast to the SIS mixer, the IF bandwidth is actually limited by the cooling time of the superconducting microbridge. In the NbTiN HEB mixer, this cooling is done through phonons, and hence, the heat produced in the microbridge by absorption of the THz photons is eventually escaped to the substrate. To make this mechanism work efficiently, we need the very thin superconducting film with high critical temperature. In order to fabricate such a high quality superconducting film, we have employed the substrate heating during the deposition of the NbTiN film by reactive sputtering of the NbTi target. When we deposit the NbTiN film on the AlN buffer layer on the glass substrate heated up to 600℃, the superconducting behavior is found to be improved dramatically. In the case of the 8 nm NbTiN film, Tc is improved by 4 K or more. Then, we have involved this method into our fabrication process of the HEB mixer. For this purpose, we have to use the etching process to make contact pads instead of the lift-off process previously used in our fabrication process. Using this new process, we have succeeded in fabricating the waveguide type HEB mixer having 3 nm thickness NbTiN microbridge. The thickness of the microbridge is less than 1/3 of that of our previous mixer (10.8 nm). We have achieved the noise temperature of 480 K at 809 GHz, where Tc is 7.5 K. We have also measured the IF bandwidth of this HEB mixer, and have confirmed that the 3 nm thickness HEB device has the IF bandwidth up to 2.8 GHz. Although we have not measured the IF response above 3 GHz due to the limitation of the IF amplifier chains, it seems likely that the mixer can work at higher frequencies than 3 GHz of IF frequency.

Intrinsic Mixing Behavior of Superconducting NbTiN HEB Mixer Based on in-situ Technique

L. Jiang[1*], T. Shiino[2], S. Yamamoto[2], and Y. F. Liu[1]

1 College of Information and Science Technology, Nanjing Forestry University, JiangSu 210037, China
2 Department of Physics, the University of Tokyo, Hongo 7-3-1, Tokyo 113-0033, Japan
* Contact: jiangling@njfu.edu.cn, phone +86-25-85427136

Abstract——**In this paper, we present the intrinsic mixing behavior of superconducting niobium titanium nitride hot electron bolometer mixer based on in-situ technique. We make detailed comparison between simulated and measured performance of the HEB mixers at 0.8 and 1.5 THz. A distributed hot spot model which is based on solving a heat balance equation is employed to characterize current-voltage curve, electron and phonon temperature distribution along superconducting microbridge, intermediate frequency gain bandwidth and intrinsic noise temperature of the mixers. The simulated intermediate frequency gain bandwidth decreases with the increase of microbridge length, which is in good agreement with measured results. For the microbridge with 0.15 μm in length, the IF gain bandwidth is simulated to be 2.6 GHz at 0.8 and 1.5 THz. When the microbridge length is increased to 0.3 μm, the calculated IF gain bandwidth is 1.8 GHz. The simulated results demonstrate the IF gain bandwidth is only related with microbridge length, independent of RF frequency.**

It's very useful to find the critical parameters which mainly affects the mixer noise temperature and IF gain bandwidth. In this paper we will give the critical factors as the reference for fabrication and measurement of HEB mixers. We have found that when the ratio of length to width of the microbridge is set to be around 0.15, the simulated and measured mixer noise temperature show the lowest value. More details will be presented in the paper.

Terahertz NbN hot electron bolometer fabrication process with a reduced number of steps

R. Lefèvre, Y. Jin, A. Féret, T. Vacelet, W. Miao, L. Pelay, F. Dauplay, M. Ba-Trung, G. Gay,
J.-C. Villégier, J. Spatazza, J.-M. Krieg, and Y. Delorme

Abstract—**We have developed a superconducting hot electron bolometer fabrication process which requires fewer steps than conventional process. NbN phonon-cooled hot electron bolometers have been fabricated without any additional superconducting interlayer to NbN/Au contact, using a single layer of Au and a single step of passivation. This process has been proved efficient, reliable and reproducible. Excellent receiver noise temperature of 800 K at 2.5 THz has been obtained with a quasi optical HEB mixer developed for a stratospheric balloon experiment. In this paper, we will present in detail the fabrication process which has been performed with different substrates including silicon, sapphire and 1.4 µm thick SiO$_2$/Si$_3$N$_4$ membrane.**

Index Terms—**e-beam lithography, hot electron bolometer, heterodyne receiver, noise temperature, terahertz.**

I. INTRODUCTION

THERE are many astrophysical relevant molecular transitions in the frequency window between 2.3-2.8 THz. Observations of the rotational transition of the deuterated hydrogen molecule, HD, at 2.7 THz, will provide critical information on the star formation history across the Galactic disk and nearby galaxies. The hydroxyl radical, OH (2.5 THz), is one of the most important molecules in interstellar chemistry. It is vital for understanding the water chemistry, and its observations will be used to derive information about shocked molecular gas and will allow to discriminate between different shock models.

Our laboratory is developing a heterodyne receiver with a multipixel camera for a balloon project called CIDRE (Campagne d'Identification du Deutérium par Réception

hÉterodyne). This project is supported by the French Space Agency (CNES). The heterodyne instrument on board a stratospheric balloon at an altitude of 40 km will be able to observe OH and HD with a very low atmospheric absorption. The first flight of CIDRE is expected in 2015. In this framework we have developed an efficient, reliable and reproducible fabrication process for the mixer element based on NbN hot electron bolometer (HEB). Our main motivations in this process development were to minimize the number of fabrication steps to perform the process more easily and to get a device yield as high as possible.

II. FABRICATION PROCESS

In standard, the devices were manufactured starting from 400 µm thick Si substrate. The planar dimensions of the substrate were 10 mm x 15 mm. Fig. 1 shows a scheme of the main steps of the HEB fabrication process. This process was the same for devices on sapphire substrate and on SiO$_2$/Si$_3$N$_4$ membrane. After the complete process the average yield was about 90 %.
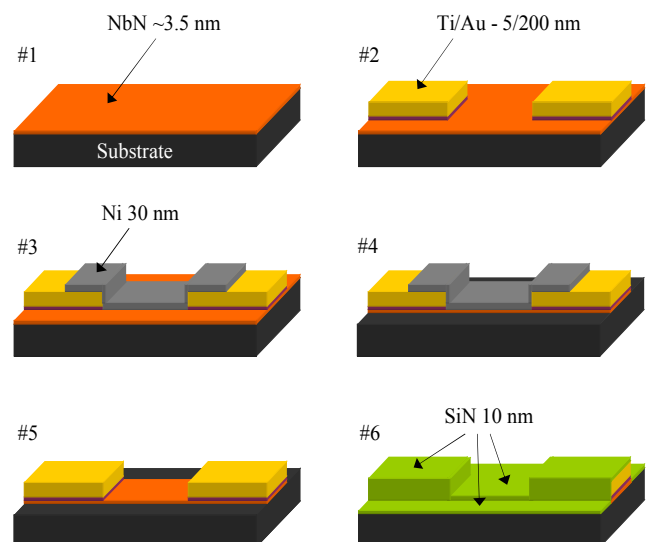
Fig. 1. Scheme of the main steps of the HEB fabrication process. #1 deposition of an ultrathin NbN film by reactive sputtering. #2 realization of the HEB electrodes; the gap between them defines the length of the bolometer. #3 protection of the bolometer with a Ni mask. #4 etching of the unprotected NbN; this defines the width of the bolometer. #5 removal of the Ni mask. #6 passivation of the whole sample with SiN.

Fig. 2. SEM image (colorized and tilted view) showing the inner part of a log-spiral antenna and the gap between electrodes where the HEB is located.

Step #1: The fabrication started with the deposition of the superconducting NbN film. This was done by Scontel or Inac by reactive sputtering [1], [2]. Since it is the active layer of the HEB mixer, it will play a key role in the performances of the receiver. We need an ultra-thin film, around 3.5 nm of thickness, with a high critical temperature T_c and a narrow transition width ΔT in order to get a wide bandwidth and a good sensitivity. The NbN films that we obtained exhibited a T_c about 11-12 K.

Step #2: The HEB electrodes, the antenna and the bonding pads were patterned at the same time by electron beam (e-beam) lithography, deposition of metals, and lift-off. For the lithography we used the e-beam writer JEOL JBX 5DIIU at 50 kV and the PMMA A7 resist. The resist, 400 nm thick, was spin-coated on the sample at 4000 RPM and baked at 170 °C for 15 min in an oven. Fine structures, like HEB electrodes, were exposed with a beam current of 200 pA and a dose of 500 µC/cm². Larger structures were exposed at 20 nA and 600 µC/cm². All the structures were exposed in the same run and aligned better than 50 nm (we used alignment marks fabricated before, not shown in Fig. 1). The resist was developed with MIBK:IPA (1:3) for 60 s. For the deposition of metals, we used the electron beam evaporator Plassys MEB 550 SL. First, the sample was cleaned *in situ* by ion beam etching with argon for 45 s. The gas pressure and flow rate were 1×10^{-4} mbar and 5 sccm. The current density and acceleration voltage of the ion beam were 7 mA/cm² and 500 V. Second, we deposited 5 nm of Ti as adhesion layer followed by 200 nm of Au, with a residual pressure below 2×10^{-7} mbar. Afterwards, we removed the resist with trichloroethylene at 90 °C and rinsed the sample in two baths of acetone and isopropanol and dried it with nitrogen. In this step the length of the HEB was defined by the gap between its electrodes ranging from 100 to 200 nm, as shown in Fig. 2 and Fig. 3(a).

Step #3: We patterned a rectangle mask of Ni 30 nm thick across the two HEB electrodes. At this stage the width of the bolometer (usually 2 µm) was defined. As in the previous step, we used e-beam lithography (alignment precision was better

than 50 nm), metal deposition by electron beam evaporation, and lift-off.

Step #4: The unprotected NbN film, either by gold metal or Ni mask, was removed by reactive ion etching with SF_6 plasma for 90 s. The RF power was 10 W, the flow rate and gaz pressure were 10 sccm and 10 mTorr, and the self-bias was - 85 V. An optical system with a laser ($\lambda = 635$ nm) focused on the sample allowed us to monitor and to detect the end of etching. We have done an over-etching to be sure that the unprotected NbN was completely removed, as illustrated in Fig. 3(b).

Step#5: Because the Ni mask short-circuits the HEB electrodes, we needed to remove it. This was done by wet etching with nitric acid at 69 % for 6 min. Then the sample was rinsed with deionized water.

Step #6: Finally, to protect the devices from the ambient atmosphere, we covered the sample with a 10 nm thick SiN passivation layer. This was performed by plasma enhanced chemical vapor deposition at 280 °C.

Finally the sample was diced into 6 chips of size 3 mm x 3 mm. Then, the chips are mounted either on a chip-carrier for DC measurements with a dipstick or into a mixer block for RF measurements with a cryostat, at the liquid helium temperature. Typically bolometers with a size of 0.15 µm x 2.0 µm (length x width) have a resistance of 75 Ω, and a critical temperature of 9-10 K.
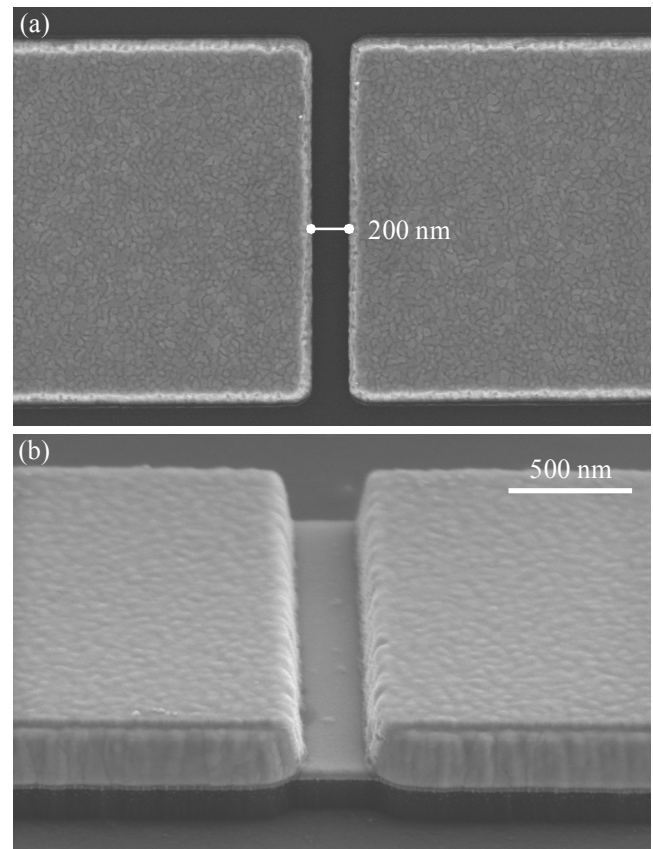

Fig. 3. SEM images of a device at different steps of fabrication. (a) HEB electrodes after lift-off; the gap between them defines the length of the bolometer. (b) Stacking of layers: the Ni on the top protects the bolometer during the NbN etching; Si substrate is partially etched due to an intentional over-etching.
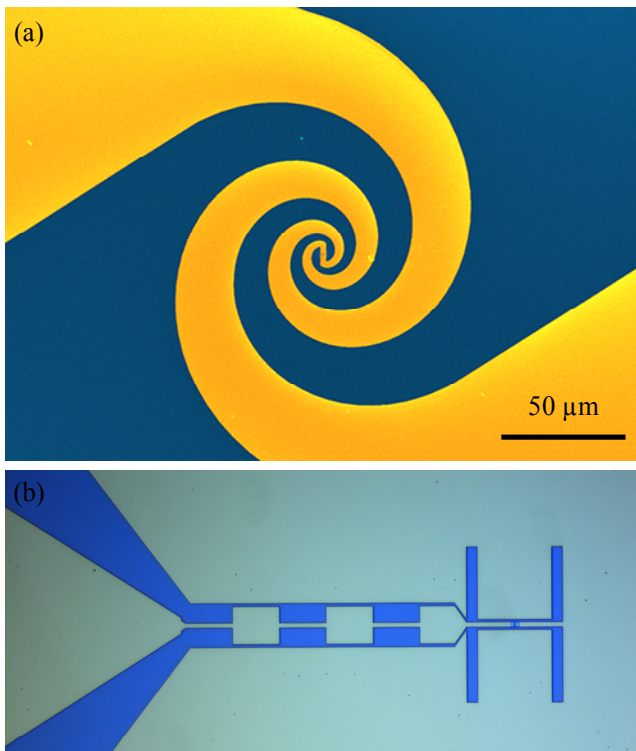
Fig. 4. (a) SEM image (colorized) of a log-spiral antenna designed for 1.3-1.6 THz. (b) Optical image of a double-slot antenna designed at 1.25 THz with a RF choke filter.

A particular case was that of the Si substrate with a SiO_2/Si_3N_4 membrane on both sides. At the end of the steps described before, we etched the Si substrate to get a suspended membrane. This was used to develop a new membrane based quasi-optical design. Details are reported elsewhere [3]-[5].

III. PROCESS KEY POINTS AND MIXER PERFORMANCES

Here, we highlight some key points, original features, and advantages of our process described above compared to conventional HEB fabrication processes found in the literature [6]–[13].

First, our process has a reduced number of steps (at least less lithography steps than conventional ones) and only e-beam lithography is required. This all e-beam process gives us a high flexibility to test in a short time different designs of antenna (shape, size, and operating frequencies ranging from 600 GHz to 2.5 THz in this work) as illustrated in Fig. 4 and reported in [14]-[16]. Typically, for a new design, it takes about one week to get the devices ready to be tested.

Second, a "direct" contact of gold on the NbN film is established without any additional superconducting layer (only the Ti adhesion layer beneath Au). In addition, there is no interface between HEB electrodes and antenna (as shown in Fig. 2) since they were processed with a single deposition of Ti/Au. By this way we hope to reduce the contact resistances close to the bolometer, which can be a source of undesired heating.

Third, the SiN passivation layer, deposited on the whole sample, did not require any lithography, lift-off or etching steps. This layer was thin enough to preserve the performance of the devices. Moreover, it is possible to wirebond the device directly through the 10 nm thick SiN (with Al wires at room temperature). The bondings we performed have withstood numerous thermal-cycles between 4 K and 300 K.

One of the quasi-optical HEB mixers, developed in the framework of the balloon project CIDRE, has been tested during a joint experimental campaign at SRON under the European research program Radionet-AMSTAR+. The lowest measured DSB receiver noise temperature at 2.5 THz without any correction was as low as 790 K and presented a relatively broad region in its voltage dependence. The LO power absorbed by the HEB was about 280 nW. The details of this experiment have been reported in [14].

IV. CONCLUSION

We have processed NbN hot electron bolometer on Si, sapphire and SiO_2/Si_3N_4 membrane substrates with a recently developed process requiring a reduced number of steps. This process has been proved to be reliable and high yielding. It also provides additional flexibility to validate new mixer designs in a relatively short time.

ACKNOWLEDGMENT

REFERENCES

[1] P. Yagoubov, G. Gol'tsman, B. Voronov, L. Seidman, V. Siomash, S. Cherednichenko, and E. Gershenzon, "The bandwidth of HEB mixers employing ultrathin NbN films on sapphire substrate," in *Proc. 7th Int. Symp. Space THz Technology*, Charlotesville, USA, Mar. 12-14, 1996.

[2] J.-C. Villégier, S. Bouat, P. Cavalier, R. Setzu, R. Espiau de Lamaëstre, C. Jorel, Ph. Odier, B. Guillet, L. Méchin, M. P. Chauvat, and P. Ruterana, "Epitaxial growth of sputtered ultra-thin NbN layers and junctions on sapphire," *IEEE Trans. Appl. Supercond.*, vol. 19-3, pp. 3375-3377, Jun. 2009.

[3] R. Lefèvre, Y. Delorme, A. Féret, F. Dauplay, W. Miao, L. Pelay, B. Lecomte, B. Guillet, G. Beaudin and J.-M. Krieg, "Development of membrane based NbN-HEBs for submillimeter astrophysical applications," in *Proc. 19th Int. Symp. on Space THz Technology*, Groningen, the Netherlands, April 28-30, 2008.

[4] G. Gay, R. Lefèvre, Y. Delorme, F. Dauplay, A. Féret, T. Vacelet, L. Pelay, W. Miao, M. Ba-Trung, J.-M. Krieg, L. Pagani, "Membrane based quasi-optical superconducting HEB mixers at Terahertz frequencies," in *Proc of SPIE Astronomical Telescopes & Instrumentation* 2012, to be published.

[5] Miao W., Delorme Y., Féret A., Lefèvre R., Lecomte B., Dauplay F., Krieg J.-M., Beaudin G., Zhang W., Ren Y., Shi S.C, "Performance investigation of a quasi-optical NbN HEB mixer at submillimeter wavelength," in *Proc. 20th Int. Symp. on Space THz Technology*; Charlottesville; USA; April 20-22, 2009.

[6] Y. B. Vachtomin, M. I. Finkel, S. V. Antipov, B. M. Voronov, K. V. Smimov, N. S. Kaurova, V. N. Drakinski and G. N. Gol'tsman, "Gain

bandwidth of phonon-cooled HEB mixer made of NbN thin film with MgO buffer layer on Si," in *Proc. 13th Int. Space THz Technology*, Cambridge, USA, Mar. 26-28, 2002.

[7] M. Kroug, P. Yagoubov, G. Gol'tsman, and E. Kollberg, "NbN Quasioptical Phonon Cooled Hot Electron Bolometric Mixers at THz frequencies", in *Proc. 3rd European Conf. on Appl. Supercond.*, Veldhoven, Netherlands, 1997 (Inst. Phys. Conf. Ser. No.158, pp.405-408,1997).

[8] M. Kroug, Ph.D. thesis, Chalmers University of Technology, Göteborg, Sweden, 2001.

[9] T. Lehnert, H. Rothermel, and K. H. Gundlach, "Low-noise heterodyne mixing with NbN microbolometers at 800 GHz," *J. Appl. Phys.*, vol. 83, p. 3892, Apr. 1998.

[10] S. Miki, Y. Uzawa, A. Kawakami, and Z. Wang, "IF Bandwidth and Noise Temperature Measurements of NbN HEB Mixers on MgO Substrates," *IEEE Trans. Appl. Supercond.*, vol 11, pp. 175-178, Mar. 2001.

[11] D. Meledin, C.-Y. Tong, R. Blundell, N. Kaurova, K. Smirnov, B. Voronov, and G. Gol'tsman, "Study of the IF Bandwidth of NbN HEB Mixers Based on Crystalline Quartz Substrate With an MgO Buffer Layer," *IEEE Trans. Appl. Supercond.*, vol 13, pp. 164-167, Jun. 2003.

[12] M. Hajenius, Ph.D. thesis, Delft University of Technology, Delft, Netherlands, 2007.

[13] A. Semenov, K. Il'in, M. Siegel, A. Smirnov, S. Pavlov, H. Richter, H.-W. Hübers, "Intermediate Frequency Bandwidth of a Hot-Electron Mixer: Comparison with Bolometric Models," *in Proc. 17th Int. Space THz Technology*, Paris, France, May 10-12, 2006.

[14] Y. Delorme, R. Lefèvre, W. Miao, A. Féret, W. Zhang, T. Vacelet, F. Dauplay, L. Pelay, J. Spatazza, M. Ba-Trung, J.-M. Krieg, Y. Jin, P. Khosropanah, J. R. Gao and S. C. Shi, "A quasi-optical NbN HEB mixer with 800 K DSB noise temperature at 2.5 THz," in *Proc. 22th Int. Symp. on Space THz Technology*, Tucson, April 26-28, 2011.

[15] W. Miao, W. Zhang, Y. Delorme, R. Lefèvre, A. Féret, and, S. C. Shi, "Non-uniform absorption of terahertz radiation in superconducting hot electron bolometer mixers," presented at the *Supercond. Centennial Conf.*, Den Haag, 2011, submitted for publication.

[16] W. Miao, W. Zhang, K. M. Zhou, Z. Lin, H., Q. J. Yao, Y. Delorme, R. Lefèvre, and S. C. Shi, "Direct detection behavior of a superconducting hot electron bolometer measured by Fourier transform spectrometer," *Proc. SPIE* 7854, 78540B, 2010.

Non-Uniform Absorption of Terahertz Radiation in Superconducting Hot-Electron Bolometer Mixers

W. Miao[1,2*], W. Zhang[1,2], Y. Delorme[3], R. Lefevre[3], A. Feret[3], T. Vacelet[3], and S.C. Shi[1,2*]

1 Purple Mountain Observatory, CAS, NanJing, Jiangsu, 210008, China
2 Key Lab of Radio Astronomy, CAS, NanJing, Jiangsu, 210008, China
3 Observeratoire de Paris, 61 avenue de l'Observatoire, 75014, Paris, France
* Contacts: wmiao@mwlab.pmo.ac.cn, scshi@mail.pmo.ac.cn, phone +86-25-8333-2204

Abstract——**We present an improved hot-spot model for superconducting hot-electron bolometer (HEB) mixers that takes into account the non-uniform absorption of terahertz radiation on the superconducting HEB microbridge. Given the fact that terahertz radiation is absorbed indeed in the region of a superconducting microbridge with its energy gap, which is in connection with the local electron temperature, lower than the photon energy of the incoming radiation, we assume that the absorption of the incoming radiation on a superconducting HEB microbridge is proportional to the local surface resistance, which can be computed in terms of the Mattis-Bardeen theory. With this improved hot-spot model, we found that LO (Local Oscillator)-pumped current-voltage and LO-pumped resistance-temperature characteristics of superconducting HEB mixers below the gap frequency can be precisely modeled.**

MgB₂ Hot Electron Bolometers for THz radio astronomy

S.Bevilacqua[1*], S.Cherednichenko[1], V.Drakinskiy[1], J.Stake[1], H.Shibata[2], and Y.Tokura[2]

1 Terahertz and Millimetre Wave Laboratory, Department of Microtechnology and Nanoscience,
Chalmers University of Technology, SE-41296 Göteborg, Sweden
2 NTT Basic Research Laboratories, 3-1 Wakamiya, Morinosata, Atsugi, Kanagawa 243-0198, Japan

`* Contact: stellab@chalmers.se`

Abstract——**We discuss Hot Electron Bolometer (HEB) THz mixers made of superconducting Magnesium Diboride (MgB₂) films. The films of 30 nm, 15 nm and 10 nm thick were deposited on sapphire substrates. The MgB₂ HEBs were patterned as a bridge at the feed point of a spiral antenna. The performance of the devices was investigated with respect to the gain bandwidth (GBW) and the noise temperature. The GBW was measured via mixing two signal sources (BWOs at 600 GHz). For the given films thicknesses, the GBW was measured to be 1.3 GHz, 2.3 GHz and 3.4 GHz, which is larger than for the NbN HEB mixers made of the same films thicknesses. Using the Y-factor technique a noise temperature of 800 K at 600 GHz local oscillator (LO) frequency was measured for mixers made of 10 nm MgB₂ film. Besides the films thickness, the gain and the noise bandwidths are functions of the films critical temperature, Tc. For 10nm films, with Tc=15K, a noise bandwidth on the order of 8GHz was measured. From these measurements and from the material parameters a GBW of 8 GHz (noise bandwidth >10GHz) is expected for 3-5 nm MgB₂ films.**

ALMA East Asia Front-End Integration Center

Yau De Huang[1], Nagayoshi Ohashi[1], Ming-Tang Chen[1], Patrick Koch[1], Ching Tang Liu[2] , Chi-Den Huang[2], Chi-Li Pin[2], Fang-Chia Hsieh[2], Yen-Hsiang Tseng[2], Chien-Ping Chen[1]

[1] *Academia Sinica, Institute of Astronomy and Astrophysics, P.O. Box 23-141, Taipei 106, Taiwan*
2 ASRD/CSIST, Aeronautical Systems Research Division / Chung-Shan Institute of Science and Technology.
Contact: ydhuang@asiaa.sinica.edu.tw, phone +886-2-2366 5342

Abstract—— **The East Asia Front-End Integration Center (EA-FEIC) was established in 2006 as one of the three Front-end Integration Centers in the world for the Atacama Large Millimeter/submillimeter Array (ALMA) project. The EA-FEIC is located in the facility of the Aeronautical Systems Research Division(ASRD) of the Chung-Shan Institute of Science and Technology (CSIST) in Taichung, Taiwan, and it was originally tasked with integrating and testing 17 sets of front-end by 2012. The first engineering model front-end, fully integrated by the EA-FEIC, was delivered to the ALMA Operations Support Facility (OSF) in Chile in 2008 December. In 2009, the EA FEIC was tasked to share the workload from the North America FEIC by taking on 5 more sets of front-end. To accelerate the overall front-end delivery rate, a second production line was added, and passed the Operation Readiness Review (ORR) in 2010 October. Currently, on average the EA-FEIC delivers one front-end equipped with four receiver bands in every 5 weeks, and it has already achieved the major milestone by completing the original 17 sets of front-end in January 2012. This report will briefly review the EA FEIC design, its test facility, and its integration and evaluation procedures. It will particularly address the key components contributing to the success of this FEIC, namely the execution, management, and quality control.**

Integration and verification of ALMA receiver front ends

T. Hasegawa[1, 2*] and the ALMA Front End Integration Subproject Team

1 Joint ALMA Observatory, Alonso de Córdova 3107, Vitacura 763 0335, Santiago de Chile
2 National Astronomical Observatory of Japan*, Mitaka, Tokyo, 181-8588, Japan
* Contact: tetsuo.hasegawa@nao.ac.jp, phone +81-422-34 3843

Abstract——We present the method and results of integration and verification of the receiver Front Ends (FEs) for the Atacama Large Millimeter/submillimeter Array (ALMA), an international partnership of Europe, North America and East Asia in cooperation with the Republic of Chile. For installation in the 66 antenna elements of ALMA, 70 FEs including four spares are being integrated. The FEs will be initially equipped with 7 bands (84 – 116 GHz, 125 – 163 GHz, 211 – 275 GHz, 275 – 373 GHz, 385 – 500 GHz, 602 – 720 GHz and 787 – 950 GHz) for all antennas and another band (163 – 211 GHz) for selected antennas. The FE is designed to include up to 10 bands with the "band cartridge" concept, which enables us to replace a faulty band cartridge or install additional bands later.

For the purpose of the assembly, integration and verification of the FE assemblies, we have established three FE Integrations Centers (FEICs); at National Radio Astronomy Observatory in Charlottesville, USA, at Rutherford Appleton Lab., STFC in UK, and at the Aeronautical Research Laboratory, Chung Shan Institute of Science and Technology in Taiwan. Each FEIC is equipped with the FE test and measurement system including cold and ambient temperature loads for noise temperature measurements and near-field beam scanners for verification of the optical performance. Tilt tables enable us to test FEs at different angle of elevation between horizontal and vertical positions.

So far, 43 FEs have been delivered to Chile from the FEICs after passing a set of verification tests and measurements. They have been installed in the ALMA antenna elements on site, and have been in use in commissioning and science observations. We also present some statistics of the performances measured at FEICs that indicates a remarkable uniformity of these FEs.

Upgraded Local Oscillator System for the ALMA Band 5 Receiver

Manju Henry[*], David Gooding, Hui Wang, Brian Ellison, Byron Alderman and P. G. Huggard

RAL Space, STFC Rutherford Appleton Laboratory, Harwell Oxford, United Kingdom.

* Contact: Manju.Henry@stfc.ac.uk, phone +44-1235446343

Abstract— **The ALMA Band 5 receiver has recently completed a trial phase of development and pre-production. The work has been led by the University of Chalmers' Group for Advanced Receiver Development, Sweden, and in partnership with the United Kingdom's Rutherford Appleton Laboratory (RAL), the latter developing the receiver local oscillator (LO) chain. During 2011 the first Band 5 receiver was successfully deployed at the ALMA Observatory site, and more receivers will follow in 2012.**

The RAL Band 5 LO system operates over the frequency range of 171-203 GHz with a levelled dual minimum power output of 0.5 mW. The LO is used to pump two independent SIS sideband separating mixers that are part of a dual polarisation receiver system encompassing the input signal range of 163-211 GHz, and with a 4 to 8 GHz instantaneous frequency bandwidth. The LO uses a tunable YIG oscillator as the fundamental source and which is harmonically multiplied to the required frequency range by a combination of commercially available and bespoke components; the latter have been developed by the Rutherford Appleton Laboratory and include a Ka band photomixer, required for frequency stabilization, and a high efficiency millimetre wave doubler. Six LO units have been constructed and delivered to date.

During the LO development phase, initial receiver trials revealed a high level of amplitude modulation (AM) noise associated with the LO which affected receiver noise performance and which was partially, though not wholly, cured by attention to inter-component matching and adjustment of millimetre wave power level settings. With the objective of totally eradicating the LO noise, RAL has subsequently performed a redesign of key sections of the LO millimetre wave circuitry that have been determined to be the source of the noise. Specifically, the millimetre doubler has been upgraded to provide high frequency up-conversion efficiency with low input power, and uses RAL fabricated varactor diodes in a more optimum configuration. The, refined design will enable the operation of the doubler in a saturated mode which, in turn, will limit the undesirable LO AM noise component.

An additional benefit of the upgraded doubler is a reduction in component count associated with the millimetre wave circuitry located within the receiver vacuum space, and which is therefore less accessible. Combining the doubler with a commercially available high-power tripler allows the removal of a W-band power amplifier, these having proved difficult to source with consistent specification performance. Moreover, reducing the number of active components located in the receiver cryostat enhances the production efficiency and lowers the unit cost; both key factors that will influence the anticipated move towards full production of the ALMA Band 5 receivers.

In addition to presenting the Band 5 LO upgraded doubler design, we will also describe an improvement to the LO phase lock circuit. This uses a novel integrated W-photomixer and subharmonic mixer and will enhance compatibility of the LO chain with the ALMA frequency reference system. A schematic of the upgraded LO chain is shown in Figure 1.
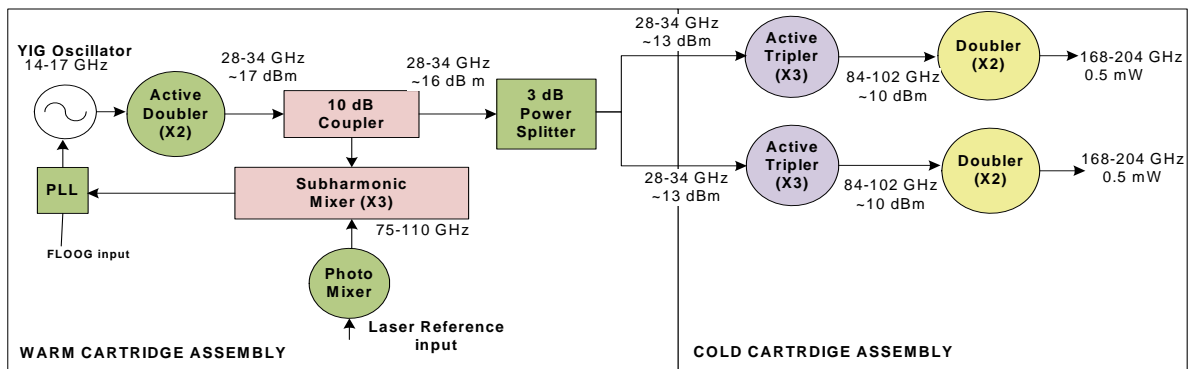
Figure 1: Schematic representation of the upgraded RAL Band 5 LO assembly

Sideband Separating Mixer for ALMA Band 9 Upgrade: operational aspects.

J. Barkhof[1*], A.V. Khudchenko[2], R. Hesper[1], A.M. Baryshev[1,2], F.P. Mena[3], T.M. Klapwijk[4] and M.C. Spaans[1]

1 NOVA/Kapteyn Astronomical Institute,University of Groningen, The Netherlands
2 Netherlands Institute for Space Research, Groningen, The Netherlands
3 Electrical Engineering Department, Universidad de Chile, Santiago, Chile
4 Kavli Institute of Nanoscience, Delft University of Technology, The Netherlands
`* Contact:  J.Barkhof@sron.nl, phone +31-50-363 4018`

Abstract──**We have built a Sideband Separating mixer (2SB), which has demonstrated a sideband rejection ratio as high as 15 dB over the full RF band, well within the ALMA specifications of 10 dB. The SSB noise temperature is also within the ALMA requirements of 336 K over 80% of the band, and 500 K over the entire band.**

The algorithms and testing procedures for Dual Sideband (DSB) Band 9 mixer were developed and successfully implemented few years ago. The DSB mixer contains only one SIS junction, whereas for 2SB mixer two SIS junctions are required. That makes an essential difference in the procedures of the receiver testing and operation.

In our report we present low time consuming procedures for 2SB receiver testing. We additionally focus on the measurements of Noise Temperature and Sideband Rejection Ratio, which both sufficiently depends on the bias voltages of both SIS junctions. The possibilities to implement "old" DSB procedures to operate 2SB mixer, which simplify the Band 9 upgrade, were also studied.

Improvements in ALMA band 10 optics:
Influence of IR filters and solutions

A. Gonzalez[1*], Y. Uzawa[1], K. Kaneko[1], and Y. Fujii[1]
1 National Astronomical Observatory of Japan*, Mitaka, Tokyo, 181-8588, Japan
* Contact: Alvaro.Gonzalez@nao.ac.jp, phone +81-4-2234-3879

Abstract—**ALMA band 10 (787 – 950 GHz) tertiary optics is located in the 4K stage of the ALMA cryostat and the RF signal has to go through two infrared filters and one quartz window in the optical path between optics and secondary. It has been found that when the standard optics design is used at cryogenic temperatures in the real receiver, performance is degraded with respect to measurements at room-temperature without filters and window. This degradation consists of strange beam side lobes or unexpected interference patterns which degrade efficiency. The origin of this degradation has been found to be multiple reflections in filters and in the plane of the corrugated horn aperture. An improved design using chamfered-rim corrugated horns and absorbent paint around the horns has been adopted and tested. Results show improvements and achieved performance is similar to performance before inserting filters and window in the optical path. Cross-polarization measurements have also been performed to guarantee there is no degradation with the new optics design. This paper proposes a very simple solution for a problem which can be potentially encountered in practical mm/sub-mm cryogenically-cooled receivers.**

Dual frequency ALMA operation extension

A. M. Baryshev[1,2], R. Hesper[2], A. Khudchenko[1], T.M. Klapwijk[3]

1 SRON Space Research of Netherlands* Groningen, 9747 AD, The Netherlands
2 Kapteyn Astronomical Institute, Groningen, 9747 AD, The Netherlands
3 Delft University of Technology, Delft, 2628 CJ, The Netherlands
* Contact: a.m.baryshev@sron.nl, phone +31-50-3638287

Abstract— **Atakama Large Millimiter Wave array (ALMA) is an submm interferometer which is currently being constructed in Atacama desert in Chile at altitude of 5 km. This interferometer consists of 12m diameter antennas each equipped with suite of state of art receivers covering atmospheric transmission windows in 30-950 GHz range. Design of current generation of receivers is finished and there is significant effort directed towards possible future improvement and eventual upgrade. In this contribution we would like to propose and consider in detail a possibility to operate ALMA interferometer at two frequencies/two polarizations at the same time and from the same point on the sky. This mode of operation has significant advantages, because it allows to increase available observing time twice, improve instantaneous UV-coverage, significantly improve atmospheric transparency variation correction algorithms, and obtain spectral line ratios with much higher calibration accuracy. Importantly, dual frequency operation also allows to use ALMA in a new way, by employing dual photon interferometry, which helps to acquire a short baseline spacing information and potentially allows to double spatial resolution of ALMA for suitable sources. In particular we will discuss possible implementations, and operation modes of dual ALMA band 9 (602-720 GHz)/band X receiver in more detail.**

Wideband THz Sources Using Waveguide Diplexers

J.L. Hesler, D. Koller, and T.W. Crowe

Virginia Diodes Inc., Charlottesville, USA (Hesler@vadiodes.com)

Abstract—**This talk will discuss the development of wideband THz sources for use as local oscillators in astronomical receivers. VDI's THz sources typically consist of a cascade of high efficiency varactor doublers followed by one or more broadband varistor multipliers. The frequency coverage of these sources is set by the varactor multipliers, which have narrower bandwidth than the varistor multipliers. In order to achieve wide bandwidth while retaining the high output power achievable with varactors, a waveguide diplexer is used to frequency multiplex two varactor chains together at the input of a single cascade of varistor multipliers. As an example, a source configuration covering 1.2-1.6 THz is shown in Fig. 1. The diplexer, in the range 130-180 GHz, consists of lowband and highband filters feeding into a single waveguide. The frequency gap at the crossover between the filters can be centered on the water absorption line. Based upon existing varactor-based VDI sources we expect an output power of 5-10 uW over the two output bands.**

A prototype WR-10 (75-110 GHz) waveguide diplexer has been designed, and a schematic and the predicted performance are shown in Fig. 2. Initial measurements of the lowband filter verified the filter frequency response and yielded an insertion loss of 0.3 dB in the passband. The nominal frequency bands of the WR-10 diplexer are 75-91.5 GHz and 93-110 GHz. VDI has developed broadband high power varactor chains at these two bands, with measured output power of 250-500 mW over the lowband, and 200-400 mW over the highband. The diplexer is being machined, and test results of the diplexer and THz sources using the diplexer will be presented at the conference.
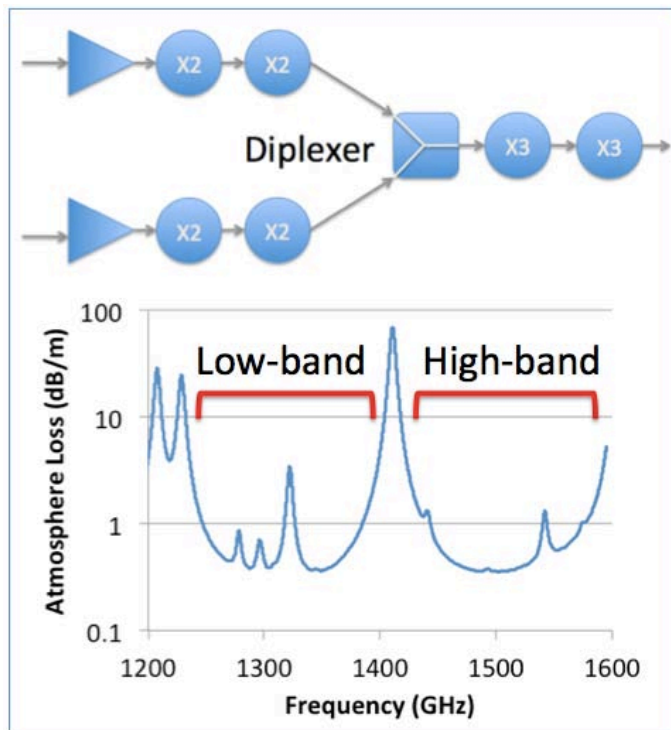
Fig. 1. Proposed configuration for a broadband 1.2-1.6 THz source, with output bands compared to atmospheric attenuation. The gap between the diplexer bands can be centered on the absorption line.
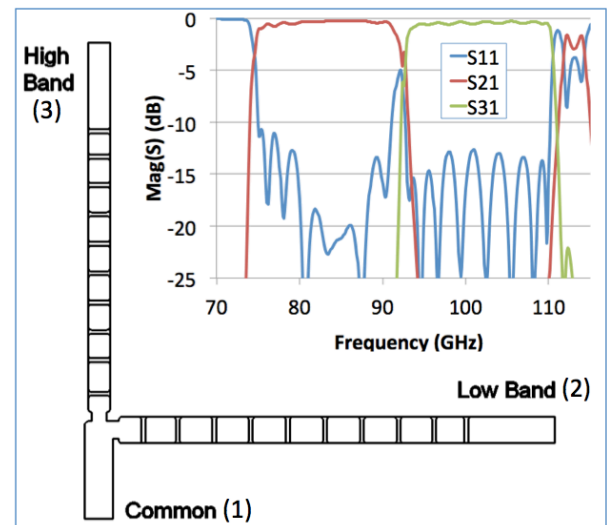
Fig. 2. Schematic and simulated performance of a WR-10 waveguide diplexer.

A High-Power Biasable 180-200 GHz Schottky Frequency Doubler Using Single-Waveguide Power-Combining

J. V. Siles[1,2*], A. Maestrini[2,3], J. Treuttel[2], H. Wang[4], H. Sanghera[4] and B. Alderman[4]

[1] *NASA Jet Propulsion Laboratory, Pasadena, CA 91109, USA*
[2] *Observatoire de Paris, LERMA, Paris, 75014, France*
[3] *Université Pierre et Marie Curie , Paris, 75005, France*
[4] *Rutherford Appleton Laboratory, STFC, Chilton, UK*

Contact: {jose-vicente.siles,alain.maestrini}@obspm.fr, phone +31 4051 2037

Abstract–

   With state-of-the-art all-solid state terahertz sources producing now power levels of tenths of microwatts beyond 2 THz [1], efforts are now focused on increasing the amount of produced LO power in order to enable both arrays and room-temperature single-pixel receivers beyond 1-2 THz. For this task, more compact and effective power-combining topologies need to be employed to increase the power generated by Schottky diode based multiplied LO sources.

   A novel dual-chip in-phase power combining doubler topology consisting in using two chips "sandwiched" within a single-waveguide channel was first introduced and successfully demonstrated in [2]. The proposed topology was robust and compact and avoids the use of Y-junctions or hybrid couplers. However, the achieved performance at 190 GHz was not state-of-the-art since the Schottky diodes available were not optimum for multiplier operation.

   In this work, we present the design of a new 180-200 GHz MMIC doubler based in this recently introduced single-waveguide dual-chip topology (see Fig. 1a) and using the 12 µm GaAs T-shape membrane process and Schottky diode process developed at the Rutherford Appleton Laboratory (RAL). The diodes are biased to achieve optimum varactor conditions and maximize the second harmonic generation. Two independent bias lines are included (one per chip) to allow the possibility of compensating possible unbalances between the two chips. State-of-the-art performance (25-30 % efficiency) is expected with power handling capabilities from 200 mW up to 400 mW (see Fig. 1b)

   This work is part of *The Millimeter-wave Integrated Diode and Amplifier Source (MIDAS)* project to develop generic integrated Schottky diode and amplifier sources using European technology. The circuits are now under fabrication at the Rutherford Appleton Laboratory.
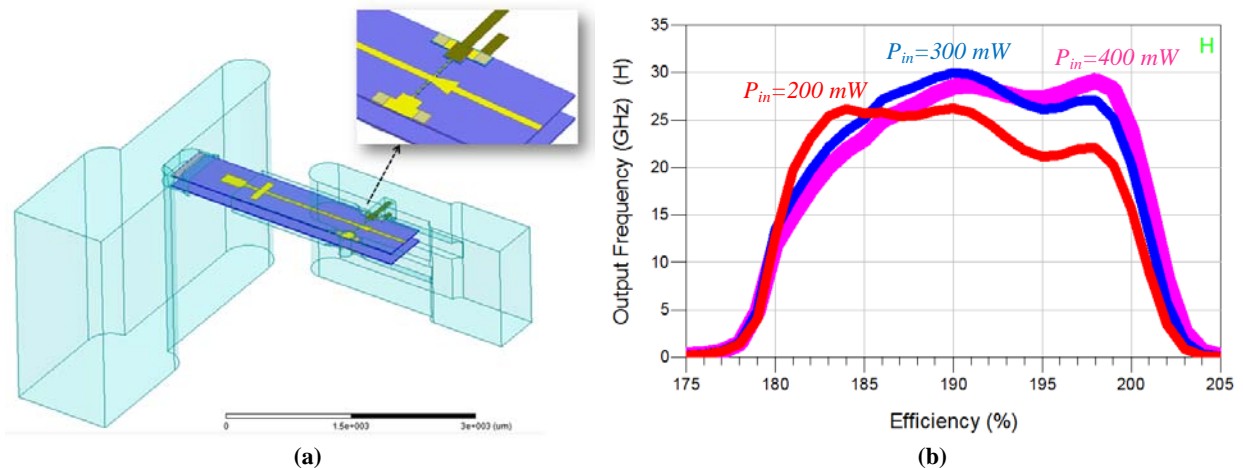
Fig. 1. MIDAS high-power dual-chip single-waveguide 190 GHz doubler design (a) and expected performance (b).

[1] A. Maestrini, I. Mehdi, J.V. Siles, J.S Ward, R. Lin, B. Thomas, C. Lee, J. Gill, G. Chattopadhyay, E. Schlecht, J. Pearson and P. Siegel, "Design and characterization of a room-temperature all-solid state source tunable from 2.48 to 2.75 THz," *IEEE Transactions on Terahertz Science and Technology*, 2012, *in press.*
[2] J. Siles, A. Maestrini, B. Alderman, S. Davies, H. Wang, J. Treuttel , E. Leclerc, T. Narhi, and C. Goldstein A single-waveguide in-phase power-combined frequency doubler at 190 GHz, *IEEE Microwave and Wireless Components Letters*, Vol.21, No. 6, pp. 332-334, Jun 2011.

W-band balanced frequency tripler using a novel coupled lines biasing scheme compatible with flip-chip mounting

B. Thomas[1*], A. Walber[1], J. Treuttel[2], R. Henneberger[1], and B. Alderman[3]

1 Radiometer Physics GmbH – RPG, Meckenheim, 53340, Germany
2 LERMA, Observatoire de Paris, 75014, France
3 Teratech Co. Ltd., RAL Space, Didcot, OX11 0QX, UK
`* Contact: thomas@radiometer-physics.de, phone +49-2225-999-81-20`

Abstract- **We present here a novel biasing scheme similar to [1] for balanced frequency triplers that is compatible with flip-chip mounting of the Schottky diodes chip onto a host carrier circuit, and that does not involve complicated lithographic fabrication techniques such as on-chip or on-circuit thin film capacitors. It uses coupled suspended striplines circuit architecture in order to bring two separate biasing lines to both half of the chips, allowing for independent biasing of each half of the diodes chip. This can be advantageous in order to correct for slight imbalances in the chip and circuit. Measurement results on a 83-105 GHz tripler using Teratech discrete tripler diodes and an AlN based circuit with a coaxial input shows a typical efficiency of approx. 7 %, with input power handling up to 200 mW, and 3 dB RF bandwidth of 83-105 GHz.**

I. INTRODUCTION

W-band sources are the base of high power and high frequency sources for millimeter and sub-millimeter spectroscopic and radiometric applications that require high spectral purity and high efficiency. For instance, good efficiency and minimum output power of 3-5 mW is required at W-band to pump a 183 GHz sub-harmonic mixer without the need to re-amplify the signal [2]. Moreover, in order to build Local Oscillator chains for the high millimeter and sub-millimeter frequencies, it is necessary to have a W-band source that does not generate undesired spurious harmonics that could mix in the following amplification/multiplication stages.

Traditionally, W-band multiplied sources that do not include an amplifier as last stage are either transistor based multipliers that are limited in efficiency due to the resistive nature of the active device (FET), or Schottky diode based, which are more efficient and have demonstrated already very good efficiencies and power handling capabilities. The possibility to reverse bias each Schottky diode is an advantage compared to unbiased devices in anti-parallel configuration for instance since it improves the efficiency and power handling capabilities. A cross-channel balanced configuration is usually preferred to a single anode device since it provides high even harmonics rejection (mainly 2nd and 4th one), and enables to put many Schottky devices in series in order to improve power handling capabilities. However, balanced triplers are traditionally more suited to MMIC technology since they traditionally require an on-chip MIM capacitor for biasing

[3-4]. At W-band, it represents a lot of real estate on the wafer (chip size is relatively big).

We present here a novel biasing scheme for balanced frequency triplers that is compatible with flip-chip mounting of the Schottky diodes chip onto a host carrier circuit, and that does not involve complicated lithographic fabrication techniques such as on-chip or on-circuit thin film capacitors.
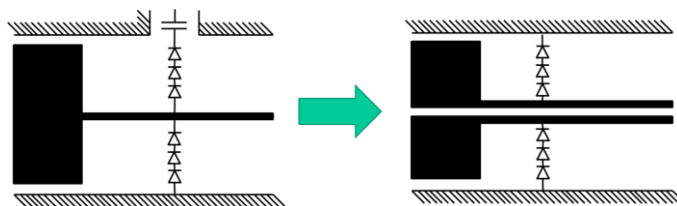
Fig.1: Proposed W-band balanced tripler using discrete Schottky diode chip using novel coupled lines biasing scheme (right) *VS* traditional biasing of balanced triplers (left).

II. W-BAND TRIPLER DESIGN

This novel approach uses a similar architecture as the multi-anode balance tripler previously described, but having a novel biasing scheme based on coupled lines. This original transmission line enables the use of discrete chip in a balanced configuration, without the need to develop a more complex on-chip or on-circuit MIM capacitor. This novel approach is illustrated in Fig. 1&2. As you can see in Fig. 1, a narrow gap in the central microstrip line allows for independent biasing of each separate transmission lines. At RF frequencies, these lines are coupled to each other, and the main propagating mode is the microstrip mode, as it would be if there was only one central microstrip line. By introducing as well gap on the GaAs tripler central pad as shown in Fig. 2, each branch of the chip featuring 3 anodes each can be reverse biased independently, making all the 6 anodes operating in Varactor mode, as it would be with a more traditional multi-anodes tripler. This architecture also allows for slightly different bias voltages to be applied on each branch of the chip, in order to compensate for any slight imbalances in the chip electrical characteristics. It is also expected that a differential biasing can be applied instead of two independent biasing voltages in order to bias the tripler.
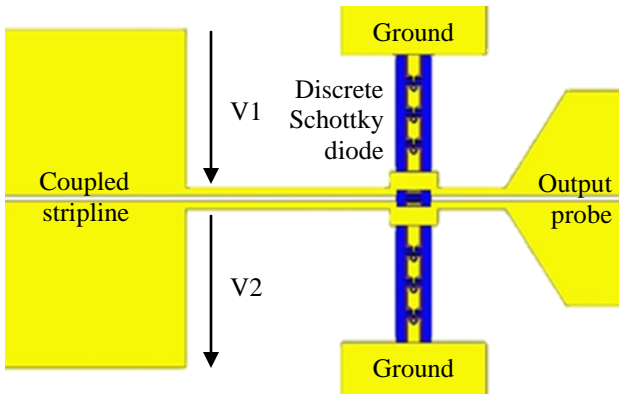
Fig.2. W-band balanced tripler based on novel coupled lines biasing scheme, and featuring a discrete 6-anodes tripler chip transferred onto AlN designed by RPG and fabricated by RAL using the standard Teratech process [5]. Chip size is approx. 700 um x 50 um.

The optimization and simulation of the tripler is done using a combination of 3D-EM simulations using HFSS (Ansys) [6], and ADS (Agilent) [7] non-linear circuit simulations. The predicted performances are shown below. For a fixed input power of 80 mW, the predicted efficiency ranges from 4% to 8% in the 82-105 GHz frequency range. The input return loss is calculated better than -10 dB, and the 4th harmonic rejection better than 30 dB. The input power range is estimated between 50 and 200 mW, thanks to the biasing capabilities of the tripler.
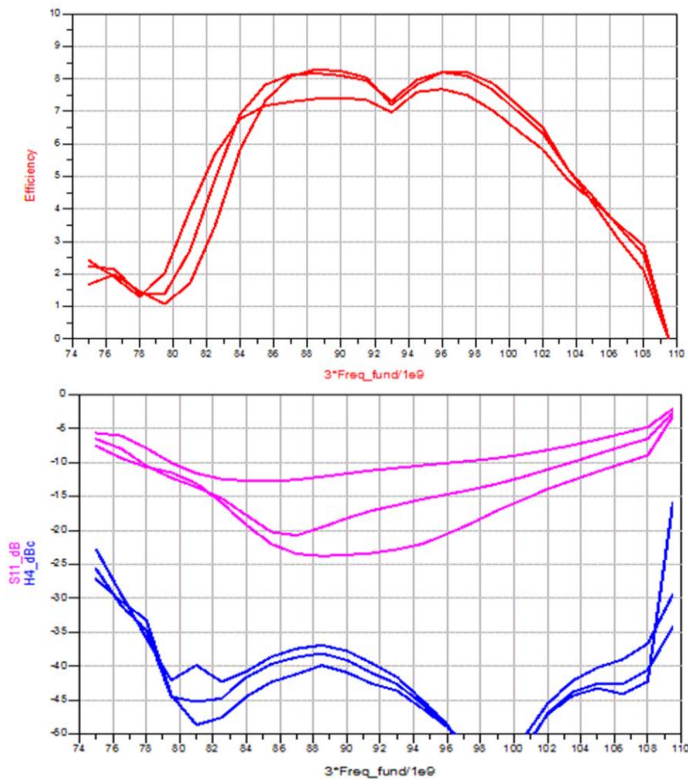
Fig.3.Top: Predicted performance of the W-band tripler for an input power of 80 mW, and differential reverse biasing between 2 V and 6 V. Bottom: upper curves shows the efficiency, lower curves show the input return losses and 4th harmonic rejection.

III. W-BAND TRIPLER FABRICATION

The W-band tripler featuring an AlN based circuit has been designed, fabricated and assembled by RPG. Two SMA connectors are used for the biasing lines. One K-type glass bead connector is used for input RF signal in Ka-band. The circuit is based on a 50 um thick AlN substrate. This choice is motivated by the high thermal conductivity of AlN (typ. 120-180 W/m.K), allowing for efficient heat dissipation of the tripler chip.
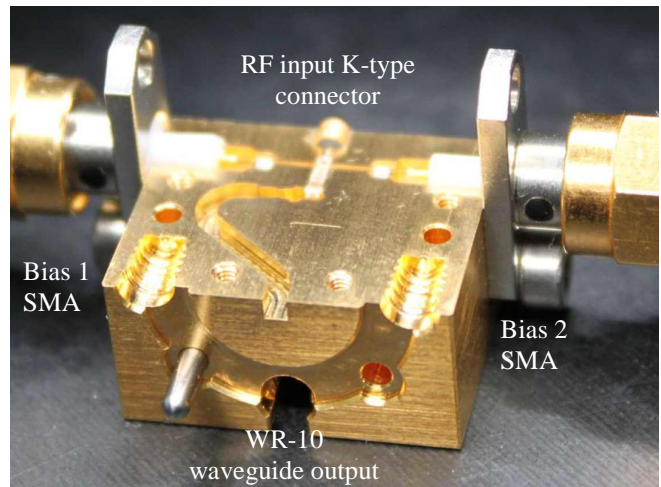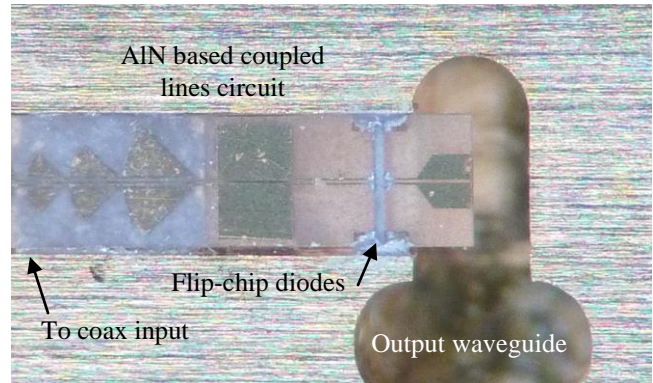
Fig.4. Top: Detailed view of the W-band tripler circuit, with the 6-anodes Varactor tripler chip flip-chip mounted onto the 50-um AlN circuit. Bottom: View of the RPG W-band tripler block (lower half), with the AlN circuit mounted inside and connected to two SMA connectors for biasing and a K-type glass bead for RF input signal.

IV. W-BAND TRIPLER TEST RESULTS

Measurement results on a 83-105 GHz tripler using RAL discrete tripler diodes and an AlN based circuit with a coaxial input shows a typical efficiency of approx. 7 %, with input power handling up to 200 mW, and 3 dB RF bandwidth of 83-105 GHz. The bias voltage ranges from 1.7 V/branch in the low power range (approx. 50 mW), up to 6.5 V/branch in the high power range (approx. 160-200 mW), demonstrating the wide range of usable input powers for this tripler. Moreover, it is noticed that a fixed offset of 0.3 V between each branch is

necessary to get optimum efficiency and output power, regardless of the input frequency and power.
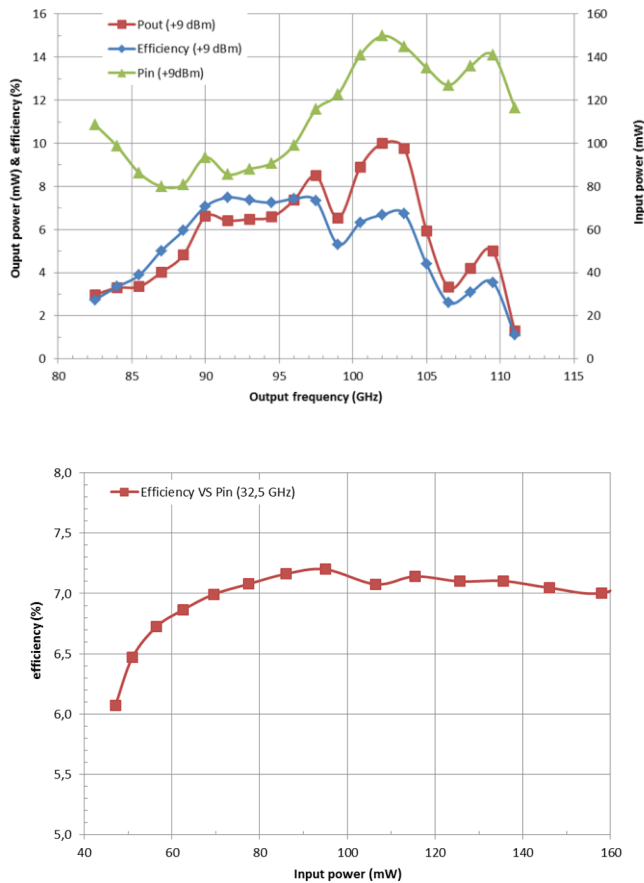
Fig.5. Top: Performances of the W-band tripler VS output frequency.
Bottom: Efficiency VS input power of the W-band tripler at 97.5 GHz output frequency.

CONCLUSION

The design, fabrication and test of a W-band balanced tripler based on discrete GaAs Schottky diodes fabricated by RAL is presented. It includes a novel simple biasing scheme based on coupled microstrip lines on AlN based substrate designed and fabricated by RPG. Test results show that the tripler exhibits performances which are in accordance with the simulations. The output power is over 5 mW between 88.5 GHz and 105.5 GHz which corresponds to almost half of the W-band. It is also possible to replace the input coaxial K-type connector by a waveguide flange connection in order to reduce spurious harmonics from the lower frequency stages.

The tripler architecture has been validated over a wide range of input frequencies (i.e. 27.5-35 GHz) and powers (i.e. 80-200 mW). The microstrip input access of this W-band tripler allows further integration of an active multiplier/amplifier driver stage which is commercially available in Europe (for instance the CHX-2095 and CHA3093c devices from UMS [8]) into a very compact W-band source.

REFERENCES

[1] J. Treuttel, "Multipixel heterodyne receiver at submillimeter wavelength for atmospheric sounding", PhD thesis, Observatoire de Paris, France, May 2011.
[2] MetOp- Second Generation, Space Requirements Document – SSRD -, ESA MetOp-SG team, MOS-RS-ESA-SYS-0001, January 2011.
[3] A. Maestrini, et al., "Multi-Anode Frequency Triplers at Sub-Millimeter Wavelengths", proceedings of the 16th International Symposium on Space Terahertz Technology, paper P5-3, Göteborg, Sweden, 2-4 May 2005.
[4] H. Wang, "Conception et modelisation de circuits monolithiques a diode Schottky sur substrat GaAs aux longueurs d'onde millimetriques et submillimetriques pour les recepteurs heterodynes multi-pixels embarques sur satellites et dedies a l'aeronomie ou la planetologie", PhD thesis, Observatoire de Paris, France, 2009.
[5] Teratech Comp. Ltd . Website : http://www.teratechcomponents.com/
[6] High Frequency Simulation Software, v9.2, Ansys Corporation, Pittsburgh, PA, USA.
[7] Advanced Design System 2011, Agilent Technology, Palo Alto, CA, USA.
[8] United Monolithic Semiconductors. Website: htpp://www.ums-gaas.com/

Solid State Frequency Multipliers at Sub-Millimeter Wavelength Using European Schottky Technology

J. Treuttel, F. Yang, M. Benzazaa, A. Maestrini, J. V-Siles, H. Wang, H.Sanghera, B.Alderman.

Abstract—We report upon the design of solid state frequency multipliers : a 380 GHz single-chip doubler, a 300 GHz single-chip tripler and a 300 GHz power combined dual-chip tripler. They are all designed with a dedicated model of european integrated Schottky diodes and in the triplers case with their on-chip capacitor for bias connection. A dedicated technology is developed in order to enhance device performance, in particular improve the power handling capabilities which vary from 50 mW for the single chip 380 GHz doubler up to 400 mW for the 300 GHz dual-chip tripler. The circuits are under fabrication at STFC-RAL.

Index Terms—Frequency multipliers, Schottky diode, Doubler, Tripler, Power-combining, Sub-millimeter wave.

I. INTRODUCTION

The terahertz spectrum is now willing to be fully exploited to enrich applications that span the physical, biological, and medical sciences. One of the remaining technology challenge at THz frequencies is to generate conveniently useful amounts of power. Schottky diodes based solid-state devices stand as first candidates where compact, non-cryogenic and efficient sources are needed. Therefore the Millimeter-wave Integrated Diode and Amplifier Source (MIDAS) project aims at developing MMIC power amplifiers and Schottky varactor diode circuits using European technology. The primary objective of the program is to demonstrate a 125 mW source operating at 270 - 300 GHz in conjunction with power combining technology. The designs of three last stage frequency multipliers using on-chip capacitor and integrated Schottky diodes are proposed during the first phase of the program and are presented in this article: a single-chip 380 GHz doubler, a 300 GHz single-chip tripler, and a 300 GHz in-phase power-combined dual-chip tripler. We report on the design and performance of these three designs.

A. Towards a high frequency and high power MMIC fabrication process

MMIC technology applied to integrated Schottky structures is the key issue to lead to reproducible circuit performances and regarding to this could bring the instrumentalists forward to build well in-phase multi-chip power-combined sources. Furthermore, the technology developments pointed here favour high frequency and high power handling operation. For these reasons the main features discussed during the program focus on lowering the transmission losses while giving a great importance to thermal management : the mesa size is lowered down to 18μm $\times$ 18μm, on-chip capacitors based on polyamide insulating layer are developped to fulfill signal propagation requirements, the diode and circuit parameters are defined during the design phase to reach wide impedance matching, and beam leads (metal membrane) allow to suspend the membrane while providing precise grounding and thermal contact with the block. Diamond membrane has also proved to be beneficial to strengthen the heat path [1] but the bonding to a GaAs membrane is critical [2]. Moreover if the dielectric constant of the processed CVD diamond is not perfectly controlled, the design cannot be optimized accurately. Therefore a thick GaAs membrane could be equivalent electrically and thermally to a thin GaAs membrane transferred onto a diamond membrane. It was decided to design MIDAS project first phase frequency multipliers with a 12μm-thick GaAs membrane providing a thermal capacitance that could be empirically compared to its diamond-substrate transferred circuit counterpart.
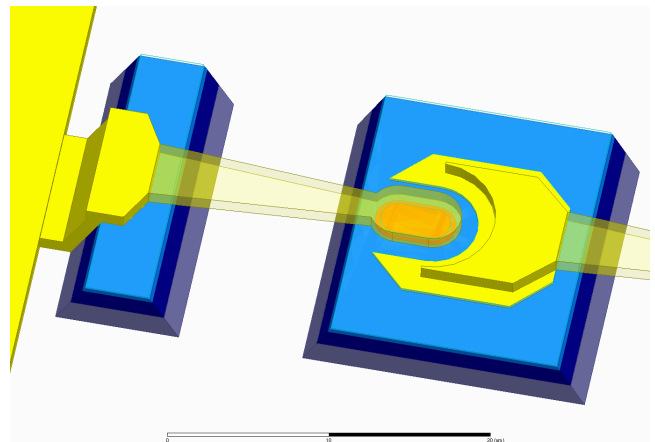

Fig. 1.   3D structure of the STFC Schottky diode upgraded for MIDAS program.

B. 380 GHz Doubler design

The circuit design of a 380 GHz fixed-tuned MMIC doubler is based on the balanced topology presented in [3]. The input frequency was chosen according to the second stage doubler output issued separately in this proceedings, which features a 190 GHz single-waveguide in-phase dual-chip doubler based on [4] and that is expected to provide between 50 to 100 mW depending on its input power handling capabilities (200 to 400 mW at W band) and on the first stage power amplifiers efficiency also developped during the program [1]. The 380 GHz doubler features an anti-serie set of four planar Schottky diodes integrated within the passive microstrip circuit onto a 12-μm thick GaAs membrane. The circuit geometry prevents the input fundamental signal from leaking into the output and also prevents the output second harmonic signal from leaking into the input waveguide. Moreover, the reduced height input waveguide cut off the input signal TM_{11} mode for a more efficient coupling to the diodes. A stepped impedance filter section at the opposite end of the circuit is used as a DC bias voltage path and avoid the leakage of the second harmonic through this port. Therefore on-chip capacitor is not necessary for this particular design. The input and output waveguides, the microstrip channel and the DC bias connector sockets are milled into two split-waveguide metal blocks. The position of the input backshort, the diodes geometry, the input stub near the diodes and the output probe were optimized to reach a wide impedance matching over the input frequency band.
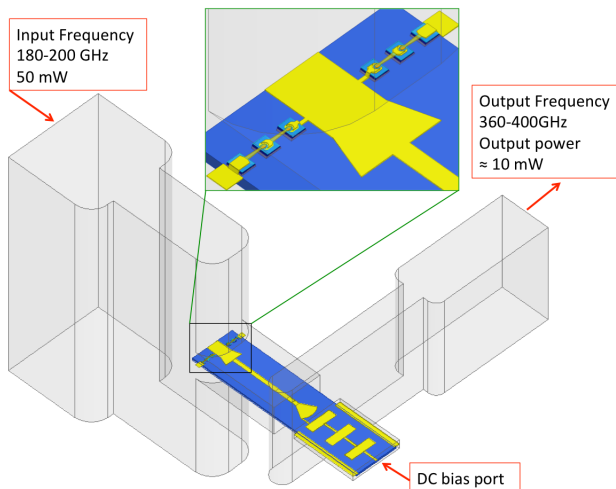
Fig. 2. Picture of the fully optimized 380 GHz doubler placed inside the waveguide cavity.

The methodology used for the design uses a combination of linear/non-linear circuit simulations (Agilent ADS) and 3D electro-magnetic simulations (Ansoft HFSS). Firstly, a standard diode model from the ADS library was implemented together with its close 3D passive environnement (diode cell), plus ideal input and output matching networks. During this simulation, the anode zero junction capacitance and the diode cell geometry (anodes positions, input channel width and input stub length) were optimized using the harmonic-balance

[1]by Radiometer Physics Gmbh

routine for 50 mW input power in order to reach optimum efficiency (see Fig. 3). The corresponding diodes impedances are Z_{IN} = 13 - j. 89 Ω, and Z_{OUT} = 33 + j. 28 Ω respectively at input and output frequencies, with a bias voltage of -5 V. These embedding impedances values as a function of frequency were exported into Z-files which were used as a first input of the linear optimization. Secondly, each of the transition in the circuit including step impedances, coupling probes and waveguide transitions were simulated within the 3-D electromagnetic environment with appropriate boundaries, waveports assignment and de-embedding planes. The simulation outcomes (2-D S-parameter matrices and their attenuations, impedances and permittivity values at central guided frequencies) were used a second input of the linear optimization. During this optimization step, the matching network was simulated with the "S-parameter" and "Optim" routines of ADS in order to find optimum lengths of the circuit. The diode impedance frequency set is accessed through a "DAC" file component and the S-parameter matrix through "Data-item" component with a number of ports that corresponds to the ports defined in the 3D EM simulation. A first set of circuit dimensions was found by optimizing the coupling between diodes and output port, which transmission magnitude should reach a maximum of $1/\sqrt{4}$ = 0.5 . The center pad, the output probe and the DC bias filter were optimized for wideband impedance matching. A second set of value was found by refining the optimization with the harmonic balance routine. Few iterations between the linear and the nonlinear optimizations were performed until the emergence of acceptable performance. Finally, the each section values found during the previous steps were feed back in HFSS to build the full doubler circuit structure as shown in Fig. 2. Its performance were then checked using the nonlinear harmonic balance routine.
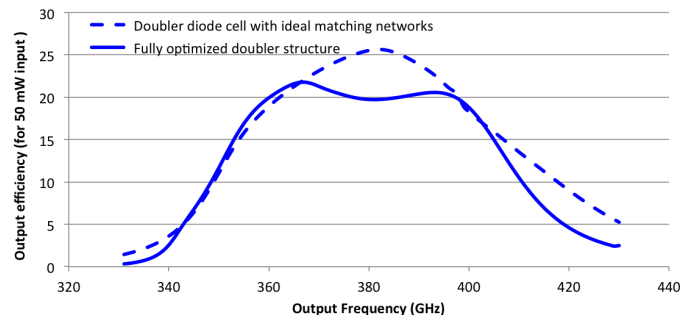

Fig. 3. Predicted performance of the 380 GHz doubler, the dot curve is the efficiency of the diode cell with ideal matching network, the full line is the fully optimized circuit as illustrated in Fig.3.

The electrical parameters of the STFC-RAL Schottky diode model considered in the simulations are a series resistance Rs = 7.5 Ω, an intrinsic zero voltage junction capacitance of Cjo = 15.7fF, a saturation current Isat = 150 fA, an ideality factor = 1.3 and a built-in potential Vbi = 0.85 V. This design was optimized for 50 mW of input power and -5 V bias voltage. The diodes anode area is 2.2μm $\times$ 4.5μm. Fig.3 shows the estimated efficiency of the doubler. Expected Performances gives 20% efficiency over 10% bandwidth.

C. 300 GHz Tripler designs

1) Tripler single chip design: The tripler features six integrated GaAs Schottky diodes in a balanced configuration based on [5]. The on-chip capacitor is integrated within the membrane according to STFC-RAL fabrication process. This integration provides a precise DC connection, but also allows a better control of the bias port, which is shifted away from the diode cell and which dimensions are chosen to avoid any leakage of the output signal. A notch in the bias line is mandatory to meet the photolitographic process requirement but has negligible impact on the circuit performance. The input and output waveguide dimensions cut off respectively the input signal TM_{11} mode and the second idler harmonic TE_{10} and TM_{11} modes. A detailed explanations of the design methodology of the circuit are given in [5]. The optimization is performed using 3D electromagnetic codes alike for the doubler, but the methodology slighty differs from the 380 GHz doubler as the initial diode cell optimization includes the diodes plus a section of the chip-channel and its on-chip capacitor. The optimum diode junction capacitance and bias voltage were determined at the same time to reach highest efficiency and power handling as possible. When the tripler circuit was achieved, then the input waveguide network had to be tuned to reach wide-band performance. This step was done with a linear optimization that allow an easy manual tuning of the matching network circuit. Firstly the tripler diodes ideal impedances were computed with the harmonic balance routine with ideal matching networks to converge to an optimum efficiency. The corresponding set of impedances are Z_{IN} = 32 -j 80 Ω, and Z_{OUT} = 24 + j 44 Ω respectively at input and output frequencies. The idler impedance is close to zero that confirms that the power is ideally transposed to the third harmonic. Secondly, the input and output matching network was divided into several individual sections, and the discontinuous parts between them were simulated in HFSS. The resulting S-parameter matrices and the diodes optimum embedding impedances were then utilized to determinate a first set of circuit dimensions using the linear simulator in ADS by optimizing the coupling between diodes and output port. The optimisation goal of the port-to-port matching is the transmission from the input port to each of the 6 anodes which maximum magnitude were $1/\sqrt{6}$ = 0.4 . When the non-linear matching had achieved the desired coupling with an optimal tuning, the circuit was simulated with the harmonic balance routine to check the tripler coupling efficiency, global efficiency and output power.
The electrical parameters of the Schottky diode model considered in the simulations are a series resistance Rs = 5.4 Ω, an intrinsic zero voltage junction capacitance of Cjo = 26 fF, a saturation current Isat = 100 fA, an ideality factor = 1.2 and a built-in potential Vbi = 0.85 V. The bias value applied to the 6 diodes in series is 13 V. Expected simulated performances gives between 5% and 10% percent efficiency over 17% bandwidth with 200 mW of input power as shown in Fig.4. The block and tripler are being fabricated at STFC
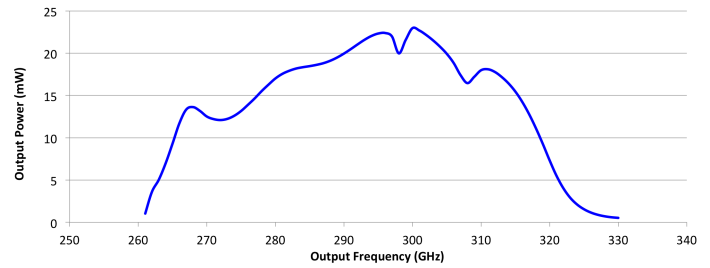

Fig. 4.   Simulation results of the Single Chip 300GHz Tripler : Output power with 200 mW of input power.

with a variation of two different epilayer doping densities : $1.10^{-17}cm^{-3}$ and $3.10^{-17}cm^{-3}$ and with the corresponding $30\mu m^2$ and $17\mu m^2$ anodes area, with $\pm$ 15% bracketing.
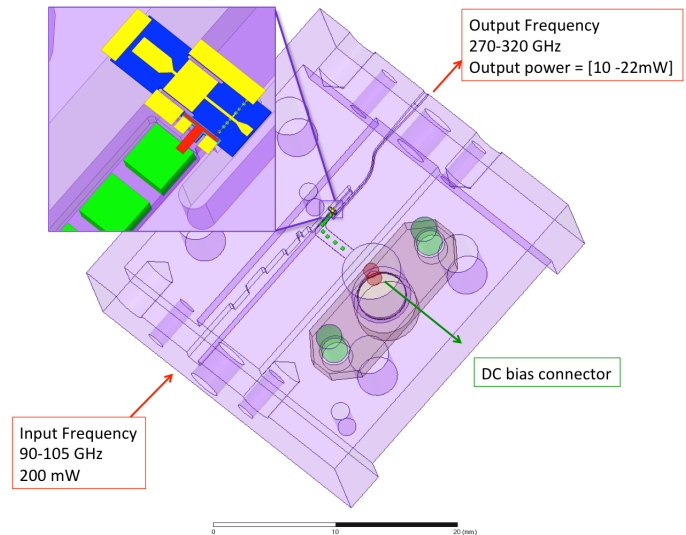

Fig. 5.   Single chip 300GHz tripler mounted in half part of the split block with its input waveguide matching network.

2) Tripler power-combined design: The topology used for this design is similar to the one presented in [6], but with bias ports reported to the other side of the input waveguide that makes possible to have in-line matching network waveguide transitions. This solution bypass the need for curvatures in the input waveguide and avoid unwanted phase shift (and imbalance) between the input port and the diodes of the two symmetrical chips. As for the doubler and tripler single-chip designs, the matching network optimization consists in a combinaison of linear / non linear simulations that converge to a final configuration. The ideal diode impedance set used in the linear simulation was the one found for the single chip tripler. The optimisation goal of the port-to-port matching was the transmission between the input port to each of the 12 diodes which maximum magnitude was $1/\sqrt{12}$ = 0.28 . Preliminary performances give above 6% efficiency over 15% bandwidth, therefore 25 mW to 35 mW of output power is expected over the 270-315 GHz band with 400 mW input power.

II. CONCLUSION

Three multiplier designs are presented : a 380 GHz single-chip doubler, a 300 GHz single-chip tripler and a 300 GHz
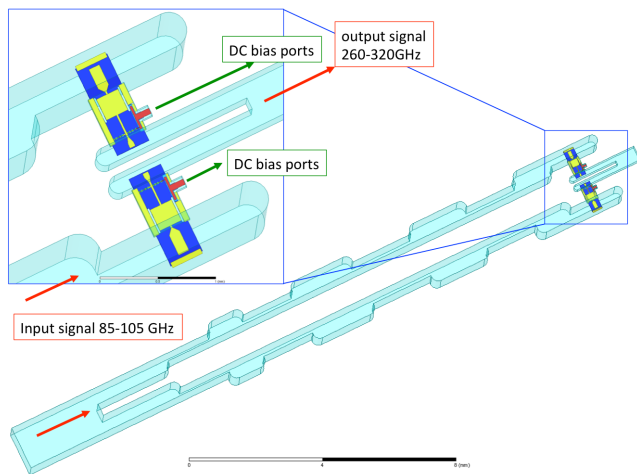
Fig. 6.　Picture of the fully optimized dual-chip 300GHz power combined tripler.
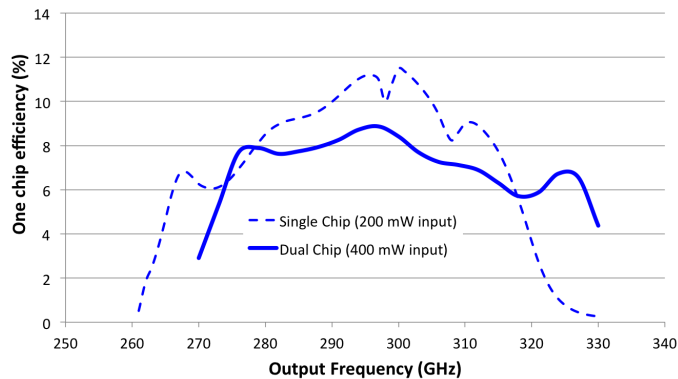
Fig. 7.　300 GHz dual-chip power-combined tripler preliminary predicted output power efficiency compared to the single chip as given in Fig.6.

in-phase power-combined dual-chip tripler. These designs use combinaison of linear/non linear optimization benches where manually tuning of the output and input matching networks is possible with dedicated transmission goals for respectively the output port to each of the diodes (doubler) and the input port to each of the diodes (tripler). This methodology helps to widen drastically the performance bandwidth of the frequency multipliers. These designs are implemented with a model of MMIC diode circuits and their on-chip capacitor developped with STFC-RAL fabrication process for MIDAS high frequency and high power requirements.

REFERENCES

[1] C. Lee, J. Ward, R. Lin, E. Schlecht, G. Chattopadhyay, J. Gill, B. Thomas, A. Maestrini, I. Mehdi, and P. Siegel, *A Wafer-Level Diamond Bonding Process To Improve Power Handling Capability of Submillimeter-wave Schottky Diode Multipliers* Microwave Symposium Digest, 2009 IEEE MTT-S International, Boston, pp. 957 - 960, 7-12 June, 2009.

[2] A. Y. Tang, E. Schlecht, G. Chattopadhyay, R. Lin, C. Lee, J. Gill, I. Mehdi, and J. Stake *Steady-State and Transient Thermal Analysis of High-Power Planar Schottky Diodes* in Proc. 21th Int. Symp. Space Terahertz Technol.,Tucson, USA, April 26-28, 2011

[3] N.R. Erickson *Wideband High Efficiency Planar Diode Doublers,*Ninth Int'l Conference on Space THz Technology, pp.473-480, Pasadena,CA,1998.

[4] J. Siles, A. Maestrini, B. Alderman, S. Davies, H. Wang, J. Treuttel , E. Leclerc, T. Narhi, and C. Goldstein *A single-waveguide in-phase power-combined frequency doubler at 190 GHz*, IEEE Microwave and Wireless Components Letters, June 2011.

[5] A. Maestrini, J. Ward, J. Gill, H. Javadi, E. Schlecht, C. Tripon-Canseliet, G. Chattopadhyay and I. Mehdi, *A 540-640 GHz High Efficiency Four Anode Frequency Tripler* IEEE Transactions on Microwave Theory and Techniques, Vol. 53, No. 9, September 2005.

[6] A. Maestrini, J. Ward, C. Tripon-Canseliet, J. Gill, C. Lee, H. Javadi, G. Chattopadhyay, and I. Mehdi : *In-Phase Power-Combined Frequency Triplers at 300 GHz* IEEE Microwave and Wireless Component Letters, Vol. 18, no. 3, pp. 218-220, March 2008.

Operation of a THz quantum-cascade laser in a compact mechanical cryocooler

H. Richter [1)*], N. Deßmann [1)], R. Eichholz[1)], S. G. Pavlov [1)], M. Wienold [2)], L. Schrottke [2)],
M. Giehler [2)], R. Hey [2)], H. T. Grahn [2)], I. Rühlich [3)], M. Mai [3)], and H.-W. Hübers [1), 4)]

*1 Institute of Planetary Research, German Aerospace Center (DLR), Rutherfordstr. 2,
12489 Berlin, Germany*

2 Paul-Drude-Institut für Festkörperelektronik, Hausvogteiplatz 5–7, 10117 Berlin, Germany
3 AIM INFRAROT- MODULE GmbH, Theresienstraße 2, D-74072 Heilbronn, Germany
*4 Institut für Optik und Atomare Physik, Technische Universität Berlin, Hardenbergstraße 36,
10623 Berlin, Germany*

`* Contact: heiko.richter@dlr.de, phone +49-30-67055 697`

Abstract⸺A major challen ge for hetero dyne receivers operating above approximately 2 THz is the local oscillator, which has to be a compact source requiring little electrical input power and providing sufficient output power not only for a single mixer but fo r an array of mixers. THz quantum-cascade lasers (QCLs) have the potential to comply with these requirements. The laser itself is only a few mm long, and the cooling system which is necessary for operation of the QCL d etermines the mass and power budget. So far, the smalle st QCL-based THz source weighs approximately 15 kg [1].

We report on the development of a compa ct, easy-to-use source, which combines a QCL operating in a very compact, low-input-power linear Stirling cooler (model AIM S L400). The cooler has been optimized for this application. The QCL is based on a bound-to-continuum design similar to the one reported in Ref. [2]. Special care has been tak en to achieve a good thermal coupling betw een the QCL and the col d finger of the cryo stat. The cryocooler with the QCL w eighs less than 4 kg. The QCL op erates on a single mode at 2.5 THz, and its output power is appr oximately 0.15 mW. With an appropriate optical beam shaping, the e mission profile of the lase r becomes a fundamental Gaussian one. We will present the performance of this THz source and discuss perspectives for improvements and applications.

[1] H. Richter, M. Greiner-Bär, S. G. Pavlov, A. D. Semenov, M. Wienold, L. Schrottke, M. Giehler, R. Hey, H. T. Grahn, and H.-W. Hübers, Opt. Express 18, 10177−10187 (2010).
[2] S. Barbieri, J. Alton, H. E. Beere, J. Fowler, E. H. Linfield, and D. A. Ritchie, Appl. Phys. Lett. 85, 1674 (2004).

Frequency selection from a multi-mode THz quantum-cascade laser by a grating monochromator

R. Eichholz[1]*, H. Richter [1], S. G. Pavlov [1], M. Wienold [2], L. Schrottke [2], R. Hey [2], H. T. Grahn [2], and H.-W. Hübers [1, 3]

1 Institute of Planetary Research, German Aerospace Center (DLR), Rutherfordstr. 2,
12489 Berlin, Germany

2 Paul-Drude-Institut für Festkörperelektronik, Hausvogteiplatz 5–7, 10117 Berlin, Germany
3 Institut für Optik und Atomare Physik, Technische Universität Berlin, Hardenbergstraße 36,
10623 Berlin, Germany

```
* Contact: rene.eichholz@dlr.de, phone +49-30-67055 697
```

Abstract⸺ **THz quantum-cascade lase rs (QCLs) are v ery attractive for applications such as a local oscillator in a heterodyne spectrometer. First, their emission is narrow in frequency (less than 20 k Hz), which allows for very high spectral resolution. Second, QCLs exhibit high output pow ers up to s everal tens of mW, suffic ient for pumping lar ge-format mixer arrays, and a third advantage is their broad gain medium, which in principle allows for a fr equency coverage of several 100 GHz. Here we report on an approach to select the f requency of a multi-mode THz QCL by an external grating, which is not part of the laser cavity. The QCL, which is based on a two-miniband design and a Fabry-Pérot resonator, has been developed for high output powers and low electrical pump powers. Up to five modes at around 3.4 THz are emitted simultaneously. Each mode has more th an 0.1 mW of power, which is suffic ient for pumping hot-electron bolometric mixers. The QCL is mounted in a compact, low-weight Stirling cooler [1]. The emission modes of the laser are spectrally resolved and spatially separated by a reflection grating and imaged onto a microbolometer camera. With an exit slit at the output port of the grating spectrometer, a single mode can be selected. In order to demonstrate the performance of this approach, an abso rption cell was placed between the QCL and the grating spectrometer, and the absorption spectrum of methanol around 3.4 THz was measured by integrating simultaneously the signal of each of the Fabry-Pérot modes on the microbolomet er camera as a function of the las er driving current [2]. In this case, a rough frequency selection is obtained by the grating, while a fr equency fine tuning, which is ne cessary for high-resolution molecular spectroscopy, is obtained by a variation of the operating current and temperature of the QCL.**

[1] H. Richter, M. Greiner-Bär, S. G. Pavlov, A. D. Semenov, M. Wienold, L. Schrottke, M. Giehler, R. Hey, H. T. Grahn, and H.-W. Hübers, Opt. Express 18, 10177–10187 (2010).
[2] R. Eichholz, H. Richter, S. G. Pavlov, M. Wienold, L. Schrottke, R. Hey, H. T. Grahn, and H.-W. Hübers, Appl. Phys. Lett. 99, 141112 (2011).

A 600 GHz Orthomode Transducer based on a Waveguide Integrated Wire Grid Polarizer

A. Hammar[1,2*], P. Sobis[1], V. Drakinskiy[2], H. Zhao[2], J. Stake[2], A. Emrich[1]

*1 Omnisys Instrument AB, Västra Frölunda, SE-42130, Sweden*
2 Terahertz and Millimetre Wave Laboratory, Department of Microtechnology and Nanoscience,
Chalmers University of Technology, SE-41296 Göteborg, Sweden
`* Contact:  ah@omnisys.se, phone +4670 488 2185`

Abstract — **We present a new type of orthomode transducer (OMT), involving the integration of a quasi-optical component, namely a wire grid polarizer (WGP), with an E-plane probe transition, in a waveguide topology. The goal has been to create a lightweight and compact device for waveguide integration, capable of covering all frequency channels to be used by the FIRE instrument[¤].**

The design consists of a metallic split block, in which a quadratic waveguide supporting the two fundamental modes of propagation (TE$_{10}$ and TE$_{01}$), is formed using regular CNC milling. Just as its quasi-optical counterpart, i.e. a free standing WGP, a waveguide integrated WGP insert is used to separate the two orthogonal TE modes, which are either reflected or transmitted (depending on polarization). A planar E-plane waveguide probe transition realized on a GaAs membrane is used inside a square waveguide to extract the reflected mode without affecting the transmitted mode. For a first proof of concept the OMT has been designed for the possibility of full characterization and therefore the transmitted mode is guided through a stepped impedance transformer to a standard rectangular waveguide interface, while a second E-plane probe transition to a rectangular waveguide, is used for the reflected mode.

Simulations carried out using Ansoft HFSS show that the OMT design can be made relatively broadband (currently about ~14% with a return loss better than 15 dBs) and with cross-polarizations better than 30 dB. The probe and WGP can be manufactured using high precision photolithography or E-beam lithography making it scalable to both lower and higher frequency bands. Assembling an OMT of this type involves mounting of small membrane structures (< 1 mm) into waveguides and the design can thus be subject to misalignment errors which may degrade the performance. Hence, a tolerance analysis identifying the most sensitive parameters will be presented together with the different design trade-offs. Practical aspects regarding the assembly of the waveguide probe and WGP into the block will also be presented along with S-parameters measurements. It is the belief of the authors that this new type of OMT concept will allow for broadband operation with relative low losses at high frequencies (i.e. above 600 GHz), where regular WGPs so far has been the most common way to separate two signals of orthogonal polarizations.
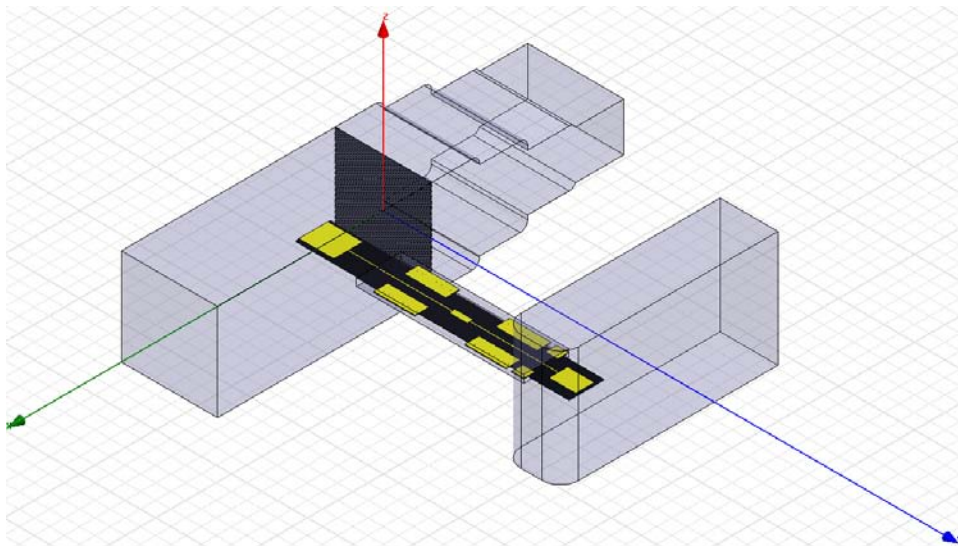
[¤] A. Emrich et.al. – The FIRE instrument, to be presented at ISSTT 2012

Loss of WR10 Waveguide across 70-116 GHz

I. Stil, A.L. Fontana, B. Lefranc, A. Navarrini, P. Serres, K.F. Schuster

Abstract— **The losses of ~1.2 m long WR10 (2.54x1.27 mm²) rectangular waveguides were measured at room temperature across the 70-116 GHz band. Ten different waveguide modules were machined in two different materials (Aluminium alloy and Brass) using different surface roughness (Ra) and different split-block waveguide geometries (E-plane and b-edge) as to establish the dependency of the losses on the various parameters.**

The measurements of the various units were performed with the IRAM mm-wave Vector Network Analyzer (MVNA) across the 70-116 GHz single-mode band of the WR10 waveguide.

Index terms---**WR10 waveguides, losses, machining, surface roughness, gold plating.**

I. WR10 WAVEGUIDE MECHANICAL BLOCKS

Ten modules with ~1.2m long WR10 rectangular waveguide were fabricated at IRAM: five in Brass (CuZn39Pb3) and five in 6060 Aluminium AlMgSi. Each module consists of two split blocks in which the waveguide was machined in a meandering pattern that fits on a surface of 140x71 mm^2. Fig. 1 shows photos of some of the assembled units together with the internal details of one of the two module halves.
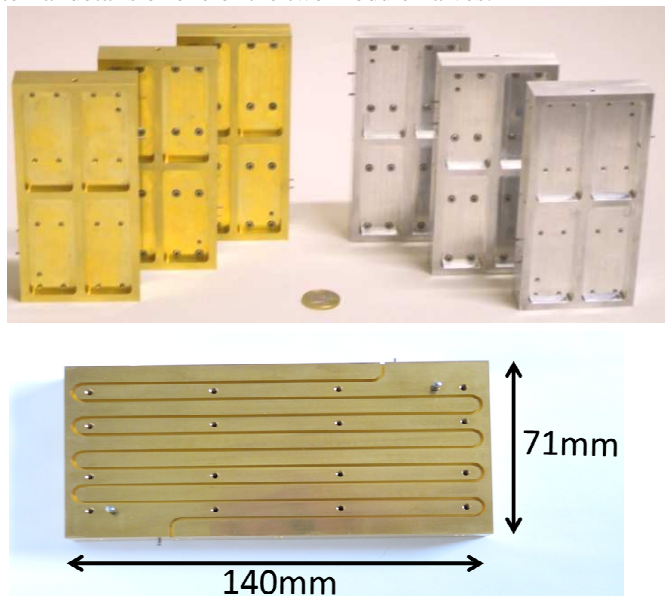
Fig. 1. Top: six assembled WR10 waveguide modules (three in Brass on the left, three in Aluminium on the right). Bottom: one disassembled split-block half showing the ~1.2 m long WR10 waveguide long cut.

The authors are with IRAM (Institut de Radio Astronomie Millimétrique), Saint Martin d'Hères, 38406 FRANCE (contact author: A. Navarrini, e-mail: navarrin@iram.fr, phone: +33476824941).

A. Different split-block geometries:

Two different WR10 split-block geometries, the E-plane split and the b-edge split, were adopted for the modules, as illustrated in Fig. 2.
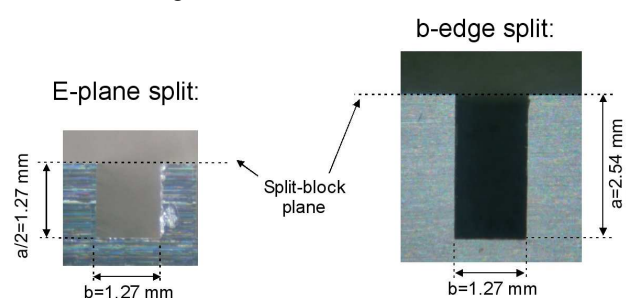
Fig. 2. Photo of WR10 waveguide cut adopted on the two split block geometries. Geometry 1: along the E-plane (left). Geometry 2: along the b-edge (right).

B. Different surface roughness:

The waveguide cuts in each module were fabricated using a numerically controlled milling machine (using machining parameters Ω=9000 rpm and V=45 mm/min). A conventional carbide drill as well as a diamond drill were used. A better surface finish is obtained using the diamond tool. Photos of the WR10 waveguide cuts fabricated with the two drill types are shown in Fig. 3.
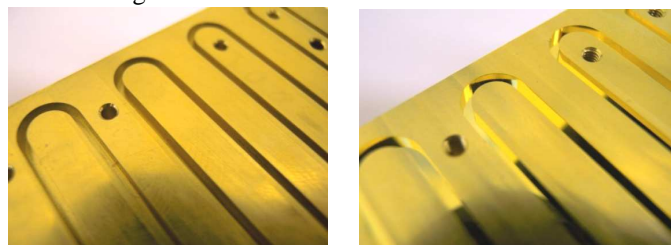
Fig. 3. Left: WR10 waveguide machined with carbide tool. Right: WR10 waveguide machined with diamond tool showing the specular effect at the waveguide bottom.

The achieved surface roughness (Ra) was measured at the bottom of the waveguide cut (narrow side) using a non-contacting optical laser equipment. The roughness along the waveguide walls (wide side) was not measured. The losses are expected to be lower in a smooth waveguide with surface irregularities which are small in comparison to the skin depth. Assuming an electrical conductivity of 1.38×10^7 S/m and of 3.24×10^7 S/m for, respectively Brass and Aluminium, the corresponding skin depths at 100 GHz are δ_{Brass}=0.40 μm and δ_{Alu}=0.28 μm. The measured surface roughness at the bottom of the waveguides machined with carbide tool were about Ra~0.34 μm for the Brass modules and about Ra~0.15 μm for

the Aluminum modules, i.e. similar in value to the skin depth. The measured Ra of the waveguides machined with diamond drill was about 0.04 µm in Brass module and about 0.02 µm in Aluminum modules, i.e. one order of magnitude less than the skin depth.

II. ELECTRICAL MEASUREMENT RESULTS

The S-parameters of the waveguide modules were measured across 70-116 GHz using a Vector Network Analyser (VNA) with WR10 mm-wave extension modules developed at IRAM [1]. A photo of the measurement setup is shown in Fig. 4. The typical uncertainty on a transmission measurement across the WR10 band of the mm-wave VNA is of the order of ~0.1 dB. To make an accurate measurement, it is necessary for this intrinsic uncertainty to be considerably smaller than the transmission to be measured. Accurate transmission measurements of low-loss devices are indeed difficult at mm-wavelengths. However, the loss of our ~ 1.2 m long WR10 waveguides, of order ~1 dB, could be measured with high accuracy, therefore decreasing the relative uncertainty of the measurement.
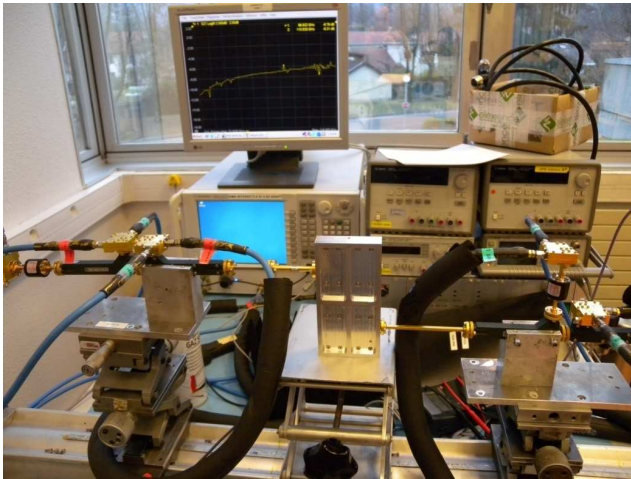
Fig. 4. Test setup for transmission loss measurement of WR10 waveguides across 70-116 GHz. A WR10 Aluminium module is connected to the mm-wave extension heads of the Agilent PNAX Vector Network Analyzer.
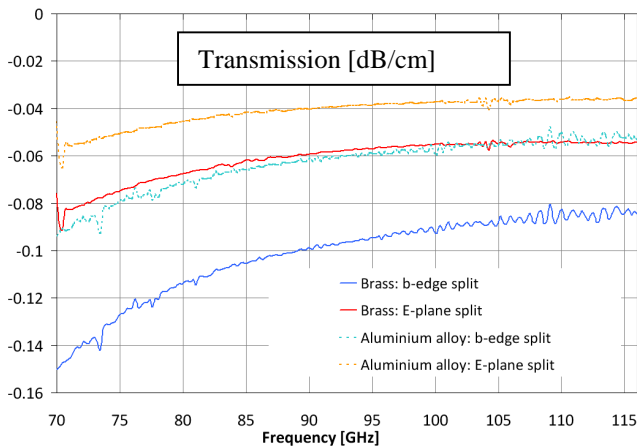
Fig. 5. Measured |S21| transmission per unit length (in dB/cm) of Brass and Aluminium alloy WR10 waveguide modules with split-block along the E-plane and the b-edge.

A. Dependence of losses on split-block geometry (b-edge cut versus E-Plane cut):

The measured transmission of Brass and Aluminium waveguide modules with waveguide cut along the E-plane and along the b-edge was rescaled to unit length. The measured results, expressed in dB/cm, are shown in Fig. 5. The highest transmission is found for the Aluminium alloy module with E-plane cut (dashed yellow curve), whose average value is about -0.04 dB across the 70-116 GHz band. As expected, the highest losses were measured for the Brass module with b-edge cut (solid blue curve), whose value ranges between -0.016 and -0.08 dB.

B. Dependence of losses on surface roughness Ra:

The measured |S21| transmission (in dB/cm) of Brass and Aluminium alloy waveguide modules fabricated with different milling tools (different surface roughness) are shown in Fig. 6. Electromagnetic simulation of the waveguide modules were performed with the 3D software CST Microwave Studio [2]. Using the theoretical electrical conductivity of 1.38×10^7 S/m and 3.24×10^7 S/m for, respectively Brass and Aluminium, the simulated results match closely the transmission measurements for modules machined with diamond drill.
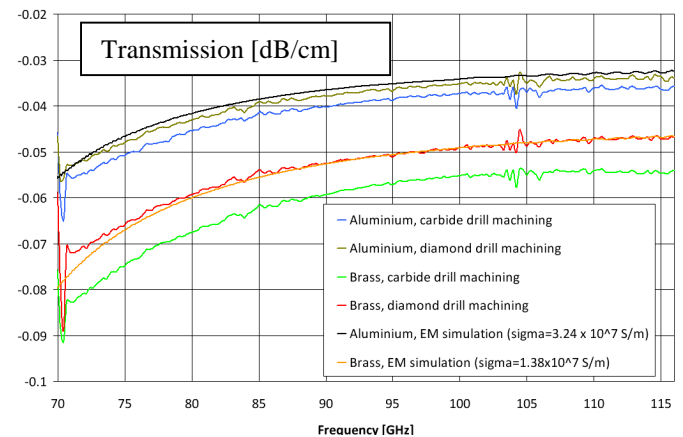

Fig. 6. |S21| transmission per unit length (in dB/cm) of Brass and Aluminium alloy waveguide modules with different surface roughnesses. All waveguide modules are cut along the E-plane. The electromagnetic simulation results of transmission of perfectly smooth WR10 waveguides made of Brass (solid yellow curve) and Aluminium (solid black curve).

III. CONCLUSION

The losses of a WR10 rectangular waveguide across 70-116 GHz are confirmed to be lower for E-plane cut geometry than for b-edge geometry. CNC milling machining with a diamond tool results in lower surface roughness than with a standard carbide tool. The measured losses are very close to electromagnetic simulation results with theoretical DC electrical conductivity values. The 6060 Aluminium AlMgSi has lower losses than Brass CuZn39Pb3.

REFERENCES

[1] F. Mattiocco and M. Carter, *80-360 GHz very wide band millimetrer wave network analyzer,* International Journal of Infrared and Millimeter Waves, Vol.16, No 12, 1995.

[2] CST Microwave Studio, CST AG Bad Nauheimer Str. 1964289, Darmstadt, Germany, http://www.cst.com

Characterization System with Cryogenically-Cooled Loads for next-generation CMB Polarimeters

K. Ishidoshiro[1*], M. Hasegawa[1], M. Hazumi[1], M. Nagai[1], and O. Tajima[1]

1 Institute of Particle and Nuclear Studies, High Energy Accelerator Research Organization,
1-1 Oho, Tsukuba, Ibaraki 305-0801, Japan
* Contact: koji@post.kek.jp, phone +81-29-864-5200 4978

Abstract⸻

Polarimeters used in the cosmic microwave background (CMB) experiments are required to be well characterized to measure faint CMB polarization patterns with low systematic errors. Reproduction of the observing condition, especially sky temperature, is important for characterization of the polarimeters, since characteristics of the polarimeters are depend on the load temperature.

We developed a characterization system with cryogenically-cooled loads for CMB polarimeters. The loads generate unpolarized radiation of (~10 K and ~30 K). The system reproduces the sky temperature at observation sites e.g., the Atacama desert in Chile (~10 K). The radiation from the loads reflects on a metal mirror in a cryostat, yielding a partially polarized radiation (~100 mK), going into a feed horn of the polarimeter. Rotation of the mirror varies the incident angle of polarization and causes a periodical variation of the load temperature. Therefore, the system enables us to simultaneously measure receiver temperature using the Y-factor scheme, polarization responsivity, and leakage from unpolarized to polarized radiation.

Using the above system, we successfully characterized the prototype polarimeter developed for an upgrade Q/U Imaging ExperimentT (QUIET), which aims to search for the 'curl-like' polarization patterns induced by primordial gravitational waves at the level of r=0.01, where r is the intensity of the primordial gravitational waves. The simultaneous characterization enables us to finalize the polarimeter parameter, e.g., bias voltages, in the laboratory. Thus far we have directly measured a polarimeter sensitivity of $400 \mathrm{uK s}^{1/2}$ under the reproduced observing condition.

The principle of our system is not limited by frequency bands or detector types. The scheme of our system is very promising for various types of state-of-the-art detectors for mm and sub-mm experiments.

Development of a Calibration Source for SAFARI on-ground calibration.

Wouter M. Laauwen, Martin Eggens, Willem Jellema, Chris de Jonge, Lenze Meinsma and Pieter Dieleman.

Abstract—**In a European consortium led by SRON, the Netherlands Institute for Space Research, the SpicA Far-infraRed Instrument (SAFARI) is being developed. SAFARI is an imaging Fourier Transform Spectrometer working in the 34 – 210 μm wavelength range with a Nyquist sampled instantaneous field of view of 2' x 2'. It has a selectable spectral resolution R of between 3 and 2000. It is to fly on the joint JAXA-ESA SPICA mission (SPace Infrared telescope for Cosmology and Astrophysics) which features a telescope that is actively cooled to ~5 K. SAFARI will be sky-background limited with the individual pixels having a goal NEP of 2*10-19 W/Hz1/2. The on-ground verification and calibration program will be performed in-house at SRON. For this a test facility is under development.**

To perform absolute calibration a radiometry source is needed that covers the full dynamic range of the individual detectors from atto-watts to pico-watts per pixel in the SAFARI bands. To obtain accurate knowledge of the spectral distribution of the source power a heatable cavity is chosen since this behaves as a perfect black body. The power spectrum of such a source is only determined by its temperature. To get the output in the SAFARI wavelength range and with the desired stability the temperature must be higher than ~40 K but then the output power, which goes with T^4, becomes too high. Additional attenuation of ~10-6 is needed which will be achieved by geometrical dilution.

The full concept of the calibration source will be presented here. This contains design solutions to achieve 10-6 attenuation, 3 octaves of bandwidth, while the profile of the spectral output of the source shall not deviate more than 5% from the best fit to a grey body with Planck spectral profile. Additionally, thermo-mechanical issues like thermally separating the black body cavity at maximum 300 K from the mechanism at 4 K and the integrating sphere at 1.7 K are covered.

Index Terms—**Calibration, Radiometry, Submillimeter wave technology.**

I. INTRODUCTION

A European consortium with SRON as PI is developing an imaging Fourier Transform Spectrometer called SAFARI.

This instrument is to fly on board the SPICA satellite, a joint JAXA-ESA mission that is scheduled for launch in 2021. SPICA's main characteristic is an actively cooled telescope with a goal temperature of ~5 K. This cooled telescope makes it possible to do background limited observations in the 5 to 210 μm wavelength band.

To take full advantage of this capability SAFARI will be equipped with TES-detector arrays with a goal NEP of $2*10^{-19}$ W/Hz$^{1/2}$ and operating at ~100 mK. SAFARI will cover 3 octaves from 34 μm to 210 μm divided in three bands. The goal is to have Nyquist sampled arrays with a 2'by 2'field of view leading to a total number of around 4000 pixels. Frequency Domain Multiplexing (FDM) is used to achieve 160 to 1 multiplexing to keep the thermal loading on the detector stage minimal

An important task within the SAFARI project is the development of a facility for the on-ground calibration of the instrument. The challenge here is to meet the required low background (~attoWatt per pixel) whilst operating the sources and mechanisms needed to do the characterization and calibration. For this the entire Optical Ground Segment Equipment (OGSE) will be inside a 4 K enclosure. Fig. 1 shows the OGSE layout as described in detail in [1].

The SAFARI instrument hangs below the optical table. It's main beam passes through a hole and into the first element which is a re-imager that refocuses the beam inside the OGSE bay. Two scanning mechanisms make it possible to do x-y scans both in the focal plane and in the pupil plane. The focal plane has an additional z-translator to determine the exact focus position. A flip-mirror can relay the focal plane to a focal plane calibration source which is the focus of this article.

In the next sections we describe development of the calibration source. We start with its functional and performance requirements. Next up is the conceptual design. From the conceptual design we model the expected optical performance. Then we describe the mechanical design from which we can model the thermal response. The last section gives the concept for a light pipe connection to room temperature to make possible the use of external sources for calibration.

II. FUNCTIONAL AND PERFORMANCE REQUIREMENTS

The SAFARI instrument has an internal calibrator which has

the following functional requirements: It should be able to act as an absolute power calibration standard, a flasher and frequency calibration standard. The AIV calibration source should have at least this functionality to be able to do cross calibration between the two sources. The performance wise it should do much better. From this we came to the following functional and performance requirements:

- The calibration source will illuminate the full re-imaged focal plane
- It will operate as an absolute calibration source with:
  Known power, tunable from ~1 aW to 10 fW with a + 20 dB boost.
  Known spectrum, within 5% of a grey body from 34 to 210 µm
  Flat field: uniform distribution to within 1 % of power over the focal plane.
- The calibration source will have a flash function with:
  A flash duration between ~10 msec and 1 sec.
  A rise time as determined by the detector readout system.
  A maximum loading of typically 1 fW/pixel for all bands.
- The calibration source wil have an external port to inject signals from, single frequency LO's, an external FTS or a gas cell

III. CONCEPTUAL DESIGN

The signal for the calibration source is generated with a cavity black body, the hot source. This hot source acts as a Planckian radiator producing a power spectrum that is only dependent on its temperature. The output of the hot source radiates over a half hemisphere. By coupling only a small solid angle to the next element geometrical dilution is created: The signal is attenuated without changing the relation between spectrum and temperature.

The next element is the Integrating Sphere. This has a small input port and a large output port. It provides additional dilution, which in the ideal case is determined by the ratio between output and input area. The inside of the integrating sphere must be low loss (emissivity > 0.99) and scattering for the SAFARI frequencies. The scattering assures that the output port is homogeneously illuminated.

The output of the integrating sphere is again in a half hemisphere from which again a small solid angle (~F/20) is coupled through the re-imager and the instrument onto the detectors. In total this geometrical dilution provides the required ~10^{-6} attenuation. Geometrical dilution is however no absorption so all unwanted radiation most be absorbed in the absorber on the baffles and housing. An absorbing material with very good absorbing properties (emissivity < 0.01) is there for needed. Potentially the coating developed for HIFI can be used [2].

In between the hot source and the input to the integrating sphere a shutter vane is mounted. This can close the hot source whilst setting a (new) temperature and it can create the flash with the required time profile.

For the external input a light pipe design is currently under investigation. In principle this will work but some design supporting tests are needed. A doodle of the conceptual design is shown in fig. 2 below.

IV. OPTICAL PERFORMANCE

In fig. 3 some Planck curves for different temperatures are plotted. The total power from a black body increases with T^4 but on the long wavelength side over the spectrum the power increases linearly with temperature which is an intrinsically much more stable regime. For temperatures over 100 K the entire SAFARI band is in this linear regime. So for stability regions the hot source temperature must be high.

High temperatures however come at a price. As can be seen in fig. 4 a hot source (diameter = 2 mm) produce 100 µW at 150 K going up to 2 mW 300 K. Looking at the in-band power levels, these range from 1 to 100 µW, still way above the fW level and again an indication of the strong requirements on the absorber material.

To get to the correct optical loading for the individual pixels is a three step optical dilution process which all dilute by approximately 2 orders of magnitude. First a set of apertures define a solid angle which is only a fraction of the half hemispheric output of the hot source containing ~1 % of the energy. Second, in the integrating sphere the ratio between input and output port together with its none-unity (but >0.99) reflectivity reduces the power with another two orders of magnitude. Finally the F-number of the instrument together with the pixel size determines the final coupling reduce the coupling with the last two orders leading to a total coupling of around 10^{-6}.

Fig. 5 shows the pixel loading versus hot source temperature for the three SAFARI bands. By varying the black body temperature between 4.5 K and 300 K we can probe the full pixel sensitivity range from noise floor to well above saturation. The long wavelength (LW) band is dominated at the low temperature end by self-emission of the instrument at 4.5 K. To prevent any contribution of the calibration source itself the integrating sphere is kept at 1.7 K which gives negligible back ground loading.

V. MECHANICAL DESIGN

The mechanical design of the calibration source starts with the hot source. This is a spherical cavity which has to be heated to 300 K in a 4.5 K environment. To keep the heat load to the environment low it has to be mounted in a low thermal conductivity suspension. For this we used a triangular stainless steel frame holding a total of 12 stainless steel wire segments created by threading a single wire through the frame and tensioning it. The twelve wires constrain all degrees of freedom of the hot source making it a very stiff suspension but with low thermal conductivity. The hot source cavity itself is made from

aluminum with a rough scattering inner surface and a polished gold plated outer surface with an emissivity > 0.99 to reduce radiative heatload to the environment. A photo of the prototype of this unit can be seen in fig. 6.

The hot source and suspension are enclosed in a housing which is absorbing on the inside to remove stray radiation. The housing holds the baffles that set the coupling to the integrating sphere and the shutter mechanism. The mechanism still has to be designed but current baseline is a low dissipative resonant pivot mechanism.

Between the housing at 4.5 K and the integrating sphere at 1.7 K there is a light tight thermal break. The integrating sphere has a diameter which is 5 times the diameter of the output port to ensure a homogeneous distribution of power. Its inner surface will be high reflectivity (> 0.99) and rough for the SAFARI wavelength to create significant scattering. For this we will be using the sandblasting process from [3]. The design drawing can be found in fig 7.

The external sources will be coupled into the integrating sphere via a light pipe. Coupling to the outside world will be done with a light cone with in its throat the vacuum window. Because the throat has a small 2 mm diameter the 300 K background load can be kept low relatively low. The light-pipe will be kept at 4.5 K with a thermal break close to the vacuum feed-through. It will be aligned to the warm part by three point contacts to keep the thermal load minimal. Connection to the integrating sphere will be through a similar system as used for the hot source including apertures and a movable shutter mechanism. This is also the place where the light-pipe is mechanically fixed. The warm point-contacts form a sliding contact to allow for thermal contraction. The concept is shown in fig. 8.
.

VI. THERMAL RESPONSE

An important aspect of any low load design is the thermal response time, the time required to heat up or cool down the source. It is clearly a trade is needed between acceptable load and response time. With a maximum allowable heat load of 100 mW to be reached for a hot source temperature of 300 K we need a suspension wire thickness of 2 mm. From this we can calculate for a nominal temperature of 90 K (~3 fW/pixel) a heat load of ~12 K. Typical warm up time for 100 mW input is just under 30 minutes. Cool down from nominal temperature takes just under 9 hours which is acceptable for the expected use. The warm-up and cool-down curves can be found in fig. and fig. 10.

VII. CONCLUSIONS

We have designed and modeled a calibration source that fulfills the requirements of the SAFRAI AIV program. We are currently in the process of building and testing a prototype. Although confidence in the design is high some design supporting tests are still needed in the areas of 1) the high reflectivity scattering surface on the inside of the integrating

spheres and 2) the absorbing coating needed to remove excess radiation.

REFERENCES

[1] P. Dieleman et al., Test facility development for the SPICA- SAFARI instrument, 2011, 21st ISSTT Proceedings.
[2] T.O. Klaassen et al., Optical Characterization of Absorbing Coatings for Sub-millimeter Radiation, 2001, 12th ISSTT Proceedings.
[3] Manuel A. Quijada et al., Hemispherical Reflectance and Emittance Properties of Carbon Nanotubes Coatings at Infrared Wavelengths, 2011, Proc. of SPIE Vol. 8150.
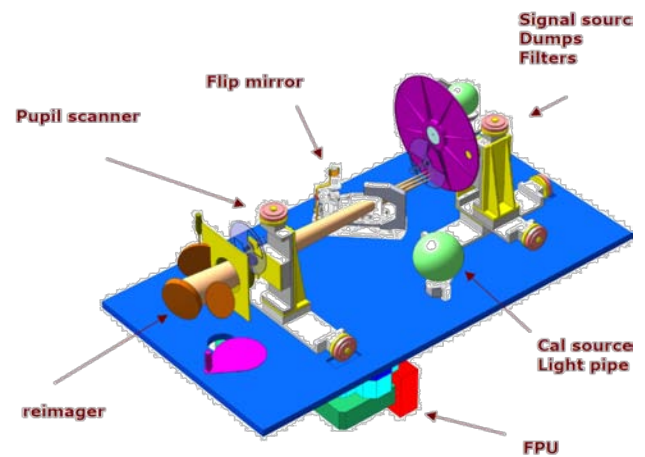
Fig. 1 Schematic layout of the Optical Ground Segment Equipment for the characterization and calibration of the SAFARI instrument.
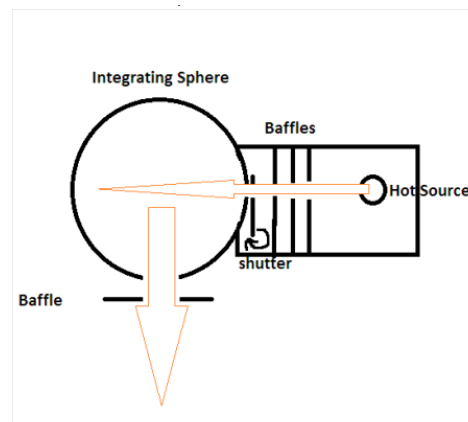

Fig. 2 Doodle of the conceptual design of the calibration source.
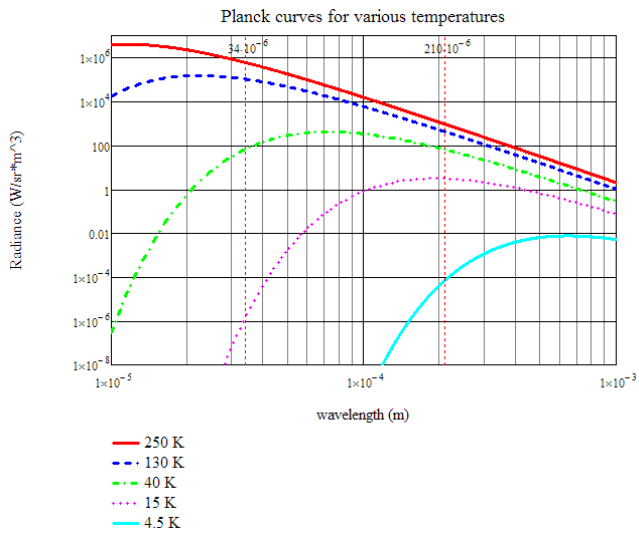
Fig. 3 Planck curves as power versus wavelength for various temperatures.
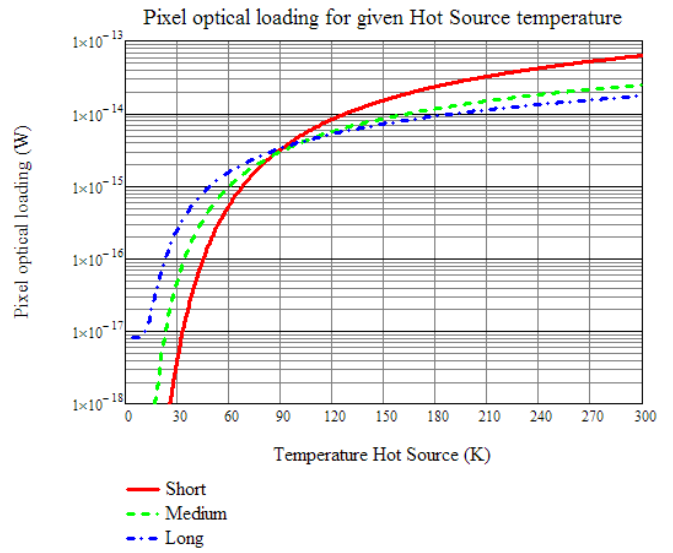

Fig.5 Pixel optical loading versus hot source temperatures for the three SAFARI bands.
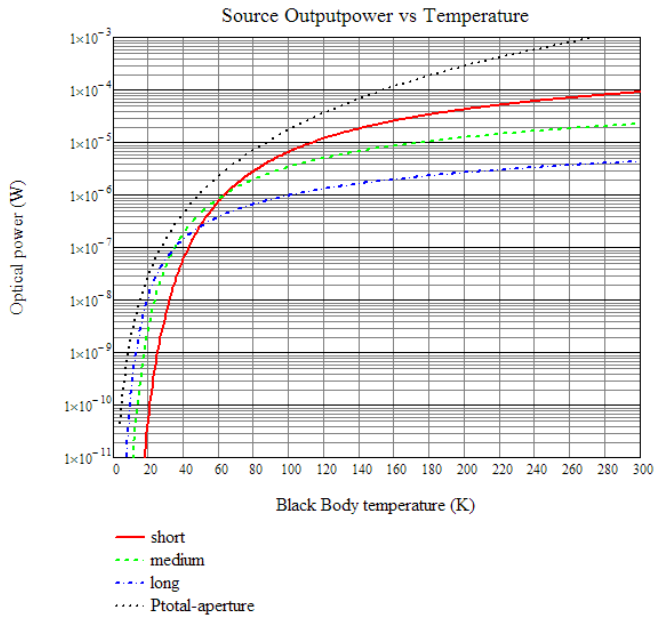
Fig.4 Output power of the hot source versus temperature for the various relevant wavelength ranges.


Fig. 6 Prototype of the hot source and suspension.
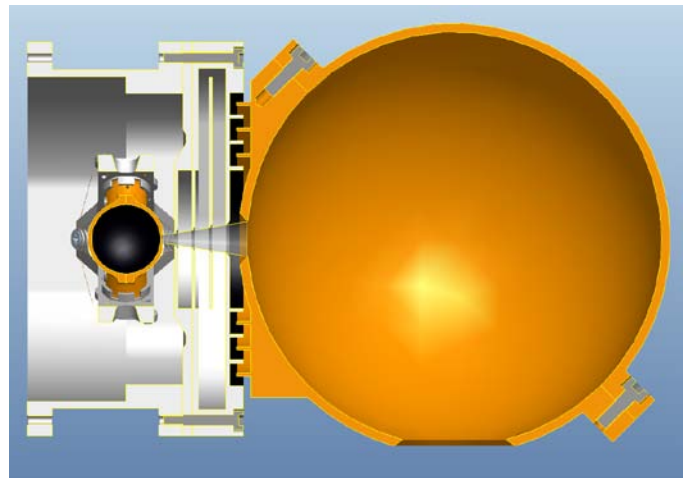

Fig 7. A cross section of the calibration source design.
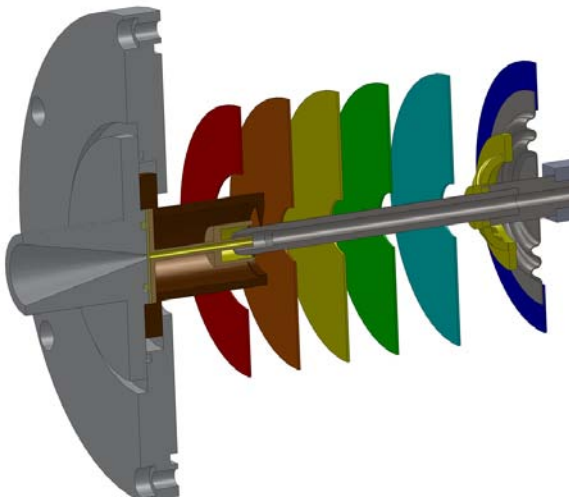
Fig. 8 Concept of the light pipe connection between the outside world and the calibration source.
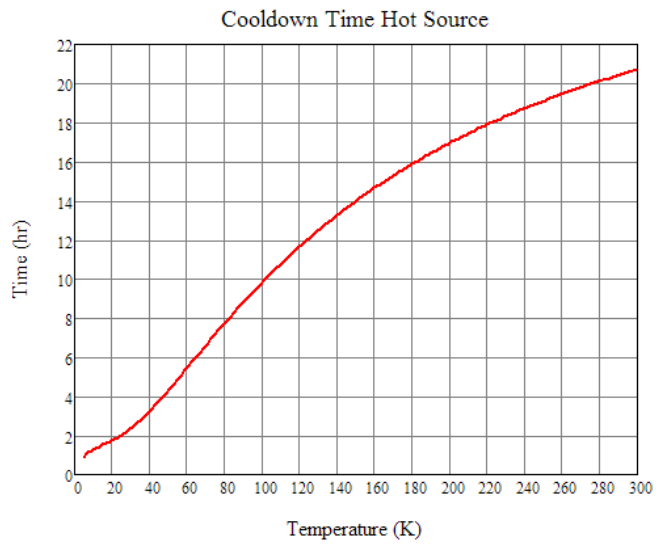
Fig. 10 Cool down curve for the hot source for passive cool down.
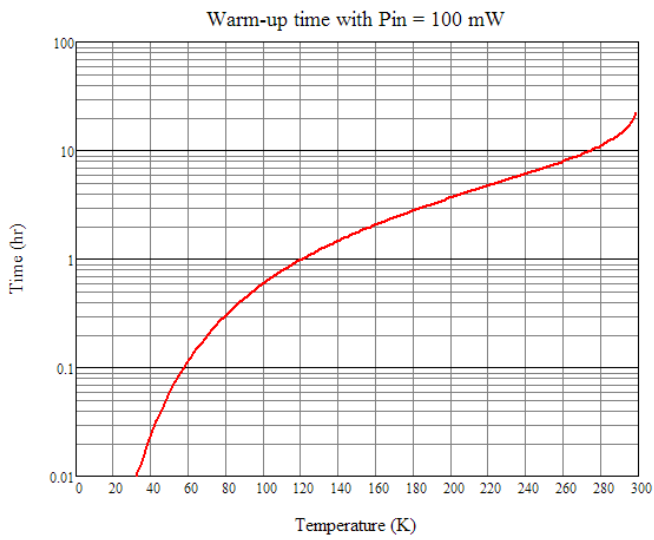
Fig. 9 Warm up curve of the hot source for 100 mW electrical input power to the heater.

Mechanical Tolerance Analysis of the Front-end Optics for the STEAMR Instrument

A. Hammar[1,2*], M. Whale[3], A. Emrich[1], A. Murk[3], J. Stake[2]

1 Omnisys Instrument AB, Västra Frölunda, SE-42130, Sweden
2 Terahertz and Millimetre Wave Laboratory, Department of Microtechnology and Nanoscience,
Chalmers University of Technology, SE-41296 Göteborg, Sweden
3 Institute of Applied Physics, University of Bern, Sidlerstrasse 5, 3012 Bern, Switzerland
* Contact: ah@omnisys.se, phone +4670 488 2185

Abstract——**The optics of the STEAMR instrument is a complex system involving off-axis mirrors designed to achieve precise imaging of the 14 receiver channel beams from the far field to the corresponding feed horns. An initial optical design was generated by Swedish Space Corporation which laid the framework for the subsequent IAP design which further developed the optical system to meet the mission performance requirements.**

Although simulations of the optics presently show good results, little is known about the sensitivity to mechanical errors for the complete optics chain. This work encompasses a tolerance analysis limited to the front-end optics consisting of the six off-axis mirrors. With six degrees of freedom for each of the six component reflectors, the scale of the required mechanical tolerancing analysis is significant. The goal of this work is therefore to identify critical locations within the optics architecture that have the largest influence on performance, specifically in terms of the farfield beam patterns. To simplify the problem, all mirrors are assumed to have no surface error. The results of this analysis will be of key importance in the eventual manufacture and assembly of the final instrument.

The main software tool used for these simulations is the optical design and analysis package ZEMAX, which offers built-in routines for performing Monte-Carlo simulations specifically for tolerancing problems. Key attention is given to errors in focusing and pointing for the elevation direction, being that this is the most crucial direction for observation. The ZEMAX tolerance analysis tool will allow for time-efficient calculation of the overall tolerance tasks. The main performance critiera here will be based upon geometrical beam pointing. Following this, the worst case scenarios will be analysed in further detail with the physical optics software package GRASP.

To lessen the numerical calculation load, only two beams (corresponding to the highest and lowest elevation) are considered in the first iteration. Besides giving a figure of the sensitivity for all mirrors, it is also the aim of this work to translate the results into corresponding sensitivity numbers for the structure supporting the entire optical system.

Cost-Effective Terahertz Quasi-Optical Components Based on Inkjet Printing of Carbon Nanocomposite Coatings

S. Subhechha[1], A. Das[2], T. M. Schutzius[2], A. Biswas[1], T. Wang[1], C. M. Megaridis[2] and L. Liu[2,*]

1 Department of Electrical Engineering, University of Notre Dame*, Notre Dame, IN 46556
2 Department of Mechanical and Industrial Engineering, University of Illinois at Chicago, Chicago, IL 60607
* Contact: lliu3@nd.edu, phone +1-574-631-1628

Abstract—Electromagnetic waves in the frequency range of 0.1-10 THz have remained the least explored and developed in the entire spectrum, creating what is widely known as the "Terahertz Gap". In recent years, THz waves have attracted much attention and continuous interests owning to their prospective applications in many important fields such as astronomy, chemical analysis, biological sensing, imaging and security screening. Among many in-development THz quasi-optical components, THz attenuators, polarizers and filters have been highly demanded in spectroscopy, polarization interferometry, polarimetric detection (e.g. polarization of Cosmic Microwave Background), and other systems. However, conventional methods for realizing the above components usually require complicated microfabrication processes such as photolithography or chemical etching. Therefore, new innovations in materials and processes for cost-effective, and potentially high performance THz quasi-optical components are of immense interest for a number of advanced technology applications.

In this paper, we report a new approach for making cost-effective THz quasi-optical components based on inkjet printing of carbon nanocomposite coatings. The coating fabrication process is inherently low-cost, and all ingredients are commercially available. The chemical inertness of the coatings along with their water repellency and self-cleaning ability prevent contamination and corrosion when exposed to outdoor conditions. In addition, the patterning of the coatings can be achieved using inkjet-printing, bypassing the complicated photolithography, nanoimprinting, or chemical etching processes, thus holding the potential promise for cost-effective, flexible THz quasi-optical components such as polarizers and filters.

In our previous work, we have demonstrated that large area carbon nanofiber (CNF)/PTFE polymer composite coatings as effective THz shielding and attenuation devices. The coating attenuation level can be modified by varying CNF loading content, and a THz shielding effectiveness (SE) of ~24 dB and ~32 dB were measured for the coating with the highest CNF content in the frequency range of 190-210 GHz and 570-630 GHz respectively. For a prototype demonstration, THz polarizers were first designed and inkjet-printed on Mylar thin films with nanocomposite coatings for operation near 600 GHz. The measured transmission, as well as calculated absorbance vary with polarization orientation as expected. An average degree of polarization of 0.35 has been demonstrated over the entire frequency range of 570-630 GHz, for a polarizer with a coating thickness of only 10 μm. The polarizer performance, specifically the extinction ratio, can be potentially improved to be near 60 dB by increasing the coating thickness and adopting dual-layer polarizer structures. Prototype THz filters using single- and cross-slot structures will be soon fabricated for performance evaluation. The manufacture process and measurement results will be presented at the conference.

Optics Design of the Multi-color TES Bolometer Camera for the ASTE Telescope

Tatsuya Takekoshi, Tetsuhiro Minamidani, Shunichi Nakatsubo, Tai Oshima, Masayuki Kawamura,
Hiroshi Matsuo, Tatsuhiro Sato, Nils W. Halverson, Adrian T. Lee, William L. Holzapfel, Yoichi Tamura,
Akihiko Hirota, Kenta Suzuki, Takuma Izumi, Kazuo Sorai, Kotaro Kohno and Ryohei Kawabe

Abstract—Wideband and high spatial resolution continuum observations in the millimeter and submillimeter wavelengths are of great importance to understand star formation history of galaxies from distant to nearby (early to recent universe), and thermal and non-thermal aspects of clusters of galaxies through Sunyaev-Zel'dovich effect. To promote such studies based on the millimeter and submillimeter continuum data, new TES (Transition Edge Sensor) bolometer camera for the ASTE telescope has been developed. We aim to observe three bands, 1100μm, 850μm and 450μm. Camera optics is designed by geometrical optics to fit into the Cassegrain system of the ASTE telescope and the spatial limitation of its receiver cabin. For the efficient observation, our optics realizes 7.5' field of view and 2-band simultaneous observation. The two focal planes can accommodate two of three TES bolometer wafers which have 169, 271, and 881 pixels at 1100, 850, and 450μm, respectively. The camera optics is accomplished diffraction limited optics, which is confirmed from spot diagrams and strehl ratios. It is evaluated via physical optics calculation, and all pixels on each focal plane have aperture efficiency of $\sim$30% in absence of reflection and absorption loss by filters and the Ruze loss. The dimensions of the optical elements are also determined based on the results of the physical optics calculations.

I. INTRODUCTION

IT is of great importance in astronomy and astrophysics to understand star formation history of galaxies from distant to nearby (from early to recent universe), and the evolution of large scale structure. Distribution and star formation rate of (sub)millimeter-bright galaxies (SMGs) are clues of galaxy evolution and the cosmic star formation history. Ultra-high temperature component of clusters of galaxies is also a clue to large scale structure formation history, because that component

may be caused by collisions of clusters of galaxies that heat up surrounding materials.

Observations using AzTEC [1] on the ASTE telescope provided large map more than 1 $\deg^2$ as deep as 0.5–1 mJy/beam, and more than 1000 sources were detected in the 1.1 mm wavelength [2]–[5]. Surveying SMGs, and determination of their redshifts and star formation rates is one of the immediate purposes of this project. Understandings of dust nature of nearby galaxies and the Milky Way is also important to reveal properties of not only themselves but also SMGs. The detection of ultra-high temperature components of clusters of galaxies through the Sunyaev-Zel'dovich (SZ) effect is another approach to understand the history of the large structure formation. Therefore, we aim to develop a new millimeter and submillimeter bolometer camera for the ASTE telescope and conduct large area surveys in the millimeter and submillimeter wavelengths.

The ASTE telescope [6], [7] is a 10-m submillimeter telescope (Figure 1) located at the Atacama Desert, Chile. Its altitude is 4850m and it is known as one of the best sites for submillimeter observations because of its good atmospheric transmission [8]. With this telescope, we aim to observe 1100 μm (270 GHz), 850 μm (350 GHz) and 450 μm (670 GHz) Bands. These bands are essentially important to determine photometric redshifts and star formation rates of distant galaxies, to understand dust nature in galaxies and the Milky Way, and to detect ultra-high temperature components of clusters of galaxies through the SZ effect. The bandwidths are determined as wide as possible avoiding the water vapor absorptions to achieve good sensitivities. Frequency bands, ranges, and bandwidths are summarized in Table I. Simultaneous observation capability of two or three bands and a large FoV at least 7.5 arcminutes diameter are necessary to achieve large area surveys within a reasonable project duration.

It is necessary to design and develop the optics to couple the TES bolometers to the Cassegrain optics of the ASTE telescope. In this paper, the optics design and design procedure for this camera is described.

II. OPTICS DESIGN

Under the scientific requirements and limitations mentioned above, we designed the optics system that couples to the Cassegrain system of the ASTE telescope whose antenna parameters are summarized in Table II. The ASTE telescope has a classical Cassegrain optics whose F-number is 8.878.

T. Takekoshi is with Department of Cosmosciences, Graduate School of Science, Hokkaido University, N10W8, Kita-ku, Sapporo, 060-0810, Japan e-mail: takekoshi@astro1.sci.hokudai.ac.jp.

T. Takekoshi, T. Oshima. M. Kawamura T. Sato, Y. Tamura, A. Hirota and R. Kawabe are with Nobeyama Radio Observatory.

T. Takekoshi, T. Oshima. M. Kawamura, H. Matsuo, T. Sato, Y. Tamura, A. Hirota and R. Kawabe are with National Astronomical Observatory of Japan.

T. Minamidani and K. Sorai are with Department of Physics, Faculty of Science, Hokkaido University.

S. Nakatsubo is with Institute of Low Temperature Science, Hokkaido University.

M. Kawamura, Y. Tamura, K. Suzuki, T. Izumi and K. Kohno are with Institute of Astronomy, The University of Tokyo.

N.W. Halverson is with Center for Astrophysics and Space Astronomy, University of Colorado.

N.W. Halverson is with National Institute of Standards and Technology.

A.T. Lee and W.L. Holzapfel are with Department of Physics, University of California.

A.T. Lee is with Physics Division, Lawrence Berkeley National Laboratory.

Fig. 1. Front and side view of the ASTE telescope. The Cassegrain system consists of a 10-m main-reflector and a 620-mm sub-reflector. The receiver cabin and the Cassegrain system move together with the elevation angle.

TABLE I
OBSERVING BANDS OF NEW BOLOMETER CAMERA FOR ASTE

Bands	Frequency range (GHz)	Band width (GHz)
270 GHz Band	244–294	50
350 GHz Band	330.5–365.5	35
670 GHz Band	630–710	80

The Cassegrain focus is located above the ceiling of the receiver cabin, and then rays reflected by the main- and sub-reflectors go into the receiver cabin with outspreading. Thus, it is necessary to set a re-imaging mirror in the receiver cabin.

The size of the receiver cabin is approximately 1.9 m in length × 2.2 m in width × 1.8 m in height, and a 19-inch standard rack occupies some space in the receiver cabin. All the optics components and the cryostat should be fit inside.

Figure 2 shows the position and design of the third mirror in the ASTE cabin. The re-imaging mirror is designed as an ellipsoidal mirror to refocus the outspreading rays into a focal plane in the cryostat. Because of the limitation described above, this ellipsoidal mirror is put at very close to the floor of the receiver cabin, and its aperture diameter becomes 560 mm to achieve 7.5 arcminutes FoV. This is the maximum size realized under the limitations of the available receiver cabin space. The preliminary ellipsoidal mirror causes large aberrations especially at the edges of the field of view, and modification is necessary to realize the diffraction-limited performance over the whole field of view and all frequency bands. We optimize the shape of the third mirror by addition of fifth order polynomials.

TABLE II
ANTENNA PARAMETERS OF ASTE

Main-reflector dia.	10 m
Sub-reflector dia.	620 mm
F/#	8.878
Surface accuracy	19 μm r.m.s.
Mainbeam efficiency	0.6-0.7 (850 μm)
Beam size	22" (850 μm)
Pointing accuracy	2" r.m.s.
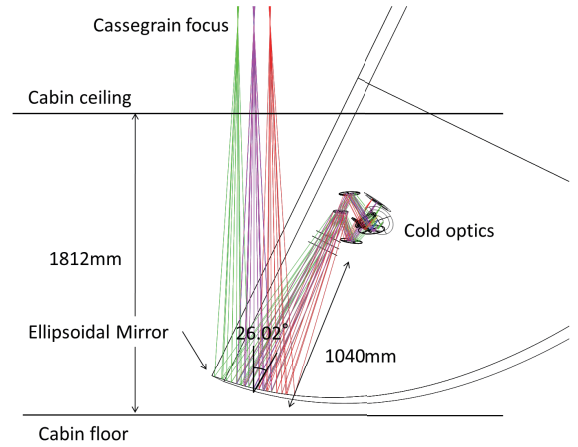
Fig. 2. Side view of the receiver cabin and optics cut along the reflected direction by ellipsoidal mirror. The ray from the Cassegrain system focuses near the ceiling of the receiver cabin.

The cryostat window is placed at a certain position to avoid the interference with rays between the sub-reflector and the re-imaging ellipsoidal mirror. This position limits the size of the cold optics to about a cube 500 mm on a side.

Inside of the cryostat, incident rays are divided into two bands using a dichroic filter. This is a key component to realize simultaneous multi-color optics without reducing the observing efficiency. This dichroic filter is placed at the pupil to reduce the filter aperture size, and inclines at 25 degree to the incident principle ray to keep good transmission and reflection characteristics. This makes it difficult to design an optics system that realizes simultaneous three bands observations, and we choose the design for the simultaneous two bands observations. Hereafter, we call the reflected band as "Band 1" and transmitted band as "Band 2". We use these bands as 270 and 350 GHz Bands, respectively, for Phase I configuration, and 670 and 350 GHz Bands, respectively, for Phase II configuration. The cold Lyot stop, which reduces unexpected optical load to bolometers, is also placed at the pupil.

The numbers of pixels of each bolometer wafer are 271, 271, and 881 pixels for 270, 350, and 670 GHz Bands, respectively and the number of readouts is limited to $\sim$400 pixels for the Phase I (270 and 350 GHz Bands) operation. Therefore, we use the only central 169 pixels of 270 GHz Band wafer. This is because the sensitivity of 350 GHz Band is worse than that of 270 GHz Band due to the differences of atmospheric transmissions and detector bandwidths, and we assign as many pixels as possible for 350 GHz Band. The diameter of the central 169 pixels of the 270 GHz Band wafer corresponds to 55 mm, and we modify the shape and position of dielectric lens to keep the FoV of 7.5 arcminutes diameter. As a result, the numbers of pixels are 169, 271, and 881 pixels for 270, 350, and 670 GHz bands, respectively. All bands cover the FoV of 7.5 arcminutes diameter.

Figure 3 shows the final design of the cold optics. The rays split by the dichroic filter are reflected by plane mirrors respectively to make a compact cold optics. In each band,
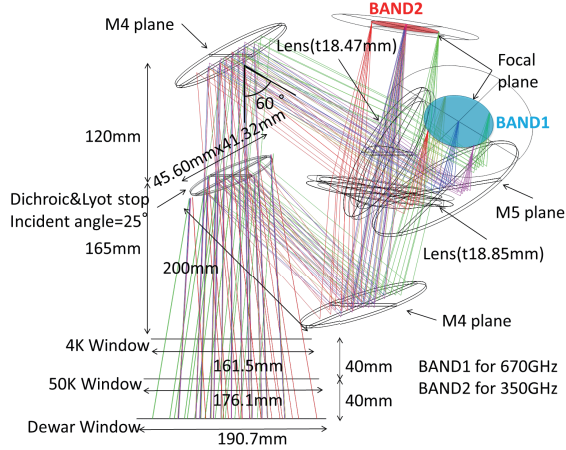
Fig. 3. Side view of Phase II cold optics cut along the reflected direction by the third mirror. The ray reflected by the third mirror goes through the 300 K, 50 K, and 4 K windows. The dichroic filter divides incoming rays into two bands, and each ray are focused after flat mirrors and HDPE lenses.

TABLE III
STREHL RATIOS AT EACH BAND AND FIELD

Field (dAZ, dEl)	270 GHz	350 GHz	670 GHz
1 (0', 0')	0.982	0.987	0.950
2 (-3.25', 1.13')	0.978	0.979	0.923
3 (3.25', -1.13')	0.998	0.995	0.984
4 (-1.13' ,-3.25')	0.979	0.969	0.892
5 (1.13' , 3.25')	0.977	0.966	0.883

TABLE IV
PARAMETERS OF BEAM PATTERNS AT EACH BAND AND FIELD

270 GHz	Field1	Field2	Field3	Field4
Gain (dBi)	84.63	84.71	84.07	84.54
Aperture efficiency (%)	36.33	37.00	31.92	35.54
FWHM minor (arcsec)	27.58	27.35	29.95	27.82
FWHM major (arcsec)	28.72	28.30	28.82	28.48
Sidelobe level (dB)	-17.87	-16.50	-17.29	-17.80
Cross pol. level (dB)	-34.62	-34.61	-34.79	-29.02

350 GHz	Field1	Field2	Field3	Field4
Gain (dBi)	86.91	86.89	86.28	86.74
Aperture efficiency (%)	36.50	36.39	31.61	35.15
FWHM minor (arcsec)	21.29	21.25	23.13	21.54
FWHM major (arcsec)	22.14	21.83	22.36	22.02
Sidelobe level (dB)	-17.58	-16.16	-17.45	-17.45
Cross pol. level (dB)	-33.89	-34.26	-34.34	-28.72

670 GHz	Field1	Field2	Field3	Field4
Gain (dBi)	92.23	92.22	91.47	91.69
Aperture efficiency (%)	33.95	33.89	28.50	29.99
FWHM minor (arcsec)	11.14	10.85	12.12	11.37
FWHM major (arcsec)	11.51	11.52	11.68	11.61
Sidelobe level (dB)	-16.89	-15.34	-17.09	-14.77
Cross pol. level (dB)	-35.02	-35.08	-35.15	-28.46

The tables are the cases of 85% diameter of the geometrical cold Lyot stop and no horn offset.

dielectric lens is placed between the dichroic filter and a horn array to make a telecentric system and to fit the size of focal plane. For Band 1, an additional flat mirror is used between the dielectric lens and the horn array.

Imaging quality of this optics is checked using spot diagrams and Strehl ratios at 49 positions of each focal plane. We measured at 4 grids and 12 grids in radial and circumferential directions, respectively, and the center position. Table III shows the Strehl ratios of the five representative positions, corresponds to the center and the four edges fields. Strehl ratio of more than 0.8 is usually considered as diffraction limited, and we follow this criterion. They are all more than 0.8, and it is confirmed that designed optics achieves diffraction limited.

III. PHYSICAL OPTICS EVALUATION

The evaluations of the optics system under the geometrical optics assumptions are in good agreement with the actual in the short wavelengths (high frequencies). However, in the millimeter and submillimeter wavelengths, which are similar to the dimensions of optical elements, it is necessary that analysis considering the effects of the diffraction and interference. We use the Physical Optics (PO) antenna analysis software GRASP9 developed by TICRA for this analysis. PO is the method to solve the propagation of electromagnetic waves based on the Maxwell's equations. The current distribution of a scatterer's surface can be calculated from the beam pattern of the previous scatterer, which is calculated by the current distributions on the previous scatterer.

We make the equivalent model of the designed optics described in Section II, which includes the main-reflector, the sub-reflector, the third mirror, the 300 K cryostat window, the 50 K shield window, the 4 K shield window, the cold Lyot stop (dichroic filter), the fourth flat mirror, the dielectric lens, the fifth flat mirror, and the conical horn. All these optical elements except the conical horn are modeled as reflective mirrors with the same aperture size as designed because of their ease to use. A dielectric lens is modeled as a spherical reflector under the assumptions of a thin lens and a telecentric optics. Optical components that limit the diameter of the beams, that is, cold Lyot stop, 4 K and 50 K shields, and cryostat windows, are modeled as plane mirrors with the appropriate aperture size. Additionally, the blockage of the sub-reflector is treated as a hole on the main-reflector, and the blockage of the sub-reflector supporting structure is neglected. As the surfaces of optical elements are assumed to be perfect, Ruze losses are neglected.

Spillovers of each optical element are also provided from the each run. We assumed that these spillovers are terminated to the certain temperature (4 K or 300 K), and estimate the photon noise originated from the optics in the form of noise equivalent power (NEP). We adopt the cold stop diameter of 85% of geometrical design because photon noise from optics is minimized. PO calculation provides us beam patterns of E-plane, H-plane, and cross polarization (Figure 4), then some beam parameters, that is, gain, beam size (FWHM), sidelobe level, and cross polarization level are obtained. Those results are summarized in Table IV.
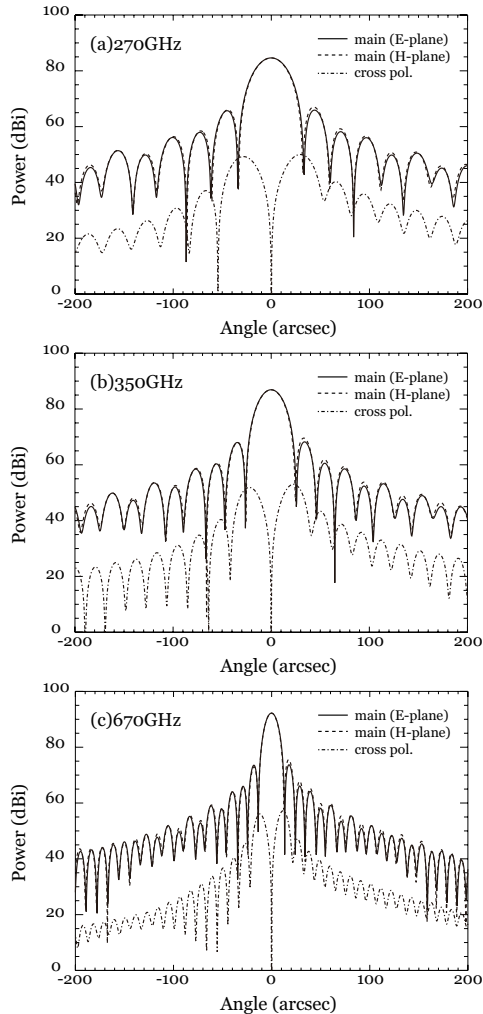
Fig. 4. Beam patterns of the central beam (Field 1) of (a) 270 GHz, (b) 350 GHz, and (c) 670 GHz Bands. These are the cases of 85% diameter of the geometrical cold Lyot stop and no horn offset.

IV. SUMMARY

We designed the optics of multi-color TES bolometer camera for the ASTE telescope. The designed optics fitted inside of the ASTE cabin and the camera cryostat. The optics for 2-color simultaneous observation and 7.5 arcminutes diameter FoV were achieved. We will operate 270 GHz and 350 GHz Bands for Phase I configuration, and 350 GHz and 670 GHz Bands for Phase II configuration. The numbers of pixels were optimized in terms of mapping speed and they became 169, 271, and 881 pixels for 270, 350, and 670 GHz Bands, respectively.

We evaluated the designed optics using physical optics (PO) method. And we adopted the cold stop diameter of 85% of geometrical design because photon noise from optics was minimized. As a result of optimization, aperture efficiencies of each beam were $\sim 30\%$ at each band. Beam sizes (FWHM) were ~ 28 arcseconds, 22 arcseconds, and 12 arcseconds, for 270 GHz, 350 GHz, and 670 GHz Bands, respectively.

REFERENCES

[1] G. W. Wilson, J. E. Austermann, T. A. Perera, K. S. Scott, P. A. R. Ade, J. J. Bock, J. Glenn, S. R. Golwala, S. Kim, Y. Kang, D. Lydon, P. D. Mauskopf, C. R. Predmore, C. M. Roberts, K. Souccar, and M. S. Yun, "The AzTEC mm-wavelength camera," MNRAS, vol. 386, p. 807, 2008.
[2] Y. Tamura, K. Kohno, K. Nakanishi, B. Hatsukade, D. Iono, G. W. Wilson, M. S. Yun, T. Takata, Y. Matsuda, T. Tosaki, H. Ezawa, T. A. Perera, K. S. Scott, J. E. Austermann, D. H. Hughes, I. Aretxaga, A. Chung, T. Oshima, N. Yamaguchi, K. Tanaka, and R. Kawabe, "Spatial correlation between submillimetre and Lyman-α galaxies in the SSA22 protocluster," Nature, vol. 459, p. 61, 2009.
[3] K. S. Scott, M. S. Yun, G. W. Wilson, J. E. Austermann, E. Aguilar, I. Aretxaga, H. Ezawa, D. Ferrusca, B. Hatsukade, D. H. Hughes, D. Iono, M. Giavalisco, R. Kawabe, K. Kohno, P. D. Mauskopf, T. Oshima, T. A. Perera, J. Rand, Y. Tamura, T. Tosaki, M. Velazquez, C. C. Williams, and M. Zeballos, "Deep 1.1mm-wavelength imaging of the GOODS-S field by AzTEC/ASTE - I. Source catalogue and number counts," MNRAS, vol. 405, p. 2260, 2010.
[4] B. Hatsukade, K. Kohno, I. Aretxaga, J. E. Austermann, H. Ezawa, D. H. Hughes, S. Ikarashi, D. Iono, R. Kawabe, S. Khan, H. Matsuo, S. Matsuura, K. Nakanishi, T. Oshima, T. Perera, K. S. Scott, M. Shirahata, T. T. Takeuchi, Y. Tamura, K. Tanaka, T. Tosaki, G. W. Wilson, and M. S. Yun, "AzTEC/ASTE 1.1-mm survey of the AKARI Deep Field South: source catalogue and number counts," MNRAS, vol. 411, p. 102, 2011.
[5] S. Ikarashi, K. Kohno, J. E. Aguirre, I. Aretxaga, V. Arumugam, J. E. Austermann, J. J. Bock, C. M. Bradford, M. Cirasuolo, L. Earle, H. Ezawa, H. Furusawa, J. Furusawa, J. Glenn, B. Hatsukade, D. H. Hughes, D. Iono, R. J. Ivison, S. Johnson, J. Kamenetzky, R. Kawabe, R. Lupu, P. Maloney, H. Matsuhara, P. D. Mauskopf, K. Motohara, E. J. Murphy, K. Nakajima, K. Nakanishi, B. J. Naylor, H. T. Nguyen, T. A. Perera, K. S. Scott, K. Shimasaku, T. Takagi, T. Takata, Y. Tamura, K. Tanaka, T. Tsukagoshi, D. J. Wilner, G. W. Wilson, M. S. Yun, and J. Zmuidzinas, "Detection of an ultrabright submillimetre galaxy in the Subaru/XMM-Newton Deep Field using AzTEC/ASTE," MNRAS, vol. 415, p. 3081, 2011.
[6] H. Ezawa, R. Kawabe, K. Kohno, and S. Yamamoto, "The Atacama Submillimeter Telescope Experiment (ASTE)," in *Proc. of SPIE*, vol. 5489, 2004, p. 763.
[7] H. Ezawa, K. Kohno, R. Kawabe, S. Yamamoto, H. Inoue, H. Iwashita, H. Matsuo, T. Okuda, T. Oshima, T. Sakai *et al.*, "New achievements of ASTE: the Atacama Submillimeter Telescope Experiment," in *Proc. of SPIE*, vol. 7012, 2008.
[8] S. Matsushita, H. Matsuo, J. R. Pardo, and S. J. E. Radford, "FTS Measurements of Submillimeter-Wave Atmospheric Opacity at Pampa la Bola II : Supra-Terahertz Windows and Model Fitting," PASJ, vol. 51, p. 603, 1999.

Tatsuya Takekoshi was born in Hokkaido, Japan in 1985. He received the degrees of B.S. in Physics and M.S in Cosmoscience from Hokkaido University, Sapporo, Japan in 2008 and 2010, respectively. His current research interests are development of the multi-color TES bolometer camera for the ASTE telescope, and an observational study of starformation process in the low metallicity environment using millimeter and submillimeter instruments.

Development of Terahertz Focal Plane Array Elements using Sb-based Heterostructure Backward Diodes

Syed Rahman, Yi Xie, Zhenguo Jiang, Huili (Grace) Xing, Patrick Fay and Lei Liu

Department of Electrical Engineering
University of Notre Dame, IN, 46556, USA
Contact: srahman@nd.edu

Abstract — **We report our initial work on the development of terahertz focal-plane array (FPA) elements by integrating Sb-based heterostructure backward diodes (HBDs) onto folded-dipole antennas (FDAs). Simulation results for a prototype FDA design at 200 GHz have shown that an embedding impedance varying from 10 Ω to 1800 Ω for its real part, and 10 Ω to 900 Ω for the imaginary part can be achieved by changing the antenna geometry   for impedance matching. The performance of the 200 GHz FDA on an extended hemispherical silicon lens (R=5 mm) has been analyzed using the ray tracing technique. Optimized antenna directivity and Gaussian coupling efficiency have been obtained with an extension length of 2.5 mm. For a prototype demonstration, an ADS lumped-element nonlinear circuit model has been employed for understanding the HBD device performance at THz frequencies, and on the basis of it, the FDA designed above has been optimized for impedance matching to a HBD device with an active area of 0.4μm×0.4μm at 200 GHz. Under conjugate matching condition, a maximum detector responsivity of ~21,000 V/W could be obtained based on simulation results. Initial work on circuits and devices fabrication is also presented.**

I. INTRODUCTION

In recent years, engineers and scientists have intensified their efforts to develop detectors and imaging systems operating in the submillimeter-wave and terahertz (THz) region. The submillimeter-wave and THz range in the electromagnetic spectrum is becoming more and more important to radio astronomy, chemical spectroscopy, bio-sensing, medical imaging, security screening, and defense [1-4]. For all the above applications, a real-time portable THz focal-plane array (FPA) system that can operate at room temperature with high performance has been in high demand for many years [5]. Due to the lack of high performance THz radiation detection devices and other technical challenges, current available THz imaging systems necessitate operation at cryogenic temperature (e.g. HEBs) and/or require slow mechanical scanning [6,7], resulting in bulky and expensive systems. THz detectors employed in room-temperature imagers (e.g. Schottky diodes) generally have relatively low

responsivity and high noise equivalent power (NEP) level [8], [9], leading to limited system dynamic range.

Integrated Sb-based heterostructure backward diodes (HBDs) are approaching to meet the demands of high performance FPAs for terahertz imaging systems and applications. Owning to HBDs' high curvature coefficient (i.e. high responsivity), low noise performance, zero bias and room temperature operation, direct detectors based on these devices have been demonstrated at millimeter-wave frequencies [9]. However, reduced HBD device area (e.g. submicron) is required for operation at THz region, resulting in high device impedance. Integrated planar antennas that can potentially achieve high embedding impedances are needed for realizing quasi-optical detector elements with maximized responsivity, which is critical in portable and LNA-less THz FPAs.

In this paper, we report our initial work on the development of FPA elements by integrating Sb-based HBDs onto folded-dipole antennas (FDAs). FDA offers a wide range impedance tuning capacity by varying its geometry such as number of turns, antenna arm width, and arm spacing, thus providing an opportunity to conjugate match the HBD device impedance for maximum responsivity without additional matching network. Ray tracing technique has been applied to calculate the far field radiation patterns of the FDAs mounted on extended hemispherical silicon lens. An optimum extension length of ~2.5 mm has been obtained for maximum directivity and good Gaussian coupling efficiency at 200 GHz [8]. To lessen parasitic effects for THz operation, an airbridge finger has been introduced for integrating HBD devices onto FDAs. For DC signal output, a PBG structure based on co-planar strip lines was designed with low dielectric BCB as the insulation layer. This single element detector design will soon be expanded into a full 2-D FPA for imaging applications.

II. HETEROSTRUCTURE BACKWARD DIODES

Shown in Fig. 1 are the epitaxial layer structure together with energy band diagram of a HBD device. The nonlinear current-voltage (I-V) characteristics of the device are determined by its interband tunneling mechanism between the InAs and GaSb layer. In contrast to Schottky diode the curvature of HBD devices can exceed q/k_BT, resulting in highly sensitive detectors. The unmatched responsivity of HBDs is expressed by,

| 1000 Å	n+-InAs	$N_D = 1.3\times10^{19}$ cm^{-3}
500 Å	n-InAs	$N_D = 1.4\times10^{17}$ cm^{-3}
32, 11, 7Å		i-AlSb
150 Å		i-Al$_{0.1}$Ga$_{0.9}$Sb
500 Å	p+-GaSb	$N_A = 1.3\times10^{19}$ cm^{-3}
4000 Å	n+-InAs	$N_D = 1.3\times10^{19}$ cm^{-3}
S.I. GaAs		

(a)
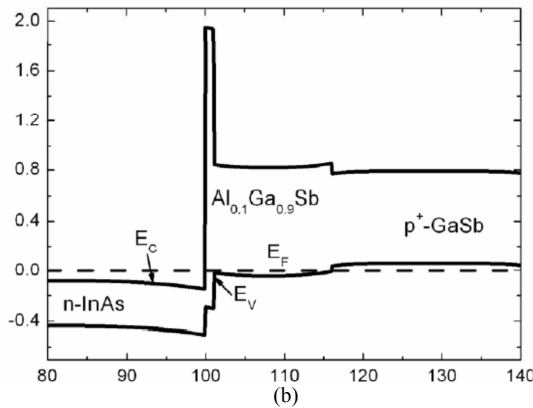
(b)

Fig. 1. (a) Epitaxial layer, and (b) band structure of a Sb-based HBD device.

$$\beta_{v,max} = \frac{\gamma R_j}{2(1+\frac{R_s}{R_j})(1+\frac{R_s}{R_j}+\omega^2 C_j^2 R_s R_j)} \qquad (1)$$

where γ, R_j, R_s and C_j are curvature coefficient, junction resistance, series and junction capacitance respectively. A very thin layer of AlSb is grown to provide an additional control over tunneling current density and this additional thin layer increase tunneling probability and reduce junction resistance. However, this layer reduces the device responsivity by lowering the curvature coefficient. The reduced responsivity could be improved by using a p-type δ doping in the cathode layer for reducing junction capacitance and record curvature coefficient has been achieved [9].

The intrinsic cutoff frequency of a HBD device is dependent on its series resistance (R_s) and junction capacitance (C_j) which could be expressed by,

$$f_c = \frac{1}{2\pi R_s C_j} . \qquad (2)$$

As the device active area scales down to submicron dimensions, the metal semiconductor contact resistance dominates and the junction capacitance exhibits a fringing capacitance components that does not scale with the active area. Therefore an optimum device area is needed to maximize the cutoff frequency. In addition, the device impedances of

Fig 2: Folded dipole antenna structure with number of turns N=3.
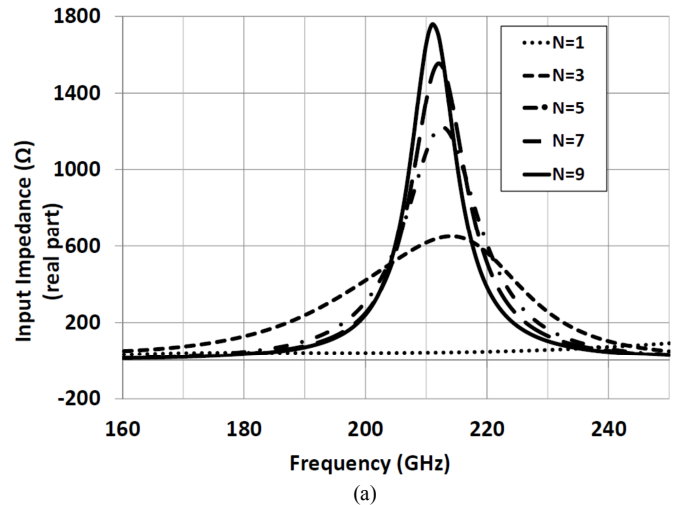
(a)
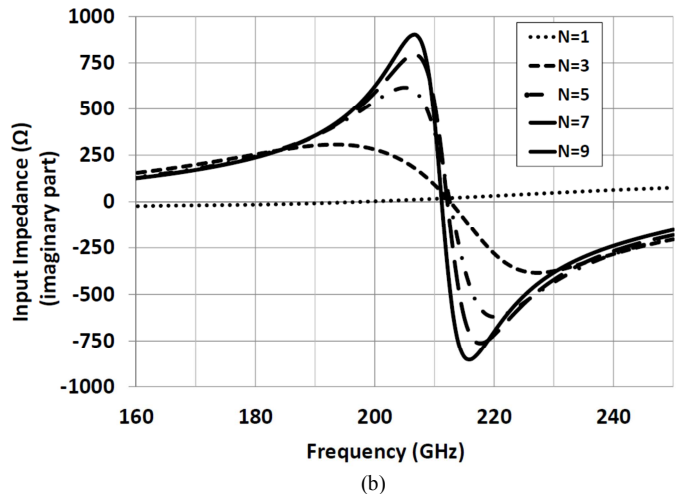
(b)

Fig. 3. Simulation results of a 200 GHz FDA embedding impedance changes with antenna number of turns (N): (a) real part antenna embedding impedance, and (b) imaginary part antenna embedding impedance.

HBDs vary with their dimensions and submicron structure HBDs exhibit high impedances at frequencies far below their cutoff frequencies.
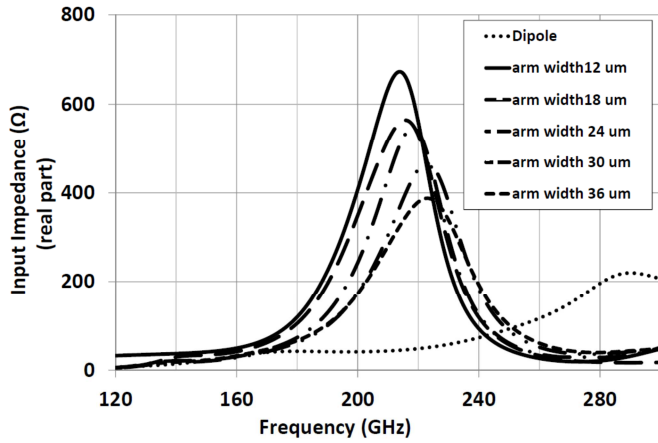
(a)
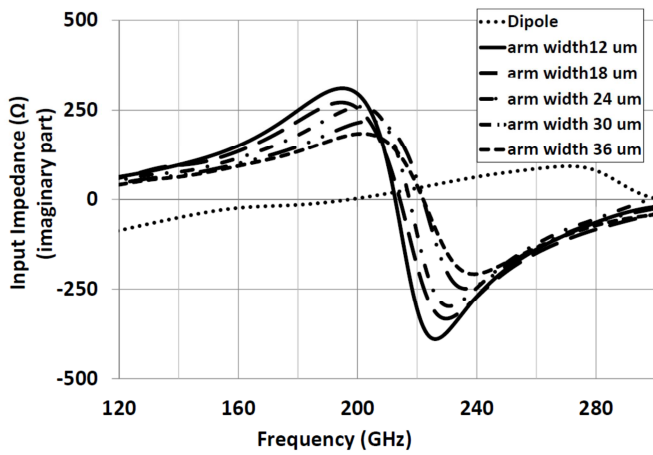
(b)

Fig. 4. Variation of real part (a) and imaginary part (b) of antenna impedance with varying arm width from 12 μm to 36 μm.

(a)

(b)

Fig. 5. FDA designs for impedance conjugate matching to a HBD device (0.4μm×0.4μm) at 200 GH: (a) FDA design with $N=3$, and (b) FDA design with $N=5$.

III.   THZ FPA DESIGN AND ANALYSIS

A. Folded Dipole Antennas for Maximum Responsivity

Since submicron scale HBDs exhibit high device impedances at terahertz frequencies, a high impedance antenna with strong tuning capacity is required to achieve maximum responsivity for portable, LNA-less FPAs. Shown in Fig. 2 is a 200 GHz FDA (antenna arm length l = 285) on silicon with number of turns N =3, arm width w=12 μm and arm gap g=12μm. According to antenna theory, the input impedance of a FDA is proportional to N by

$$Z_{in} = N^2 Z_o, \qquad (3)$$

where Z_0 is the impedance of a single dipole antenna ($N=1$) with same antenna arm length and arm width. By varying the antenna geometry such as number of turns, antenna arm width and arm gap, a FDA may provide a wide range of embedding impedances at certain frequency for impedance matching to a HBD device without additional matching network. HFSS simulation has been performed to verify the impedance tuning

Fig. 6. Simulated detector responsivity under conjugate matching condition at 200 for two antenna designs ($N=3$ and $N=5$).
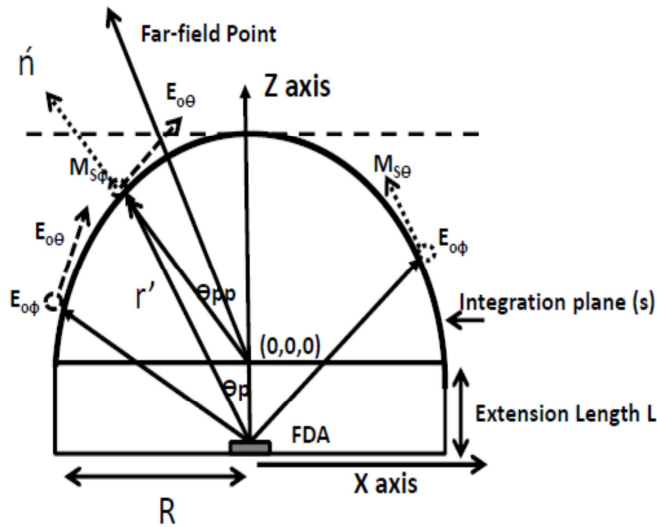
Fig. 7. Ray tracing techniques on extended hemispherical silicon lens.

capability of FDAs as shown in Fig. 3 and Fig. 4. Fig. 3 shows the simulation results for the embedding impedance of a FDA designed with center frequency of ~210 GHz. When the antenna number of turns N increases from 1 to 9, the real part of the impedance at 200 GHz changes from 10 Ω to 1800 Ω, while the imaginary impedance varies from 10 Ω to 900 Ω. Fig. 4 illustrates the FDA embedding impedance varies with its arm width w. When w increase from 12 μm to 36 μm, the antenna real part impedance at 200 GHz changes from 180 Ω to 400 Ω, and the imaginary part impedance varies from 200 Ω to 270 Ω. In addition, HFSS simulation also shows that a FDA impedance can be varied by changing its arm gap from 12 μm to 36 μm (not shown), demonstrating the strong tuning capability of FDAs for impedance matching to achieve a maximum responsivity at certain THz frequency. Two FDAs have been designed for impedance matching to a HBD device with an active area of 0.4μm×0.4μm at 200 GHz. On the basis of a lumped element circuit model, the HBD device
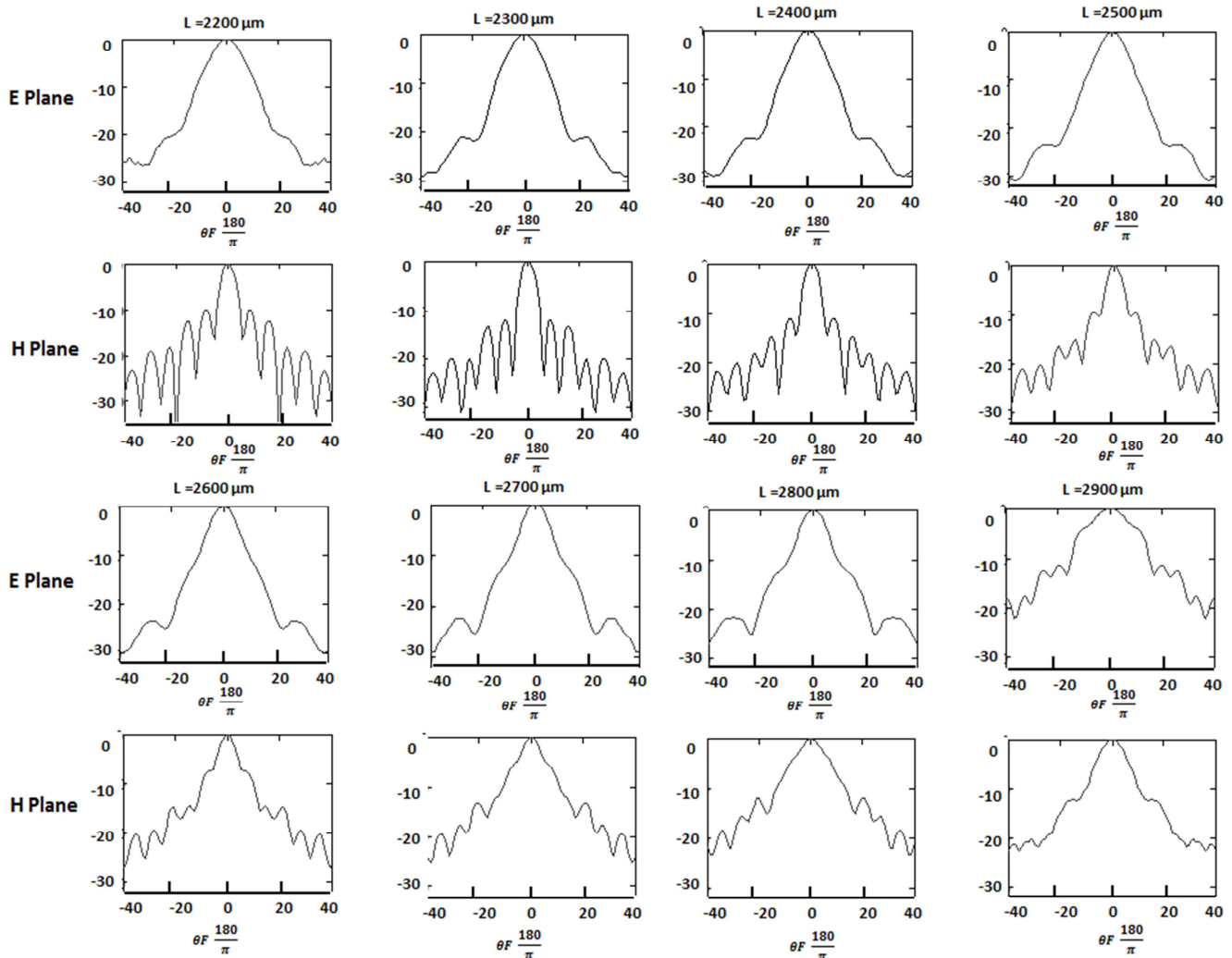
Fig. 8. E and H plane radiation patterns of FDA with N=3 at 200 GHz calculated for extension lengths varying from 2200 μm to 2900 μm.

antenna arm length of 275 μm, an arm width of 15 μm and an arm gap of 12 μm. The second design uses the antenna parameters of *N=5, l= 275 μm,w=12 μm,* and *g = 10* μm. As shown in Fig. 5 (a) and (b), nearly perfect conjugate impedance matching has been achieved for both antenna designs. Under this impedance matching conditions, the detector responsivities have been calculated as shown in Fig. 6. Maximum responsivities of 19500 V/W and 20000 V/W have been demonstrated for *N=3*, and *N=5* antennas respectively. Because FDAs are resonant antennas with reduced bandwidth for increased number of turns, the detector element with *N=5* design shows relatively narrower bandwidth as compared to the design with *N=3*.

B. Lens-Coupled FDA Far-Field Radiation Patterns

To calculate far field radiation pattern of the folded dipole antennas mounted on an extended hemispherical silicon lens with radius *R = 5* mm, ray tracing technique has been applied [8] to choose an extension length for highest antenna directivity while keeping an acceptable Gaussian coupling efficiency, as shown in Fig. 7.

Fig. 8 shows the simulation results of far-field radiation patterns of the lens-coupled *N=3* FDA at 200 GHz. For an extension length varies from 2200 μm to 2900 μm the far-field patterns in both the E-plane and H-plane become narrower first and then broader with a highest directivity achieved for 2.5 mm extension length.

C. Low Pass Filter Design

A co-planar strip-line stepped-impedance low-pass filter has been designed to extract DC signal, while presenting open-circuit to the designed FDA [12]. The length of each section is 135 μm. For the high impedance sections, the strip line width (*h*) is 2 μm and the gap between the lines (*t*) is 82 μm, while for the low impedance sections, *h*= 41 μm and t = 4 μm. Fig. 9 shows the simulated s-parameters and the obtained RF suppression at around 200 GHz is as high as 32 dB.

IV. Integrated HBD Detector fabrication

The fabrication of the designed HBD FPA detector element has been performed at the nanofabrication facility of the University of Notre Dame. Fig. 10 shows the process flow including 1) epitaxial layer growth (see Fig. 1) on semi-insulation GaAs wafer, 2) HBD device active area definition and mesa etching, 3) antenna layer photolithography, 4) airbridge formation, and 5) BCB layer insulation and LPF layer photolithography. The active area of HBD devices was defined by top contact cathode layer of Ti/Au/Ti (20 nm/250 nm/ Au). This layer also serves as the mask layer in the subsequent self-aligned wet chemical etching of the active device junction fabrication. The bottom Ti layer increase adhesion of the cathode contact and the top Ti layer minimize the electro chemical effects in the sub-sequent chemical etching since electro chemical effect degrade the process and degrade lateral scaling of the device.

Two types of etchants: citric acid+H_2O_2 (1:2) and NH_4OH+H_2O (1:5) have been used to etch the InAs and Sb bearing materials, respectively. Following the active area

etching the device was isolated by wet etching of InAs anode contact to define the mesa anode layer. The FDA antenna layer was then fabricated using a photolithography and lift-off process.

To minimize parasitic effects, an airbridge finger has been introduced across the antenna and device cathode contact as shown in fig 9. Polyimide material was utilized as the sacrificial layer for airbridge development. The polyimide sacrificial layer was spanned, partially cured and etched down using RIE. After exposing the antenna layer and cathode contact, a very thin Ti layer (15 nm) was deposited to protect the polyimide layer from the subsequent airbridge fabrication process. The airbridge finger was then fabricated using conventional photolithography followed by lift-off process.

A layer of BCB was spanned, hard cured and patterned by RIE to serve as the isolation material between the antenna layer and LPF circuits. The polyimide sacrificial layer was removed by isotropic dry etching before developing the DC output/LPF circuits (1 μm). Fig. 11 shows a SEM picture of a HBD device with an airbridge finger integrated at the center of a FDA. The fabricated HBD detector elements will soon be tested and expanded into a full 2-D FPAs.


(a)

(b)
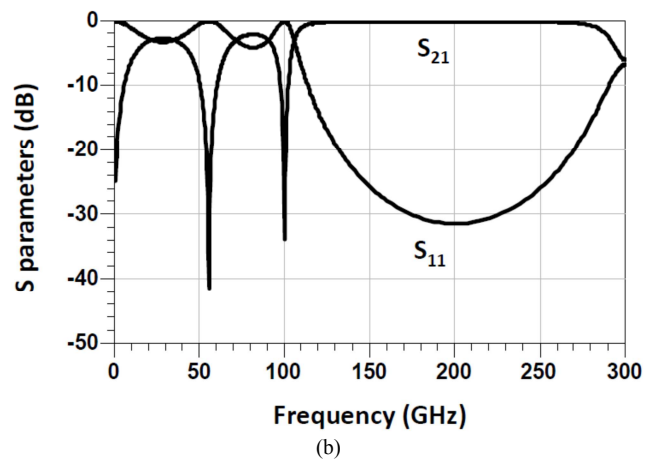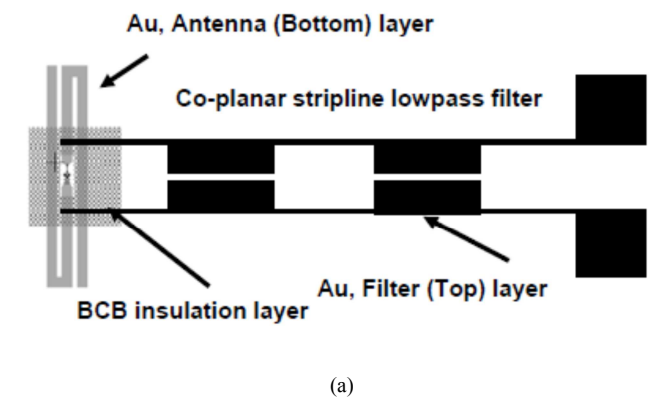
Fig. 9. Low pass filter design to suppress 200 GHz signal (a) and simulated S_{11} and S_{21} parameters (b).
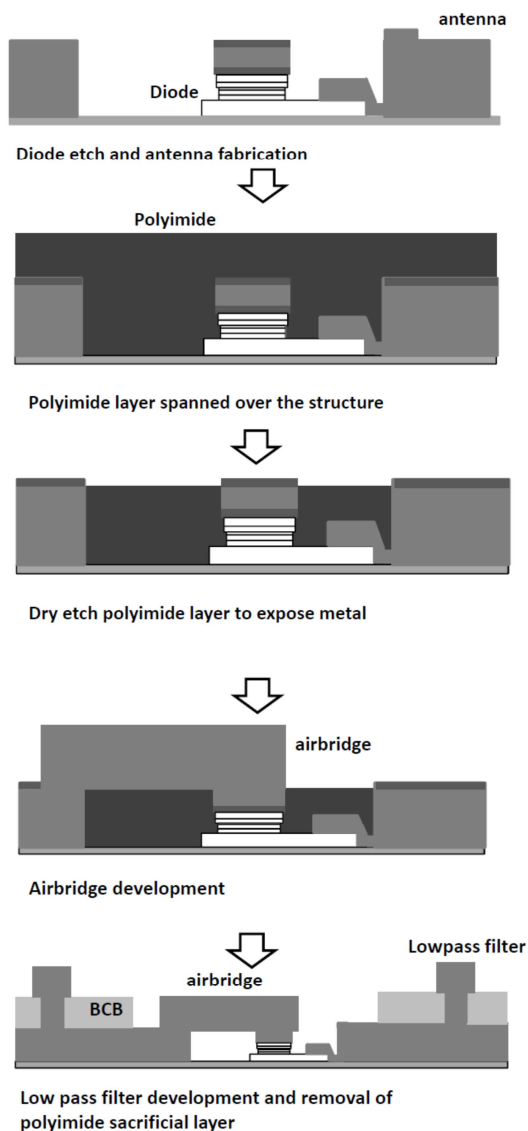
Fig. 10. Process flow diagram for the development of integrated HBD detector.

V. CONCLUSION

High performance THz detector elements for focal-plane imaging array applications have been designed, simulated and fabricated based on heterostructure backward tunneling diodes. For conjugate impedance matching to achieve maximum detector responsivity, FDAs with strong tuning capability have been simulated and designed. A detector responsivity of ~ 20000 V/W can be potentially achieved at 200 GHz using FDAs without additional impedance matching network, making the element design suitable for portable, LNA-less THz FPAs. Ray tracing technique has been applied to calculate the far field radiation patterns of the FDAs mounted on extended hemispherical silicon lens. An optimum extension length of ~2.5 mm has been obtained for maximum directivity and good Gaussian coupling efficiency at 200 GHz. To lessen parasitic effects of HBDs for THz operation, an airbridge finger has been introduced for integrating HBD

devices onto FDAs. For DC signal output, a PBG structure based on co-planar strip lines was designed with low dielectric BCB as the insulation layer. This single element detector design will soon be expanded into a full 2-D FPA for imaging applications.
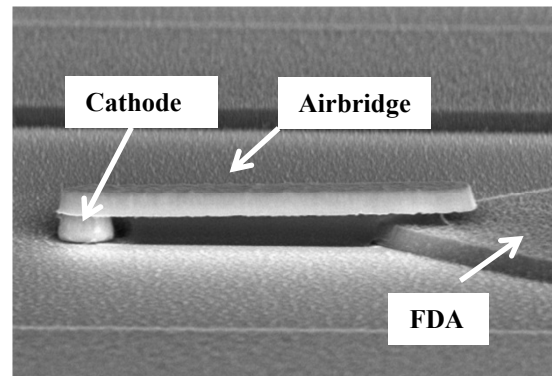
Fig. 11. The integrated HBD device at the center of a FDA with airbridge structure for reducing parasitic effects.

REFERENCES

[1] P.H. Siegel, "THz Technology" *IEEE Trans. Microwave Theory Tech.,* vol. 50, no. 3, pp. 910-928, March 2002.

[2] D.B. Rutledge and M.S. Muha, "Imaging antenna arrays," *IEEE Trans. Antennas and Propagat.*, vol. AP-30, no. 4, pp. 535–540, July 1982.

[3] P.H. Siegel, "THz Technology in Biology and Medicine*," IEEE Trans. Microwave Theory Tech.*, vol. 52, no. 10, pp. 2438-2448, Oct. 2004

[4] L. Liu, J. L. Hesler, H. Xu, A. W. Lichtenberger, and R. M. Weikle, "A broadband quasi-optical terahertz detector utilizing a zero bias Schottky diode," *IEEE Microw. Wireless Compon. Lett.*, vol. 20, no. 9, pp. 504–506, Sep. 2010.

[5] S. Cherednichenko, A.Hammar, S. Bevilacqua, V. Drakinskiy, J. Stake, and A. Kalabukhov, "A Room Temperature Bolometer for Terahertz Coherent and Incoherent Detection", *IEEE Trans..on Terahertz Science Tech.*, Vol. 1, No. 2, pp. 395-402, Nov 2011

[6] Z. Zhang,"Sb-Heterojunction backward diodes for direct detection and passive millimeter-wave imaging", *PhD thesis,* University of Notre Dame, 2011.

[7] N. Su, R. Rajavel, P. Deelman, J. N. Schulman, and P. Fay, "Sb-Heterostructure millimeter-wave detectors with reduced capacitance and noise equivalent power," *IEEE Electron Device Lett.*, vol. 29, no. 6, pp. 536–539, Jun. 2008.

[8] D. F. Filipovic, S. S. Gearhart, and G. M. Rebeiz, "Double-slot antennas on extended hemispherical and elliptical silicon dielectric lenses*," IEEE Trans. Microwave Theory Tech.*, vol. 41, no. 10, pp. 1738-1749 Oct. 1993.

[9] Z. Zhang, R. Rajavel, P. Deelman, and P. Fay, "Sub-Micron Area Heterojunction Backward Diode Millimeter-Wave Detectors With 0.18 pW/Hz^{1/2} Noise Equivalent Power", *IEEE Microw. Wireless Compon. Lett.*, vol. 21, no. 5, 2011.

[10] H. C. Ryu, S. I. Kim, M. H. Kwak, K. Y. Kang, and S. O. Park, "Afolded dipole antenna having extremely high input impedance for continuous-wave terahertz power enhancement," *33rd Int.Conf.*

Infrared, Millimeter, and Terahertz Waves (IRMMW), Pasadena, California, USA, Sep. 2008.

[11] C.A. Balanis, "Antenna Theory", Third Edition, 2005

[12] L. Liu, H. Xu, Y. Duan, A. W. Lichtenberger, J. L. Hesler, and R. M. Weikle, II,"A 200 GHz Schottky Diode Quasi-Optical Detector Based on Folded Dipole Antenna", *ISSTT 2009,*   Charlottesville, VA, USA.

Research of Micro-stripline STJ Detector for Terahertz Band

Kenta Takahashi[a,b], Seiichiro Ariyoshi[a], Takashi Noguchi[c] ,Masahiko Kurakado[d] ,Kensuke Koga [a,b], Noboru Furukawa[b], Chiko Otani[a,b]

[a] Terahertz Sensing and Imaging Team, RIKEN Advanced Science Institute, Sendai 980-0845, Japan
[b] Department of Physics, Graduate School of Science, Tohoku University, Sendai 980-8578, Japan
[c] National Astronomical Observatory of Japan (NAOJ), Mitaka, Tokyo 181-8588, Japan
[d] Techno X Co.,Ltd., Higashiyodogawa-ku, Osaka 533-0033, Japan

Abstract—**We have proposed and demonstrated a new broadband and high efficiency THz wave detector using a superconducting tunnel junction (STJ). The detector consists of an impedance transformer and a long (micro-stripline) STJs, which are both located on a wing of a log-periodic antenna in the mirror-symmetrical arrangement. The detector utilizes the excess tunneling current caused by the Cooper pair breaking due to the radiation whose photon energy is greater than the energy gap of the used superconductor (around 0.7 THz for niobium). If the length of STJ is long enough compared with the mean free path of the emergent quasiparticles (~10 μm for niobium), the energy of THz waves is absorbed and we detect it.**

We have fabricated the device and performed the experiments for confirming the principle of this detector. We have succeeded the detection for the first time and the detector has sensitivity from 0.35 THz by the CPB process and some peaks by the PAT process.

Index Terms—**THz wave, Detector, STJ, Transmission-line**

I. INTRODUCTION

Terahertz (THz) waves are electromagnetic waves with frequencies between high-frequency edge of the microwave band and the long-wavelength edge of far-infrared light. Although THz waves has been remained largely undeveloped due to the difficulty of generation and detection at these frequencies, a study of THz band has been significantly advanced in late years and THz waves are attracting a lot of attention in the field of not only basic research but also industrial applications [1].

For example, it is the shortest wavelength band having high permeability for various materials (particularly soft materials). By making use of the high permeability and moderate space resolving power, it is expected as a new non destructive inspection technology with minimizing the risk of radiation exposure. Furthermore, the THz wave may be used for powerful probe for early space exploration, since it is expected
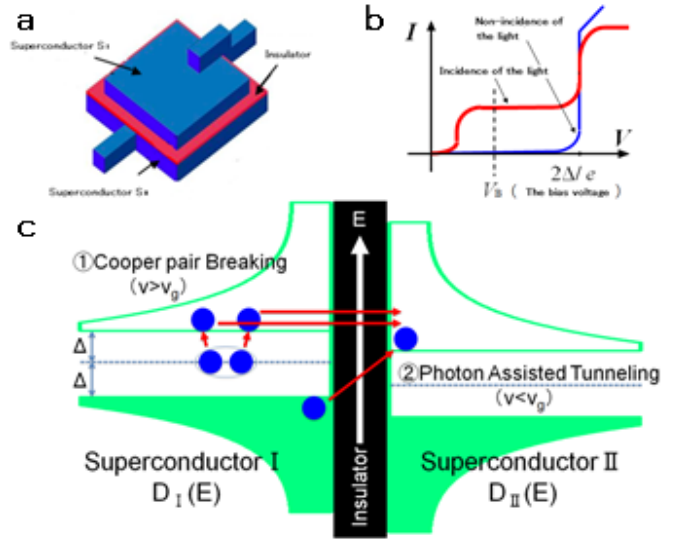

Figure1. Superconducting Tunnel Junction
a:Materials shown in blue are superconductors. Material in red is an insulator. b:Blue and red lines are I-V curves without and with radiation, respectively. c:Blue particles are represent electrons.

basically to have enough sensitivity to detect radiation at THz frequency, which is red-shifted light coming from the distant space. Our detector is a super high sensitive detector and we expect that it is used in the fields of basic research needing ultimate sensitivity.

II. SUPERCONDUCTING TUNNEL JUNCTION

THz detector using superconductor is more sensitive than any other room temperature detectors. The noise equivalent power (NEP) of a superconducting tunnel junction (STJ) to express minimum detection performance is

$$\text{NEP} = \frac{N}{\eta GS} = \frac{2\Delta}{\eta G}\sqrt{\frac{I_0}{2e}}, \qquad (1)$$

where N is the current noise, η is the coupling efficiency, G

corresponds to the gain related to the back-tunneling effect, S is the current responsivity, Δ is gap energy of superconductor, and I_0 is leakage current. The STJ is three levels of structure of Superconductor-Insulator-Superconductor (SIS) (Fig.1a) and it shows strong non-linear current-voltage characteristics. We detect the light by using the characteristic current-voltage. There are two detection processes in the STJ detector. One way is the Cooper-pair Braking (CPB) and the other is the Photon Assisted Tunneling (PAT) process. They are separate by the gap frequency of the superconductor (Fig.1c). Gap frequency is found from the next expression.

$$\mathrm{h}\nu_g = 2\Delta(0) = 3.528 k_B T_C. \qquad (2)$$

Where h, ν_g, and k_B are Planck's constant, signal frequency, and Boltzmann's constant, respectively, and $\Delta(0)$ and T_C are the gap energy at zero temperature and transition temperature, respectively.

If superconductor is niobium, the gap frequency is approximately 0.7 THz. When the STJ is irradiated by THz radiation with a frequency greater than 0.7 THz, Cooper-pairs are broken by the incident radiation into quasiparticles which can tunnel across the barrier and a measurable increase of current can be observed if the bias voltage is applied to the STJ. Thus, we can detect the radiation by observing increase of quasiparticle tunneling current. The other process is that electrons below Fermi level are excited with the help of bias voltage and energy of the radiation less than the gap energy. It is our main purpose to make a broadband detector based on the CBP process.

III. Micro-Stripline STJ Detector

Since a long-length STJ can be considered as a micro-strip transmission line (Fig.2) [2], the energy of the electromagnetic wave coupled to the STJ is absorbed during propagation in the STJ transmission line. We can calculate a decay constant α for the electromagnetic wave in the STJ transmission line by the following equation,

$$A = \exp(-\alpha L_j) \approx exp\left\{-(\tfrac{R_s}{Z_j} + \tfrac{Z_j}{R_n})/2\right\}, \quad (3)$$

where A is amplitude of THz wave in the STJ, L_j is length of the STJ, Z_j is a characteristic impedance of the STJ transmission line, R_s is the surface resistance of niobium, R_n is normal resistance of STJ. Since the longer length of the STJ, the higher absorption of energy, we have made STJs with four kinds of lengths to determine the optimum length. On the other hand, since the coupling efficiency of the radiation between the antenna and STJ depends on the width of STJ keeping the width of the impedance transformer constant, we have made STJs with three kinds of widths to find an optimum one.
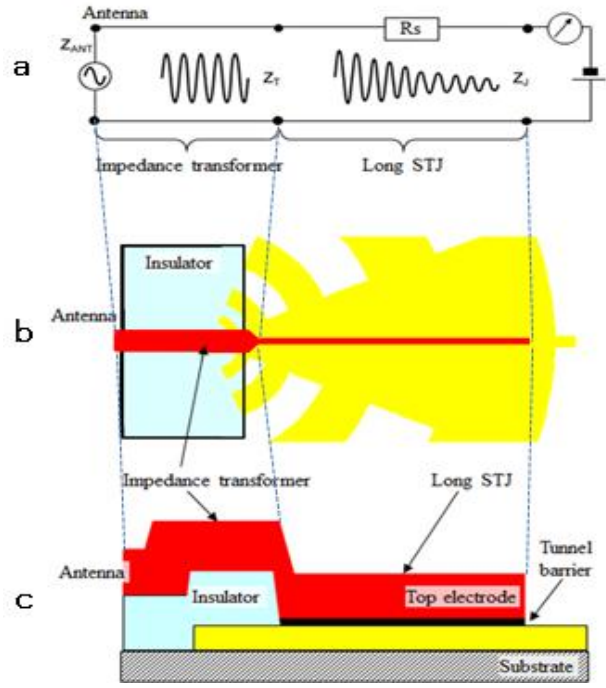

Figure2. Structures of micro-stripline STJ [3]
a:Circuit diagram, b:Top view, c:cross section

IV. Fabrication And Measurement

We fabricated these STJs in the RIKEN west clean room. Substrate is sapphire (Fig.3). STJ structure is five level of Nb/Al/AlO$_x$/Al/Nb=200/10/1/10/200nm. Oxidation is done at the condition of pressure-time product of 10 [Torr·hour]. At first, dc I-V curve is measured at 1.5 K and it is found that leakage current I_0 at 1mV is 25nA and that 2Δ is 2.2meV. If we suppose η and G to be 1, then NEP in the dark is expected to be 1×10^{-16}[W/√Hz]. This NEP is low enough to be used for some applications such as the observation of cosmic radiation from the ground. In the next step, we measured optical properties of the STJ detector at 0.3K by a Fourier transform infrared spectrometer (FT-IR). We successfully detected THz wave above the gap frequency and found that STJ showed different optical properties which are strongly dependent on the bias voltage applied to the STJ (Fig.4).
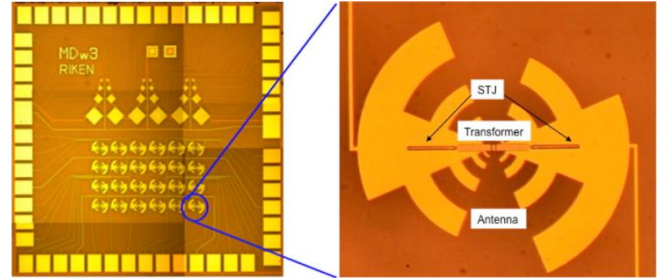

Figure3. Picture of a micro-stripline STJ
Left picture shows a picture of a chip with a dimension of 5×5 mm^2. 12 kinds of STJ devices with different combinations of length and width are located on the chip. Right picture is a magnified image of a STJ device
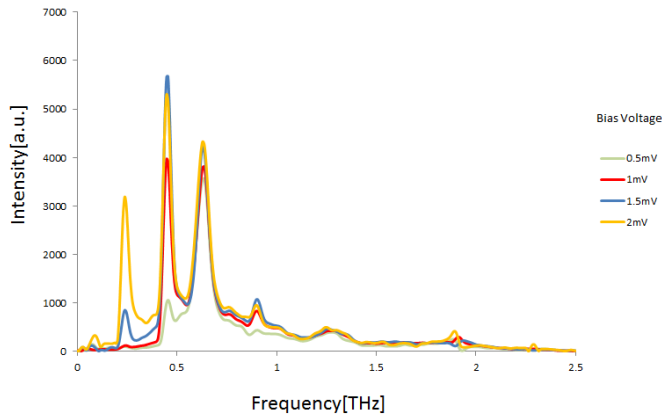
Figure4. Optical measurements (FT-IR)
Peaks located between 0.25 and 0.6THz may be attributed to the absorption by the PAT process, while those between 0.6 and 2.4THz may be attributed to the absorption by the CPB process.

V. CONCLUSION

We successfully detected radiation with frequency at 0.6THz, which is thought to be lowered from gap frequency of niobium by an effect of aluminum, or higher by CPB process. We found several sensitivity peaks below the gap frequency of 0.6 THz in the FTS response. Those peaks are attributed to the absorption of radiation by the PAT process, because the frequencies and height of the peaks decrease and increase, respectively, asincreasing the bias voltage. It is shown that our detector has sensitivity from 0.6THz to 2.4THz by the CPB process and from 0.25THz to 0.6 THz bythe PAT process. In the next step we are going to move on the detailed analysis on some peaks observed in the FTS response, and at the same time, to make an actual THz detector based on the present technology.

REFERENCES

[1] Lee Y-S, "Principles of Terahertz Science and Technology" New York 2009 (New York: Springer)
[2] T Noguchi and T Suzuki, "The 10th Workshop on Submillimeter-Wave Receiver Technology in Eastern Asia" 2009 http://mwlab.pmo.ac.cn/easternasia2009/proceeding.html
[3] S Ariyoshi *et al*, "Terahertz detector with transmission-line type superconducting tunnel junction" 2012 Supercond. Sci. Technol. 25 075011

Cryogenic Multi-Channel Readout System for Submillimeter/Terahertz Photon Detectors

Y. Hibi[1*], H. Matsuo[1], T. Ookawa[1], S. Sekiguchi[1], D. Torii[1], D. Watanabe[1], H. Ikeda[2], and M. Fujiwara[3]

1 National Astronomical Observatory of Japan (NAOJ), 2-21-1, Osawa, Mitaka, Tokyo, Japan 181-8588
2 Institute of Space and Astronautical Science (ISAS), 3-1-1, Yoshinodai, Sagamihara, Kanagawa, Japan, 229-8510
3 National Institute of Information and Communications Technology (NiCT), 4-2-1, Nukui-Kitamachi, Koganei, Tokyo, Japan, 184-8795
`* Contact: yasunori.hibi@nao.ac.jp, phone +81-432-3932, fax +81-432-3864`

Abstract——**We have been investigating the submillimeter/terahertz camera with the large format SIS (Superconductor - Insulator - Superconductor) photon detector array. The SIS photon detectors are one of the most promising candidates for the submillimeter/terahertz camera, because the SIS detectors have higher response speed to input photon and higher dynamic range to input energy than other type of detectors. These detectors must be cooled below 1 K and have relatively high impedance, the cryogenic readout system matching these properties is necessary to realize the submillimeter/terahertz camera. For this readout system, we have developed several kind of ICs (Integrated Circuits) constructed with n-channel GaAs-JFETs.**

We confirmed that the n-channel GaAs-JFETs have good cryogenic performances even when those power dissipation are low (<1 µW). We designed several kinds of ICs constructed with those GaAs-JFETs and demonstrated their cryogenic performance. We also designed and manufactured the 32-channel multi-chip-module with these ICs. Size of this is 40 mm x 30 mm x 2 mm. This module is able to make 32-channel parallel input current signals into 2 serial voltage signals. We have demonstrated those functions of the modules at the reset frequency of charge integration amplifier from 1 kHz to 1 Hz. As input current signal, this frequency range is corresponding to from 1 nA to 1 pA. The power dissipations of the modules are around 350 µW. We also have investigated those output voltage noise performances and confirmed that the noise value is appropriate. In parallel, we have investigated to connect the SIS photon detectors with the readout circuits.

In this presentation, we show the cryogenic performances of the module and the results of combination test the SIS detectors and the readout circuits. We also show applicable possibilities of this cryogenic readout system.

LiteBIRD Optics, Focal Plane Layout and Sensitivity

T. Matsumura[1*], M. Hazumi[1], K. Hattori[1], H. Ishino[2], N. Katayama[1], A. T. Lee[3], and A. Suzuki[3]

1 High Energy Accelerator Research Organization*, Institute of Particle and Nuclear Studies, Tsukuba, Ibaraki, 305-0301, Japan
2 University of Okayama, Department of Physics, Okayama 700-8530 Japan
3 University of California, Berkeley, Department of Physics, Berkeley, CA 94720 USA
* Contact: tomotake.matsumura@kek.jp, phone +81-29-864-5200 EXT. 4984

Abstract⸻We present the optics and focal plane layout for LiteBIRD, a space-borne project to measure the polarization of Cosmic Microwave Background (CMB) radiation. LiteBIRD is designed to probe the existence of the inflation, the rapid expansion of the Universe at ~10^{-38} seconds after the Big Bang. The design concept of LiteBIRD is to search the inflation signal at the large angular scale by a degree scale beam size, i.e. compact millimeter wave telescope, and therefore the small telescope size is favored to a mass limited satellite platform. On the other hand the required sensitivity of 2 µKarcmin forces us to have a cryogenically cooled telescope and kilo-pixel array focal plane in space. It is essential to understand the trade-off among the design parameters and maximize the sensitivity of the experiment within the limited focal plane size.

In this presentation we assume that LiteBIRD uses multi-color antenna-coupled transition edge sensor pixel to utilize the limited focal plane area. While the prime frequency to observe the CMB polarization is around 100 GHz, the experiment needs to cover the frequency range of 50-250 GHz in order to subtract the dust and synchrotron foreground emissions. We discuss how the sensitivity depends on the pixel size and the telescope temperature in each observing frequency. From this study we show that we achieve the required sensitivity of 2 µKarcmin as the integrated sensitivity over the frequency range of the observations.

Development of Superconducting Cooper-pair-breaking Detectors for LiteBIRD

K. Hattori[1], M. Hazumi[1], H. Ishino*[2], A. Kibayashi[2], S. Mima[2], T. Noguchi[3], N. Sato[1], T. Tomaru[1], M. Yoshida[1], and H. Watanabe[4]

1 High Energy Accelerator Research Organization, Tsukuba, Ibaraki, 305-0801, Japan
2 Okayama University, Okayama, 700-8530, Japan
3 National Astronomical Observatory of Japan, Mitaka, Tokyo, 181-8588, Japan
4 SOKENDAI, Tsukuba, Ibaraki, 305-0801, Japan
`* Contact: ishino@fphy.hep.okayama-u.ac.jp, phone +81-864-251-7818`

Abstract——We present our recent development of superconducting detectors for the satellite LiteBIRD (Lite Satellite for the studies of B-mode polarization and Inflation from cosmic background Radiation Detection). LiteBIRD is aimed to make precise measurements of the B-mode polarization of cosmic microwave background and requires about 2000 detectors capable of detecting a frequency range from 50 to 250 GHz with ultra low noise. Superconducting detectors are the candidate for LiteBIRD. We have fabricated and tested two types of detectors, i.e. superconducting tunnel junction (STJ) and microwave kinetic inductance detector (MKID).

We have designed an antenna-coupled microstrip STJ detector. The antenna is a log-periodic antenna that has a wide bandwidth. The millimeter radiation received by the antenna is transmitted to the microstrip STJ where the millimeter power create quasi-particles by breaking Cooper pairs or by using photon assisted tunneling. The quasi-particles are detected as an electric current. A test of 90 GHz light irradiation has demonstrated that our STJ detector detects the millimeter waves with photon assisted tunneling. An optimization of the fabrication procedure is being made for reducing a leak current.

We have also fabricated antenna-coupled MKIDs. For LiteBIRD, we propose to use a transmission-type MKID consisting of half wavelength resonators: it enables us to have a readout system that can track the resonant frequency change based on the phase measurements and hence provides us a larger dynamic range. A dipole antenna is attached at the middle point of the half wavelength resonators where the responsivity becomes maximal. The transmission type MKID made of Nb shows the quality factor of about 10^5 at a temperature of 0.3K. An Al MKID having the same design has successfully received 96 GHz radiation. We also have developed a new MKID readout system. The system generates multi-tones of microwaves, sends them to the MKID, and monitors the phase change of each tone. Based on the change of the phase, the system changes the microwave frequency and responds to the movement of the resonance. We present a demonstration of the performance of the system using the transmission type MKID irradiated by millimeter waves.

Development of Microwave Kinetic Inductance Detector and its Readout System for LiteBIRD

Y. Kibe[1,*], K. Hattori[2], M. Hazumi[2], H. Ishino[1], A. Kibayashi[1], S. Mima[1,**], N. Sato[2], T. Tomaru[2],
Y. Yamada[1], M. Yoshida[2], T. Yuasa[1], and H. Watanabe[3]

1 Okayama University, Okayama, 700-8530, Japan
2 High Energy Accelerator Research Organization, Tsukuba, Ibaraki, 305-0801, Japan
3 SOKENDAI, Tsukuba, Ibaraki, 305-0801, Japan

Abstract—We have developed a microwave kinetic inductance detector (MKID) and its readout system for the satellite LiteBIRD (Light satellite for the studies of B-mode polarization and Inflation from cosmic background Radiation Detection). Primordial gravitational waves generated by inflation have produced an odd-parity pattern B-mode in the cosmic microwave background (CMB) polarization. LiteBIRD aims at detecting this B-mode polarization precisely. It requires about 2000 detectors capable of detecting a frequency range from 50 to 250 GHz with ultra low noise. Superconductive detectors are suitable for this requirement. We have fabricated and tested an MKID and its readout system.

We have designed an antenna-coupled MKID. Quasi-particles are created by incident radiation and are detected as a change of the surface impedance of a superconductor strip. This change of the surface impedance is translated to the change of the resonant frequency of a microwave signal transmitted through the resonator.

We also have developed a new readout system for an MKID. An MKID can detect signals with a wide dynamic range, and can be multiplexed in a single readout line. The commonly used readout system that monitors the amplitude and phase at a certain resonant frequency is not suitable for LiteBIRD that requires a large dynamic range. We have developed a new readout system capable of tracking the resonant frequency change based on the phase monitoring. We report the recent R&D status of developing a MKID and its readout system for LiteBIRD.

Index Terms—LiteBIRD, MKID, Readout, Tracking.

I. Introduction

PPRIMORDIAL gravitational waves (PGW) are relics of the inflation epoch observed in the cosmic microwave background (CMB) radiation.PGW gives us the characteristic polarization pattern, so-called "B-mode" polarization. The precise measurement of this specific polarization pattern corresponds to the detection of primordial gravitational waves, and also leads to the verification of various inflation models.

LiteBIRD(Light satellite for the studies of B-mode polarization and Inflation from cosmic background Radiation Detection) [1] is being designed to aim a detection of the B-mode polarization pattern imprinted on the CMB. The goal of LiteBIRD is precise measurement of the CMB polarization and verification of the inflation model. About 2,000 high sensitive detectors with wide frequency band (50 250 GHz) are

* author, conntact: kibe@fphy.hep.okayama-u.ac.jp
** Current address is: Terahertz-wave Research Group, RIKEN, 2-1 Hirosawa, Wako, Saitama, 351-0198, Japan

needed for this purpose. Due to the limited cooling power, a high multiplexing factor is required for building a large detector array, and the MKID [2] is one of the candidates as suitable detector.

MKID (Microwave Kinetic Inductance Detector) is a kind of the superconductive detectors. A typical MKID is made of a feed line and many resonators which have various resonant frequencies. A resonator has a capacitive coupling to the feed line and the feed line is fed by microwaves of different frequencies. The resonator absorbs appropriate microwaves. When a MKID is irradiated, quasiparticles created by incident radiation are sensed by measuring the change in the surface impedance of a strip superconductor. This effect can be monitored as the phase transition or shifting the resonant frequency of a microwave signal transmitted through the resonator.

One of the remarkable feature of MKID is high multiplexing power. Actually, MKID can be multiplexed in a single feed line, and this characteristic point is suitable for the large focal plane detector array in the satellite. The readout system uses the IQ mixing technique [3] or Fast Fourier Transform (FFT) [4], but they are not enough to take advantage of the multiplexing power. Our newly developing readout system tracks the movement of the resonant frequency for individual resonator by monitoring the phase transition, and hence, it enable us to have a large dynamic range. The new readout system is based on the change of the phase to measure the resonant frequencies. Thus, it is free from fluctuation of the amplitude.

II. Readout System

OUR newly developing readout system make use of IQ mixing technique except the tracking of the resonant frequencies. IQ mixing enables us to readout resonators with random spacing of resonant frequencies. This feature is superior to FFT, and the readout for random spacing frequencies is essential for continuous measurement.

Our readout system handles the microwave signal transmitted through the MKID with FPGA (Field Programable Gate Array). FPGA generates the In-phase ($\sum_n \cos \Delta\omega_n t$) and quadrature ($\sum_n \sin \Delta\omega_n t$) of the probe microwaves, and these microwaves are up-converted into $\sum_n \cos (\omega \quad \Delta\omega_n) t$ with mixers and hybrid couplers, where ω shows the local oscillator frequency and $\omega \quad \Delta\omega_n$ is the frequency of the
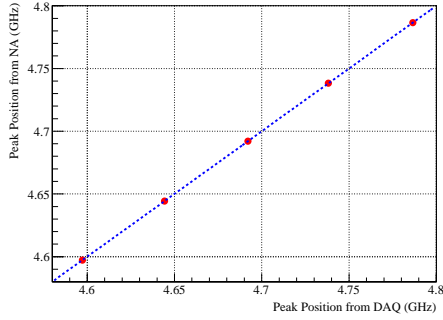
Fig. 1.   Resonant Frequencies measured with Our Readout System and Network Analyzer


Fig. 2.   Variation of the Amplitude of the Resonant Peak (Resonant Cavity). Vertical black dot line shows the time when the resonant frequency was changed.


Fig. 3.   Behavior of Tracking the Resonant Frequency (Resonant Cavity). Vertical black dot line shows the time when the resonant frequency was changed.

resonator. The transmitted microwaves through the resonators are down-converted and divided into I and Q elements. The I and Q microwaves are mixed with $\cos \Delta\omega_n t$ and $\sin \Delta\omega_n t$ respectively, and averaged over certain length of time. A sequence of these steps can be expressed as the following equation.

$$\frac{1}{T} \int_T dt \sum_m A_m \cos \Delta\omega_m t \cos \Delta\omega_n t = \begin{cases} \frac{A_n}{2} \cos \phi_n & (m = n) \\ 0 & (m \neq n) \end{cases}$$

$$\frac{1}{T} \int_T dt \sum_m B_m \sin \Delta\omega_m t \sin \Delta\omega_n t = \begin{cases} \frac{B_n}{2} \sin \phi_n & (m = n) \\ 0 & (m \neq n) \end{cases}$$

Here, A_m, B_m show the amplitude, ϕ_n is the phase of the resonator, and T is the duration time for averaging the products, which is sufficiently longer than $2\pi/\Delta\omega_n$.

The key feature of our readout system is to be able to track the resonant frequency of target resonator. When the resonator is irradiated with millimeter-wave, the surface impedance of superconductor changes and then the phase at initial resonant frequency shifts from ϕ to $\phi + \Delta\phi$. With this event, our system accommodates the frequency to keep the initial value of the phase. Therefore, the resonant frequency of the resonator moves from f to f + Δf.

III. R & D STATUS

WE built a digital readout system with XtreamDSP Development Kit-IV consisting of a Virtex-4 User FPGA, two ADC channels (14-bit, 105 MHz) and two DAC channels (14-bit, 105 MHz). DACs can create sinuous waves with approximately a quarter of the clock rate. Therefore, bandwidth of the readout system covers about 50 MHz (25 MHz). The actual bandwidth was evaluated by sweeping frequency, finding out several resonate peaks, and comparing them with those of network analyzer. The resonate frequencies measured with our system is in well agreement with the results of network analyzer (Fig.1).

We made a slight modification to our system from previous version [5]. Specifically, we made it possible to control resonant frequencies to be monitored by address. This modification enables us to simplify VHDL code and facilitate the expansion of multiplexed readout. To verify new algorithm, we performed two experiments. One is the experiment with the resonant
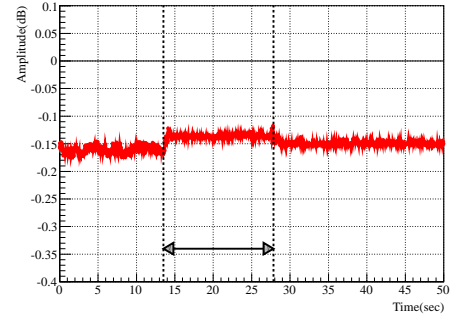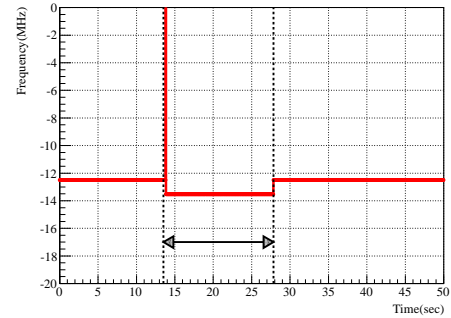
cavity whose resonant frequency can be changed by hand, and second is that with MKID. In the experiment with MKID, we observed the behavior of the resonant frequency by our system when a MKID was irradiated by visible wavelength. We got positive results from the experiment with resonant cavity (see Fig.2, 3). However, in the experiment with MKID, it is difficult to see the change of the resonant frequency due to the noise although the amplitude was slightly changed.

IV. CONCLUSION

MKIDS is one of a suitable detector for LiteBIRD, which aims to observe the characteristic pattern of cosmic microwave background polarization. The remarkable feature of this detector is high multiplexed power. We are developing the readout system for MKIDs to maximize its multiplexed power. The key feature of our readout system is tracking the resonant frequency by keeping initial value of the phase. It enables us to have a large dynamic range.

We made a slight modification to our system from previous one, and verified the new algorithm by resonant cavity or irradiating a MKID with optical wavelength. Our system could monitor the resonant frequencies, and follow the variation of the amplitude after irradiation. In addition to this, we confirmed new algorithm worked properly in the experiment with the resonant cavity. On the other hand, it is difficult to observe the change of the resonant frequency due to the noise

equivalent of signal when a MKID was irradiated by visible wavelength.

On the basis of these results, we try to test the readout system again after improving the signs-to-noise ratio. Aside from this, we plan to introduce more powerful User FPGA (Virtex-6) to deal with more complicated on-board signal processing.

REFERENCES

[1] M. Hazumi, *AIP Conf. Proc.*, 1040, 78, (1999)
[2] P. K. Day, H. G. LeDuc, B. A. Mazin, A. Vayonakis, and J. Zmuidzinas, *Nature*, 425, 817, (2008)
[3] L. J. Swenson, A. Cruciani, A. Benoit, M. Roesch, C. S. Yung, A. Bideaud, and A. Monfardini, *Appl. Phys. Lett.*, 96, 263511, (2010)
[4] S. J. C. Yates, A. M. Baryshev, J. J. A. Baselmans, B. Klein, and R. Gsten, *Appl. Phys. Lett.*, 95, 042504, (2009)
[5] K. Hattori, S. Ariyoshi, M. Hazumi, H. Ishino, A. Kibayashi, S. Mima, C. Otani, N. Satoh, T. Tomaru, M. Yoshida, and H. Watanabe, *Low Temperature Detectors LTD 14, Proceedings of the 14th International Workshop* (2011)

GroundBIRD - An experiment for CMB polarization measurements at a large angular scale from the ground

O. Tajima[1*], M. Hazumi[1], M. Kawai[1], M. Yoshida[1], and GroundBIRD group

*1 High Energy Accelerator Research Organization (KEK) *, 1-1 Oho, Tsukuba, Ibaraki, 305-0801, Japan*
* Contact: osamu.tajima@kek.jp, phone +81-29-864-5341

Abstract——**The B-mode polarization of the cosmic microwave background (CMB) at large angular scales is a smoking-gun signature of the inflationary universe. Especially, detecting an ionization bump at l<=10, where l is the multipole of the B-mode power spectrum, should be a clear evidence for the primordial gravitational wave induced by inflation. GroundBIRD is designed to detect such a large angular-scale B-mode power from the ground.**

We are going to use a superconducting detector array with a small telescope which is also in the cryogenic system. The basic design can be applied to a future satellite experiment. GroundBIRD employs a special turn table for continuously rotating the telescope instead of the system for the ordinary azimuth scan. This allows us to perform high-speed scans (20 rpm) without any deceleration. As a result, the sky coverage is extended without suffering from the detector 1/f noise. Our target l range is $6 <= l <= 300$.

We plan to start commissioning the system in Japan in early 2014. The instruments will then by moved to the Atacama desert in Chile for science observations. We will present the status of the system development.

Development of a MKID camera with high-quality Al films for millimeter-wave astronomy

M. Naruse[1,2*], Y. Sekimoto[1], A. Miyachi[1], Y. Uzawa[1], T. Nitta[1,3], K. Karatsu[1], M. Sekine[1,2], and T. Noguchi[1]

1 National Astronomical Observatory of Japan*, Mitaka, Tokyo, 181-8588, Japan
2 The University of Tokyo, Bunkyo, Tokyo, 113-033, Japan
3 University of Tsukuba*, Tsukuba, Ibaraki, 305-8577, Japan
* Contact: masato.naruse@nao.ac.jp, phone +81-422-34-3870

Abstract— **We have been developing millimeter and sub-millimeter wave cameras with microwave kinetic inductance detectors (MKID) and silicon lens arrays. MKID consists of a coplanar waveguide to be easily coupled to a double slot antenna. MKID is patterned on a high-quality aluminum film which has been developed by a molecular beam epitaxy method (MBE). The millimeter-wave camera has sensitivity at the frequency from 200 to 240 GHz, whose bandwidth is restricted by the impedance properties of the double slot antenna. The antenna properties have been simulated with 3D EM simulator (CST). The radius of the silicon lens is 2.05 mm, and the geometry of the lens is determined so that beam patterns from the lens become symmetrical and main lobe levels become -10 dB at around 20 degrees. The lens array is shaped with a direct machining technique.**

To investigate the effect of the quality of superconducting films on MKID, the properties of MKID are compared between an MBE-Al film and an aluminum film deposited with electron beam evaporation (EB) with thickness of 150 nm. Although the residual resistivity ration of the MBE film is twice higher than that of the EB film, the quasiparticle lifetime, noise level, and responsivity of the both MKID are comparable. In consequence, the electrical NEP of the both films are indistinguishable. The quasiparticle lifetime is 450 μs at 0.1 K and shorter than the lifetime reported in Baselmans et al., therefore the performance of the both MKID could be limited by stray light. A measurement set-up is under reconstruction to reduce unexpected radiation which enters the detectors.

Noise equivalent power (NEP) and optical efficiencies of the MKID camera with the high-quality aluminum films have been evaluated with a 0.1 K refrigerator. In a dark circumstance, the electrical NEP of the MKID is around 6*10-18 W/Hz. Under 8 K blackbody radiation, the optical NEP and the optical efficiency of the camera including the lens are evaluated to be 7 *10-15 W/Hz and around 15 %, respectively, at the sample-bath temperature of 0.1 K.

Stray Light Shielding in Transmission Lines for Integrated Filterbanks

D.J. Thoen[1*], A. Endo[1], R.M.J. Janssen[1], J.J.A. Baselmans[2], Y.J.Y. Lankwarden[2], and T.M. Klapwijk[1]

1 Kavli Institute of NanoScience, Faculty of Applied Sciences, Delft University of Technology,
Lorentzweg 1, 2628 CJ Delft, The Netherlands
2 SRON, Sorbonnelaan 2, 3584 CA Utrecht, The Netherlands
* Contact: d.j.thoen@tudelft.nl, phone +31 15 2787163

Abstract——**The Delft SRON High-z Mapper (DESHIMA) is a submillimeter-wave spectrometer that uses an integrated filterbank (IFB) to achieve a resolving power of 10^3. This spectral resolution reduces the optical loading on the Microwave Kinetic Inductance Detectors (MKIDs) used to read each channel, which makes stray light coupling a performance limiting factor for DESHIMA's MKIDs. From previous measurements it is understood there are two relevant sources of stray light. The first is radiation from the optical chain that directly couples to the MKID instead of through the planar antenna and IFB. This can be mitigated by applying a light-tight optical design. The second is radiation reflected by the planar antenna. In the current IFB design based on coplanar waveguides (CPW) a significant part of this radiation will travel through the silicon in a substrate mode, which enables it to couple directly into the individual resonators. To minimize the effect of this second stray light source, we study a new chip design that replaces CPW by microstrip lines (MSLs). The low loss at microwave and submillimeter wavelength required for DESHIMA would be difficult to achieve with MSLs using conventional sputtered dielectrics. However, it was recently shown that by using a single-crystal silicon dielectric layer, MSL microwave resonators can approach a quality factor, Q, of 10^6, which is sufficient for DESHIMA. The process towards realization of an MKID based on a single-crystal dielectric consists of three steps: 1) develop a fabrication process for blind MSL resonators designs, which also include structures on the ground plane, 2) attach an antenna to the resonator to couple radiation into it, and 3) construct an MSL IFB that operates in the submillimeter. We will report on the progress in design and fabrication of this new MSL design for MKIDs.**

Development of antenna-coupled KIDs for large cameras

L. Ferrari[1*], A. M. Baryshev[1,2], J. J. A. Baselmans[3] , A. Endo[4], R. Güsten[5], S. Heyminck[5], S. Hochgürtel[5], B. Klein[5], Y.J.Y. Lankwarden[3], and S.J.C. Yates[1]

1 SRON Space Research of Netherlands Groningen, 9747 AD, The Netherlands*
2 Kapteyn Astronomical Institute, Groningen, 9747 AD, The Netherlands
3 SRON Space Research of Netherlands, Utrecht, 3584 CA, The Netherlands
4 Delft University of Technology, Delft, 2628 CJ, The Netherlands
5 Max Planck Institute for Radio Astronomy, Bonn, 53121, Germany
* Contact: lorenza@sron.nl, phone +31-50-3638321

Abstract— **Large-scale arrays of Microwave Kinetic Inductance Detectors (MKIDs) are attractive detector candidates for imaging instruments in sub millimeter-wave telescopes such as APEX. We are developing antenna-coupled KIDs. Our detector design employs a quarter-wave coplanar waveguide (CPW) resonator. One end of the resonator is coupled via a capacitor to the readout transmission line and the other end is shorted to ground. A twin-slot antenna transfers incident on the shorted end. The radiation is concentrated and focused onto antenna by means of a lens glued to the back-side of the KID sample. We present the last developments of the detector design and recent results of the detector performance**

Quasiparticle Diffusion and Detection Efficiency of Hybrid Kinetic Inductance Detectors

R.M.J. Janssen[1*], A. Endo[1], J.J.A. Baselmans[2], S.J.C. Yates[3], P.J. de Visser[1,2],
Y.J.Y. Lankwarden[2], and T.M. Klapwijk[1]

1 Kavli Institute of NanoScience, Faculty of Applied Sciences, Delft University of Technology, Lorentzweg 1, 2628 CJ Delft, The Netherlands
2 SRON, Sorbonnelaan 2, 3584 CA Utrecht, The Netherlands
3 SRON, Landleven 12, 9747 AD Groningen, The Netherlands
`* Contact:  R.M.J.Janssen@tudelft.nl, phone +31 15-2786077`

Abstract⎯Superconducting coplanar-waveguide (CPW) resonators made of NbTiN and Al have shown photon noise limited detection for optical loading equivalent to the typical sky signal at modern sub-mm telescopes. While the detection efficiency of these hybrid MKIDs is equal to the value expected based on antenna simulation and the known efficiency of quasiparticle generation, this is not the case for conventional CPW MKIDs made from pure Al. Given that the hybrid MKIDs use the large gap superconductor NbTiN to trap photo-excited quasiparticles in the sensitive area of the resonator made from Al, it is postulated that the origin of the lower detection efficiency of pure Al resonators is due to quasiparticle diffusion. During the conference we will report on the measurements comparing NbTiN/Al and pure Al resonators and the effect of quasiparticle diffusion on the detection efficiency of these MKIDs.

Cold Payload Module of SPICA

H. Matsuhara[1*], T. Nakagawa[1], Y. Kawakatsu[1], H. Murakami[1], M. Kawada[1], H. Sugita[2], K. Shinozaki[2], T. Yamawaki[2], S. Mitani[2], Y. Sato[2], SPICA preproject team

1 Institute of Space and Astronautical Science, Japan Aerospace Exploration Agency, Sagamihara, 252-5210 Japan
2 Aerospace Research and Development Directorate, Japan Aerospace Exploration Agency, Tsukuba, 305-8505 Japan
* Contact: maruma@ir.isas.jaxa.jp, phone +81-50-3362 4560

Abstract— **The Space Infrared Telescope for Cosmology and Astrophysics (SPICA) is a large (3.2m physical diameter), cooled (below 6K) telescope mission which covers mid- and far-IR astronomy with unprecedented sensitivity. Here we present an overview of cold payload module (PLM) and its recent design updates. The PLM consists of the Scientific Instrument Assembly (SIA) cooled without cryogen, the mechanical coolers, and the radiation shields to block the heat from the sun and the bus module. The SIA consists of the telescope assembly and the instrument optical bench equipped with focal plane instruments(FPIs). The SIA is refrigerated to below 6 K by two sets of 4K-class Joule-Thomson (JT) cooler, and a long-wavelength detectors of FPIs are refrigerated to 1.7 K by two sets of 1K-class JT coolers.**

SPICA is transferred into the sun-earth L2 point, where radiation cooling is very efficient. However, since the cold telescope is mandatory for the success of the mission, extremely high reliability of the cooling system is required. We will present the redundancy policy, the thermal margin philosophy, and basic experimental activities to establish the high reliability.

The current FPI suite will be consolidated based on the international science and engineering review. The baseline FPIs are: a mid-IR coronagraph (SCI), a mid-IR camera and spectrometer (MCS), an imaging Fourier-transform spectrometer operating in the far-IR (SAFARI), and a focal plane camera (FPC) used for fine guidance. The FPC has two channels for redundancy, one of which is proposed for scientific use at the 0.7–5 micron waveband. The US community is proposing a far-IR/submillimetre spectrometer, which is more sensitive than SAFARI but has no imaging capability, and hence can be complementary with SAFARI.

Performance Requirements for the SAFARI Detector System

B.D. Jackson[1]*, W. Jellema[1], B.M. Swinyard[2], P.A.J. de Korte[3], D.A. Naylor[4], D. Griffin[5], P. Mauskopf[6], P.R. Roelfsema[1], T. Nakagawa[7]

1 SRON Netherlands Institute for Space Research*, Landleven 12, 9747 AD, Groningen, The Netherlands
2 University College London, Department of Physics and Astronomy, Gower Street, London WC1E 6BT, UK
3 SRON Netherlands Institute for Space Research, Sorbonnelaan 2, 3584 CA, Utrecht, The Netherlands
4 University of Lethbridge, Institute for Space Imaging Science, Department of Physics and Astronomy, Lethbridge, Alberta T1K 3M4, Canada
5 Science and Technology Facilities Council, Rutherford Appleton Laboratory, Chilton, Didcot, Oxfordshire OX11 0QX, UK
6 University of Cardiff, Department of Physics and Astronomy, University of Cardiff, 5, The Parade, P.O. Box 913, Cardiff, CF24 3YB, UK
7 Institute of Space and Astronautical Science (ISAS) Japan Aerospace Exploration Agency (JAXA) 3-1-1 Yoshinodai, Sagamihara, Kanagawa 229-8510, Japan

`* Contact:  B.D.Jackson@sron.nl, phone +31-50-363 8935`

Abstract—— **The SAFARI instrument is a far-infrared imaging Fourier transform spectrometer (FTS) for JAXA's SPICA mission. Taking advantage of the low thermal emission of SPICA's 5 K telescope, SAFARI will provide background-limited, Nyquist-sampled spectroscopic imaging of a 2'x2' instantaneous field-of-view over 34-210 μm. The extremely low-noise detector performance that SAFARI requires is provided by 3 large-format Transition Edge Sensor (TES) detector arrays operating at 50 mK base temperature, with operation of 4000 pixels within SPICA's tight thermal constraints enabled by a unique frequency division multiplexed SQUID readout system in which 160 pixels are simultaneously read-out using a single SQUID amplifier chain.**

This paper presents the flow-down of SAFARI science requirements to functional and performance requirements for the instrument's TES detector system, taking into account the instrument's dual-model operation as both an imaging Fourier transform spectrometer and a photometer. Beyond the driving requirement of sensitivity, important issues include detector frequency response, baseline and gain stability, non-linearity, the timing between the detector and FTS metrology readouts, and the effect of glitches in the detector readout due to cosmic ray hits on the detector arrays.

The SAFARI Focal Plane Array Design Concept

H. van Weers[1], P.P. Kooijman[1], J. van der Kuur[1], B.D. Jackson[2]*

1 SRON Netherlands Institute for Space Research, Sorbonnelaan 2, 3584 CA, Utrecht, The Netherlands
2 SRON Netherlands Institute for Space Research*, Landleven 12, 9747 AD, Groningen, The Netherlands
* Contact: B.D.Jackson@sron.nl, phone +31-50-363 8935

Abstract— **The SAFARI instrument is a far-infrared imaging Fourier transform spectrometer (FTS) for JAXA's SPICA mission. Taking advantage of the low thermal emission of SPICA's 5 K telescope, SAFARI will provide background-limited, Nyquist-sampled spectroscopic imaging of a 2'x2' instantaneous field-of-view over 34-210 µm. The extremely low-noise detector performance that SAFARI requires is provided by 3 large-format Transition Edge Sensor (TES) detector arrays operating at 50 mK base temperature, with operation of 4000 pixels within SPICA's tight thermal constraints enabled by a unique frequency division multiplexed SQUID readout system in which 160 pixels are simultaneously read-out using a single SQUID amplifier chain.**

The extreme sensitivity of the SAFARI detectors and their first-stage SQUID amplifiers cause this system to be sensitive to environmental disturbances such as quasi-static magnetic fields, thermal radiation from the instrument's 1.7 and 4.5 K temperature stages, and high-frequency radiated E-fields from (for example) the satellite transponders. Also, the 50 mK detectors and first-stage readout electronics must be thermally isolated from the 1.7 K environment of the instrument's cold optical box. Finally, SAFARI's large TES chips must be mounted and aligned with respect to their optical coupling elements (horn and backshort arrays) while also surviving repeated deep cryogenic thermal cycles and launch vibration loads.

These shielding, thermal isolation, and detector chip mounting functions are combined in the instrument's Focal Plane Arrays (FPAs), with one FPA for each of the instrument's 3 detector arrays. This paper describes the preliminary design concept for the SAFARI FPAs and their critical enabling technologies, including an isostatic and modular Kevlar suspension system; an isostatic and thermal expansion compensating mounting technique for the TES wafers; and the shielding of the detectors from the spacecraft environment.

Low Noise TES Array for the Short Wavelength Band of the SAFARI Instrument on SPICA

P. Khosropanah, R. Hijmering, M. Ridder, M. A. Lindeman, L. Gottardi, M. Bruijn, J. van der Kuur,
J.R. Gao, B.D. Jackson, H. Hoevers, D. Morozov, and P. D. Mauskopf

Abstract—**SPICA is an infra-red (IR) telescope with a cryogenically cooled mirror (~5K) with three instruments on board, one of which is SAFARI that is an imaging Fourier Transform Spectrometer (FTS) with three bands covering the wavelength of 34-210 μm. We develop transition edge sensors (TES) array for short wavelength band (34-60 μm) of SAFARI. These are based on superconducting Ti/Au bilayer as TES bolometers with a Tc of about 105 mK and thin Ta film as IR absorbers on suspended silicon nitride (SiN) membranes. These membranes are supported by long and narrow SiN legs that act as weak thermal links between the TES and the bath. Previously an electrical noise equivalent power (NEP) of 4×10^{-19} W/√Hz was achieved for a single pixel of such detectors. As an intermediate step toward a full-size SAFARI array (43×43), we fabricated several 8×9 detector arrays. Here we describe the design and the outcome of the dark and optical tests of several of these devices. We achieved high yield (>93%) and high uniformity in terms of critical temperature (<5%) and normal resistance (7%) across the arrays. The measured dark NEPs are as low as 5×10^{-19} W/√Hz with a response time of about 1.4 ms at preferred operating bias point.**

Index Terms—**Transition-edge sensor, TES, far infra-red spectrometer, submm spectrometer, SiN membrane.**

I. INTRODUCTION

$\mathbf{S}$PICA is a Japanese-led mission to fly a 3.25 m diameter IR telescope with a cryogenically cooled mirror (~5K) [1]. Cooling the optics reduces the background radiation caused by the ambient temperature of the FIR space telescopes that limits the sensitivity. The loading is then dominated by astrophysical background sources. The SAFARI instrument is an imaging Fourier Transform Spectrometer (FTS) on SPICA with three bands covering the wavelength ranges: 34-60 μm (S-band), 60-110 μm (M-band), and 110-210 μm (L-band) [2]. Transition edge sensor (TES) is the chosen detector technology for the SAFARI instrument that is currently being developed in collaboration with several European institutes. Here the focus is on the detector arrays for the S-band. These

are based on superconducting Ti/Au bilayer as the sensitive element on a suspended silicon nitride (SiN) membrane. In order to take full advantage of the cooled optics, the detectors need to have a background-limited sensitivity that translates to a dark NEP of 6.5×10^{-19} W/√Hz as a requirement and 2.8×10^{-19} W/√Hz as a goal. This is about 2 orders of magnitude higher sensitivity than what is required for detectors on a ground based telescope and imposes a great challenge on the detector technology. Among other tight specifications are the array size (43×43), pixel size of 840×840 μm² (likely), a speed of 40-100 Hz (i.e. response time of 0.8-4 ms) and a saturation power of about 5 fW.

Previously we presented dark measurements of single pixel TESes with different designs and geometries [3,4], where an electrical (dark) NEP as low as 4×10^{-19} W/√Hz was achieved [5]. Also the optical tests on some of these devices have been reported, where a coupling efficiency of about 40% was measured for a detector with a large absorber (200×200 μm²) that was sitting in the center of a hemispherical cavity with a conical horn in the front [6-8].

As an intermediate step toward full-size SAFARI detector arrays, we have fabricated arrays of 8×9 of these devices on two different membrane thicknesses. This paper reports on the electrical tests of some of these devices. First the details of TES detectors are explained. Then we move on to the description of the arrays followed by the results of the dark tests.

II. TES DEVICES AND ARRAYS

The devices under test are based on Ti/Au (16/65 nm) bilayer, deposited on 500 or 250 nm thick SiN membrane. The TES size is 50×50 μm² and the critical temperature (T_C) is around 105 mK. In order to test these devices optically, we have an absorber close to each TES, which is a 75×75 μm² Ta with thickness of 8 nm. The sheet resistance of Ta is about 400 Ω that matches well with the free-space impedance (377 Ω). The absorber and the TES are sitting on a 140×80 μm² suspended membrane that is supported by four SiN legs. The legs are 2 μm (nominal) wide and 1000 or 1500 μm long in order to thermally isolate the TES from the reservoir and insure high sensitivity. As it is shown in Fig. 1 parallel legs geometry was used in order to have long supporting legs while keeping the pixel size according to the SAFARI specifications (840 μm).

Fig. 1. (Left) A single pixel TES as a part of the 8×9 array. The size of the SiN island is 140×80 µm² that is 250 or 500 nm thick. The TES is a 16/50 nm thick Ti/Au bilayer (50×50 µm²) and the absorber is an 8 nm thick Ta (75×75 µm²). (Right) A picture of a part of the array with parallel legs geometry. The length of the legs is 1000 or 1500 µm while the pitch size is 840 µm.

III. DARK TESTS

Two arrays with 8×9 detectors were selected for the dark tests and overall 14 devices were measured during 4 runs. The designs of TES detectors in the two chips are identical apart from the fact that one was fabricated on a 500 nm thick SiN membrane and the other on a 250 nm one. Fig. 2 shows a picture of one of these arrays.
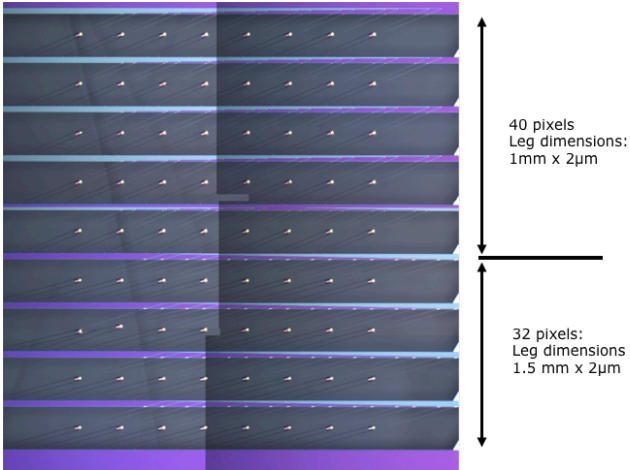
Fig. 2. Picture of an 8×9 TES array. It consists of two TES designs, 40 devices on the top with 1 mm long legs and 32 devises in the bottom with 1.5 mm log legs. The nominal width of the legs for all devices is 2 µm.

For the dark tests the detector chip is mounted in a light tight box that is shown in Fig. 3. It is designed to minimize the background loading due to possible stray light. The electrical wiring of the light tight box to an array chip goes through a meander path that is filled with Stycast mixed with SiC grains, which should act as a perfect blackbody absorber. After a TES chip is mounted, the box is closed, indium sealed and vacuum pumped.

An additional module is attached to this box that accommodates a heater, a coil and a thermometer. The heater and thermometer are used to regulate the temperature on the chip mount locally. The coil is for applying a magnetic field in the vertical direction to cancel a remnant magnetic field if present. Maximum four devices were wired in every run and read out by separate SQUIDs.
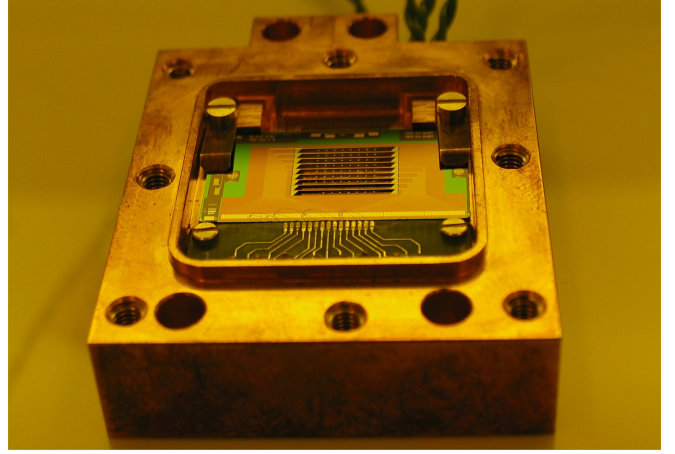
Fig. 3. The light tight box with the array chip mounted inside.

The dark tests start with measuring a series of current-voltage (IV) curves at different bath temperature. The bias power in the superconducting transition determines the saturation power for each of these bath temperatures, which in turn gives the thermal conductance (G) between the TES and the bath. Besides, the responsivity at very low frequency for each bias point is calculated, using the bias voltage across the device and the bias circuit. Next, the noise current spectra are measured at different bias points. Dividing the noise current by the corresponding responsivity gives the dark noise equivalent power (NEP), which is the same at all the bias points in the transition. The details of this characterization method can be found elsewhere [3,4].

The NEP at low frequency is dominated by the phonon noise that can be estimated as [9]:

$$NEP = \sqrt{4\gamma k_B T_C^2 G} \qquad (1)$$

where k_B is the Boltzmann's constant and γ is a number between 0.5 and 1 that depends on the heat transport mechanism and the critical temperature of the TES (T_C) and the bath temperature (T_{bath}). In our case γ is about 0.5 with T_C and T_{bath} being 105 mK and 30 mK, respectively.

Table 1 and 2 summarize the measurement results on the chip with 500 nm thick SiN membrane. In run #1 four devices with 1 mm long legs were tested. The critical temperature (T_C) and the normal resistance (R_n) of these devices were very uniform. The T_C lies between 103 to 106 mK, which is pleasingly close to what we designed (100 mK). Despite having exactly the same geometry, large variations in saturation power and the thermal conductance (G) were measured. We repeated this run by measuring the same devices again but swapped the channels to investigate if the SQUIDs had influenced the results and measured very similar values. In run #2 four devices with 1.5 mm long legs were measured. As one can see, similar uniformity in T_C and R_n were observed and similar non-uniformity appeared in the saturation powers and the G's. The T_C and R_n variations for these devices are about 3% and 6%, respectively. The saturation power difference for 1 mm leg devices can be as large as a factor of 1.5 and for 1.5 mm leg devices the difference can increase to 1.9. The lowest measured dark NEP is 7×10⁻¹⁹ W/√Hz for a 1.5 mm long leg TES.

TABLE 1 Summary of the measurements for 500 nm thick SiN membrane array in run #1

TES Parameter	P33	P16	P32	P09
Leg length [μm]	1000	1000	1000	1000
Tc [mK]	106	103	106	105
Rn [mΩ]	167	164	158	160
Sat. power [fW]	22.4	28.9	35.6	33.4
G [pW/K]	0.57	0.73	0.87	0.83
Exp. NEP [aW/√Hz]	4.15	4.15	4.15	4.15
Meas. NEP [aW/√Hz]	0.85	0.9	1.05	1.05

TABLE 2 Summary of the measurements for 500 nm thick SiN membrane array in run #2

TES Parameter	P56	P45	P41	P70
Leg length [μm]	1500	1500	1500	1500
Tc [mK]	103	103	103	103
Rn [mΩ]	168	166	163	160
Sat. power [fW]	13.1	15.8	14.2	24.7
G [pW/K]	0.31	0.38	0.34	0.59
Exp. NEP [aW/√Hz]	0.3	0.33	0.32	0.42
Meas. NEP [aW/√Hz]	0.7	0.8	0.75	1

TABLE 3 Summary of the measurements for 250 nm thick SiN membrane array in run #3

TES Parameter	P16	P69	P09
Leg length [μm]	1000	1500	1000
Tc [mK]	103	106	105
Rn [mΩ]	169	158	160
Sat. power [fW]	21.3	3.5	10
G [pW/K]	0.55	0.07	0.25
Exp. NEP [aW/√Hz]	0.4	0.14	0.27
Meas. NEP [aW/√Hz]	0.75	0.5	0.6

TABLE 4 Summary of the measurements for 250 nm thick SiN membrane array in run #4

TES Parameter	P66	P64	P72
Leg length [μm]	1500	1500	1500
Tc [mK]	105	101	102
Rn [mΩ]	170	170	166
Sat. power [fW]	3.6	5.5	3.4
G [pW/K]	0.07	0.11	0.07
Exp. NEP [aW/√Hz]	0.15	0.18	0.14
Meas. NEP [aW/√Hz]	0.5	0.6	0.5

Table 3 and 4 summarize the measurement results on the chip with 250 nm thick SiN membrane. This time we were only able to measure three devices in each run. In run #3 the T_C and R_n were very uniform. However we observed a factor of two difference in saturation power between device P16 and P09 despite of having exactly the same geometry. Three out of four devices with 1.5 mm long legs were very uniform. The variations in terms of the T_C and R_n for these devices are about 5% and 7%, respectively. Although the device P64 has 1.6

times higher saturation power than other three (including P69 in run #4), in general the variation seems to be smaller. Dark NEPs as low as $5×10^{-19}$ W/√Hz were measured. This is particularly interesting because this is the first time such a low NEP is demonstrated in an array. The devices made on 250 nm SiN membrane have a lower NEP and a lower saturation power in comparison with those on 500 nm SiN membrane. This is expected because the thinner SiN gives a lower thermal conductance.

The speed of these devices was measured by applying a small pulse to the bias line and recording the response. The amplitude of the pulse was less than 5% of the bias. The time constants vary between 1-4.5 ms depending on the bias point. At the typical operating point that is R/R_n=0.3, the time constant is 1.4 ms. The time constants for the devices with relatively higher G, saturation power and noise (NEP=1 aW/√Hz) are shorter and vary between 0.4-0.7 ms in the transition.

IV. SUMMARY AND OUTLOOK

We have successfully fabricated various types of 8×9 S-band test arrays on 500 nm and 250 nm thick SiN membranes. The overall yield was almost 100 % for devices processed on 500 nm SiN an above 93% for devices processed on 250 nm SiN. The variation of the critical temperatures and normal resistances of devices across the arrays are less than 5% and 7% respectively. Large variations in saturation power and the thermal conductance (G) were measured. Despite having exact nominal device geometries this difference can be as large as factor of two with in an array. Optical microscopic inspection of the SiN legs revealed formation of spots on sections of the legs that can be partly the reason for the large variation in G. We also see deviations in the width of the SiN legs compared to the pattern on the photo mask (nominal value). The width of the legs for 8 pixels on the chip in Table 1 and 2 was measured between 3.3-3.6 μm, where the nominal value was 2 μm. This is mainly due to our current process that implies on-membrane lithography that suffers from reflection of the light from the Al layer under the membrane. The leg width variation alone cannot explain the large variation we see in our devices. We expect to solve this problem by acquiring Deep Reactive Ion Etching (DRIE) process that enables us to pattern the legs on bulk Si before etching away the substrate. The measured dark NEPs for devices fabricated on 250 nm SiN membrane are $5-6×10^{-19}$ W/√Hz and for devices on 500 nm SiN membrane about $7-10×10^{-19}$ W/√Hz. For long leg devices on a 500 nm membrane (Table 1 and 2) the measured NEP is about a factor of 2-2.5 higher than the expected NEP from the measured G using Eq. (1). For similar devices on a 250 nm membrane (Table 4), this factor increases to 3-3.5. This is somewhat surprising since less excess noise is expected from devices with lighter legs [5]. On the other hand we also see that the measured G's in Table 3 and 4 are about a factor of 4 smaller than for the devices in Table 1 and 2, while the membrane is only thinner by a factor of 2. Answering these questions requires further investigation. One possible explanation might be the accuracy of our G estimations. In presence of any external loading power, we would measure

lower saturation power and therefore underestimate the *G*. The matter is worse for more sensitive devices, where the saturation power is well below 10 fW.

We have made substantial progress towards a generic technology that is capable of delivering the required detectors for SAFARI. While most of the individual performance numbers are approaching or exceeding the requirements, there is still significant work required to optimize the designs. For the S-band pixels the fabrication process should be modified to use DRIE Si etching in order to achieve better uniformity in the array and to be able to scale up the current design to the full-size (43×43) array. In addition, to increase the sensitivity, the silicon nitride legs should be shorter, and therefore thinner and narrower.

REFERENCES

[1] B. Swinyard, T. Nakagawa, P. Merken, P. Royer, T. Souverijns, B. Vandenbussche, C. Waelkens, et al. "The space infrared telescope for cosmology and astrophysics: SPICA A joint mission between JAXA and ESA", Experimental Astronomy, 23(1), 193-219 (2008).

[2] B.D. Jackson, P.A.J. de Korte, J. van der Kuur, P.D. Mauskopf, J. Beyer, M.P. Bruijn, A. Cros, J.-R. Gao, D. Griffin, R. den Hartog, M. Kiviranta, G. de Lange, B.-J. van Leeuwen, C. Macculi, L. Ravera, N. Trappe, H. van Weers, and S. Withington, "The SPICA- SAFARI detector system: TES detector arrays with frequency-division multiplexed SQUID readout" IEEE Transactions on Terahertz Science and Technology, 2(99), 1–10 (2011).

[3] P. Khosropanah, B. Dirks, J. van der Kuur, M. Ridder, M. Bruijn, M. Popescu, H. Hoevers, J. R. Gao, D. Morozov, and P. Mauskopf, "Low thermal conductance transition edge sensor (TES) for SPICA", AIP Conf. Proc. 1185, 42 (2009), doi:10.1063/1.3292369

[4] P. Khosropanah, B.P.F. Dirks, M. Parra-Borderías, M. Ridder, R. Hijmering, J. van der Kuur, L. Gottardi, M. Bruijn, M. Popescu, J.-R. Gao, H. Hoevers, "Transition edge sensors (TES) using a low-G spider-web-like SiN Supporting structure", IEEE transitions on Applied Superconductivity, Vol. 21, No. 3, P. 236-240 (2011), doi:10.1109/TASC.2010.2089408

[5] P. Khosropanah, R.A. Hijmering, M. Ridder, M.A. Lindeman, L. Gottardi, M. Bruijn, J. van der Kuur, P.A.J. de Korte, J. R. Gao and H. Hoevers, "Distributed TES model for designing low noise bolometers approaching SAFARI instrument requirements", J. Low. Temp. Phys. 167:188–194, (2012), doi:10.1007/s10909-012-0550-6

[6] D. Morozov, P.D. Mauskopf, P. Ade, M. Bruijn, P.A.J. de Korte, H. Hoevers, M. Ridder, P. Khosropanah, B. Dirks, and J.-R. Gao, "Ultrasensitive TES bolometers for space based FIR astronomy", AIP Conf. Proc. 1185, 48 (2009), doi:10.1063/1.3292385

[7] D. Morozov, P.D. Mauskopf, P. Ade, M. Ridder, P. Khosropanah, M. Bruijn, J. van der Kuur, H. Hoevers, J.-R. Gao, D. Griffin, "Ultrasensitive TES bolometers for space-based FIR astronomy", IEEE Transactions on Applied Superconductivity, 21, p. 188-201, 2011.

[8] M.D. Audley, L. Ferrari, J.-R. Gao, P. Khosropanah, G. de Lange, P. Mauskopf, D. Morozov, and M. Ranjan, "Optical Measurements of TES Bolometers for SAFARI", in this proceedings (2012).

[9] J. Mather, "Bolometer noise: none-equilibrium theory", Appl. Opt. 21, 1125-1129 (1982).

Optical Measurements of TES Bolometers for SAFARI

Michael D. Audley, Axel Detrain, Lorenza Ferrari, Jian-Rong Gao, Darren Hayton, Gert de Lange,
Philip D. Mauskopf, Dmitry Morozov, Manisha Ranjan Neil A. Trappe, and Willem Jan Vreeling

Abstract— **We have measured the optical response of detectors for SAFARI, the far-infrared imaging spectrometer for the SPICA satellite. SAFARI's three bolometer arrays, coupled with a Fourier transform spectrometer, will provide images of a 2'×2' field of view with spectral information in three bands covering the wavelength range 34—210 μm. Each bolometer consists of a transition edge sensor (TES) with a transition temperature close to 100 mK and a resistive absorber on a thermally-isolated silicon nitride membrane. Each detector sits behind a concentrating horn and in front of a hemispherical backshort. SAFARI requires extremely sensitive detectors (NEP~2×10^{-19} W/√Hz) to take advantage of SPICA's cooled optics. To meet the challenge of testing such sensitive detectors we have constructed an ultra-low background test facility with a cryogen-free high-capacity dilution refrigerator, paying careful attention to stray-light exclusion. The SAFARI Detector System Test Facility provides a high degree of electrical, magnetic, and mechanical isolation for the detectors, allowing us to use a pulse-tube cooler to pre-cool the dilution refrigerator. We have verified the test facility's performance in terms of background power loading and carried out cross-calibrations with other test systems. The SAFARI Detector Test Facility is now being used for routine dark and optical measurements of ultra-sensitive TES bolometers. We report on optical measurements of prototype SAFARI detectors.**

Index Terms—**Bolometers, infrared detectors, superconducting devices, immunity testing, calibration**

I. INTRODUCTION

T HE Japanese Space Agency's satellite observatory SPICA will use a large (3.5-m diameter) primary mirror cooled to <6 K to enable high angular-resolution, sky-background limited observations of the cold dusty Universe in the mid- and far-infrared [1]. The mission promises to revolutionize our knowledge of the origin and evolution of galaxies, stars and planetary systems. The SAFARI [2] instrument is a far-infrared imaging Fourier transform spectrometer (FTS) for the SPICA satellite. SAFARI has three detector arrays with a total of ~6000 pixels for a Nyquist-sampled field of view of 2'×2' covering the wavelength ranges 34—60 (short wave), 60—110 (medium wave), and 110—210 μm (long wave). The detectors are Transition Edge Sensor (TES) bolometers [3]. The Ti/Au bilayer TES and a Ta absorber are suspended on thin (<1-μm) silicon nitride membrane (see Fig. 1). SAFARI will provide wide-field spectroscopic maps in the far infrared, giving us the ability to study the dynamics and chemistry of a wide range of objects. To take advantage of SPICA's low-background cold mirror, SAFARI's short-wave detectors require a dark noise equivalent power (NEP) less than 6.5×10^{-19} W/√Hz, with a goal NEP of ~2×10^{-19} W/√Hz. This is over two orders of magnitude more sensitive than TES bolometers previously developed for ground-based applications [4] and the SAFARI detectors have correspondingly low saturation powers (~5 fW).

Testing such sensitive detectors is challenging and requires careful attention to magnetic and RF shielding, stray-light exclusion, and vibration isolation. We have built a test facility which will be used to qualify and characterize the SAFARI focal plane units and readout before they are integrated into the instrument. In addition to the strict requirements on background and interference, we require that this facility be flexible and re-configurable so that we can use it for dark and optical tests of single pixels through to the full focal-plane arrays. Through a systematic program of incremental modifications we have improved the performance of the SAFARI Detector Test Facility to the point where it is capable of testing SAFARI's ultra-sensitive bolometer arrays. The test facility is now being used for routine measurements of prototype SAFARI detectors. We have measured the optical response of two prototype detectors designed for SAFARI's short-wave band (33—60 μm) array. These are of the type shown in Fig. 1, and have moderate sensitivity (NEP = 1—2 aW√Hz). While these detectors have been far surpassed in sensitivity by the latest detectors for SAFARI, they absorb radiation in the same way [5], and are thus representative for optical characterization.

Fig. 1. Photograph of a TES detector similar to the ones measured here.

II. DESCRIPTION OF THE TEST FACILITY

The SAFARI Detector Test Facility is based on a Leiden Cryogenics dilution refrigerator with a cooling power of ~200 µW at 100 mK [6]. We have found that we can reach a base temperature on the mixing chamber below 8 mK and have operated detectors in the dark with bath temperatures, T_{bath}, as low as 15 mK. This bath temperature is well below the value required for testing the SAFARI detectors and gives us plenty of headroom for experiments that place additional heat loads on the system, e.g. black-body illuminator. The refrigerator uses no expendable cryogens and is precooled by a Cryomech PT-415 pulse-tube cooler which is attached to the 50-K and 3-K stages of the cryostat. To mitigate the effects of vibrations, the pulse-tube cooler has two expansion tanks and its rotary valve motor is separated from the cryostat. The expansion tanks and valve motor are mounted on the cryostat's support tripod. One advantage of using a mechanical cooler is that it is closer to the flight configuration which also uses mechanical cooling than a wet cryostat would be. The main disadvantage is that we need to protect the detectors under test from mechanical and electrical interference from the cooler. For detector readout and thermometry there are eight woven looms of 12 twisted pairs. Two have Cu conductors for low electrical resistance (and hence low Johnson noise) and are used for the SQUID bias. The rest have CuNi conductors to minimize thermal conductance. The looms are enclosed in stainless steel tubes and heatsunk at various points. RF shielding is provided by two nested Faraday cages. The outer one is formed by the Dewar main shell and contains the room-temperature readout electronics as well as a multiplexer box, which allows us to connect the readout to different SQUIDs. The inner Faraday cage is the 3-K shield. Wires entering the 3-K shield are low-pass filtered at several hundred MHz. The system has been designed for flexibility: a reconfigurable patch board on the 8-mK stage redistributes the signals from the looms between the two experiment boxes currently installed. One of these experiment boxes is being used for dark testing and system optimization. The other is used for optical detector testing and provides the results presented here.

Each experiment box comprises a tin-plated copper can, with light-tight feedthrough for wiring and an absorbing labyrinth where it attaches to its base, all surrounded by a Cryoperm can (see Fig. 2). We have verified that this provides good magnetic shielding and is light-tight. We had originally intended to replace the tin-plated copper can with a niobium can, but we found that the copper can provided adequate magnetic shielding with the advantage over niobium of a high thermal conductivity.
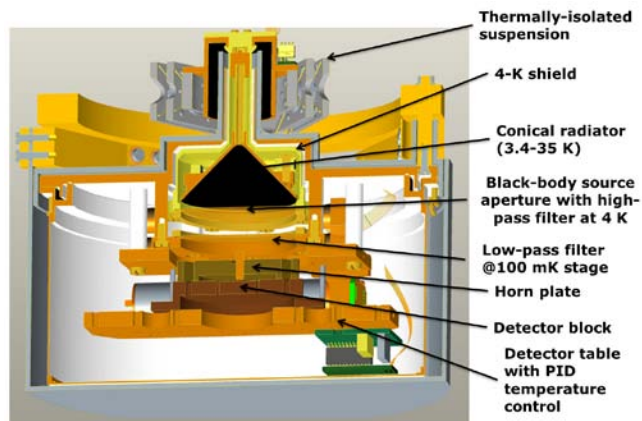

Fig. 2. Cutaway view of detector box showing the black-body illuminator and detector table inside the nested shields. The diameter of the outer, Cryoperm shield is 15 cm.

III. OPTIMIZATION OF THE TEST FACILITY

Our challenge was to build an ultra-low background test facility that still had the flexibility to accommodate the various experiments that will be needed until the SAFARI focal plane arrays have been fully characterized. Starting with a well-engineered system, we carried out a comprehensive program of optimization, making improvements to the system in small steps until we arrived at the point where were confident that the system was suitable for testing ultra-sensitive TES bolometers.

The optimization program comprised many small improvements that came under four general areas. First, we took some steps to mitigate the effect of vibrations and electrical interference from the pulse-tube cooler. We replaced the hose between the rotary valve and the cold head with a longer one that could accommodate the motion of the valve. We also replaced the square-wave driver for the rotary-valve motor with a linear drive. Second, we paid careful attention to eliminating ground loops. We isolated the gas-handling system electrically from the cryostat and instrument rack. Third, we ensured that the signal wiring inside the cryostat was immobilized as much as possible. Because this system is a test bed and needs to be flexible, it was not always possible to use rigid conductors everywhere. Any wiring associated with the input circuits of the SQUIDs was made from the stiffest wire available and shielded with superconducting Al tubing. Fourth, we made sure that the Faraday cages were closed as much as possible. We found that opening one of the boxes surrounding the room-temperature readout electronics increased the loading on the detectors by several fW. There is still room for improvement here.

To confirm the low-noise performance of the system, we mounted an ultra-sensitive TES fabricated at SRON in the test facility. This particular detector had previously been characterized in a different low-background test facility [7], [8]. We found that when the TES is in the superconducting state we see a few lines in the power spectrum, from radio-frequency interference and microphonic pickup, that disappear when the pulse-tube cooler is switched off. These are small compared with the current noise when the TES is biased on the transition and do not interfere with the measurement of the detector NEP. We were thus able to conclude that the SAFARI Detector Test Facility was ready for characterizing SAFARI's ultra-low NEP detectors.

IV. OPTICAL TEST SETUP

A. Physical Layout

We measured two detectors of the type shown in Figure 1. Optical measurements of these detectors had previously been carried out in a different test system [7]. These detectors do not have the extreme sensitivity of the latest SAFARI detectors [5], but the way in which radiation couples to the bolometer is the same. The detectors have square Ta absorbers 200 µm on a side. Each detector sits in front of a hemispherical backshort and behind a conical feed horn (see Fig. 3). The horn is 4.5 mm long and the diameters of its entrance and exit apertures are 450 and 46 µm, respectively. The horn is contained in a plate that can be positioned over any of the five detectors on the chip. In front of the horn is a high-pass/low-pass pair of filters. The optical measurement setup is as shown in Fig. 2. The detector block is mounted on a table with a thermometer and heater to allow PID control of the detector-table temperature. The optical source is defined by an aperture in the 3-K shield of the black-body illuminator. This aperture is located 17 mm in front of the horn. The temperature of the illuminator is also controlled by a PID control loop.

We measured the beam pattern of the horn using a 5.3-THz (57-µm) FIR laser and found an angular width of about 9.1° FWHM, in good agreement with the calculated far-field beam pattern at that frequency (see Fig. 5). This gives a beam size at the aperture of the illuminator of about 2 mm (radius) at a wavelength of 50 µm. We carried out the optical measurements of the detectors with two different aperture diameters: 5 mm and 12 mm. The 5-mm aperture has a size comparable to the expected beam size of the horn, which means that the throughput is reduced by the aperture and is sensitive to the alignment between the aperture and horn. With the 12-mm diameter aperture we illuminate the beam of the horn fully, and should be insensitive to small errors in alignment. As expected, we measured a higher throughput than with the 5-mm aperture.
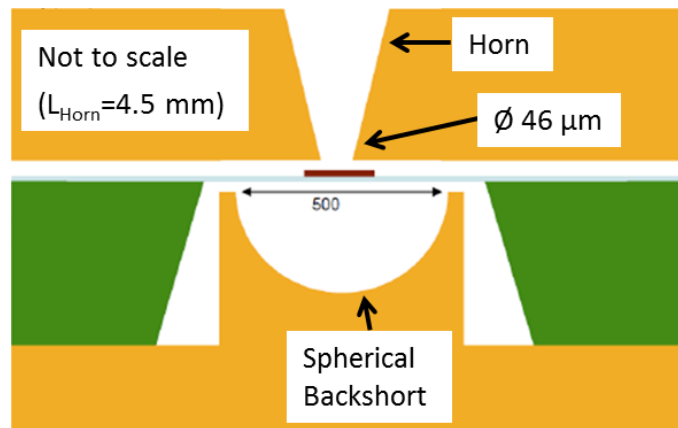

Fig. 3. Cross-section of feedhorn and spherical backshort showing position of detector (not to scale). The diameter of the spherical backshort is 500 µm.
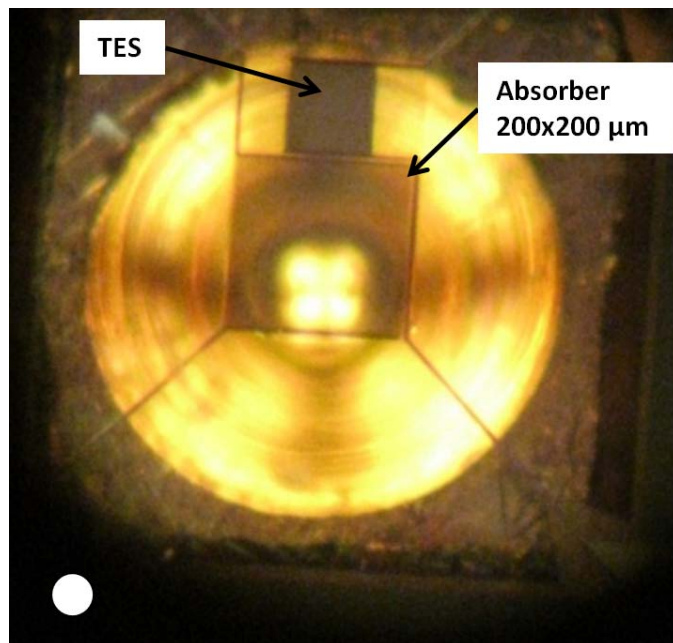

Fig. 4. Photograph of detector sitting above spherical backshort. The white circle in at the lower left represents the footprint of the 46-µm exit aperture of the horn. This has been displaced from its position over the center of the backshort for clarity.

B. System Throughput

In order to measure the absorption efficiency of the combination of detector, backshort, and horn, it is necessary to estimate the incident power from the illuminator accurately. The horn's 46-µm diameter exit aperture should block wavelengths longer than about 90 µm. This small exit aperture was chosen for these tests so that it would act as a mode filter. Given the band-pass of our filter stack (33—50 µm), and the low temperature of the black-body illuminator (< 32 K to saturate the detectors), we make the assumption of only a single mode propagating through the horn. In the case of a large source aperture, where the beam of the horn is fully illuminated, we expect the throughput of the system to be $A\Omega=\lambda^2$. The power incident on the detector is then (assuming a source emissivity of 1)

$$P_{\text{inc}}(T) = \int \frac{2hc^2}{\lambda^5} \frac{1}{e^{\frac{hc}{\lambda kT}}-1} \tau(\lambda)\lambda^2 d\lambda \qquad (1)$$

where $\tau(\lambda)$ is the measured transmission of the filter stack. The efficiency of the horn-cavity-detector combination is then

$$\eta = \frac{P_{\text{det}}(T)}{P_{\text{inc}}(T)} \qquad (2)$$

where $P_{\text{det}}(T)$ is the detected optical power at illuminator temperature T. If the source aperture is not large compared to the size of the horn's beam the throughput will be reduced by a factor of $1-\exp(-2(r_{\text{ap}}/w(\lambda))^2)$ where r_{ap} is the radius of the aperture and $w(\lambda)$ is the beam radius [9]. The throughput will be further reduced if there is also an offset between the centers of the horn and the aperture.
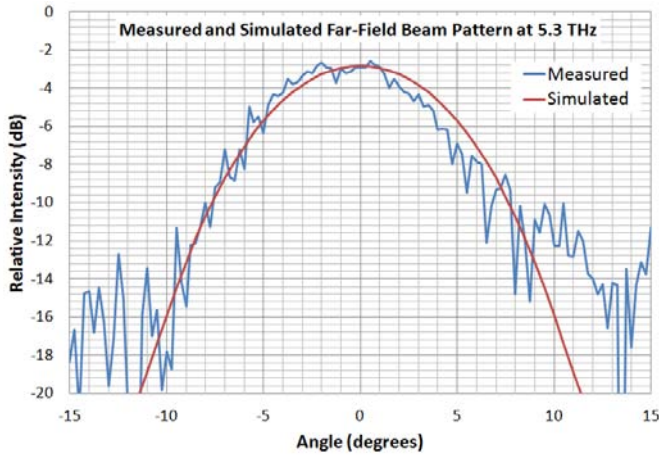
Fig. 5. Measured and simulated beam pattern of horn. The beam has a FWHM of 9.1°.

V. MEASUREMENTS

A. Readout and calibration

Each TES detector was voltage-biased using a shunt resistor of 1—2 mΩ and the TES current was read out using a Superconducting Quantum Interference Device (SQUID). We used single-stage SQUIDs from PTB [10] with Magnicon readout electronics [11]. The SQUIDs and shunt resistors were mounted on the detector table at the same temperature-stage as the detectors. The shunt resistors were formed from short gold wire bonds. The resistance of the shunt resistor was verified from its Johnson noise power spectrum.

B. IV Curves

We measured current-voltage characteristic curves (IV curves) of the detectors at different bath temperatures and used the known component values of the bias circuit to produce calibrated IV curves which show the current through the TES against the voltage across it (Fig. 6). We then calculated the Joule power, P_{Joule}, at each TES voltage, V_{TES}, to convert the IV

curves into power curves: $P_{\text{Joule}}=V_{\text{TES}}I_{\text{TES}}$, where I_{TES} is the TES current. Each power curve comprises a parabolic region corresponding to the normal state, a flatter region commonly called the power plateau [12] where the TES is on the transition, and a point at the origin corresponding to the superconducting state. Examples are shown in Fig. 7 where the Joule power is plotted against the absolute value of the TES voltage. The data corresponding to positive and negative voltages coincide almost exactly, verifying that the calibration is good.
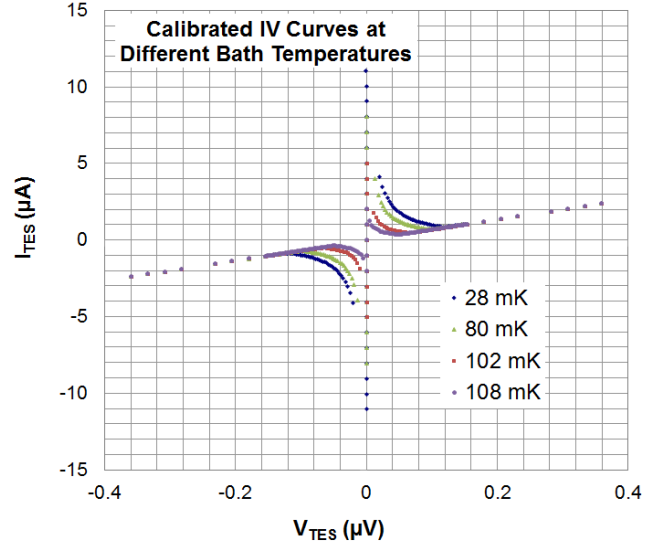

Fig. 6. Calibrated IV curves at different detector-table temperatures for detector 17E.
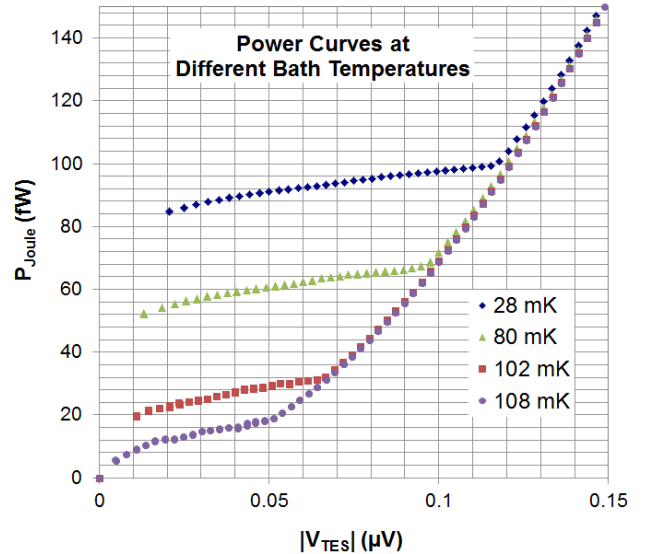

Fig. 7. Power Curves at different detector-table temperatures for detector 17E, calculated from the IV curves in Fig. 6. The Joule power dissipated in the TES is plotted against the absolute value of the voltage across the TES. Note how the data points corresponding to bias voltages of opposite signs are almost coincident.

We used the power plateaus to estimate the Joule power at each bath temperature, T_{bath}, and fitted the results to a function of the form $P = K(T_c^n-T_{\text{bath}}^n)$ to obtain the transition temperature T_c and thermal conductance $G=nKT_c^{n-1}$ of each detector. This is the model plotted in Fig. 8. The best-fit thermal parameters are shown in Table I, which also shows the measured dark NEP.

TABLE I

MEASURED THERMAL PROPERTIES FOR THE TWO DETECTORS

Parameter	Detector:	17D	17E
Power-flow Exponent: n		3.07	3.15
Power-flow Factor: K (pW/K^n)		89	92
Transition Temperature: T_c (mK)		115	114
Thermal Conductance: G (pW/K)		3.1	2.7
NEP_{dark} (aW/√Hz)		1.7	1.7

For optical measurements we regulated the detector-table temperature at a fixed value (usually 70 mK) and recorded IV curves at different illuminator temperatures. The power dissipated in the illuminator loads the refrigerator and raises its base temperature. The detector-table temperature of 70 mK was chosen so that it could be maintained even when the illuminator was hot enough to saturate the detectors with radiation. From the power plateaus we could calculate the Joule power dissipated in the detector at each illuminator temperature. As can be seen in Fig. 8, optical loading has the effect of depressing the power plateaus. The absorbed optical power at each temperature is then the difference between the power plateau when the illuminator is off and the power plateau at that temperature. In these estimations we consider the illuminator to be off when its temperature is below 3.5 K.
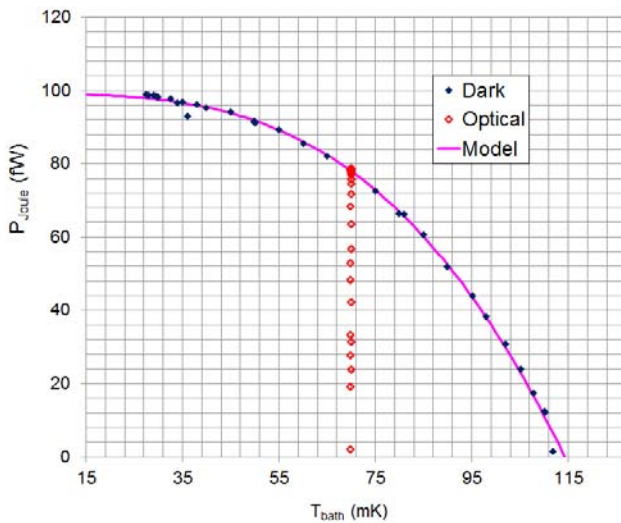
Fig. 8. Measured power plateaus at different bath temperatures in the dark and at fixed bath temperature (70 mK) with optical illumination.
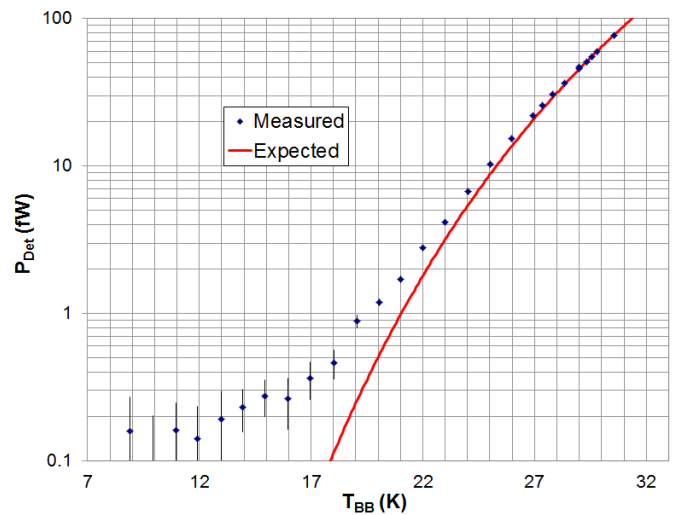
Fig. 9. Absorbed optical power, P_{Det}, calculated from the data in Fig. 8, compared with expected power at different illuminator temperatures, T_{BB}.

We find good agreement between measured and expected power at high illuminator temperatures, but at low illuminator temperatures there is an apparent excess in the detected power (see Fig. 9). This is almost certainly due to a long-wavelength light leak through the filters on the 8-mK shield. This is discussed in Section VII.B.

C. Fixed TES Bias

IV curves give us well-calibrated, precise measurements of the absorbed power, but they can be time-consuming. We need the illuminator temperature to be steady for the duration of the IV-curve acquisition. In principle, this should present no problem, but at high illuminator temperatures the illuminator time constant becomes very long, which means that we must wait a long time for the temperature to settle down. An alternative approach is to allow the illuminator temperature to vary slowly and record data quickly at a few discrete TES bias values. This gives much finer resolution on illuminator temperature and a more precise measurement of the dependence of absorbed power on illuminator temperature. In particular, this allows us to investigate in detail the temperature-dependence of the excess power detected at low illuminator temperatures. The raw data from such a measurement are shown in Fig. 10. Each point on this plot corresponds to a single point used to build up an IV curve, which gives us a considerable time saving over taking a full IV curve at each illuminator temperature. As expected, the dark pixel has a much smaller response to illumination. The illuminated pixel can be seen to saturate at different temperatures, depending on how high on the transition it is biased. We can convert these data into absorbed power in the same way as for IV curves. The absorbed power for a single TES bias voltage is shown in Fig. 11. Although the dark pixel sees less power than the optical pixel, both pixels have an almost identical linear dependence of the absorbed power on illuminator temperature for low illuminator temperatures (the ratio is shown in Fig. 12). We discuss possible causes for this in Section VII.B.
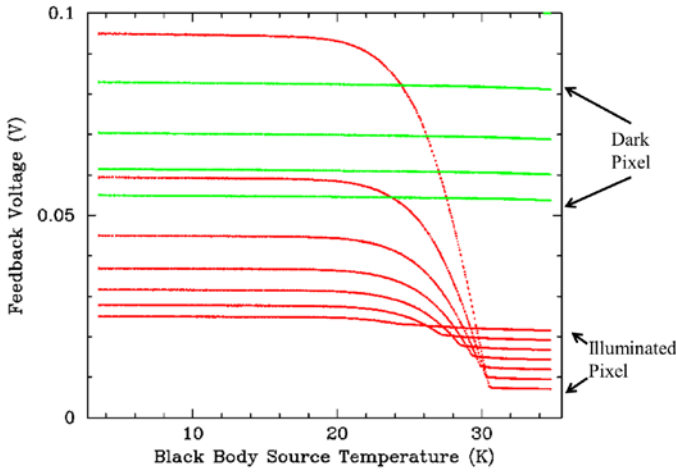
Fig. 10. Response of flux-locked-loop feedback voltage to optical illumination for dark and illuminated pixels at different bias. Some of the dark-pixel traces have been omitted for clarity.

Fig. 13 shows the response of the optical pixel with the power detected in the dark pixel subtracted. The noise floor estimated from the bandwidth of the measurement and the NEP of the detector is also shown. With the dark pixel subtracted, power becomes undetectable around the noise-floor level, showing that the excess at low illuminator temperatures has been effectively subtracted. However, this correction subtracts too much power at high illuminator temperatures where the 2.6% optical crosstalk is significant. Aside from this over-subtraction, the estimated detected optical powers in Fig. 13 are lower than predicted for high illuminator temperatures. This is due to the fact that when the TES is biased at a fixed voltage, the resistance of the TES (and hence the actual bias point on the transition) will depend on the external power loading. Since the power plateaus in Fig. 7 are not flat the Joule power dissipated in the TES depends on the TES resistance. This effect is not seen when estimating the absorbed power from IV curves if care is taken to ensure that the power plateau is always measured at the same point on the transition (i.e. the same TES resistance).
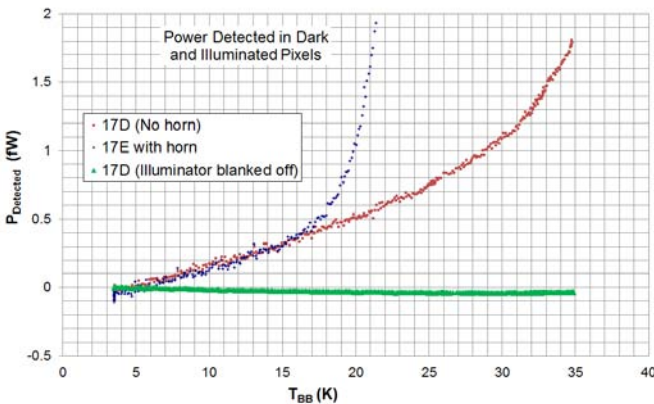
Fig. 11. Absorbed power vs illuminator temperature in the dark pixel (squares), illuminated pixel (diamonds), and with the illuminator closed off with a blanking plate (triangles).
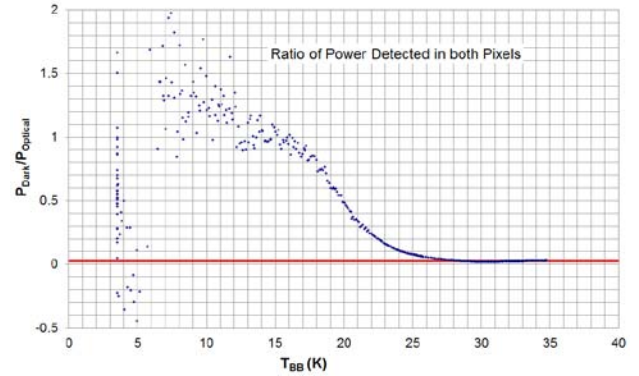

Fig. 12. Ratio of power detected in the dark pixel to that detected in the illuminated pixel. The solid line denotes the ratio above 30 K, which is about 0.026. We interpret this as the level of optical cross-talk between the pixels.
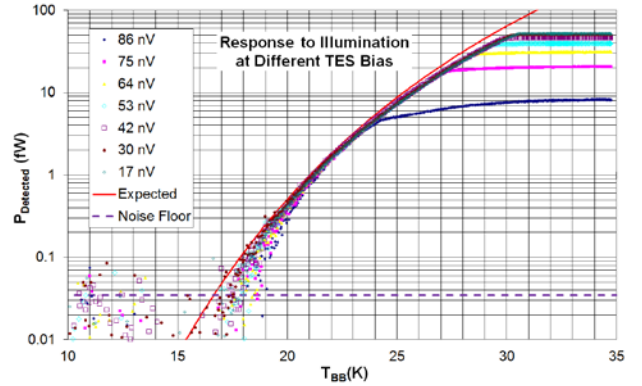

Fig. 13. Response to optical illumination at different fixed TES bias voltages. The detected power, P_{Detected} at each illuminator temperature, T_{BB}, has had the corresponding power detected in the dark pixel subtracted.

D. Photon Noise

We also measured the noise in the detectors at different illuminator temperatures (Fig. 14) and find that the measured photon noise agrees with the value expected from the predicted incident power

$$NEP_{\text{photon}}{}^2(T) = 2 \int \frac{hc}{\lambda} \frac{2hc^2}{\lambda^5} \frac{1}{e^{\frac{hc}{\lambda kT}} - 1} \tau(\lambda)\lambda^2 d\lambda \qquad (3)$$

and the optical efficiency found from the IV curves and fixed-bias measurements (Fig. 15).
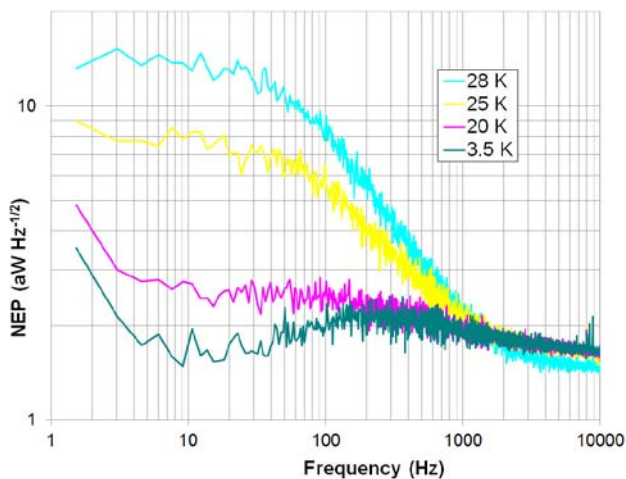
Fig. 14. Photon noise detected at different illuminator temperatures. In this case the detector was biased at $R/R_N \approx 0.34$, where R is the TES resistance at its bias point and R_N is its normal-state resistance.
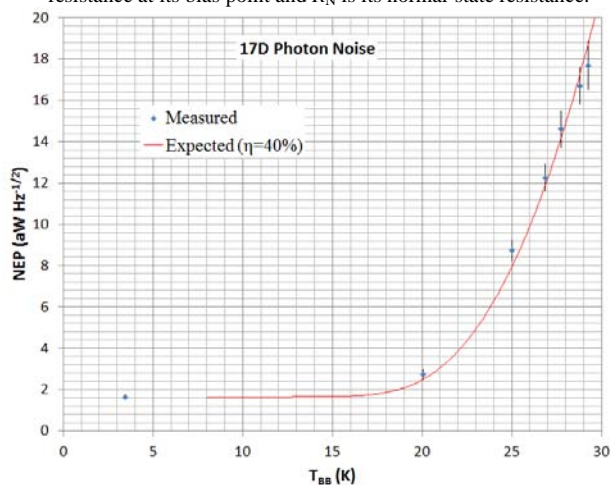

Fig. 15. Measured and expected photon noise.

E. Absorber Resistance

The SAFARI bolometers use a resistive film to couple to incident radiation. Radiation is dissipated in a thin film of Ta and the resulting temperature rise is detected by the TES. For efficient absorption the sheet resistance of this film should be close to the wave impedance of free space (~377 $\Omega/\square$). As can be seen in Fig. 1, there are Nb leads connected to the absorber which allow electrical measurements. We attached four wires to the absorber of one of the detectors and measured its resistance as a function of temperature. As shown in Fig. 16, the resistance of the film when in the normal state is 367 Ω, which is close to the required value. Comparing this with a measurement made three years previously, we find that the sheet resistance has increased by 30% in that time. This would suggest that the oxidation of the Ta film is self-limiting and that further passivation measures are not necessary. However, we shall continue to monitor the films over the coming years to confirm this. In Fig. 16 the resistance is plotted against the temperature of the detector table and the apparent transition temperature of the film is about 700 mK, which is lower than the expected value of 900 mK. It is likely that the actual temperature of the nitride island will be higher than the detector-table temperature.

Connecting the Ta absorber to the input coil of a SQUID should give us a more accurate estimate of the Ta film's transition temperature, by observing the change in Johnson noise between the resistive and superconducting states.
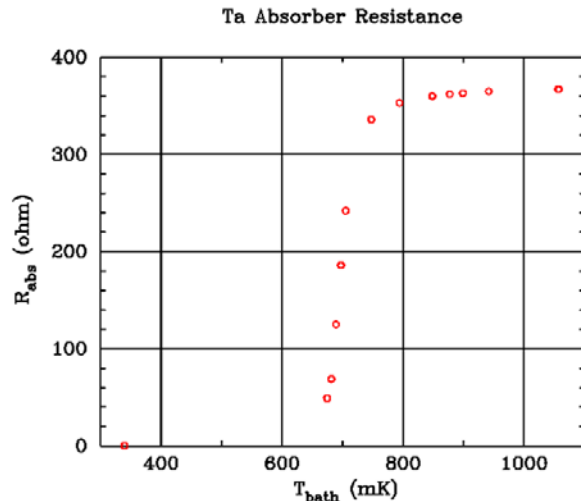

Fig. 16. Measured resistance, R_{abs}, of the Ta absorber on the detector as a function of the temperature of the detector-table, T_{bath}. The normal-state resistance is about 367 Ω.

VI. FUTURE ENHANCEMENTS OF THE TEST FACILITY

We have successfully measured the optical response of SAFARI prototype detectors all the way to saturation using the illuminator shown in Fig. 2. However, because of the low temperature of the black-body emitter (3.4—34 K), the passband of the short-wave detectors is illuminated by the Wien tail of the black-body spectrum. This means that only the long-wavelength end of the passband sees significant power. In order to illuminate the passband more uniformly with a black-body source, we need that source to have a much higher temperature. We thus plan to add a hot (200 K) source, with cold attenuation to reduce the power, as shown in Fig. 17. In addition, there will be a light-pipe to room temperature so that we can inject power from an external FTS or a modulated source. A reference detector will allow us to measure the spectral content of the radiation. The reference detector is a TES bolometer, similar to that shown in Fig. 1, suspended in a large absorbing cavity so that its optical absorption coefficient is flat over a broad wavelength range. The light-pipe, reference detector, and hot illuminator are attached to a reflective summing cavity that has a temperature of 4 K. A narrow light pipe leading to a hole in the center of the cold illuminator allows radiation from the summing cavity to illuminate the detectors under test. Both the hot and cold illuminators can be operated during the same cool-down,, allowing cross-calibration. This second-generation optical calibrator has been tested in a 4-K cryostat and will be integrated into the SAFARI Detector Test Facility in preparation for the optical tests of SAFARI prototype detector arrays.
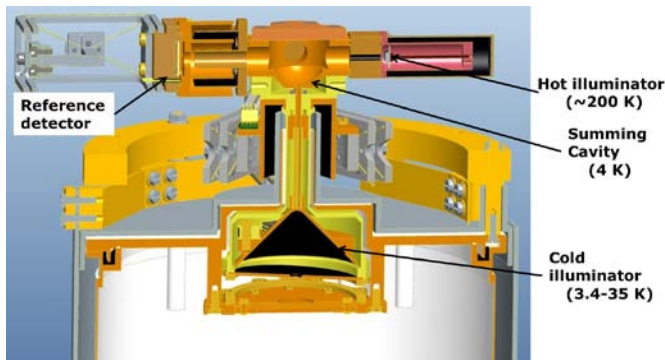
Fig. 17. Second-generation optical illuminator.

VII. DISCUSSION

A. Optical Efficiency

For the two detectors we calculated the optical efficiency from Equation 1, which assumes a single mode propagating through the feedhorn, and Equation 2. We obtained virtually identical efficiencies, η=40%, for both, even though the detectors have slightly different thermal properties. We note that this 40% efficiency is also consistent with the measured photon noise. From electromagnetic simulations we expect the efficiency of the horn/cavity/absorber combination to be 66% at 50 µm. The slightly lower measured value may be due to deviations from the ideal case simulated. In particular, we observe a ~50-µm misalignment between the spherical backshort and the absorber for both detectors. This misalignment might affect the optical efficiency. It is also possible that the gap between the detector and horn is different. Our estimate of the incident power assumes that the radiator is a perfect black body. This estimate is also critically dependent on our knowledge of the high-pass filter that defines the long-wavelength end of the passband.

We also note that the presence of the TES to one side of the absorber may have an effect on the optical efficiency. The sheet resistance of the TES seen by incoming radiation will be very low (~150 mΩ). In particular, it is possible that this could make the setup polarization-dependent. Measurements with a polarizer placed between the feedhorn and the illuminator will detect any polarization dependence.

It should be noted that the configuration tested here is different from that which will be used for the actual SAFARI detector arrays. In particular, instead of single- or few-moded feedhorns, SAFARI will use multi-mode collecting horns to achieve a high filling factor and optical efficiency. The optical efficiencies measured in this work are for a single mode feedhorn.

B. Excess Power at Low Illuminator Temperatures

As Fig. 11 shows, the detected power increases linearly with illuminator temperature in a very similar way for both the optical and dark detectors up to about 15 K. We have investigated this to determine its cause. One possibility we considered was that the current used to heat the illuminator was being detected by the SQUIDs. To check for this we reversed the direction of the current in the illuminator's heaters, but saw no change in the effect. We also ruled out the influence of the detector-table heater as a possible cause by taking data with the temperature free-running and no current through the heater: the effect was unchanged. We also considered whether the effect might be related to thermometry. The difference between the actual bath temperature of the detectors and the detector-table thermometer might depend on the thermal environment which could change as the power in the illuminator is ramped up. Since the thermal conductance of the detectors is about 3 fW/mK, a bath-temperature difference of less than 200 µK could reproduce the apparent 500-aW loading of the dark pixel that we see when the illuminator temperature is 15 K.

One obvious candidate for the cause of this effect is a long-wavelength light leak. We replaced the aperture in the 20-mK shield with a blank copper plate and measured the detected power at different illuminator temperatures. As shown in Fig. 11, the effect then disappeared. This would suggest that the effect is, in fact, due to a long-wavelength light leak. If this is the case, the long-wavelength radiation enters the detector cavities by some route other than through the feedhorn. One possible entry route is the electrical leads to the detectors. These enter the detector block through holes filled with loaded epoxy. The long-wavelength radiation must have a wavelength longer than about 90 µm or it would enter through the feedhorn also and be stronger in the optical pixel. More experiments are planned to investigate and eliminate this effect.

VIII. CONCLUSION

We have carried out optical measurements of two TES bolometers designed for SAFARI's short-wavelength band (33—60 µm) in combination with a spherical backshort and conical horn. Under the assumption of a single mode propagating through the horn we find an overall optical efficiency of 40% for both detectors, compared with a value of 66% calculated for an ideal model of this combination.

REFERENCES

[1] B. Swinyard., T. Nakagawa., P. Merken, P. Royer, T. Souverijns, B. Vandenbussche, C. Waelkens, et al. "The space infrared telescope for cosmology and astrophysics: SPICA A joint mission between JAXA and ESA." Experimental Astronomy, vol. 23, no. 1, 2008, p.p. 193–219.
[2] B. Jackson, P. de Korte, J. van der Kuur, P. Mauskopf, J. Beyer, M. Bruijn, A. Cros, et al "The SPICA-SAFARI Detector System: TES Detector Arrays With Frequency-Division Multiplexed SQUID Readout," IEEE Transactions on Terahertz Science and Technology, vol. 2, no. 99, 2011, p.p. 1–10.

[3] K. D. Irwin and G. C. Hilton,. "Transition-edge sensors", in *Cryogenic Particle Detection*, C. Enss, Ed., Springer, 2005, p.p. 81-97.

[4] M. D. Audley, D. M. Glowacka, D. J. Goldie, V. N. Tsaneva, S. Withington, L. Piccirillo, G. Pisano, et al. "Performance of a Microstrip-coupled TES Imaging Module for CMB Polarimetry," in *Proc. Twenty-First International Symposium on Space Terahertz Technology*, 2010, p.p. 76–84.

[5] P. Khosropanah, R. Hijmering, M. Ridder, J.-R. Gao, D. Morozov, P. D. Mauskopf, N. Trappe, et al. "TES Arrays for the Short Wavelength Band of the SAFARI Instrument on SPICA," in Proc. SPIE, 2012, submitted for publication.

[6] Leiden Cryogenics BV, Galgewater 21, 2311 VZ Leiden, The Netherlands, http://www.leidencryogenics.com.

[7] A. Beyer, M. Kenyon, P. Echternach, B. H. Eom, J. Bueno, P. Day, J. Bock, et al. "Characterization of an Ultra-Sensitive Transition-Edge Sensor for Space-Borne Far-IR/Sub-mm Spectroscopy," IEEE Transactions on Applied Superconductivity, vol. 21, no. 3, 2011, p.p. 199–202.

[8] M. D. Audley, G. de Lange, L. Ferrari,J.-R. Gao, R. A. Hijmering, P. Khosropanah, M. Lindeman, et al. "Performance of a Low-Noise Test Facility for the SAFARI TES Bolometer Arrays," Journal of Low Temperature Physics, vol. 167, 2012, p.p. 208.

[9] D. Morozov, P. D. Mauskopf, P. A. R. Ade, M. Ridder, P. Khosropanah, M. Bruijn, J. van der Kuur, et al. "Ultrasensitive TES Bolometers for Space-Based FIR Astronomy," IEEE Transactions on Applied Superconductivity, vol. 21, no. 3, 2011, p.p. 188–191.

[10] D. Drung., C. Aßmann, J. Beyer, A. Kirste, M. Peter., F. Ruede., and T. Schurig,). "Highly sensitive and easy-to-use SQUID sensors," IEEE Transactions on Applied Superconductivity, vol. 17, no. 2, 2007, p.p. 699–704.

[11] Magnicon GbR, Lemsahler Landstraße,171, D-22397 Hamburg, Germany; http://www.magnicon.com.

[12] K.D. Irwin, G. C. Hilton, J. M. Martinis, and B. Cabrera., "A hot-electron microcalorimeter for X-ray detection using a superconducting transition edge sensor with electrothermal feedback," Nuclear Instruments and Methods in Physics Research A, vol. 370, 1996, p.p. 177–179.

[13] P. F. Goldsmith, "Quasi-Optical Techniques," Proceedings of the IEEE, vol. 80, no. 11, 1992, p.p. 1729–1747.

Focal plane scanning-system design for SAFARI on Ground Calibration

Lorenza Ferrari, Axel Detrain, Pieter Dieleman, Martin Eggens, Robert Huisman, Willem Jellema,
Chris de Jonge, Wouter M. Laauwen, Lenze Meinsma, Heino Smit

Abstract—**The SpicA FAR infrared Instrument (SAFARI) is the far-infrared spectrometer for the SPICA satellite. Its 34 μm to 210 μm wavelength range is divided into three bands. Each bolometer consists of a Transition Edge Sensor (TES) and a resistive absorber on a thermally-isolated silicon nitride membrane. Each detector is placed in an integrating cavity with a feed-horn in the front. The readout of the TES arrays will be performed with SQUID based current sensors in frequency domain multiplexing configuration. One of the challenges of the SAFARI instrument development is the characterization of the Focal Plane Unit (FPU) models. For this FPU characterization a dedicated cryogenic test facility is being designed. The test cryostat will be equipped with a cryogenic XYZ translation system that will allow scanning the object focal plane, created inside the cryostat by a re-imager, and to determine the image/spot quality, field curvature, and image distortion. We present the concepts and components for the intended measurements, in particular, the plate scale characterization, point spread function, and stray-light.**

Index Terms—**Transition Edge Sensor, Focal plane characterization, Cryogenic XYZ scanner, Far-Infrared camera.**

I. INTRODUCTION

S AFARI is the Far-Infrared camera in the SPICA satellite, programmed to be launched in 2021[1]. It consists of an imaging Fourier Spectrometer with a 2'x2' Field of View (FoV) covering the 34- 210 μm wavelength region. This range is divided in three bands: Short Wavelength (SW) band between 34 and 60 μm, the medium wavelength (MW) band between 60 and 110 μm and the long wavelength (LW) band that spans from 110 to 210 μm. The detectors, TES bolometers [2], are required to exhibit a noise performance limited by the celestial background that translates into a detector NEP requirement of $2x10^{-19}$ W/√Hz. The total number of pixels is roughly 4000, determined by the Nyquist sampling of the FoV. Efficient readout of the high number of detectors is obtained by use of Frequency Domain Multiplexing (FDM)

[3], reaching a multiplexing ratio of 160.

SAFARI will represent, with the low background bolometers, (few attoWatts per pixel), one of the most sensitive space instruments, for which a full characterization and calibration is necessary. The characterization focuses on these main aspects: radiometry (described in detail in [4]) and image quality, measuring sky position of the pixels, frequency resolution and accuracy and to calibrate the spectrometer function of the instrument. Moreover critical issue such as EMI (Electro-Magnetic Interference) or stray light and micro-phonics effects can be investigated. This study is intended to enable an early optimization and verification.

A dedicated test facility is now being designed as part of the SAFARI on ground calibration program (see Fig. 1).In order to perform the above mentioned tests the following units are required: a reimager with similar optical properties as the telescope, a pupil scanner, a calibration source in the reimaged focal plane (OFP) and a XYZ scanner with a broadband source illuminating pinhole masks. For narrower bandwidth measurements a cryogenic etalon is employed.
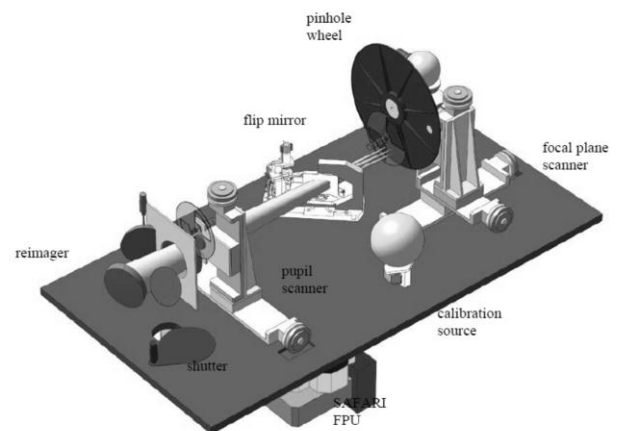

Fig. 1. OGSE (Optical Ground Support Equipment) layout within the SAFARI test cryostat. The plate is the optical bench where the test equipment is mounted. The FPU (Focal Plane Unit) is upside-down at the bottom. The FPU beam goes via the reimager and can be deflected towards the calibration source or the XYZ scanner system. The scanner moves a pinhole wheel back-illuminated by a signal source into the OFP.

In the following sections the strategy followed for focal plane (FP) characterization is described in details, in particular the requirements for the FP scanner.

II. OPTICAL CHARACTERIZATION TESTS

The FP optical characterization will be performed with the following measurements: pixel spatial response (PSF), focal plane geometry study and focal position, and stray light. The characterization setup allows for XYZ motion of a pinhole or pinhole array that are back-side illuminated by a signal source. Two measurement configurations are considered: FTS in 'home' position and FTS in scan mode. With the FTS in 'home' position the source signal is directly incident on the pixel arrays and the signal modulation is generated by means of a chopper; in this measurement configuration narrow spectral band-pass filters can be inserted into the optical path. The center frequencies of these filters are chosen to be at the low and the high edge of each wavelength band. In the scanning mode the filters are not used because the spectral content of the radiation incident on the pixels is determined by the FTS itself.

The signal source concept adopted is identical to the calibration source used for radiometry characterization. The principles are similar to that of the MIRI telescope simulator [5]. For the FP characterization the signal source will provide a spectrum that is flat within the SAFARI bands. This is achieved for temperatures of the hot source between 130 and 150 K. The power incident on an individual pixel is determined by the dimensioning of the source's integrating sphere in conjunction with the pinhole size. The required power on the pixel is about 50% of the TES saturation power assumed to be 4 fW; this power level ensures a sufficiently high signal-to-noise ratio and linear response of the detector. The principle XY scanning operation will be continuous as opposed to 'stepping and integrating'. The reason for this choice is twofold. Firstly, a continuous scanning with constant speed is expected to reduce vibrations. Secondly it will reduce the scanner motor power dissipation. In order to reduce the complexity of the scanner system the scan will be performed first in X and then in Y. The constant velocity is ensured in the desired range but the total scan range will be bigger (roughly 10% in both sides) to allow deceleration of acceleration of the motors. Based on the way of the operation and dissipation the motor can give a parasitic load equivalent to a black-body at a certain temperature. The requirements on the motor background is <10K during measurements. In addition a well-defined reference position associated with a certain pixel will be approached multiple times in all scans, such a procedure is necessary to mitigate drift-induced measurement errors. A redundantly measured line (an X scan or Y around a pixel) will be used to calibrate out errors due to time synchronization between scanner and detector readout or other systematic errors.

A. Z scan

The focal plane will be curved; as a consequence the position of the pinhole is not 'in focus' for all pixels in the reimaged FP. For further characterization as PSF the focus position needs to be identified. An initial Z scan for some XY positions (grid 5x5) in the focal plane is performed. This scan generates a matrix of weighting factors that allow for correction of the incident power distribution on 'out of focus' pixels. The XY scan, for the different Z positions, will be similar to the one described for the focal plane geometry. Moreover a low resolution FTS scan will be performed to extract the spectral information.

The field amplitude in the focal region is calculated using a Gaussian beam approximation [6] (see Fig. 2). The Z scanning range is between -20 mm and 200 mm. The asymmetric shape is chosen to limit the size of the cryostat. The lowest limit is determined by the FP radius of curvature, this value ensures to hit the focus position of each pixel while measuring the near field distribution. The highest limit is given by the long wavelength distribution in the far field. A measurement of 10 equidistant Z positions is enough to map the total field distribution. For each XY pixel the field distribution as a function of Z can be fitted with a Gaussian to extract the beam waist w (see Fig. 3). An accuracy of 100 µm in focal position can be reached. This will allow the verification of the instrument-tilting alignment requirements.
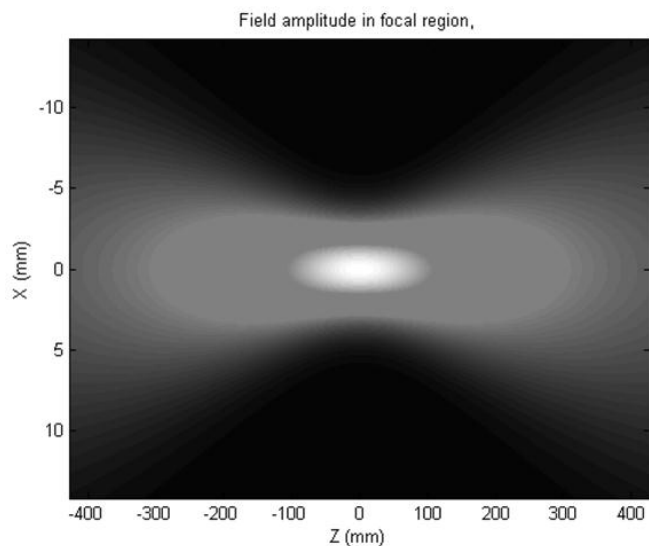

Fig. 2. Field amplitude in the focal region. The field in function of Z is calculated using a Gaussian beam approach.
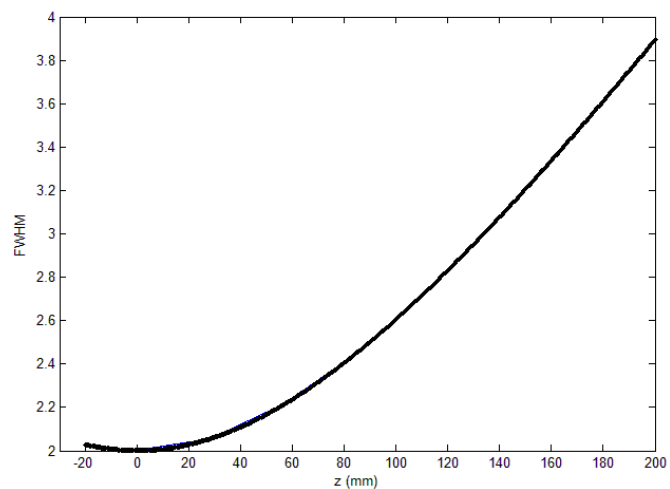

Fig. 3. Beam waist distribution in function of Z. The curve refers to the LW band array.

B. Pixel Spatial Response

The purpose of the spatial response measurement for individual pixels is to verify the image/spot quality, detector-

to-detector optical cross talk and to investigate in more detail pixels considered problematic. It is planned to measure the point spread functions of 20 pixels distributed over the FP area with one pinhole mask. The requirement in the detector spatial response accuracy and optical cross talk is to be within 1% of the model prediction. In order to avoid smearing of the point spread function a sampling criterion of Nyquist/10 is applied. This translates into a scanner constant speed of 60 µm/s for the SW band and 200 µm/s for the LW band. The relative positional accuracy requirement on the scanner is 5 µm to meet the above specification of 1%. This precision can be reached only with a good calibration of the scanner system at the cold in a separate campaign before the measurements. The pinhole sizes are calculated from the convolution of the OFP Airy disk and various pinhole patterns and for an etalon bandwidth of roughly 100 GHz (see Fig. 4). The optimum pinhole sizes for the 3 wavelength bands are found to be: 120 µm for the SW band, 220 µm for the MW band, and 400 µm for the LW band.
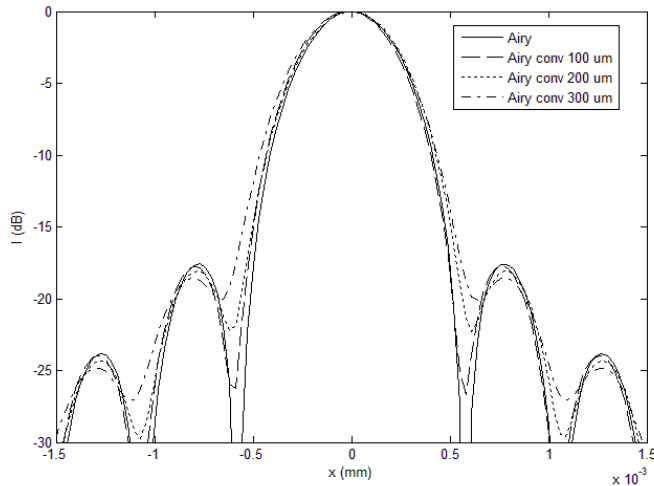

Fig. 4. Convolution of Airy disk in the OFP with various pinhole sizes for a 3% bandwidth etalon. The Airy disk calculated is for the SW band.

C. Focal plane geometry

The FP geometry characterization is based on scans of the full FP. The positions of all pixels of the array need to be determined so that they can be translated in position on sky. Arrays of pinholes will be used to reduce the measurement time for this investigation. The second advantage of using an array of pinholes to illuminate the reimaged focal plane is that image distortions can be directly measured. The optimum distance between the pinholes is calculated taking a figure for the distortion of the Airy pattern of both the instrument and the OGSE; this together gives an estimate of the tail of the PSF for each pixel. In order to avoid overlapping of pinhole illumination the neighboring pinhole in the mask is positioned at < 0.1 % of the PSF peak. This level is calculated assuming a Strehl ratio of 0.8 for the reimager and FPU combined [7] (see Fig. 5). The resulting distances between pinholes in the masks are 3 mm for the SW band, 5 for the MW and 7 mm for the LW band. The requirement with respect to the detector focal plane geometry accuracy is to be within 5% of the model prediction; that translates into less stringent requirements compared to the measurement of the PSF for the centroid and extension of the Airy disks.

When using a pinhole mask each sub-scan should ensure as part of the scanning strategy the overlap of first pinhole with the second one. In this way errors due to non-flat illumination of the pinhole mask can be removed.
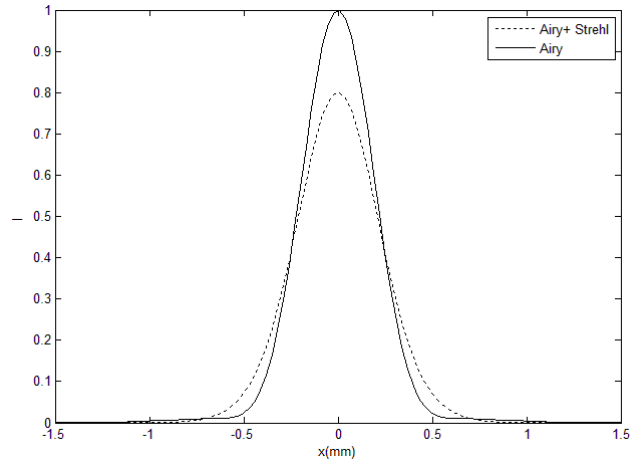

Fig. 5. Comparison between the ideal SW Airy and the Strehl version.

D. Stray-light verification

Stray light tests are performed both in the pupil as well as in the object focal plane. In the OFP one can discriminate two categories: 'in-field' and 'out of field' stray light. Here, in-field stray light refers to optical cross talk between illuminated pixels and nominally non-illuminated pixels. The entire FP will be mapped using a mask with a single pinhole. In contrast out of field stray light refers to parasitic illumination of pixels when the source is positioned out of the expected field of view. The test for this category of stray light is done by scanning with a single pinhole the outer perimeter of the FP, the area scanned will be extending outwards in both directions for a distance of 30% of the FP dimension. This distance is determined by the baffle positions in the cryostat. A larger illumination power compared to the in-field stray-light test has to be used. The pinhole size can be calculated assuming to have a source of 150 K in the cryostat and assuming to get a signal on the TES of a few fW for all bands (see Fig. 6). The size is set to about 1 mm.
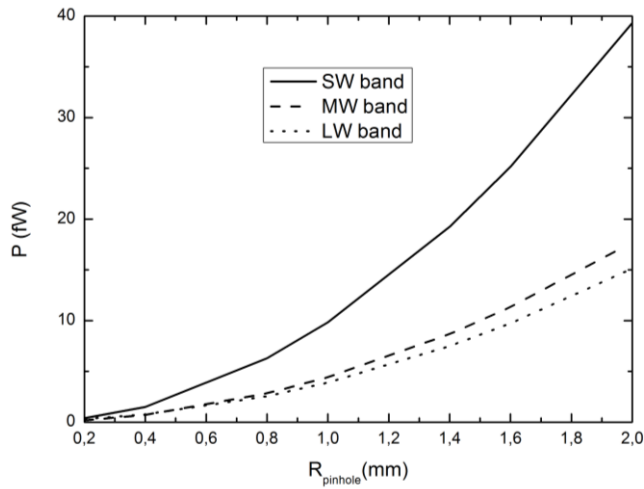
Fig. 6. Optical loading on the TES bolometers for the 3 bands in function of the pinhole sizes.

III. CONCLUSION

The requirements for a cryogenic FP scanner are determined as part of the SAFARI on ground calibration program. The system designed has to perform the optical characterization of .the SAFARI FPU. The hardware is now in definition phase with an accurate study of the scanner mechanisms.

REFERENCES

[1] B. Swinyard et al, "The space infrared telescope for cosmology and astrophysics: SPICA A joint mission between JAXA and ESA" in *Exp Astron*, 2009, pp 193-219.
[2] K. Irwin and G. Hilton, TES chapter.
[3] R. den Hartog et al, "Frequency Domain Multiplexed Readout of TES Detector Arrays with Baseband Feedback", *IEEE Transactions on Applied Superconductivity*, 2011, vol. 21 n.3.
[4] W. M. Laauwen, M. Eggens, W. Jellema, C. de Jonge, L. Meinsma, P. Dieleman, "Development of a Calibration Source for SAFARI on-ground calibration", this proceeding.
[5] T. Belenguer et al, "MIRI Telescope Simulator", *SPIE*, 2008, 7010-39
[6] P.F. Goldsmith, *Quasioptical systems,* IEEE Press
[7] Marc Ferlet private communication

SQUID current sensor to read out the TES-bolometers arrays for SAFARI

J. Beyer[*], D. Drung, J. H. Storm, M. Regin, M. Fleischer-Bartsch, M. Schmidt

Physikalisch-Technische Bundesanstalt, Berlin, D-10587, Germany

* Contact: joern.beyer@ptb.de, phone +49-30-3481 7379

Abstract— **The SpicA FAR-infrared Instrument (SAFARI) will use large-format arrays of bolometers based on transition-edge sensors (TESs). The SAFARI detectors will be operated at a temperature of 50 mK in order to meet the aspired very low noise equivalent power levels of ~2e-19 W/sqrt(Hz). The readout of the TES arrays will make use of SQUID based current sensors in a current-summing frequency division multiplexing configuration. The allowable readout contribution to the total detector noise and to the cross-talk between pixels, the envisaged multiplexing ratio (~160) and the refrigerator setup translate into a set of requirements for the SQUID sensor regarding its coupled energy sensitivity, maximum power dissipation and analog signal bandwidth. Furthermore, the current sensor configuration should ensure sufficient noise margin to a semiconductor amplifier at 135K and address potential electromagnetic interference along a ~6m cryo-harness in between the SQUID output and the amplifier. A concept for the SAFARI current sensor based on a 2-stage SQUID cascade consisting of a front-end operated at 50mK and a signal booster with differential output located at 1.7K has been developed. Single-SQUID front-ends and serial-parallel SQUID arrays as the signal booster stage have been fabricated and tested at their foreseen operational temperatures. Their characteristics support the feasibility of the current sensor concept and allow estimations of the overall noise and dynamic performance that are consistent with the TES array readout requirements.**

Tunable speed single-photon THz nanobolometers

B.S. Karasik[1*], D.F. Santavicca[2], D.E. Prober[2], and A.V. Sergeev[3]

1 Jet Propulsion Laboratory, California Institute of Technology, Pasadena, CA 91109, USA
2 Dept. of Applied Physics, Yale University, New Haven, CT 06520, USA
3 Dept. of Electrical Engineering, SUNY at Buffalo, Buffalo, NY 14260, USA
* Contact: boris.s.karasik@jpl.nasa.gov, phone +1-818-393-4438

Abstract—— **The superconducting hot-electron nanobolometer (nano-HEB) has been demonstrated to be the most sensitive detector of sub-mm/THz radiation with a recently achieved optical NEP = 3×10^{-19} W/Hz$^{1/2}$. Beside its impressive sensitivity in the power detection mode, additional improvements are expected in the photon counting mode. The latter will be possible for wavelengths less than 300 µm where the minimum detectable energy of a submicron-size bolometer becomes much smaller than the photon energy. With the proper thresholding, such a photon counter becomes nearly "noiseless" with the sensitivity limited by the photon statistics only. Given the very low rate of the background photons arriving on space spectrometers (e.g., SPICA/BLISS), photon counting operation is very attractive for achieving the NEP ~ 10^{-20} W/Hz$^{1/2}$ with the advantages of high dynamic range (40-60 dB) and higher operating temperature compared to micromachined TES.**

We have already achieved extremely small Ti nano-HEBs with the dimensions 0.3µm x 0.1µm x 20 nm, critical temperature ~ 300 mK, and large critical current. Currently, a single-photon detection experiment utilizing a 3-THz quantum cascade laser as a gated pulsed source is in progress. The nano-HEB devices can be used throughout the entire far-IR range (30-300 µm) where planar microantennas are available.

A novel element of our development effort is engineering of the photon-counter speed using a controllable cooling of electrons in a sensor via microwave photon emission. In its original version, the nano-HEB relies on the electron-phonon cooling process with the characteristic time ~ a few µs at 300 mK and a T^4 temperature dependence. Operating below 300 mK reduces the detector noise but also slows it down significantly. A small microwave circuit integrated with the sensor allows for emission of the 1D blackbody radiation of hot-electrons in the frequency range kT/h ~ GHz into a small heat-sunk resistor. The process bypasses the electron-phonon cooling and increases the count rate limit to ~ 2 Mcps independent of the temperature. Even a much higher speed (~ 10 Gcps) can be realized in such nanodevices when normal metal contacts are used to enhance the electron diffusion. The latter, however, requires new approaches for low-noise and broadband readout since SQUID amplifiers cannot be that fast.

Realization of a ~ 1000-pixel nano-HEB photon-counting array with an adequately fast microwave SQUID multiplexed readout is now quite feasible. Another area of interest for these devices may be in the single-photon THz interferometry.

Development of TES Bolometers with High-Frequency Readout Circuit (on-line issue)

Artyom A. Kuzmin, Sergey V. Shitov, Alexander Scheuring, Johannes M. Meckbach,
Konstantin S. Il'in, Stefan Wuensch, Alexey V. Ustinov and Michael Siegel

Abstract—**In order to improve the frequency division multiplexing in transition-edge sensor (TES) arrays, it is suggested to replace commonly used SQUID amplifiers with a semiconductor high-frequency cooled amplifier. This would result in a single 10-GHz bandwidth amplifier serving up to and possibly more than 1000 TES detectors of an imaging array. The basic idea is to implement an antenna-coupled TES as a load for high-Q resonator, weakly coupled to an RF throughput line. To verify new concept, prototype TES absorbers made of Ta and Nb films are developed and tested above 4 K. The NEP of about 1.5×10^{-15} is estimated for experimental micron-size prototype devices made of Nb at 4.5 K. The *IV*-curves of the absorber at different temperatures are recovered; presence of negative electrothermal feedback is verified that may qualify the new approach as "TES with GHz readout".**

Index Terms—**Frequency division multiplexing, FDM, transition edge sensor, TES, bolometer, electrothermal feedback, imaging array, high-Q resonator, terahertz range.**

I. INTRODUCTION

THE superconducting bolometers based on transition-edge sensing (TES) are nowadays of active interest, due to their great potential for ultra-low-noise operation with noise equivalent power (NEP) down to 10^{-19} W/Hz$^{0.5}$ and below [1]. Usually TES acts as a thermometric device, which changes its resistance abruptly near the temperature of the superconducting transition, thus detecting the power coupled to the attached absorber. The antenna-coupled TES devices are relatively new;

they comprise absorber and thermometer in the same sub-micron-sized film [2]-[4]. In fact, it is a bad thermometer, which is operated with too high probe current. Under such condition a little extra current from the feeding antenna combined with the probe current makes a noticeable effect. In order to read out the imaging array, the frequency division multiplexing method (FDM) [5] is tested successfully with practicable systems for more than 1000 pixels. However, the restricted bandwidth of SQUID-sensor sets a limit for FDM for about 100 channels.

II. CONCEPT AND APPROACHES

A. General Idea

To improve the capability of the multiplexing circuit, we suggest to go for a higher frequency band [6]. This could result in creating a relatively simple system, containing just single amplifier (connected to room with only one or two coaxial cables), which serves up to 1000 or even more TES detectors of an imaging array integrated with the FDM filter system. In fact, it is suggested to replace the low-frequency wires and lumped LC circuits with coaxial cables and RF IC's. TES-loaded Resonant Circuit.

The basic idea is to use the high-Q resonator technology, which is similar to one used for microwave kinetic inductance detection (MKID) [4]. We suggest reading the response caused by variations in resistivity of the tiny antenna-coupled TES absorber inserted in the quarter-wave resonator. The equivalent scheme of such resonator is shown in Fig. 1. When the extra heat is provided from the THz antenna, the resistance of the absorber will grow, and the Q-factor will change, changing the RF throughput signal. Such joint heat effect can be expected
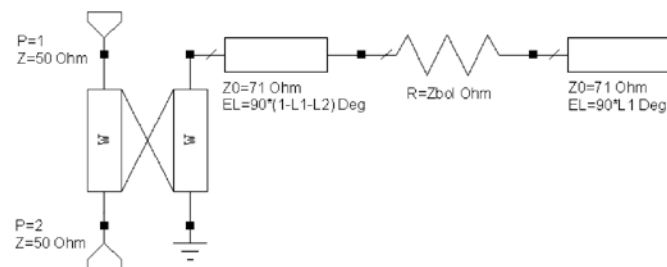

Fig. 1. Equivalent scheme of RF driven TES bolometer. The *open-end* quarter-wave resonator ($Z0 = 71$ Ohm) is weakly coupled to the throughput line (ports P1 and P2, Z = 50 Ohm). The resonator is split in two arbitrary parts *L1* and *L2* (*L1* + *L2* ≈ 1) by the inserted antenna-coupled TES absorber (Zbol).

when the bolometer/absorber are slow enough.

The new approach might bring a few advantages over both traditional MKID and TES. i) Better signal coupling, since the TES absorber is a lumped resistor, which is definitely easier to match to the receiving antenna. ii) TES is generally independent of receiving frequency, since only the heat effect is important. iii) In respect to present TES technology, the *open-end* high-Q resonator will provide almost perfect protection of the nanometer-scale absorber from electrical shocks including static discharge, since there is no wire chain connected to the absorbing film and the effective capacitance of the RF "connection" is extremely small.

B. *Design Approach and Estimate for Ultimate Sensitivity*

To evaluate the new concept, we design a prototype detector circuit operated at temperature 280-300 mK. The TES absorber can be made of thin (20-30 nm) films of Titanium (Ti, T_c about 300 mK), which demonstrated a pronounced effect of electron gas heating at this temperature [7]. The compact THz-range double-slot antenna [8] loaded with TES absorber is placed in the CPW resonator and then positioned in the focus of hyper-hemispherical lens.

We have estimated the sensitivity of the new device using S-parameters of a particular layout and its EM-model. Setting the noise figure for the cooled LNA as $T_N = 3$ K, which surely dominates the noise of the 300-mK device, we get for the whole detector-amplifier chain $NEP = 1.6 \cdot 10^{-19}$ W/Hz$^{1/2}$. This result [6] is encouraging enough to be verified experimentally.

III. EXPERIMENTAL DETAILS AND DISCUSSION

A. *Fabrication*

Since the low-temperature experiments are quite laborious, expensive and time consuming, we decided to verify our EM-model and most basic approaches, at 4-K temperature level. A pilot device was designed and fabricated using thick (200 nm) Nb with $T_c = 8.8$ K for the throughput line and quarter-wave resonator. The films of Nb were sputtered in UNIVEX 450 magnetron sputtering system with deposition rate 0.27 nm/s.

The geometry of the device was formed by standard contact photolithography. At the first step thin (15 nm) Nb film was deposited on the whole sapphire substrate. At the second step the throughput line, CPW resonator and planar antenna were patterned from a thick (200 nm) Niobium film by lift-off process. Finally, the TES bridge with sizes of $5 \times 2.5 \times 0.015$ µm^3 was formed by etching away the bottom layer with Ar$^+$ ion gun.

B. *DC measurement*

Since the small Nb bridge of the TES absorber is completely decoupled at DC, the measurement of its superconducting and thermal properties were done using witness structures of the same size and fabricated on the same wafer as the resonators. The optimized witness bridges had critical temperature $T_c = 6.7$ K and transition width $\Delta T_c = 50$ mK. TES absorber has

volume $v = 5$ µm $\times 2.5$ µm $\times 15$ nm. The NEP as low 1.5×10^{-15} W/Hz$^{1/2}$ can be estimated at 4.5 K.

The estimate for time constant gives $\tau = C/G_{th} \approx 0.5$ ns, where C is calculated from material parameters as in [9], is in good agreement with the value in Nb HEBs [10]. Referring to the value of τ, one may suggest experimental study the bias frequency higher than 4 GHz.

C. *RF measurements*

The frequency response at 4 K is measured with the Agilent PNA-X series network analyzer with incident power ranged from -27 dBm up to +6 dBm. Figure 2 presents the effect of hot-spot response to a high power signal, with current amplitude close to the I_c of the TES absorber. The response did not change below the power range presented in the inset for Fig. 2, since the absorber remains in the superconducting state. The Q-factor of about 7000 can be estimated from the graph, along with both the dip and the resonant frequency close to their design values of -0.8 dB and 5.85 GHz respectively. These data have validated the RF design successfully.

D. *Discussion on Regime of Operation*

To prepare the optical sensitivity measurements, we have to go for low-power regime. The dynamic model of the system is developed along with procedure for extraction of *IV*-curve at RF. The dynamic model exploits the *S*-parameters of the structure along with physical parameters of the absorber, including $R(T)$ for the particular experimental batch (for its witness device, actually).

We found that for the case of $R/R_{emb} < 1$ the operation is unstable, since the resonator acts as a current source, so we got *positive* electrothermal feedback. This is exactly what we can see in the experiment (see Fig. 2) – fast triggering from very low (nearly zero) resistivity to the normal state – hot-spot nucleation in the middle of the dip. In case of $R/R_{emb} > 1$ the resonator
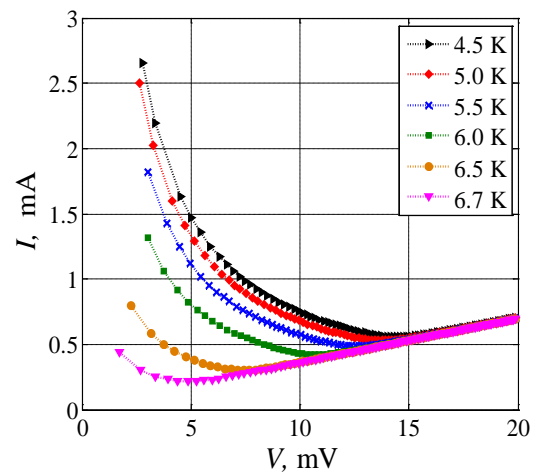

Fig. 3. *IV*-curves of experimental TES absorber calculated using *S*-parameters of EM-model. Each point is a self-consistent solution for the dependence $P(R(T_e(P,T_{bath})))$ for various bath temperature T_{bath} (see inset) and scanning incident power P across the absorber.
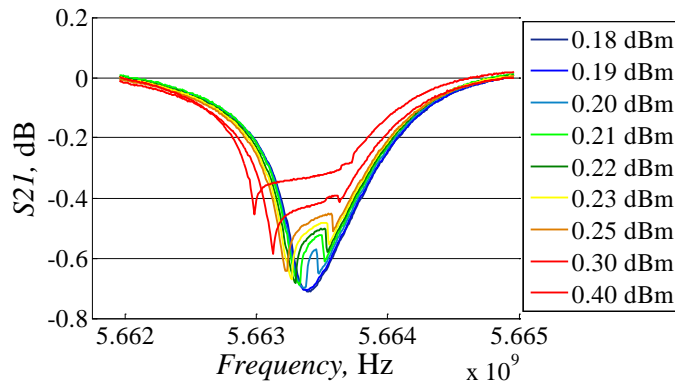
Fig. 2. Frequency dependence transmission of the throughput line of the Nb TES-loaded resonator device at bath temperature about 5 K. The triggering to hot-spot regime occurs at the same RF power. The two lowest dips correspond to superconducting state of the resonator, its Q-factor can be estimated to $Q = 7000$.

acts as a voltage source. Here we got *negative* electrothermal feedback.

To estimate *IV*-curves of our RF-connected devices, we have searched for self-consistent solutions for RF power *P* and resistance *R* across the absorber as $P(R(T_e(P,T)))$. The RF power transfer to TES absorber is calculated using S_{31}-parameter of EM-model. Each point in Fig. 3 is a self-consistent solution for various bath temperatures T_{bath} and scanning incident power P_{in} at the input of the throughput line. These *IV*-curves are very similar to ones reported for HEB mixers and traditional (low-frequency) TES bolometers, which are stabilized with negative electrothermal feedback. From these data one may clearly conclude that the new device is indeed a TES bolometer operated at GHz bias frequency suitable for combination in large imaging arrays served with fewer cooled semiconductor LNA's.

REFERENCES

[1] K. D. Irwin and G. C. Hilton, "Transition-edge sensors," in *Cryogenic Particle Detection,* Topics Appl. Phys., vol. 99, Ch. Enss, Ed., Berlin: Springer-Verlag, 2005, pp. 63-149.

[2] S Ali, L. D. Cooley, D. McCammon, K. L. Nelms, J. Peck, D. Prober, D. Swetz, P. T. Timbie, and D.van der Weide*, "*Planar Antenna-Coupled Transition-Edge Hot Electron Microbolometer", *IEEE Trans. Applied Supercond.*, vol. 13, no. 2, June 2003.

[3] Daniel F. Santavicca, Matthew O. Reese, Alan B. True, Charles A. Schmuttenmaer, and Daniel E. Prober, "Antenna-Coupled Niobium Bolometers for Terahertz Spectroscopy," *IEEE Trans. Applied Supercond*. vol. 17, no. 3, June 2007.

[4] J. Wei, D. Olaya, B. S. Karasik, S. V. Pereverzev, A. V. Sergeev, M. E. Gershenson, "Ultrasensitive hot-electron nanobolometers for terahertz astrophysics", *Nature Nanotechnology* vol. 3, pp. 496 – 500, 2008

[5] Ian S. McLean, "Instrumentation and detectors" in *Electronic imaging in astronomy*, 2nd ed., Springer and Praxis Publishing, UK, 2008.

[6] S. V. Shitov, "Bolometer with high-frequency readout for array applications," Technical Physics Letters, 2011, Vol. 37, No. 10, pp. 932–934. Original Russian text published in Pis'ma v Zhurnal Tekhnicheskoi Fiziki, 2011, Vol. 37, No. 19, pp. 88–94. DOI: 10.1134/S1063785011100117 http://www.springerlink.com/content/c0j 57m70w0m37607/

[7] P. Day, H. leDuc, B. Mazin, A. Vayonakis, J. Zmuidzinas,"A broadband superconducting detector suitable for use in large arrays" *Nature,* vol. 425, pp. 817–821, 2003.

[8] D. F. Filipovic, S. S. Gearhart, and G. M. Rebeiz, "Double-slot antennas on extended hemispherical and elliptical silicon dielectric lenses," *IEEE Trans. Microw. Theory Tech.*, vol.41, no.10, pp. 1738-1749, Oct. 1993

[9] P. J. Burke, R. J. Schoelkopf, D. E. Prober, A. Skalare, B. S. Karasik, M. C. Gaidis, W. R. McGrath, B. Bumble, and H. G. LeDuc, "Mixing and noise in diffusion and phonon cooled superconducting hot-electron bolometers", *J. Appl. Phys.*, vol. 85, no. 3, pp. 1644–1653, 1999.

[10] E. M. Gershenzon, M. E. Gershenzon, G. N. Gol'tsman, A. M. Lyul'kin, A. D. Semenov, and A. V. Sergeev, "Electron-phonon interaction in ultrathin Nb film", *Sov. Phys. JETP*, vol. 70, no. 3, pp.505–511, 1990.